

V. Advanced Battery Materials Research (BMR)

V.A Introduction

The Vehicle Technologies Office (VTO) supports focused fundamental research to identify, develop and analyze new materials for high-performance, next-generation, rechargeable batteries for use in HEVs, PHEVs, and EVs. Over the last few years the focus has shifted to EV applications in response to the EV Everywhere Grand Challenge targets. These efforts were previously under the umbrella of the Batteries for Advanced Transportation Technologies (BATT) Program. In the beginning of FY2015, the BATT Program was reorganized and transitioned to the Batteries Materials Research (BMR) Program. The goal of the BMR Program is to develop long-life batteries that are superior to commercial Li-ion systems (graphitic anode and metal oxide cathodes) in terms of cost, vehicle range, and safety.

Background and Program Context

The BMR Program addresses the fundamental problems of electrode chemical and mechanical instabilities that have slowed the development of affordable, high performance, automotive batteries. The aim is to identify electrode/electrolyte materials that yield enhanced battery performance and lead to greater acceptance of electric vehicles. The Program not only supports research that leads to improvements to existing materials, but also investigations into high-risk “leap-frog” technologies that might have a tremendous impact in the marketplace. Novel diagnostics and modeling methods are employed to gain a better understanding of key factors that limit cell and material performance and to provide guidance in designing next-generation materials. Once promising materials are identified, materials are then evaluated in small prototype research-cells. If good cell performance is validated, novel materials and preliminary cell designs are then transitioned to the Advanced Battery Research (ABR) Program within the VTO for further development, scale-up and assessment. An overview of the approach used in the BMR program is shown in Figure V- 1.

Solving applied problems using a fundamental approach

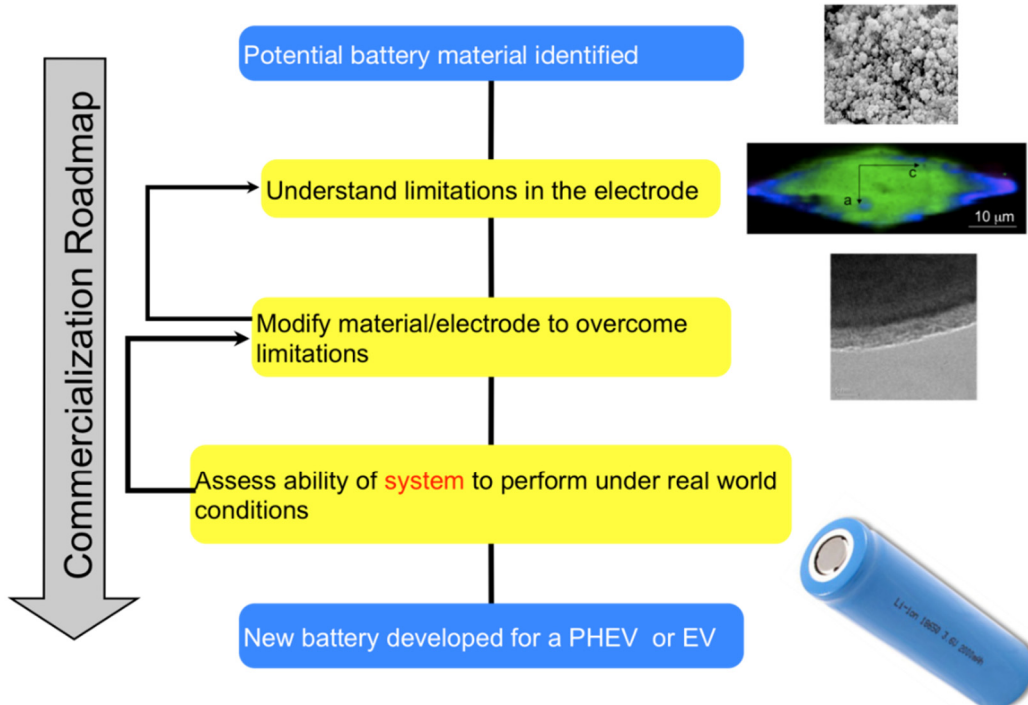


Figure V- 1: BMR approach overview

The BMR program has a portfolio of topics to ensure success in the short, intermediate, and long term. The focus is on optimizing all three components of the battery, namely, the anode, cathode and electrolyte. To aid in these activities, the BMR program integrates three cross-cutting techniques: (i) advanced mathematical modeling, including tools across multiple length scales, (ii) diagnostics, especially *in situ* techniques to understand the behavior of the materials, and (iii) electrochemical characterization, to ensure that material level understanding can be translated into device-level performance. The program funds a multidisciplinary team of world-renown researchers using state-of-the-art equipment and facilities. In the pursuit of their activities, the BMR investigators push the boundaries on advanced battery technology by developing better tools and techniques to address the challenges. The structure of the BMR program and the areas of focus are illustrated in Figure V- 2. A summary of the individual tasks is listed below.

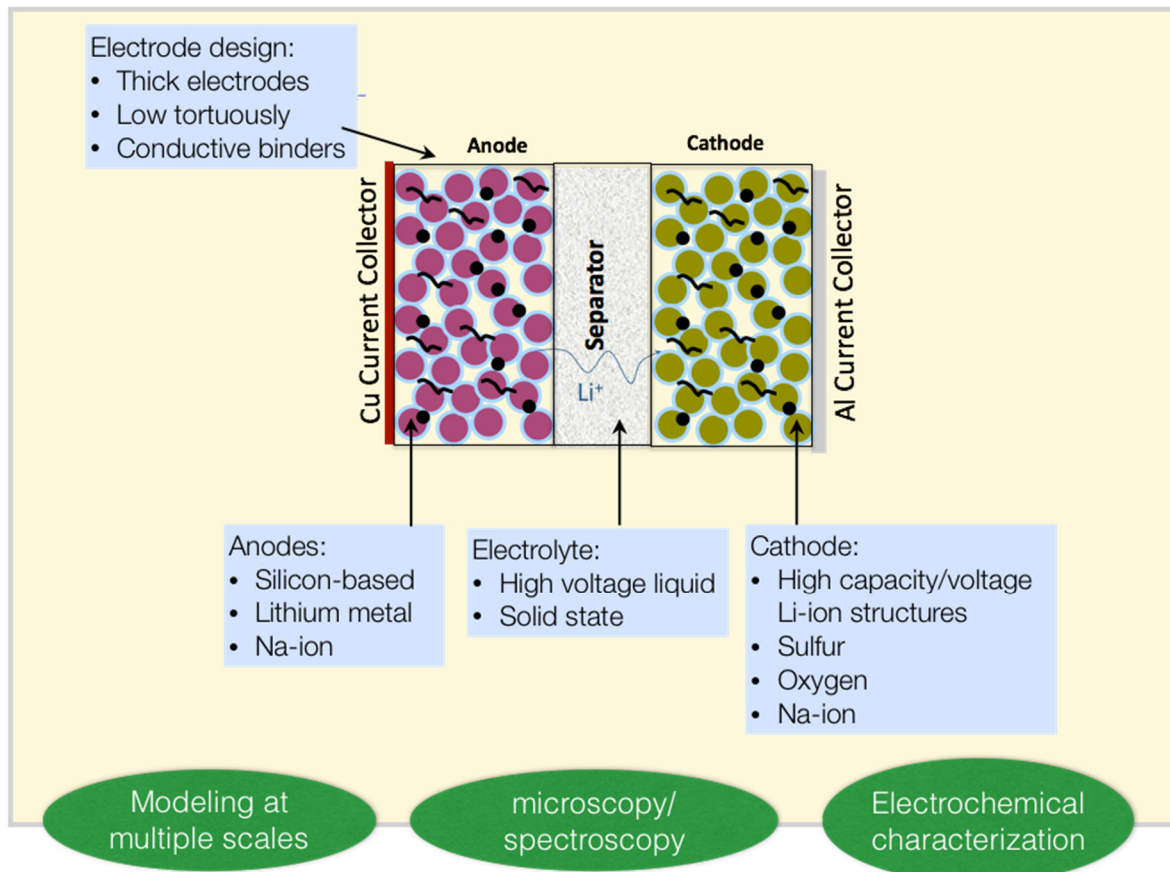


Figure V- 2: Areas of focus in the BMR program with materials discovery aided by modeling and diagnostics

Task 1: Advanced Electrode Architectures involves understanding the performance, life, and abuse tolerance of battery electrodes using advanced electrochemical techniques. In addition, the tasks also focus on finding ways to redesign the electrode architecture and extract more energy and power from existing materials, for example, by increasing the thickness of the electrodes. Emphasis is placed on understanding how electrodes behave and using this knowledge to decrease the tortuosity and increase the thickness of the electrodes. Projects are presently concentrating on graphite and silicon-based anodes, and on metal oxide cathodes.

Task 2: Silicon Anode research focuses on finding ways to enable the use of silicon as an anode material to take advantage of the order of magnitude extra capacity compared to currently-used graphite anodes. A big issue with this system is the large first-cycle irreversible capacity loss due to the formation of the solid electrode interface (SEI) and the large volume expansion when intercalating silicon. Efforts are focused on prelithiating the anode to compensate for this loss.

Task 3: High Energy Density Cathodes for Advanced Li-ion Batteries aims to find novel cathode materials and processing methods that offer significant improvements in volumetric and specific energy and/or power over current state-of-the-art materials, like $\text{Li}(\text{NiCoMn})_{1/3}\text{O}_2$. Current projects include work on the high-voltage, high-energy layered/layered or Li rich cathode materials, investigating Li bearing mixed polyanion glasses,

investigating polyanions that may cycle more than one Li ion per transition metal ion (e.g., silicates), optimization of ion transport in high-energy composite cathodes, and developing *in situ* reactors designed to investigate solvothermal synthesis reactions in real-time using synchrotron-based tools.

Task 4: Electrolytes for High-Voltage, High-Energy Li-ion Batteries aims to increase the oxidative voltage stability of presently-used electrolytes to take advantage of the higher capacity achievable at these potentials in addition to increasing the energy *via* the voltage increase. The present focus is on fluorinated electrolytes and electrolytes that allow stable cycling of silicon anodes.

Task 5: Diagnostics involve the use of advanced techniques, such as Fourier transform infrared (FTIR), X-ray absorption fine structure (XAFS), X-ray diffraction (XRD), and nuclear magnetic resonance (NMR) to investigate interfacial and micro-scale failure mechanisms in Li-ion batteries. Projects often use DOE's user facilities and include advanced *in situ* diagnostic techniques, study of interfacial processes, *in situ* electron microscopy of electrical energy storage materials, microscopy investigation on the fading mechanism of electrode materials, and NMR and pulse field gradient studies of SEI and electrode structure.

Task 6: Advanced Electrode Material Modeling spans multiple length scales from *ab initio* methods to continuum-scale techniques. Models are combined with experiments and extensive collaborations are established with experimental groups to ensure that the predictions match reality. Efforts are also focused on obtaining the parameters needed for the models either from lower length scale methods or from experiments. Projects emphasize pushing the boundaries of the modeling techniques used to ensure that the task stays at the cutting edge. Projects are focused on discovery of new cathodes materials, predicting SEI structure and behavior, understanding limitations in Li-S systems, and understanding the impact of electrode processing on performance.

Task 7: Metallic Lithium and Solid Electrolytes aims to solve the long-standing problems of lithium metal anodes: dendritic growth and poor efficiency during cycling. Approaches include protection layers based on ceramic single-ion conductors, ceramic/polymer hybrid membranes, nano engineering the surface to protect the anode, and changing the electrolyte composition to improve cycleability. Focus areas include surface reactions, decreasing the impedance at the interface, understanding the nature of the surface instability, and fabricating devices. A major emphasis is on looking at the interplay between mechanical, electrochemical, and structural relationships and get at the heart of the interfacial challenges with the metal anode.

Task 8: Lithium Sulfur Batteries focuses on solving the problems related to the sulfur cathode, especially the migration of polysulfides to the anode. The areas of focus include: (i) encapsulating the sulfur in polymer, carbon matrices, (ii) protecting the Li metal to prevent side reactions with polysulfides, (iii) changing the cathode by additives and other substitutions, and (iv) understanding the reactions using x-ray spectroscopy and *ab initio* and mesoscale modeling. The goal is ensuring stable cycling without the detrimental effects of the dissolution/precipitation reaction.

Task 9: Li-Air Batteries aims to solve the issues related to this very promising, yet high-risk system. The approaches taken include: (i) changing the electrolyte composition, (ii) using a molten salt as an electrolyte, and (iii) understanding the mechanisms that limit the system. The projects are specifically chosen to ensure that the most important challenges are examined and a path forward identified.

Task 10: Na-Ion Batteries seeks to understand the fundamental mechanisms in Na-ion based systems. Na-ion systems promise to be lower cost than Li-ion, assuming new anode, cathode, and electrolytes can be found. Due to the high-risk nature of the project, the BMR program uses this project to ensure that it stays abreast with the challenges in the system.

V.B Advanced Electrode Architectures

V.B.1 Physical, Chemical, and Electrochemical Failure Analysis of Electrodes and Cells (LBNL)

Objectives

This project investigates failure modes of targeted chemistries as defined by the BMR Program and its Focus Groups. The emphasis of this effort for 2015 will be on materials designed for high-voltage. The objectives are to identify and quantify the chemical and physical aspects of cell cycling and aging that lead to reduced electrochemical performance.

- Research will focus on the effects on material stability as a result of increasing the cell voltage of Li/High Voltage Chemistry cells from 4.2 to 4.5 V
- Research will focus on the effects of “high-voltage” electrolytes on the performance of cathodes pushed to 4.5 V.
- Research will focus on the effects on cell performance when the lithium electrode is replaced with a graphite electrode of comparable capacity as the cathode and the cells are pushed to 4.4 V.

Project Details

Vince Battaglia (Lawrence Berkeley National Laboratory - PI)

Energy Storage and Distributed Resources Division
1 Cyclotron Road
Berkeley, CA 94720
Phone: 510-486-7172; Fax: 510-486-4260
E-mail: vsbattaglia@lbl.gov

Start Date: October 2011

Projected End Date: October 2015

Technical Barriers

- Preparing electrodes that cycle well despite changes to the active material.
- Preparing full cells that cycle well.
- Preparing cells where one can distinguish if gassing is occurring.
- Ability to assess different forms of cell failure
 - Due to resistance rise
 - Due to side reactions
 - Due to loss of Li sites in the active materials

Technical Targets

- Performance: Specific energy – 350 Wh/kg cell level; 235 Wh/kg system level.
- Performance: Specific power – 700 W/kg cell level; 470 W/kg system level.
- Life: 15 years.

Accomplishments

- Half-cells of nickel-cobalt-manganese layered oxide (3,3,3) (NCM), lithium cobalt oxide (LCO), and high-voltage LCO (HV-LCO) were cycled for over 100 cycles between 2.8 and 4.3 V. NCM and HV-LCO cycled with negligible capacity loss.
- The LCO cell experienced significant average voltage decline with cycling.
- Half-cells of NCM were cycled with baseline electrolyte and high-voltage electrolyte to 4.5 V with negligible capacity fade after 100 cycles. The cells with high-voltage electrolyte showed slightly lower capacity fade.
- Inspection of the superimposed voltage versus capacity curves indicated that the side reaction of the baseline electrolyte was greater than that of the high-voltage electrolyte.
- In full cells of NCM and MCMB anodes at 55°C, the high-voltage electrolyte cell showed 6% more capacity fade than the cell with baseline electrolyte.

- The energy loss of the cells mirrored the capacity fade of the cells indicating that the capacity fade was most likely the result of side-reactions on the anode.

Introduction

Today's Li-ion battery performs very well between 3 and 4.2 V with capacities of around 140 mAh/g (of cathode). This results in an average energy density on a chemistry basis of approximately 400 Wh/kg. After the cell is constructed and the pack assembled, the energy density drops to around 150 Wh/kg. To meet the target of 235 Wh/kg will require new materials of higher voltage and capacity. However, Li-ion cells are presently used in EVs, and to maintain this trend in an accelerated fashion, the cost needs to come down and the energy density needs to go up. One approach is to push today's Li-ion chemistry to higher voltages by extracting more lithium per cycle. This combination of higher capacity and voltage is compounding with regards to energy, for example, a 20% increase in capacity and a 10% increase in voltage will result in a 32% increase in energy. We will study some modified materials that result in greater lithium extraction and higher voltage utilization.

Approach

Innovative Approach: The objectives listed above will be accomplished by utilizing the Battery Materials Characterization, Fabrication, and Testing (CFT) Facility at LBNL. The facility allows for the fabrication of electrodes and coin- and pouch-cells in a moisture- and air-free environment. Materials characterization techniques include PSA, BET, SEM, and ICP. The testing facilities include over 350 test channels and the ability to perform electrochemical impedance spectroscopy. Testing includes a combination of data analysis consisting of impedance data, cycling data, and reference performance tests (RPTs) and post-test analysis consisting of SEM, TEM, ICP, and gas analysis with an MS. What follows is our approach to evaluating materials:

1. With the DOE Program Manager, define topics and materials of interest. This year the topic was high voltage performance of NCM with and without high-voltage electrolytes when compared to LCO and HV-LCO.
2. Identify quality materials and suppliers willing to provide the materials and terms of engagement necessary to perform the work.
3. Fabricate electrodes of baseline materials and demonstrate that the materials perform as good as is found in industry under typical operating conditions.
4. Push the materials for increased energy density by extracting lithium at ever increasing voltages. Accelerate failure by operating at higher temperatures.
5. Identify failure mode.
6. Deduce a theory for failure.
7. Perform an independent experiment to qualify theory.

Results

We have achieved the following progress:

Cycle Performance of NCM, LCO, and HV-LCO in half cells from 2.8 to 4.3 V

Upon establishing baseline performance at a cutoff voltage of 4.1 V for the NCM, LCO, and high-voltage LCO (HV-LCO) (see annual report V.B.5), cells were constructed and cycled between 2.8 and 4.3 V against Li metal counter electrodes (see Figure V- 3).

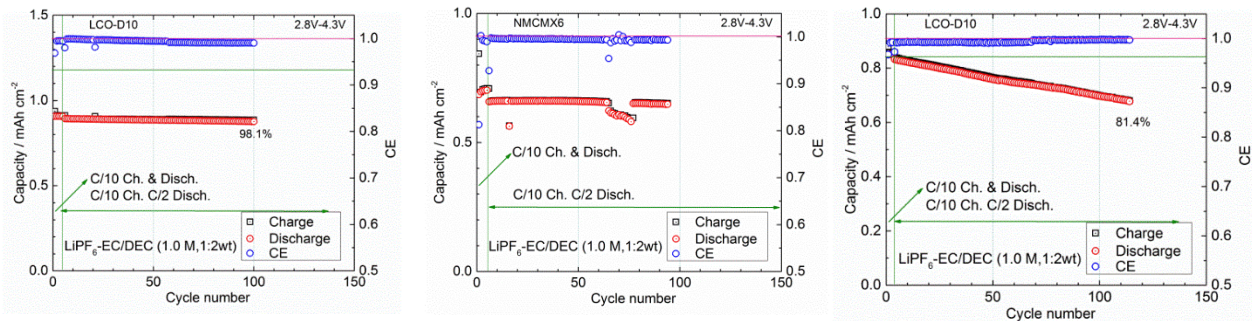


Figure V- 3: Cycling performance of NCM (left), LCO (center), and HV-LCO (right) between 2.8 and 4.3 V at C/10 charge and C/2 discharge

One can see that of the three cells, the LCO is showing the most capacity fade. (For the NCM cells, there is a series of cycles between cycles 60 and 80 that were of lower capacity than the cycles that preceded or followed them. These cycles occurred over the holiday break where an electrical shutdown occurred where Facilities did not fully comply with instructions. The cells cycled but at lower temperatures than the 30°C that is typical. Fortunately, the cells recovered their full cycling capacity once full power was restored to the building.) After 115 cycles, the LCO cell showed a capacity loss of nearly 19 %, this is to be compared to a capacity loss of just 5% when only cycled to 4.1 V. The high-voltage LCO, on the other hand, lost about two percent of its capacity in the first 100 cycles when charged to 4.3 V. Clearly, the HV-LCO is demonstrating significant improvement.

To better understand the source of this improvement XRD, SEM, and TEM were performed on the starting materials. The starting materials were also fully digested and run through the ICP-OES for elemental analysis. The results of these studies cannot be reported here but these measurements have provided some insight into the mechanism of improved performance. It will be interesting to see if future high-voltage materials rely on this type of chemical and physical manipulation.

Typically, cells die as a function of three factors, Li-ion cell imbalance from side reactions, impedance rise, or loss of Li sites (the original sites for lithium intercalation become inaccessible.) In half cells, side reactions do not result in capacity fade. Thus, fade in the cells is a result of either loss of Li sites or impedance rise. If the cells fail from resistance rise then the average discharge voltage of a half-cell will decrease with cycle number. It is also possible for the average voltage to drop as a result of loss of Li-sites for the available sites see a higher current density, but this dependence on current density is less severe than that seen from resistance rise. Conversely, if there is capacity fade without voltage decay, then the cell most likely suffers from loss of Li sites.

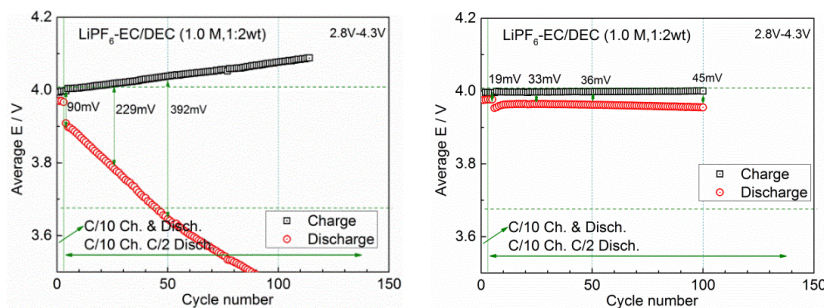


Figure V- 4: Average voltage on charge and on discharge of LCO (left) and HV-LCO (right) in half cells. Charge was performed at C/10 and discharge at C/2

Figure V- 4 shows the corresponding average cell voltage on charge and discharge of the LCO and HV-LCO cells cycled between 2.8 and 4.3 V at C/10 charge and C/2 discharge. If there is impedance rise in the cell, the average voltage of the cell on charge will rise at a slower rate than the rate of decline of the average voltage on discharge because of the difference in charge and discharge rate. This is observed in Figure V- 4 for both cells. However, the slopes of the average voltage on charge and discharge are much more severe for the LCO cell than they are for the HV-LCO cell. This data suggests major impedance rise in LCO cells.

Cycle Performance of NCM in half cells with high-voltage electrolyte from 2.8 to 4.5 V.

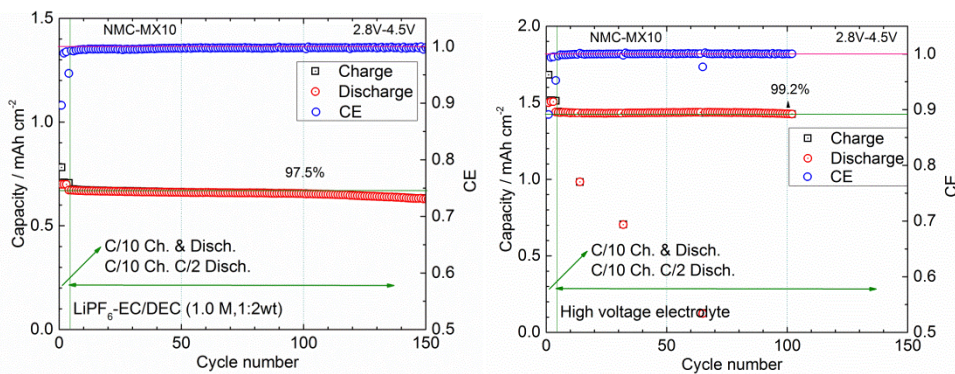


Figure V- 5: Capacity versus cycle number of a half cell of NCM cycled between 2.8 and 4.5 v with baseline electrolyte (left) and high-voltage electrolyte (right)

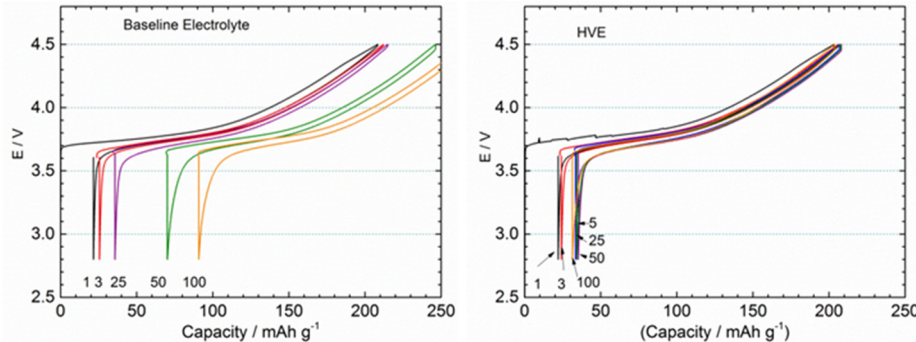


Figure V- 6: Superimposed voltage curves for baseline electrolyte (left) and high-voltage electrolyte (right)

V- 5. This cell also shows excellent cycling performance for the first 100 cycles. The difference in loss of capacity between the two chemistries is just 1.7%, which is approximately 0.017% per cycle.

A bigger difference in the two electrolytes can be observed when the voltage curves *versus* capacity are superimposed on each other for multiple cycles (Figure V- 6). Here we see the side reaction in the cell with baseline electrolyte is resulting in an exaggerated sliding to the right of the voltage curves with each cycle. The sliding is at a rate of 0.27% per cycle, which is *ca.* 15 times greater than the rate of fade of the cell. There is negligible movement of the curves with the high-voltage electrolyte indicating negligible side reactions.

Cycle Performance of NCM in full cells with high-voltage electrolyte and MCMB from 2.8 to 4.4 V

With these preliminary results, the electrodes and electrolytes were tested in full cells with MCMB graphite as the counter electrode. After some break-in cycles, the cells were cycled at C/3 charge and C/2 discharge between 2.8 and 4.4 V. To accelerate fading mechanisms the cells were tested at 55°C. The graphs in Figure V- 7 provide the capacity as a function of cycle number for the first 100 cycles or so. One can see that the data for the baseline electrolyte shows a 10.7% capacity fade after 100 cycles whereas the full cell with the high-voltage electrolyte shows a 16.7% capacity loss after the same number of cycles. Thus, the slightly improved performance gained in the half cell using high-voltage electrolyte was more than lost in the full cells.

Inspection of the discharge energy of the cells at 55°C shows that the energy in the baseline electrolyte declines by 11%, indicating that the voltage must be slightly improving with cycling. The energy of the cell with high voltage electrolyte declined by approximately 16%, indicating little impedance rise in this cell. This indicates that most of the capacity fade is a result of side reactions at the anode and those reactions more detrimental in the high voltage electrolyte cells.

The baseline electrolyte (1M LiPF₆ in EC:DEC 1:2) was tested in a NCM half-cell and compared side-by-side to a "high-voltage" electrolyte in a cell of the same chemistry. Both cells were cycled to a 4.5 upper cut-off voltage. The cycling data of the baseline electrolyte is provided in Figure V- 5. The cell shows very good capacity retention for the first 100 cycles. Similar cycling data of the high-voltage electrolyte is also provided in Figure

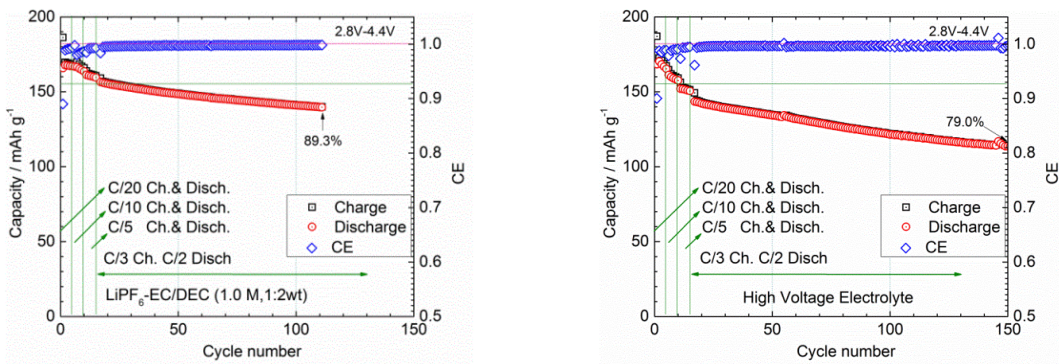


Figure V-7: MCMB/NCM full cells cycled with baseline electrolyte (left) and high-voltage electrolyte (right)

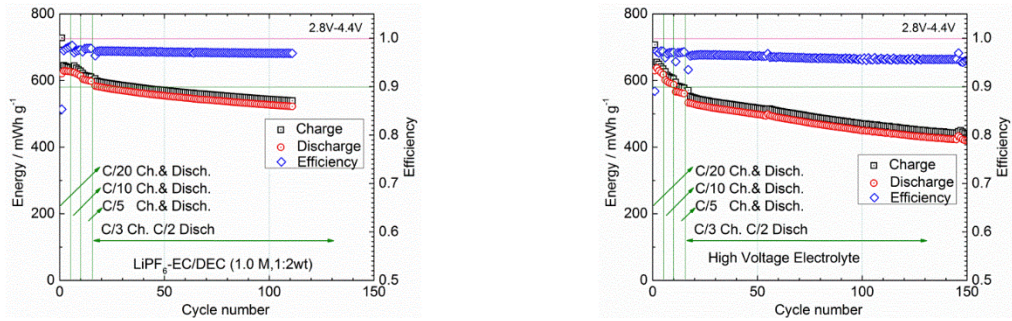


Figure V-8: MCMB/NCM full cells cycled with baseline electrolyte (left) and high-voltage electrolyte (right)

Conclusions and Future Directions

This fiscal year consisted of a superficial investigation of the high-voltage capabilities of NCM compared to LCO and high-voltage LCO and with high-voltage electrolytes and of full cells with high-voltage electrolytes. The results indicate that the LCO is not stable above 4.1 V, and that cycling above this voltage results in significant impedance rise. NCM and HV-LCO were both found to cycle well up to 4.5 V *versus* Li with little impedance rise in the cells. Above 4.5 V, both cells demonstrated significant impedance rise (data not shown here.) In cells where the electrolyte was modified for improved high voltage stability, NCM showed very little capacity fade and negligible side reactions indicating excellent stability. The cell with a baseline electrolyte showed a little more capacity fade and significant side reactions. When the NCM was then tested with the same electrolytes but with a graphitic anode (MCMB) the cell with the baseline electrolyte showed better capacity retention than the cell with the high-voltage electrolyte. Inspection of the energy curves revealed little resistance rise in the cells and that the capacity fade is most likely the result of higher rates of side reaction in the anode than the cathode.

Future work will on this system should try to identify why the high-voltage electrolyte results in no side reactions, is there a passive film or is the electrolyte more stable, and finding an additive to the high-voltage electrolyte that will allow for stability at the anode. Lessons learned about how changes to the LCO resulted in more stable HV-LCO may want to be tried with the NCM to see if stability of that material can be pushed over 4.6 V.

FY 2015 Publications/Presentations

This year there were over 10 publications from this group, however, the work presented here is just being written-up.

V.B.2 Electrode Architecture-Assembly of Battery Materials and Electrodes (HydroQuebec)

Objectives

- Develop high-capacity, low-cost electrodes with good cycle stability and rate capability to replace graphite in Li-ion batteries.
- Identify an alternative supplier of Si powder material as baseline for the BMR.
- Fabrication of large format stacking li-ion cells of 20 Ah capacities based on Si-anode and $\text{LiMn}_{3/2}\text{Ni}_{1/2}\text{O}$ cathode.

Technical Barriers

- The technical barrier is to overcome the electrochemical capacity limitations (both gravimetric and volumetric) of conventional carbon anodes by developing low-cost electrode architectures based on silicon. One of the biggest challenges of this anode material is its volume expansion and structural changes which lead to capacity fade and shorter cycle life. These failures are due in part to loss of electrolyte by reduction and a SEI that is not stable on the surface with repeated cycling due to the exposure of fresh surfaces of Si particles, and thus a perpetual reaction to form more SEI.
- Life: Poor cycle life.
- Cost: High \$/kWh.

Technical Targets

- Redesign the anode architecture based on Si-nano produced at HQ.
- Design the architecture of the high-voltage cathode (LMNO) to match with anode.
- Identify the optimum parameters for large-scale electrodes fabrication.
- Deliver laminate electrodes and large format Li-ion cells (20 Ah) to BMR PIs.

Accomplishments

- Gas evolution problem was suppressed with the aqueous binder by protecting the surface of the nano-Si particles with PAA.
- We found that controlling the pH of the nano-Si slurry is another way to suppress the gas evolution.
- The loading level of the Si-anode has been improved by forming secondary particles with spray dryer.
- Using polyimide binder increases the adhesion strength of the Si-anode.
- Laminated nano-Si-electrodes (10 m) were shipped to BMR PIs.
- Large format of stacking cells with 21 Ah capacity and Si-nano/NCM chemistry were shipped to BMR PIs.

Introduction

The target of the DOE's Program is to identify the next generation of high-energy batteries. Achieving this target will require materials of higher capacity and improved coulombic efficiency or cells with higher voltage. High-capacity anode materials such as Si or Sn alloys have the potential to fulfill the energy density requirements for EV/PHEV applications. However, large volume expansion during the lithiation process of these materials usually leads to fast capacity fade that hinders its practical applications. Real-time SEM studies on charge/ discharge of Si-anodes have demonstrated that decreasing the particle size to nanometer scale can be an effective means of accommodating the volume change, and thus delaying its degradation.

Project Details

Karim Zaghib (HydroQuebec, IREQ)

1800 Lionel Boulet

Varennes, QC, J4X 1S1

Canada

Phone: 450-652-8019, Fax: 450-652-8566

E-mail: Zaghib.Karim@ireq.ca

Start Date: October 2012

Projected End Date: September 2016

HQ proposed a strategy to design the architecture of the Si-anode material that can tolerate the volumetric expansion and provide acceptable cycle life with low capacity fade. The particle size, binder type and electrode composition are the main parameters that define the formulation of the Si-anode. The porosity of the electrode has a direct impact on the performance, and therefore was optimized by investigating various mixing methods.

Approach

1. Explore a variety of synthesis methods to produce low cost Si-nano materials with controlled purity and particle morphology.
2. Develop an appropriate silicon anode architecture that can tolerate volumetric expansion and provide an acceptable cycle life with low capacity fade.
3. Identify a binder and an electrode composition by investigating parameters that define the electrode structure such as porosity, loading and electrode density. The optimized Si-anode will be matched with high-voltage NMC cathode to fabricate large format Li-ion cells.
4. Use *in-situ* techniques such as SEM and impedance spectroscopy to monitor the particle and electrode environment changes during cycling.
5. Achieve cost reduction by moving from (>\$50/kg) to metallurgical Si which is projected to be \$3-\$5/kg.

Results

We have achieved the following progress:

Loading level effect on cycle life

Since the Si material suffers from high volume expansion, one of the weak parts is increasing the loading level. To achieve a high-energy battery with the Si-anode and NMC or LMNO cathodes, our calculations indicate the anode loading must be $\geq 2\text{mg/cm}^2$. Then, the effect of loading on the architecture and performance of the anode is a key parameter which should be studied. Figure V- 9 shows the cycle life of the nano-Si/Li cells with different total loading level of $0.45 \sim 1.96\text{ mg/cm}^2$. Charge and discharge was controlled with %DoD and was fixed at 40% of the theoretical capacity of Si material. The cycle life reached more than 900 cycles with 1670 mAh/g capacity in a cell with a low loading of 0.45 mg/cm^2 . This cycle number is very close to that of current Li-ion batteries with graphite anodes. However, with this loading level, the battery delivers a low gravimetric energy density of $\sim 120\text{ Wh/kg}$. To obtain a higher gravimetric energy density $\geq 250\text{Wh/kg}$, the anode loading should be $\geq 2.0\text{ mg/cm}^2$. Towards this goal, alternative binders such as polyimide-type are being investigated in order to increase the anode performance both electrochemically and mechanically. Further work in the anode formulation is necessary to overcome this limitation in the loading level.

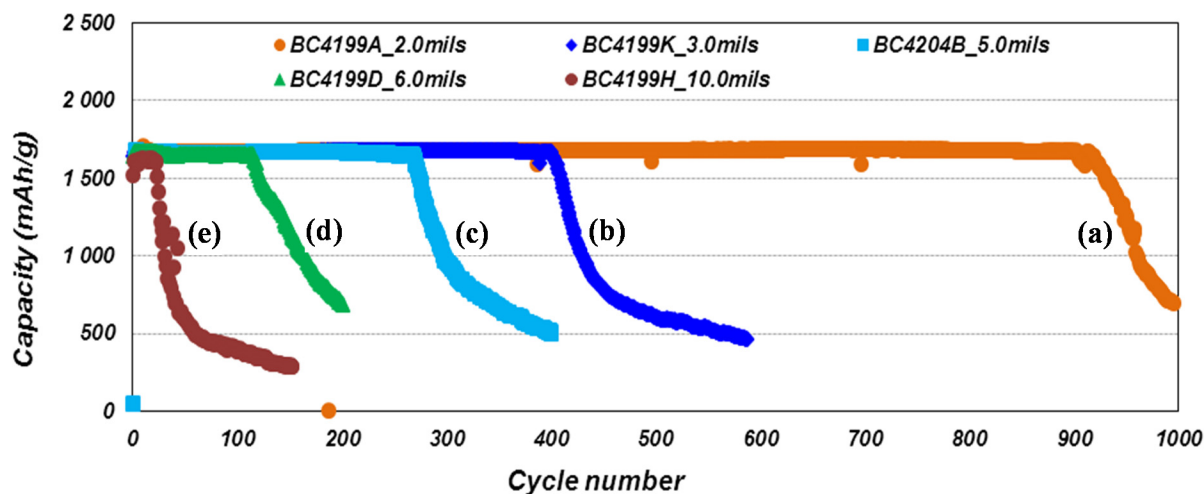


Figure V- 9: Cycle life of Li/Si cells at 40% DoD with different loading levels (a) 0.45 mg/cm^2 , (b) 0.75 mg/cm^2 , (c) 0.99 mg/cm^2 , (d) 1.26 mg/cm^2 and (e) 1.96 mg/cm^2

Surface coating of nano-Si powder

In order to reduce the production cost of the Li-ion battery based on the Si material, water based binder is promoted. In contrast, when an aqueous binder is used, a large volume of gas was generated during the mixing and coating processes. This gas causes many problems during the anode processing; unstable slurry, difficult control of the loading level and inhomogeneous surface of the anode. In order to overcome this problem, we protected the *nano*-Si surface particles with poly acrylic acid (PAA) by using a spray-dry technique, and gas generation was suppressed. Figure V- 10 shows the photos of the slurries during the mixing process. In the case of bare *nano*-Si powder (a), a strong release of gas in the suspension was observed, even after aging overnight. However, the *nano*-Si powder that was surface treated with PAA showed no gas evolution during the slurry mixing (b) and coating process.

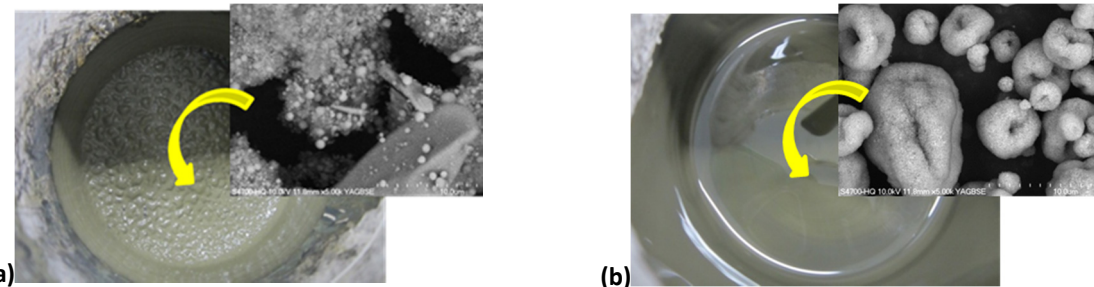


Figure V- 10: Photos of anode slurries obtained from (a) nano-Si, (b) PAA surface coated nano-Si powder

The morphology of *nano*-Si powder, after spray drying with PAA, was completely changed. The PAA-coated *nano*-Si powder shows some hollow spherical secondary particles with a size distribution of 1-5 μm . However, the electrochemical performance shows less reversible capacity and low cycle life than bare *nano*-Si powder. This finding is probably associated with the effect that the carbon conductor is found separated from the Si particles (Figure V- 11a). Hence, the *nano*-Si powder was not well dispersed with carbon and the *nano*-Si powder formed secondary particle after spray drying.

Nano-Si/PAA/Carbon composite

To increase the electrochemical performance by producing an intimate mixing of Si-C and protecting surface of particles to prevent the gas generation during the mixing and coating processes, the *nano*-Si/PAA/C composite was spray dried. Different type of carbon; carbon black and VGCF are added in the composite. Figure V- 11 shows the comparison between *nano*-Si powder (a) and spray dried *nano*-Si/PAA/C composite with secondary particles having size distribution of 1~10 μm (b) and the cross-section view *nano*-Si/PAA/C composite (c). These secondary particles were followed by a heat-treatment at 200°C in N₂ for 12 hours.

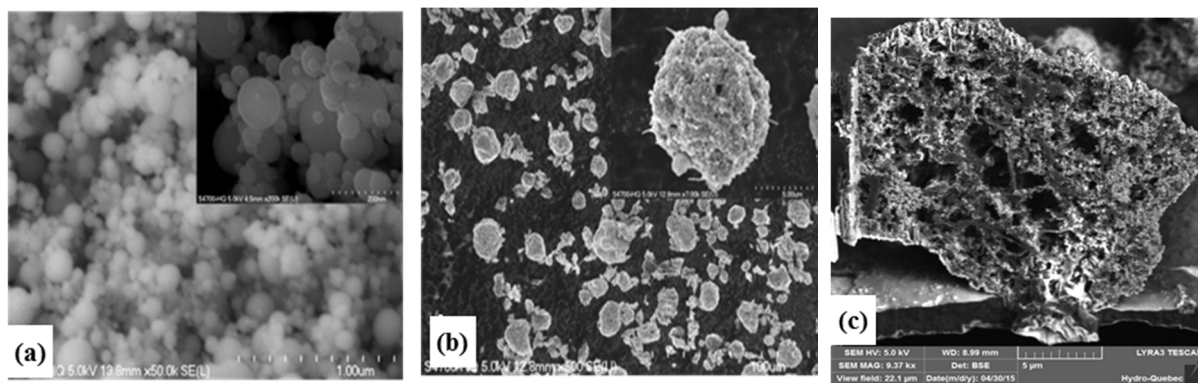


Figure V- 11: Photos of anode powders (a) nano-Si, (b) nano-Si/PAA/C composite and (c) the cross-section of nano-Si/PAA/C composite

However, by using an aqueous binder the adhesion strength with water-based alginate binder was not sufficient to have more than 2mg/cm² of total loading level. This result led us to change to a non-aqueous binder such as polyimide base to increase the adhesion strength of the electrode.

Polyimide binder with nano-Si/PAA/C composite

During this year, we focused on increasing the loading level by making the secondary particle of *nano-Si/PAA/C* composite. But with water-based alginate binder, even with *nano-Si/PAA/C* composite, the adhesion strength was poor; the loading level was limited to less than $1.5\text{mg}/\text{cm}^2$. In order to get the loading level higher than $2\text{mg}/\text{cm}^2$, we attempted to explore NMP-based polyimide binder.

Figure V- 12 shows the surface of the anode electrode of *nano-Si/PAA/C* composite with polyimide binder. The effect of the loading level on the cycle life performance using polyimide based anodes is shown in Figure V- 13. With *nano-Si/PAA/C* composite and polyimide binder, the manufacturing process, especially mixing and coating were improved, but the electrochemical performance, particularly, the cycle life still far from satisfactory. A comparative cycle life of anode based on *nano-Si/PAA/C* with different loading; 1.5, 2.0, 3.0 mg/cm^2 is shown in Figure V- 13. We notice that the adhesion strength of the anode was improved with polyimide binder. The cycling performance at C/6 is clearly affected by the loading; with $1.5\text{ mg}/\text{cm}^2$ the capacity fades by 22% compared to 80% when the anode loading is doubled.



Figure V- 12: Photo of anode electrode of nano-Si/PAA/C composite with polyimide binder

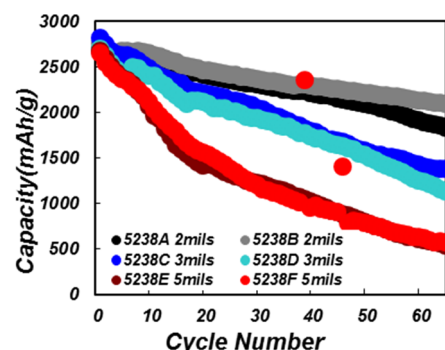


Figure V- 13: Cycle life of Si/PAA/C composite with different loading: 2mils of $\sim 1.5\text{mg}/\text{cm}^2$, 3mils of $\sim 2\text{mg}/\text{cm}^2$, 5mils of $\sim 3\text{mg}/\text{cm}^2$

Despite the improvement in adhesion of the anode, the high irreversible capacity during 1st formation cycle and higher loading level are the challenges to overcome with this polyimide binder system.

PH Control of water-based Slurry

To prevent the gas generation problem during the mixing and coating process, we explored in parallel the effect of pH in the slurry. The acetic acid was used to control the pH of the slurry. Figure V- 14a shows huge amount of gas generation after 10 minutes of mixing with pH=7.5 compared to the slurry in Figure V- 14b where there is no gas generation when the pH is reduced to 4.



Figure V- 14: Photos of anode slurry (a) nano-Si in H₂O with pH7.5, (b) nano-Si in H₂O with pH 4 and (c) the electrodes of slurry (a) left and of slurry (b) right

The electrochemical performance is undergoing and Hydro-Quebec will focus on increase the loading level with appropriate adhesion strength.

Large format Li-ion battery

As a result of this year, we made the large format Li-ion battery; designed at 49Ah, 210Wh/kg but the real capacity was 43.6Ah capacity and 185Wh/kg specific energy. The chemistry was based on nano-Si /PAA/C(Si 50%)/NCM. For better mechanical property, the NMP-based polyimide binder was used in this deliverable

(Figure V- 15a). Figure V- 15b shows the formation cycle of the 43.6Ah cell at C/3 rate between, 4.4V and 2.5V. The cell is under characterization for additional electrochemical tests such as; C-rate, cycle-life and aging.

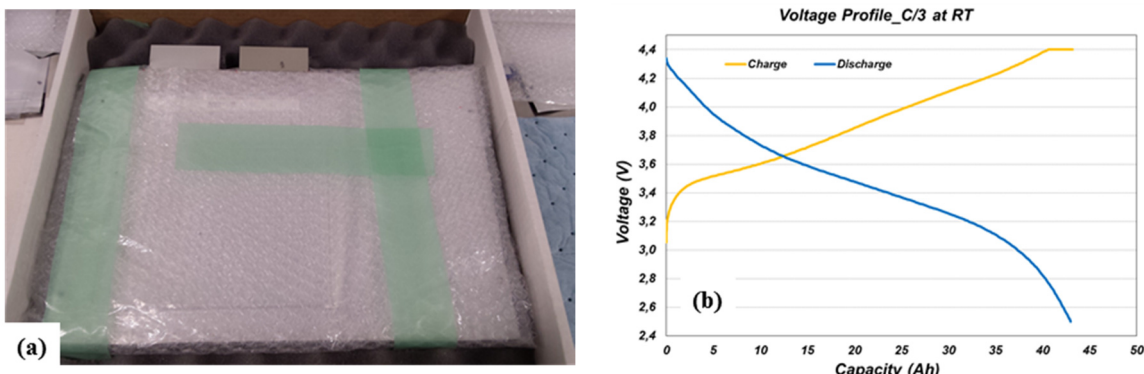


Figure V- 15: (a) Photos of cell nano-Si/PAA/C composite/EC-DEC-FEC LiPF₆/ NCM and (b) charge/discharge voltage profile between 4.4V and 2.5V at RT

Conclusions and Future Directions

We succeeded to suppress the gas generation during the anode processing with water based binder. Two methods has been explored by protecting the surface of the nano-Si binder and by controlling the pH of the slurries. We have demonstrated a cycle life of more than 900 cycles at capacity retention of 98% for the nano-Si anode with 1670 mAh/g in half cell with loading of 0.45mg/cm².

Therefore, we are able to make full cells with high capacity using the nano-Si anode and NCM cathode. Determining the optimal Si%, electrode density and loading are important controlling parameters must be further studied in order to achieve high performed cells with high energy density, good C-rate performance and long cycle life.

We have delivered 2 large format prismatic pouch cells and 10m of anode material as 2015 deliverables for characterisation; the cells are based on NCM/nano-Si and have capacity of 49Ah.

FY 2015 Publications/Presentations

1. Zaghib, Karim. "Electrode Architecture- Assembly of Battery Materials and Electrodes." Presented at the BMR Program Review, Berkeley, CA, January 2015.
2. "Electrode Architecture- Assembly of Battery Materials and Electrodes," ES222_Zaghib_2015_O, U.S. DOE Vehicle Technologies AMR, 2015.

V.B.3 Design and Scalable Assembly of High Density Low Tortuosity Electrodes (MIT)

Objectives

- Develop scalable high density low-tortuosity electrode designs and fabrication processes to enable increased cell-level energy density compared to conventional Li-ion technology.
- Characterize electronic and ionic transport as a function of state-of-charge in relevant electrode systems and downselect based on the superior performance.
- Maximize active material utilization and lower cost of Li-ion cells for EV applications
- Test electrochemical performance of fabricated electrodes in continuous and pulse modes representative of vehicle drive cycles.

Technical Barriers

- Achieving high usable area capacity ($>5 \text{ mAh/cm}^2$) under realistic automotive drive cycles
- Avoiding mechanical failure upon cycling.
- Lowering processing cost.

Technical Targets

- Identify high energy density cathode compositions with electronic transference number >0.5 across the SOC range for use in additive-free electrodes.
- Fabricate conductive additive free sintered cathodes with controlled pore volume fraction and topology yielding tortuosity values less than 2.
- By the end of the program, achieve 3 times the area capacity of current technology while satisfying model drive cycles for vehicle applications.

Accomplishments

- Demonstrated a directionally-solidified non-sintered graphite anode with 18 mAh/cm^2 at C/10, 15 mAh/cm^2 at C/5, and 6 mAh/cm^2 at 1C continuous rates.
- Demonstrated 14 mAh/cm^2 for pulsed 1C/10% SOC + 2C/30s discharge of the above electrode.
- Demonstrated an electrode that provides 11.5 mAh/cm^2 in the USABC dynamic stress test (DST) with peak discharge rate of 2C.
- Developed two variants of a novel magnetic alignment process for producing low tortuosity porosity normal to the electrode plane.

Introduction

The high cost (\$/kWh) and low energy density of current automotive lithium-ion technology is in part due to the need for thin electrodes and associated high inactive materials content. The number of separator and current collector layers per Ah of cell capacity is inversely proportional to the area capacity (mAh/cm^2) of the electrode. While area capacity (i.e., active materials loading) can be increased arbitrarily by increasing electrode thickness and/or density, increased loading does not contribute *usable* energy unless the capacity can be accessed at practical C-rates, or under realistic automotive drive cycles. Thus, concepts that can provide higher usable area capacity, e.g. during $\sim 2\text{C}$ pulses in an EV or PHEV drive cycle, are needed. This project

Project Details

Yet-Ming Chiang (Massachusetts Institute of Technology – PI)
77 Massachusetts Avenue
Cambridge, MA 02139
Phone: 617-253-6471; Fax: 617-253-6201
E-mail: ychiang@mit.edu

Antoni P. Tomsia (Lawrence Berkeley National Laboratory - Collaborator)
Materials Sciences Division
1 Cyclotron Road
Berkeley, CA 94720
Phone: 510-486-4918
E-mail: aptomsia@lbl.gov

Start Date: October 2012
Projected End Date: September 2016

aims to develop alternative electrode architectures and scalable fabrication methods that result in thick, high density electrodes with low tortuosity porosity oriented normal to the electrode plane, using electrode-active materials of interest for future EV battery systems.

Approach

Two processing approaches for producing directional, low-tortuosity porosity are explored in this project. One is the directional freezing of aqueous suspensions, carried out as a collaboration between MIT and LBNL. For the cathode compounds, directional freezing and lyophilization is followed by sintering. For anode compounds, sintering requires excessively high temperatures and/or reducing conditions. Thus, the directional freezing approach has also been applied to electrode suspensions, initially graphite anodes, to yield low tortuosity electrodes without further processing. Another goal is to develop a freeze-casting geometry for thin sheet format, with the freezing direction oriented normal to the plane of the electrode, as is preferred for a scaled process.

The second process being explored is magnetic alignment of sacrificial, anisotropic pore-forming entities. This approach has the advantage of being fast, potentially low-cost, and compatible with continuous electrode fabrication. Two variants of this approach are being explored. One utilizes sacrificial polymer fibers that are magnetized by coating with iron oxide nanoparticles, with the fibers being pyrolyzed after alignment to produce aligned pores. The second uses the chaining of magnetic emulsion droplets to form aligned pores after evaporation of the solvent in the emulsion droplets.

For all of the electrodes fabricated, the large thickness (200-500 μm) and high capacity ($>8 \text{ mAh/cm}^2$) produces electrode kinetics with different behavior compared to conventional thin electrodes. Specifically, it has been found that continuous discharge behavior over large SOC swing (e.g., 100%-0% SOC) underestimates the pulse power capability of the electrodes. Thus, the electrodes in this project are also tested under simplified electric vehicle drive cycles such as HPPC and DST.

Results

Directional Freezing of Graphite Anodes

Aqueous suspensions were prepared using battery-grade graphite and CMC binder (5 wt% relative to the graphite) and containing no conductive carbon additive. The formulations prepared are similar to suspensions for an aqueous electrode coating process for Li-ion. Directional freezing experiments were conducted in similar manner to previous experiments for cathodes conducted in this project, except that electrodes were not sintered after lyophilization. As shown in Figure V- 16, highly oriented low-tortuosity pore channels were obtained at cooling rates of 5°C/min and 7.5°C/min. The final porosity of the electrodes was 58-60 vol%. When sectioned to 800 μm thickness, the anodes have theoretical area capacity of about 25 mAh/cm^2 .

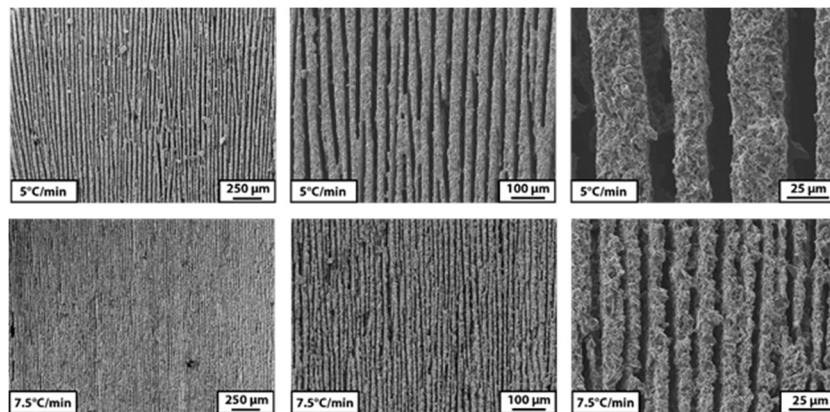


Figure V- 16: Cross sections of graphite anodes formulated with CMC binder and freeze-cast at the cooling rates indicated. Electrodes were lyophilized to retain structure. Total porosity is 58-60 vol%

When tested at C/5 rate, stable cycling was observed over 10 cycles, as shown in Figure V- 17 with area capacity of 15 mAh/cm^2 . At C/10 rate, approximately 18 mAh/cm^2 is reached, as shown in Figure V- 17. At 1C rate, the area capacity is 6 mAh/cm^2 .

Evaluations of the capability of such electrodes to perform under pulse conditions appropriate to EV use were

then initiated. HPPC characterization of the above described graphite anodes was conducted in which half-cells charged at C/5 rate were sequentially discharged at 1C rate for 10% of SOC, followed by 2C pulse discharge for 30s. The sequence was repeated after 1h rest until 0% SOC was reached. Results are plotted in Figure V- 18 as voltage vs. area capacity. It is notable that whereas the same electrode at continuous 1C discharge only yields 6 mAh/cm^2 , the HPPC sequence allows the electrode to deliver 14 mAh/cm^2 . This provides evidence that for the thick, high area capacity, low tortuosity electrodes being fabricated in this project, continuous discharge tests underestimate to a large extent the energy that can be delivered in EV-type duty cycles.

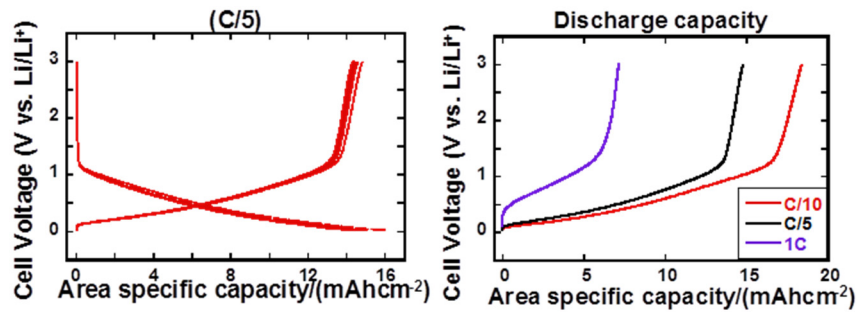


Figure V- 17: Galvanostatic discharge voltage vs. capacity for $800 \mu\text{m}$ thick electrode sectioned from sample directionally freeze-cast at $7.5^\circ\text{C}/\text{min}$. Left: Multiple cycles at C/5 rate. Right: Comparison of result at C/10, C/5 and 1C discharge rate

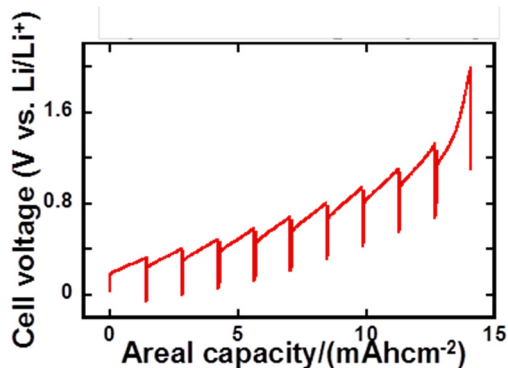


Figure V- 18: Voltage-area capacity results from HPPC test of $800 \mu\text{m}$ thick electrode

Magnetic Alignment of Sacrificial Pore Formers

A new magnetic alignment approach to fabricating low-tortuosity high density electrodes was developed, the test results from which met this year's Go/No-Go Milestone. As schematized in Fig. V-4, a LiCoO₂ particle suspension was prepared and mixed with short nylon rods that were magnetized by coating with iron oxide nanoparticles. The suspension was placed in a dc magnetic field and the rods aligned upon application of field for a short period of time ($<1 \text{ min}$). The electrode was then pyrolysed in air to remove the nylon rods, then sintered to $\sim 60\%$ of theoretical density.

The sintered samples with aligned low-tortuosity porosity were then sectioned into electrodes of 200-220 μm thickness, and tested in Li half-cells using the

Dynamic Stress Test (DST) protocol. This test protocol applies charge and discharge pulses of defined C-rate and duration, as shown in Fig. V-4. The highest C-rate pulse discharge is 2C for 30 sec. In order to test the effectiveness of the electrode fabrication technique, a control sample consisting of sintered LiCoO₂ with homogenous porosity, and similar sintered density and thickness, was prepared for testing via the same DST protocol. As shown in Fig. V-4, the DST protocol was run repeatedly on each electrode, beginning with a fully charged cell, until a lower cut-off voltage of 3.0V was reached during pulse discharge. As shown in Figure V- 19, the sample with aligned pore channels exhibits more than twice the discharge capacity of the sample with homogeneously distributed pores, and reaches an area capacity of 8.1 mAh/cm^2 . This performance meets the Go/No-Go Milestone of 7.5 mAh/cm^2 under DST testing.

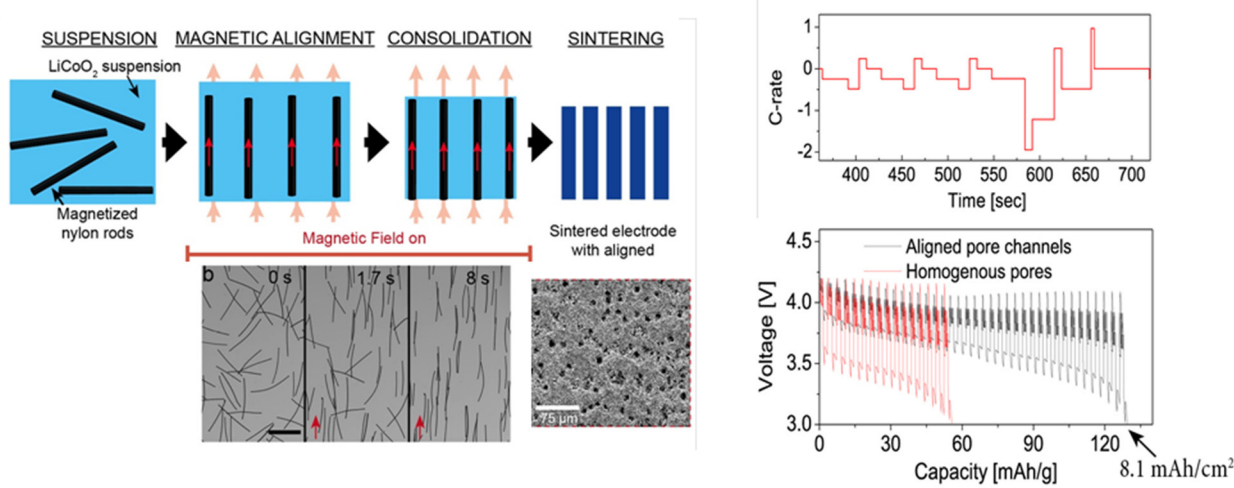


Figure V-19: (left) Scheme for magnetic alignment of removable pore former followed by pyrolysis and sintering. Lower right image shows end-on view of aligned pores. (right) DST test protocol (top) and comparison of discharge capacity for homogeneous and aligned porosity electrodes of same density and thickness

DST Testing of Cathodes Fabricated by Directional Freezing and Sintering

The final milestone for the year was to demonstrate an electrode with at least 10 mAh/cm² that passes the USABC dynamic stress test (DST) with peak discharge rate of 2C. This was accomplished using a sintered NCA electrode prepared by directional freezing of an NCA electrode (7.5C/min cooling rate) and sintering at 840C to reach 35 vol% porosity. A 160 μm thick electrode tested in a half-cell exhibited 11.5 mAh/cm² area capacity in this test, which is 91% of the theoretical capacity of 12.7 mAh/cm².

Conclusions and Future Directions

Results over the past year have extended the current approach in two significant new processing directions. One is the application of directional freezing to composite electrode formulations, in this case graphite anode formulations, which do not require the sintering step of previous work. This suggests that the directional freezing approach may be more broadly applicable than initially considered. The second new direction is the development of a magnetic alignment approach, which is potentially rapid, cost effective, and tends naturally to align the porosity normal to the electrode plane. Over the next year, we will further explore both of these novel approaches to establish processing-structure relationships.

In addition, test results using HPPC and DST protocols have confirmed earlier indications that deep galvanostatic cycling of thick, high areal capacity electrodes underestimates the capabilities of such electrodes to perform application-relevant drive cycles. In the coming year, we plan to carry out both electrode modeling and further experiments to understand the fundamental basis for this type of responses.

FY 2015 Publications/Presentations

1. Amin, R., D. B. Ravnsbæk, and Y.-M. Chiang, "Characterization of Electronic and Ionic Transport in Li_{1-x}Ni_{0.8}Co_{0.15}Al_{0.05}O₂ (NCA)," *J. Electrochem. Soc.* 162, no. 7 (2015): A1163-A1169.
2. Behr, S., R. Amin, Y.-M. Chiang and A. P. Tomsia, "Highly-Structured, Additive-Free Lithium-Ion Cathodes by Freeze-Casting Technology," *Process engineering DKG* 92, no. 4 (2015): E39-E43.
3. Swamy, T. and Y.-M. Chiang, "Electrochemical Charge Transfer Reaction Kinetics at the Silicon-Liquid Electrolyte Interface," *J. Electrochem. Soc.* 162, no. 3 (2015): A7129-A7134.

V.B.4 Hierarchical Assembly of Inorganic/Organic Hybrid Si Negative Electrodes (LBNL)

Objectives

- This proposed work aims to enable Si as a high capacity and long cycle-life material for negative electrode to address two of the barriers of lithium-ion chemistry for EV/PHEV application, insufficient energy density and poor cycle life performance. The proposed work will combine material synthesis and composite particle formation with electrode design and engineering to develop high capacity, long life and low cost hierarchical Si based electrode. State of the art Li-ion negative electrodes employ graphitic active materials with theoretical capacities of 372 mAh/g. Si, a naturally abundant material, possesses the highest capacity of all Li-ion anode materials. It has a theoretical capacity of 4200 mAh/g for full lithiation to the Li_2Si_5 phase. However, Si volume change disrupts the integrity of electrode and induces excessive side reactions, leading to fast capacity fade.

Project Details

Gao Liu (Lawrence Berkeley National Laboratory – PI)

Energy Storage and Distributed Resources Division

1 Cyclotron Road, MS 70R108B

Berkeley, CA 94720

Phone: 510-486-7207; Fax: 510-486-7303

E-mail: gliu@lbl.gov

Start Date: October 2014

Projected End Date: September 2015

Technical Barriers

This project addresses the following technical barriers from the Energy Storage section of the Vehicle Technologies Program Multi-year Research, Development and Demonstration Plan:

- Calendar and cycle life.
- Energy densities.
- Cost

Technical Targets

- Relevant USABC goals
- EV
 - \$150/kWh
 - 230 Wh/dm³
 - 1000, 80% capacity, discharge cycles
 - 10-year system life
- PHEV 40-mile
 - \$220/kWh
 - 193 Wh/dm³
 - 2750, 75%-capacity, discharge cycles +80,000 HEV cycles
 - 15-year system life

Accomplishments

- High energy-density SiO enabled by conductive polymer binder and stabilized lithium metal powder (SLMP) prelithiation.
- A simple and convenient calendaring process is proved to be effective to enhance and active material loading of a Si-based anode to above 3.5 mAh/cm².
- To move on from the backbone conjugating polyfluorene type conductive polymer binder, a new generation of side-chain conjugating pyrene-based binder is developed and shown as effective conductive binder for Si-based anode.
- A robust and convenient free-radical polymerization is used for the synthesis of new side-chain conjugating polymer binder, incorporation of extra functionality is facile to allow custom-design of the binder toward different anode materials.
- Incorporation of other functionalities, such as methacrylic acid or polyethylene oxide structure does not influence the side-chain conjugation, which bringing improved mechanical properties to the modified polymer binder.
- A single-molecule atomic force microscopy (AFM) adhesion test is used to quantitatively measure the adhesion between different polymer binders with substrates.
- Incorporating only 30 mol% acid functionality into the pyrene-based polymer enhances the adhesion to a similar level as polyacrylic acid, while maintaining the electronic conductivity of the polymer.
- Based on the new generation of conductive polymer binder, a high-tap density nanoSi material achieved stable cycle with a high 1st cycle coulombic efficiency.

Introduction

Achieving the DOE energy, cycle life and cost targets will require materials of higher capacity and improved coulombic efficiency or cells with higher voltage. High capacity Si alloy based anode material has the potential to fulfill the energy density requirements for EV/HEV applications. However, full capacity cycling of the alloy anode materials results in significant capacity fade due to a large volume change during Li insertion and removal. Decreasing the particle size to nanometer scale can be an effective means of accommodating the volume change. However, it is very challenging to make electric connections to all the alloy nanoparticles in the electrode by using similar size acetylene black conductive additive. The repeated volume change of the alloy nanoparticles during cycling can lead to repositioning of the particles in the electrode matrix and result in particle dislocation from the conductive matrix. This dislocation of particles causes the rapid fade of the electrode capacity during cycling. An effective polymer binder is important to enable a satisfactory cycling performance of Si-containing anode. Our previous work established the advantage of conductive polymer as a binder of Si anode; further investigation showcases a practical application of this class of conductive polymer in the SiO-based electrode design. A further study leads to a new generation of side-chain conjugating conductive polymer that allows facile fine tune of the binder structure, as well as to lower the cost.

Approach

Innovative Approach: Use functional polymer design and synthesis to develop new conductive polymers with proper electronic properties, strong adhesion and improved flexibility to provide electric pathways in the electrode, and to accommodate large volume change of the Si or Sn alloy active material during lithium insertion and removal. The rational design of binder is assisted with advanced diagnostic techniques such as XAS at Advance Light Sources and with advanced molecular computation at National Energy Research Scientific Computing Center – both are DOE National User Facilities.

Results

We have achieved the following progress:

A Practical Application of Conductive Polymer Based on SiO Anode

Silicon monoxide (SiO) has been considered a promising alternative anode material for lithium-ion batteries (LIBs), with a specific capacity of 1000~1500 mAh/g, much higher than the current graphite anode (372 mAh/g). One caveat for the application of SiO is its low 1st cycle efficiency. In the 1st cycle lithiation process,

besides the reversible reaction with the Si phase, lithium reacts with silicon dioxide to form silicate. Only 65% of those lithium could reversible delithiate, this is a detrimental problem in the full cell application. Thus, an appropriate prelithiation method is critical.

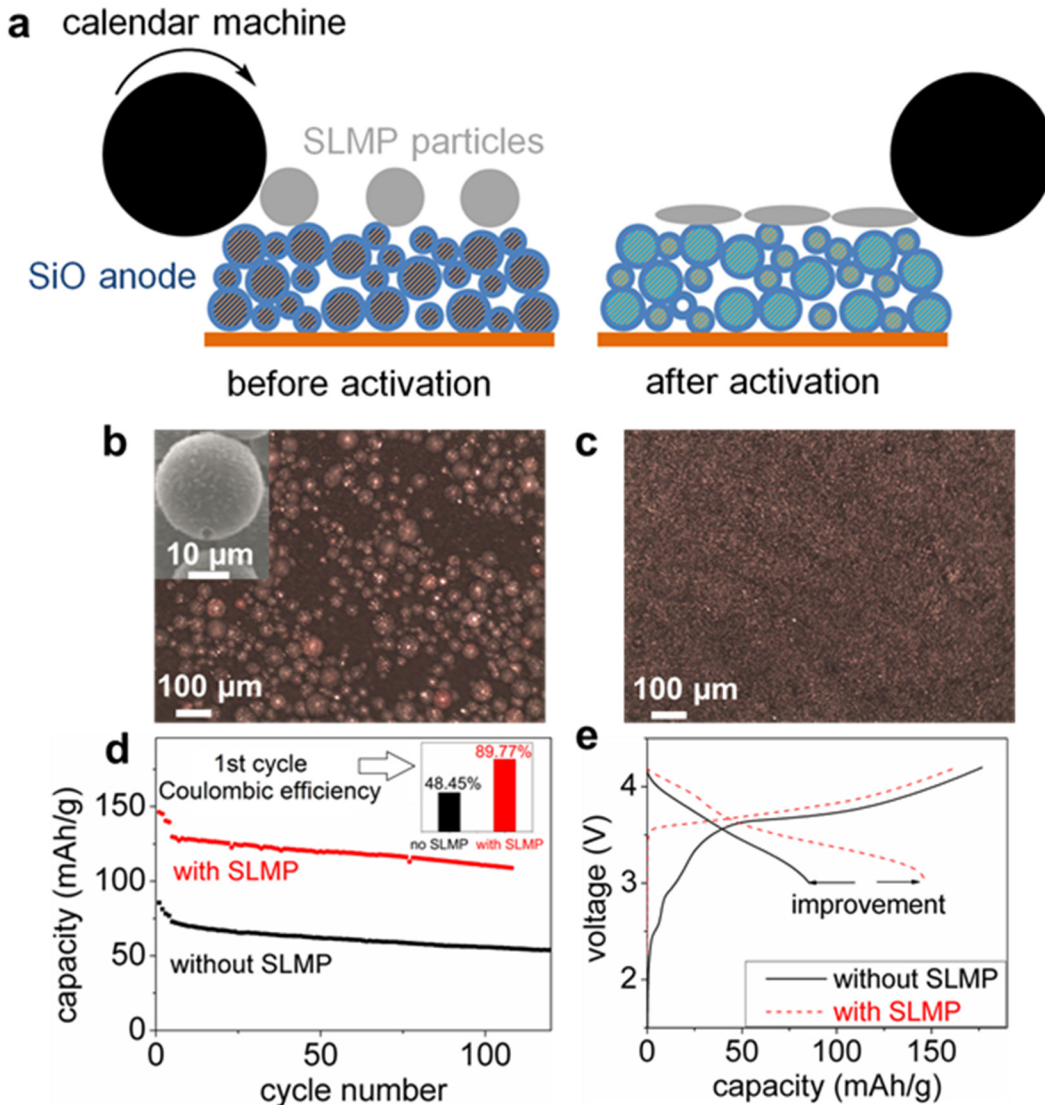


Figure V- 20: (a) Schematics of the utilization of SLMP for the SiO electrode. SLMP particles are loaded on to the SiO anode. Rolling compression was used to crush the Li_2CO_3 shell of SLMP to release lithium metal and laminate it on the surface of SiO electrode. This process is called SLMP activation. (b) SLMP particles loaded on the SiO electrode before activation. The inset shows the SEM image of a single SLMP particle. (c) The SiO electrode surface after electrolytes are added onto the SiO electrode with activated SLMP after 12 hours. This shows the disappearance of SLMP and indicates the successful prelithiation of the SiO electrode. (d) SiO/NMC full cell performance with or without the SLMP capacity-enhancement additive, two cycles at C/20, two cycles at C/10, and then C/3. (e) The first cycle voltage curves of the two cells

Stabilized lithium metal powder (SLMP[®]) is used to prelithiate the SiO anode in the SiO/NMC full cell. SLMP is a micro-size lithium metal powder with ~2 wt% lithium carbonate surface coating. The amount of loaded SLMP was calculated to theoretically eliminate all the irreversible capacity in the first cycle. A calendar machine was used to pressure-activate the SLMP particles (Figure V- 20a). This operation breaks the lithium carbonate (Li_2CO_3) shell and allows lithium to be in direct electrical contact with the SiO materials in the anode.

A 96-hour rest period was used to allow the crushed SLMP to fully prelithiate the SiO anode before current-driven charging of the cells. As a good control, the SiO/NMC full cell without SLMP was also rested for 96 hours before cycling. Both full cells were put in a formation process consisting of two cycles at C/20 and two

cycles at C/10 prior to C/3 cycling. Apparent improvement was shown for the SLMP-loaded full cells. The first cycle CE increased from 48% to ~90% with the SLMP (shown in the inset of Figure V- 20d). SLMP enabled the NMC/SiO full cell to maintain a reversible capacity of ~110 mAh/g after more than 100 cycles at C/3.

A Convenient Calendering process that enhances the Electrochemical Performance of Conductive Polymer/SiO Electrode

High capacity and high density functional conductive polymer binder/SiO electrodes are fabricated and calendered to various porosities. The effect of calendering is investigated to the reduction of thickness and porosity, as well as the increase of density. SiO particle size remains unchanged after calendering. When compressed to an appropriate density, an improved cycling performance and increased energy density are shown compared to the uncalendared electrode and over-calendared electrode. The calendered electrode has a high-density of ~1.2 g/cm³. A high loading electrode with an areal capacity of ~3.5 mAh/cm² at a C/10 rate is achieved using functional conductive polymer binder and simple and effective calendering method.

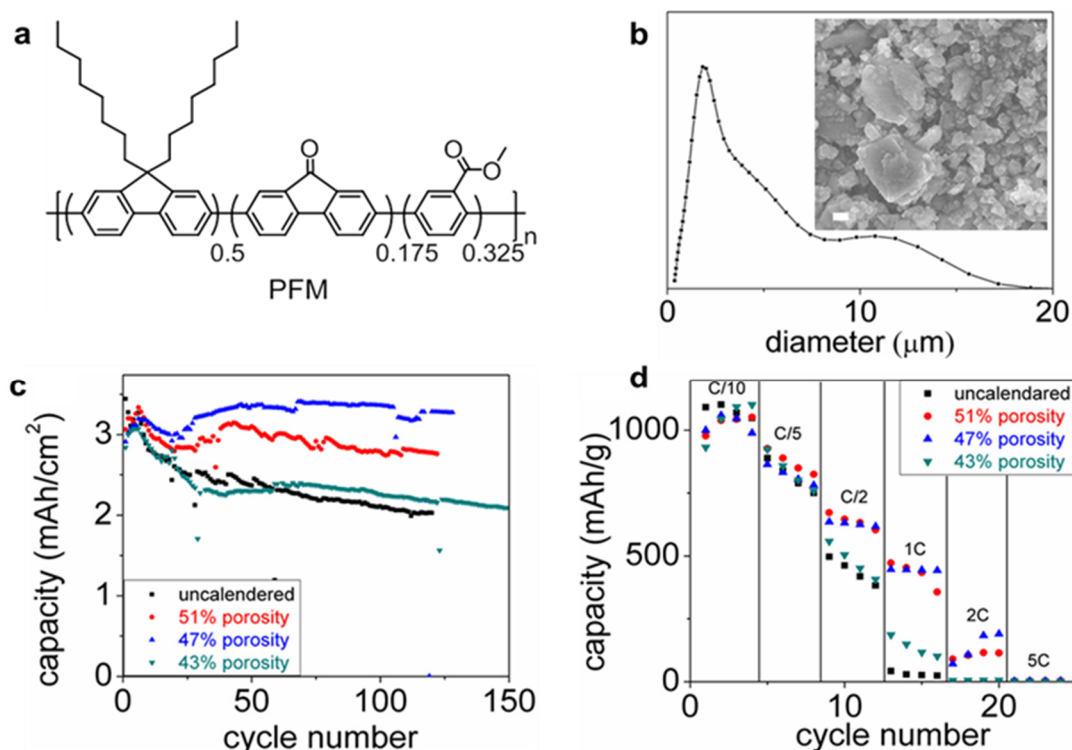


Figure V- 21: (a) Chemical structure of PFM conductive polymer binder. (b) Particle size analysis via light scattering for the SiO pristine particles, embedded is the SEM image of the particles with a scale bar of 1 μm . (c) Cycling performance of the SiO/PFM electrode after calendered into different porosities. (d) Rate performance

Figure V- 21a and b shows the chemical structure of the PFM conductive polymer binder and morphology of the SiO anode used in this work. 47% porosity is determined to deliver the best cell cycling performance (Figure V- 21c), with a high coulombic efficiency. Electrodes with 51% porosity may still have too much porosity, the charge transport path is not improved to an ideal case, although the performance is indeed improved compared to the uncalendered electrode. The electrodes with 43% porosity, on the other hand, are over compressed. The improved electrochemical performance is further proved in the rate performance shown in Figure V- 21d. This high loading electrode with high density is enabled by the dual strategy of utilizing conductive polymer binder and an effective calendering method.

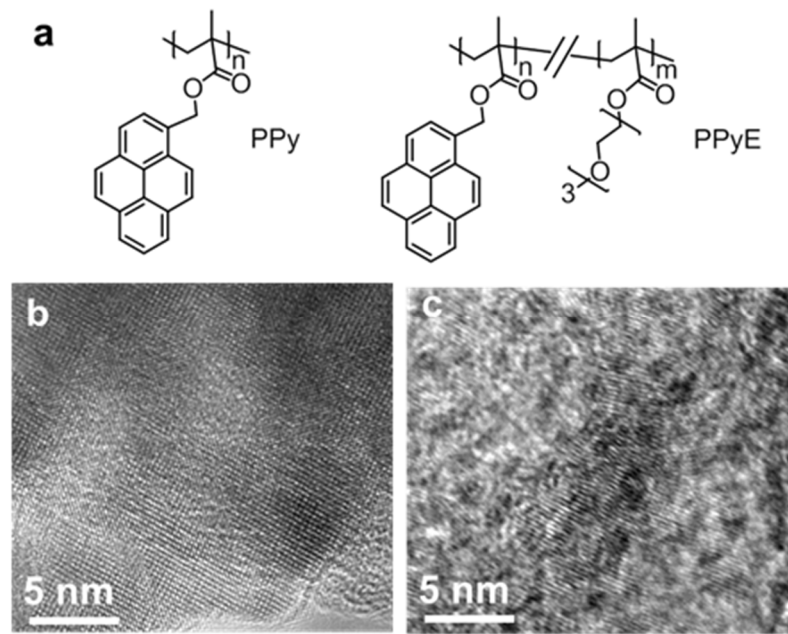


Figure V-22: (a) Structure of poly(1-pyrenemethyl methacrylate) (PPy) and poly(1-pyrenemethyl methacrylate-co-triethylene oxide methyl ether methacrylate) (PPyE). High-resolution TEM (HRTEM) images of (b) PPy and (c) PPyE

Here we describe a class of electric-conducting polymers that conduct electron via the side chain π - π stacking. These polymers can be designed and synthesized with different chemical moieties to perform different functions, extremely suitable as conductive polymer binder for lithium battery electrode. A class of methacrylate polymers based on a polycyclic aromatic hydrocarbon side moiety, pyrene, was synthesized and applied as an electrode binder to fabricate a silicon (Si) electrode. The electron mobilities for PPy and PPyE are characterized as $1.9 \times 10^{-4} \text{ cm}^2 \text{V}^{-1} \text{s}^{-1}$ and $8.5 \times 10^{-4} \text{ cm}^2 \text{V}^{-1} \text{s}^{-1}$, respectively. These electric conductive polymeric binders can maintain the electrode mechanical integrity and Si interface stability over a thousand cycles of charge and discharge. (See Figure V-22, and Figure V-23.)

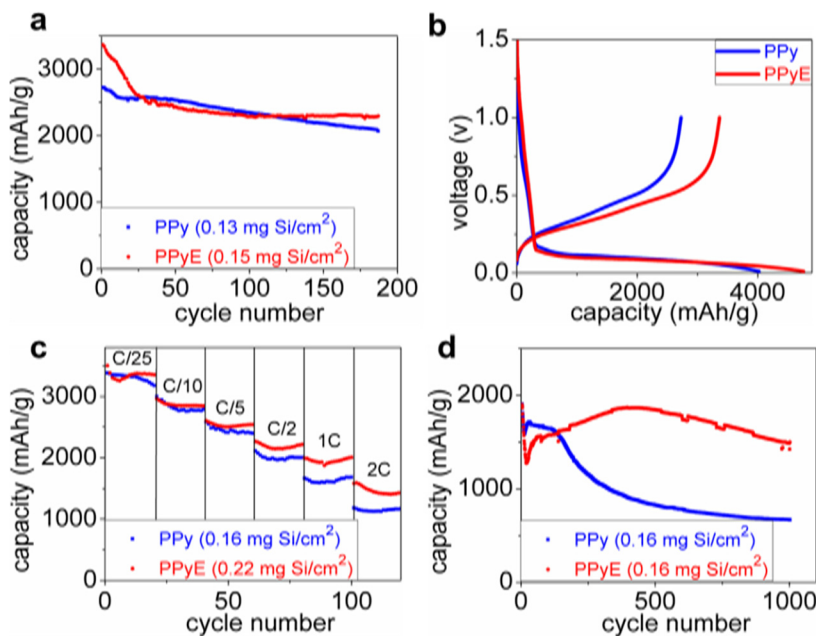


Figure V-23: (a) Charge (delithiation) capacities of PPy and PPyE-based Si electrodes at C/10. (b) First-cycle voltage curves. (c) Rate performance. (d) Charge (delithiation) capacities of PPy and PPyE-based Si electrodes at 2C rate. The mass loadings of Si for each cell are labeled in the plot

The as-assembled batteries exhibit a high capacity and excellent rate performance due to the self-assembled solid-state nanostructures of the conductive polymer binders. The physical properties of this polymer are further tailored by incorporating ethylene oxide moieties at the side chains to enhance the adhesion and adjust swelling to improve the stability of the high loading Si electrode.

A Conductive Polymer Binder for High-tap Density NanoSi with High 1st Cycle Coulombic Efficiency

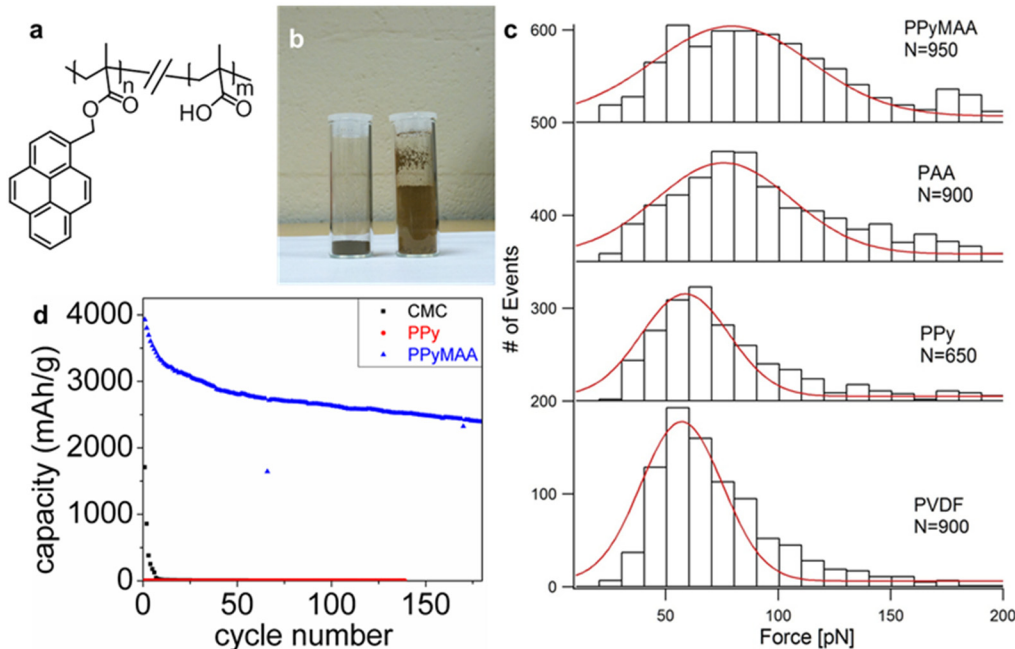


Figure V-24: (a) Chemical structure of PPyMAA conductive polymer binder. (b) A comparison of 0.3 g of high-tap-density nanoSi (left) and regular nanoSi produced by chemical vapor deposition (right). (c) Histograms of AFM rupture force distribution corresponding to pulling a single polymer chain from a glass surface. Averaged rupture forces for PPyMAA, PAA, PPy, and PVDF on glass substrate were 95 ± 58 , 99 ± 54 , 72 ± 40 and 68 ± 38 piconewton (pN), respectively, with mean rupture forces \pm standard deviations and N= # of observed unbinding events. The pulling velocity is 1000 nm/s and dwell time is 0.5 seconds. (d) Charge (delithiation) capacities of high tap density Si electrodes at C/10 with different binders

This study introduces a new binder, Poly(1-pyrenemethyl methacrylate-co-methacrylic acid) (PPyMAA), for a high-tap-density nano-silicon electrode cycled in a stable manner with a first cycle efficiency of 82% - a value that is further improved to 87% when combined with graphite material. Incorporating the MAA acid functionalities does not change the lowest unoccupied molecular orbital (LUMO) features or lower the adhesion performance of the PPy homopolymer. Our single-molecule force microscopy measurement of PPyMAA reveals similar adhesion strength between polymer binder and anode surface when compared with conventional polymer such as homo-polyacrylic acid (PAA), while being electronically conductive. The combined conductivity and adhesion afforded by the MAA and pyrene copolymer results in good cycling performance for the high-tap-density Si electrode. (See Figure V-24.)

Conclusions and Future Directions

Different engineering methods, such as prelithiation by SLMP and calendaring are shown as effective methods for high-capacity Si-containing anode materials in the battery application. New generations of side-chain conjugating conductive polymer allow fine tune of the binder structure for custom-design toward different anode materials. The single molecule AFM technique proves to be a good way of monitoring the mechanical property and adhesion strength of the newly designed binders with different functionalities, combined with the electronic conductivity of the side-chain conjugation structure, this new chemistry presents unprecedented capability of enabling desirable electrochemical performance of different high-capacity anode materials.

FY 2015 Publications/Presentations

1. Ling, Min, Hui Zhao, Xingcheng Xiao, Feifei Shi, Mingyan Wu, Jingxia Qiu, Sheng Li, Xiangyun Song, Gao Liu, and Shanqing Zhang, "Low cost and environment-benign crack-blocking structure for

- long life and high power Si electrodes in Lithium ion batteries," *J. Mater. Chem. A* 3 (2015): 2036-2042.
- 2. Zhao, Hui, Neslihan Yuca, Ziyan Zheng, Yanbao Fu, Vincent S. Battaglia, Guerfi Abdelbast, Karim Zaghir, and Gao Liu, "High capacity and high density functional conductive polymer and SiO anode for high-energy lithium-ion batteries," *ACS Applied Materials & Interfaces* 7, no. 1 (2015): 862-866.
 - 3. Ling, Min, Yanan Xu, Hui Zhao, Xingxing Gu, Jingxia Qiu, Sheng Li, Mingyan Wu, Xiangyun Song, Cheng Yan, Gao Liu, and Shanqing Zhang, "Dual-functional gum arabic binder for silicon anodes in lithium ion batteries," *Nano Energy* 12 (2015): 178-185.
 - 4. Wu, Mingyan, Xiangyun Song, Xiaosong Liu, Vincent Battaglia, Wanli Yang, and Gao Liu, "Manipulating the polarity of conductive polymer binders for Si-based anodes in lithium ion batteries," *J. Mater. Chem. A* 3 (2015): 3651-3658.
 - 5. Park, Sangjae, Hui Zhao, Guo Ai, Cheng Wang, Xiangyun Song, Neslihan Yuca, Vincent S. Battaglia, Wanli Yang, and Gao Liu, "Side-chain conducting and phase-separated polymeric binders for high performance silicon anodes in lithium-ion batteries," *J. Am. Chem. Soc.* 137 (2015): 2565-2571.
 - 6. Yuan, Wen, Mingyan Wu, Hui Zhao, Xiangyun Song, Vincent Battaglia, and Gao Liu, "Baseline Si electrode fabrication and performance for the Battery for Advanced Transportation Technologies program," *J. Power Sources* 282 (2015): 223-227.
 - 7. Shi, Feifei, Phillip N. Ross, Hui Zhao, Gao Liu, Gabor A. Somorjai, and Kyriakos Komvopoulos, "A catalytic path for electrolyte reduction in lithium-ion cells revealed by in-situ attenuated total reflection-fourier transform infrared spectroscopy," *J. Am. Chem. Soc.* 137, no. 9(2015): 3181-3184.
 - 8. Zhao, Hui, Wen Yuan, Gao Liu, "Hierarchical electrode design of high-capacity alloy nanomaterials for lithium-ion batteries," *Nano Today* 10, no. 2 (2015): 193-212.
 - 9. Bai, Ying , Yang Tang, Zhihui Wang, Zhe Jia, Feng Wu, Chuan Wu, Gao Liu, "Electrochemical performance of Si/CeO₂/Polyaniline composites as anode materials for lithium ion battery," *Solid State Ionics* 272 (2015): 24-29.
 - 10. Dai, Kehua , Jing Mao, Xiangyun Song, Vincent Battaglia, Gao Liu, "Na_{0.44}MnO₂ with very fast sodium diffusion and stable cycling synthesized via polyvinylpyrrolidone-combustion method," *Journal of Power Sources* 285(2015): 161-168.
 - 11. Mao, Wenfeng, Yanbao Fu, Hui Zhao, Guo Ai, Yiling Dai, Dechao Meng, Xinhe Zhang, Deyang Qu, Gao Liu, Vincent Battaglia, Zhiyuan Tang, "Rational design and facile synthesis of Li₃V₂(PO₄)₃@C nanocomposites using carbon with different dimensions for ultrahigh rate lithium ion batteries," *ACS Applied Materials & Interfaces* 7, no. 22 (2015): 12057-12066.
 - 12. Ai, Guo, Yiling Dai, Yifan Ye, Wenfeng Mao, Zhihui Wang, Hui Zhao, Yulin Chen, Junfa Zhu, Yanbao Fu, Vincent Battaglia, Jinghua Guo, Venkat, Srinivasan, Gao Liu, "Investigation of surface effects through the application of functional binders in lithium sulfur batteries," *Nano Energy* 16 (2015): 28-37.
 - 13. Ling, Min, Jingxia Qiu, Sheng Li, Cheng Yan, Milton Kiefei, Gao Liu, Shanqing Zhang. "Multi-functional SA-PProDOT binder for lithium ion batteries," *Nano Letters* 15, no. 7 (2015): 4440-4447.
 - 14. Qiao, Ruimin, Kehua Dai, Jing Mao, Tsu-Chien Weng, Dimosthenis Sokaras, Dennis Nordlund, Xiangyun Song, Vince Battaglia, Zahid Hussain, Gao Liu and Wanli Yang, "Revealing and suppressing surface Mn(II) formation of Na_{0.44}MnO₂ electrodes for Na-ion batteries," *Nano Energy* 16 (2015): 186-195.
 - 15. Feng, Caihong , Le Zhang, Menghuan Yang, Xiangyun Song, Hui Zhao, Zhe Jia, Kening Sun, and Gao Liu, "One pot synthesis of copper sulfide nanowires/reduced graphene oxide nanocomposites with excellent lithium storage properties as anode materials for lithium ion batteries," *ACS Applied Materials & Interfaces* 7, no. 29 (2015): 15726-15734.
 - 16. Yan, Xiaodong , Zhihui Wang, Min He, Zhaozhi Hou, Ting Xia, Gao Liu, and Xiaobo Chen, "TiO₂ nanomaterials as anode materials for lithium-ion rechargeable batteries," *Energy Technology* 3 (2015): 801-814.
 - 17. Zhao, Hui, Zhe Jia, Wen Yuan, Heyi Hu, Yanbao Fu, Gregory Baker, and Gao Liu, "Fumed silica based single-ion nanocomposite electrolyte for lithium batteries," *ACS Applied Materials & Interfaces* 7 (2015): 19335-19341.

18. Dai, Kehua, Zhihui Wang, Guo Ai, Hui Zhao, Wen Yuan, Xiangyun Song, Vincent Battaglia, Chengdong Sun, Kai Wu, and Gao Liu, "The transformation of graphite electrode materials in lithium ion batteries after cycling," *J. Power Sources* 298 (2015): 349-354.
19. Zhao, Hui, Fadi Asfour, Yanbao Fu, Zhe Jia, Wen Yuan, Ying Bai, Min Ling, Heyi Hu, Gregory Baker, and Gao Liu, "Plasticized polymer composite single-ion conductors for lithium batteries," *ACS Applied Materials & Interfaces* 7 (2015): 19494-19499.
20. Bai, Ying, Xingzhen Zhou, Zhe Jia, Chuan Wu, Liwei Yang, Mizi Chen, Hui Zhao, Feng Wu, and Gao Liu, "Understanding the combined effects of microcrystal growth and band gap reduction of $\text{Fe}_{(1-x)}\text{Ti}_x\text{F}_3$ nanocomposites as cathode materials for lithium-ion batteries," *Nano Energy* 17 (2015): 140-151.
21. Jia, Zhe, Hui Zhao, Ying Bai, Ting Zhang, Amanda Siemens, Andrew Minor, and Gao Liu, "Solvent processed conductive polymer with single-walled carbon nanotube composites," *Journal of Materials Research*, Accepted.
22. Zhao, Hui and Gao Liu. Electrical conductive polymer binder for Si alloy materials. U.S. Patent Application Ser. No.14/632,907, filed February 2015.
23. Liu, Gao, Hui Zhao, and Zhihui Wang. SiO anode enabled by conductive polymer binder and performance enhancement by stabilized lithium metal powder (SLMP). U.S. Patent Application Ser. No. 14/741, 350, filed June 2015.
24. Liu, Gao and Hui Zhao. High capacity and high rate electrodes for lithium-ion batteries. U.S. Patent Application Ser. No. 14/741, 383, filed June 2015.
25. Liu, Gao, Guo Ai, and Hui Zhao. Three dimensional ant-nest structure electrode for high ratio and high loading lithium-sulfur batteries. U.S. Patent Application, filed October 2015.
26. Ai, Guo. "Toward a Better Understanding of the Surface Effect Through the Design of Binders in Lithium Sulfur Battery." Paper presented at the 227th Electrochemical Society Meeting, Chicago, IL, May 2015.
27. Zhao, Hui. "Toward Practical Application of Functional Conductive Polymer Binder for a High-Energy Lithium-Ion Battery Design." Paper presented at the 227th Electrochemical Society Meeting, Chicago, IL, May 2015.
28. Zhao, Hui. "Toward a Single-Ion Nanocomposite Electrolyte for Lithium Batteries." Paper presented at the 227th Electrochemical Society Meeting, Chicago, IL, May 2015.
29. Ai, Guo. "Toward a Better Understanding of the Surface Effect Through the Design of Binders in Lithium Sulfur Battery." Paper presented at the Materials Research Society Spring Meeting 2015, San Francisco, CA, April 2015.
30. Zhao, Hui. "Side-Chain Conducting and Phase-Separated Polymeric Binders for High-Performance Silicon Anodes in Lithium-Ion Batteries." Paper presented at the Materials Research Society Spring Meeting 2015, San Francisco, CA, April 2015.
31. Zhao, Hui. "Toward Practical Application of Functional Conductive Polymer Binder for a High-Energy Lithium-Ion Battery Design." Paper presented at the Materials Research Society Spring Meeting 2015, San Francisco, CA, April 2015.
32. "Hierarchical Assembly of Inorganic/Organic Hybrid Si Negative Electrodes," ES223_Liu_2015_O, U.S. DOE Vehicle Technologies AMR, 2015.

V.B.5 Studies in Advanced Electrode Fabrication (LBNL)

Objectives

This project supports BMR PIs through the supply of electrode materials, laminates, and cells as defined by the BMR Focus Groups. The emphasis of the 2015 effort will be on the High-Voltage Focus Group. The objectives are to fabricate electrodes that result in excellent cycling of cathode materials when tested under standard conditions, screen sources of materials, define baseline chemistries, and benchmark performance of materials. This provides a common chemistry and performance metrics that other BMR institutions can use as a benchmark for their own efforts on the subject. In addition, test configurations will be designed and built to identify and isolate problems associated with poor performance.

- Fabricate electrodes of NCM, LCO, and HV-LCO that cycle well between 2.8 and 4.1 V.
- Investigate the ability to disassemble and reconstruct cells to determine the source of impedance in full cells.
- Develop pouch cells.
- Develop a method for gas sampling.
- Begin investigations into fabricating thicker electrodes.

Technical Barriers

- Preparing electrodes that cycle well despite changes to the active material.
- Preparing full cells that cycle well.
- Preparing cells where one can distinguish if gassing is occurring.
- Ability to assess different forms of cell failure.
- The ability to make thick electrodes that do not delaminate.

Technical Targets

- Performance: Specific energy – 350 Wh/kg cell level; 235 Wh/kg system level.
- Performance: Specific power – 700 W/kg cell level; 470 W/kg system level.
- Life: 15 years.

Accomplishments

- An electrode formulation was established for nickel-cobalt-manganese layered oxide (3,3,3) (NCM), lithium cobalt oxide (LCO), and high-voltage LCO (HV-LCO) which allowed for cycling to 100 cycles between 2.8 and 4.1 V with performance equivalent to what is found in the literature.
- Electrochemical impedance spectroscopy was obtained on two full cells. The cathodes from the cells and anodes from the cells were combined in symmetric cells. The impedance in the anode cells is similar to the impedance in the full cells. The impedance of the cathode cell is significantly higher. The best way to establish impedance of the cathode is to subtract the impedance of the anode from the full cell or use a cell with a reference electrode.
- Pouch cells were assembled that show improved cyclability of full-cell chemistry. Coin cells typically show a capacity fade for full cell chemistry. The reason for this is still being investigated.
- Pouch cells with vents have been developed that allow for gas sampling. The gas formed in a cell during cycling could be a clue to the failure mechanism.

Project Details

Vince Battaglia
(Lawrence Berkeley National Laboratory - PI)
Energy Storage and Distributed Resources Division
1 Cyclotron Road
Berkeley, CA 94720
Phone: 510-486-7172; Fax: 510-486-4260
E-mail: vsbattaglia@lbl.gov

Start Date: October 2011
Projected End Date: October 2015

- Electrodes of thicknesses ranging from 80 to 275 microns were cast at our typical casting speeds and with doctor blades set between 250 and 750 microns. Laminates greater than 180 microns easily delaminated from the current collector.

Introduction

Today's Li-ion battery performs very well between 3 and 4.1 V with capacities of around 140 mAh/(g of cathode). This results in an average energy density on a chemistry basis of approximately 400 Wh/kg. After the cell is constructed and the pack assembled, the energy density drops to around 150 Wh/kg. To meet the target of 235 Wh/kg will require new materials of higher voltage and capacity and cells with less inactive material than active material. Li-ion cells are presently used in EVs, but to accelerate this trend, the cost needs to come down and the energy density needs to go up. One approach is to push today's Li-ion chemistry to higher voltages by extracting more lithium per cycle. This combination of higher capacity and voltage is compounding with regards to energy, for example, a 20% increase in capacity and a 10% increase in voltage will result in a 32% increase in energy. The problem with this is that these conditions prematurely end the life of the cells. To understand the failure mechanisms, specialized cells need to be constructed such as pouch cells, pouch cells with reference electrodes, coin cells with reference electrodes, and pouch cells with vents. Another approach to higher energy density is to make thicker electrodes. We will develop ways methods for better understanding life limitations of chemistries pushed to their limits and begin to develop techniques for making thicker electrodes.

Approach

Innovative Approach: The objectives listed above will be accomplished by utilizing the Battery Materials Characterization, Fabrication, and Testing (CFT) Facility at LBNL. The facility allows for the fabrication of electrodes and coin- and pouch-cells in a moisture- and air-free environment. Materials characterization techniques include PSA, BET, SEM, and ICP. The testing facilities include over 350 test channels and the ability to perform electrochemical impedance spectroscopy. Testing includes a combination of data analysis consisting of impedance data, cycling data, and reference performance tests (RPTs) and post-test analysis consisting of SEM, TEM, ICP, and gas analysis with an MS. What follows is our approach to developing cells for performance evaluation.

- With the DOE Program Manager, define topics and materials of interest. This year the topic was high voltage performance of NCM with and without high-voltage electrolytes when compared to LCO and HV-LCO.
- Identify quality materials and suppliers willing to provide the materials and terms of engagement necessary to perform the work.
- Fabricate electrodes of baseline materials and demonstrate that the materials perform as good as is found in industry under typical operating conditions.
- Push the materials for increased energy density by extracting lithium at ever increasing voltages. Accelerate failure by operating at higher temperatures.
- Identify failure mode.
- Develop cells that can better assess the failure.
- Perform an experiment to qualify the new method of data abstraction.

Results

We have achieved the following progress:

Baseline Electrodes for the High-Voltage Study

Baseline electrodes for the high-voltage study needed to be developed. The study includes the active materials LCO, High-Voltage LCO (HV LCO), and NCM, all from the same commercial supplier. Once fabricated, the electrodes were to be cycled against Li to test their cyclability. The approach is to start with conditions demonstrating excellent cyclability and then to push the voltage up until the cyclability begins to suffer. To demonstrate excellent cyclability, electrodes of modest loadings were formulated and cycled against Li metal under the typical use conditions of 30°C and between 2.8 and 4.1 V. (See Figure V- 25.)

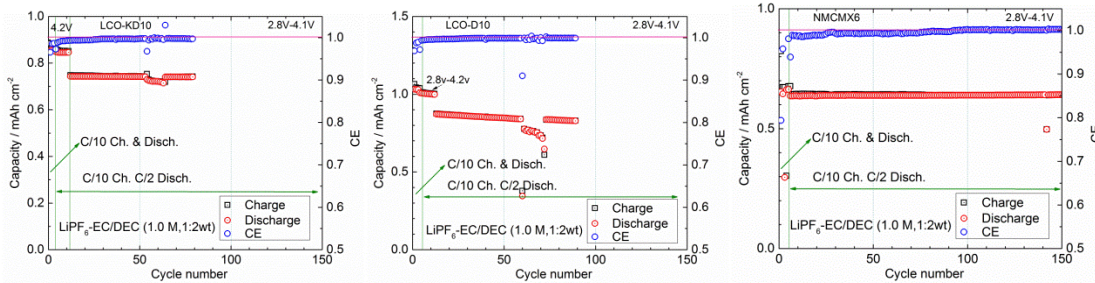


Figure V- 25: Capacity versus cycle number for NCM (left), LCO (center) and HVLCO (right) in half cells cycled between 2.8 and 4.1 V at C/10 charge and C/2 discharge

The cells with NCM and HV LCO show almost no capacity fade for the first 150 and 80 cycles, respectively. The LCO shows a slight capacity fade by the 90th cycle. These results mimic those found in the literature for LCO and NCM. Our typical formulation was used for these electrodes - active material:binder:carbon black = 85:8:7. With the benchmarking nearly completed, the next step was to start pushing up the voltage and investigating modes of capacity fade.

Full-cell Impedance Study

Two coin cells were assembled from the same NCM and graphite laminates. The cells were cycled identically and after 10 cycles were discharged to 3.6 V and electrochemical impedance spectroscopy performed. The cells were then disassembled with the cathodes combined and the anodes combined in separate symmetric coin cells. Again, electrochemical impedance spectroscopy was taken of these two-electrode cells. The results are provided in the graphs of Figure V- 26.

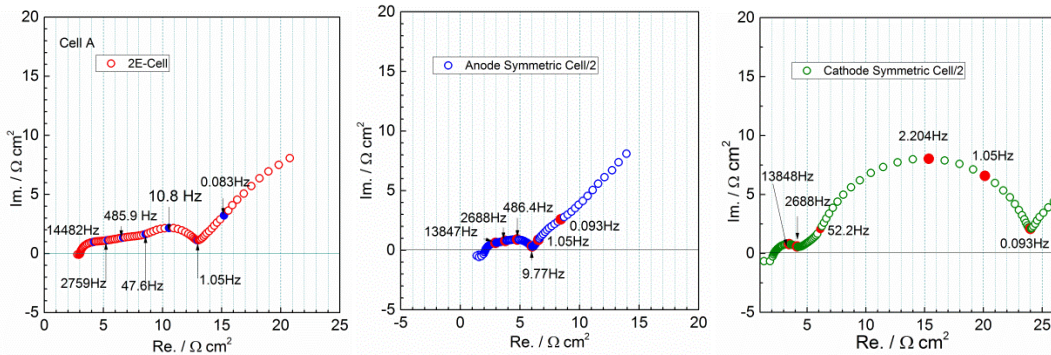


Figure V- 26: Nyquist plots of electrochemical impedance data taken of the full-cell (left), two anodes divided by 2 (center), and two cathodes divided by 2 (right)

The graph on the left is the two electrode impedance data of the Gr./NCM cell, the graph in the middle is of the symmetric anode impedance divided by two, and the graph to the right is of the symmetric cathode impedance divided by two. The data in the middle graph can be associated with some of the impedance of the full cell; however, the graph to the right shows impedance much greater than that found in the full cell. This finding, though not well understood, is often found in symmetric cells of the cathode and make them an unreliable method for directly sourcing contributions from the cathode to the full cell data. This requires relying on recent methods we have developed for interpreting three-electrode impedance data obtained from coin cells.

Pouch Cells

It was discovered that full cells assembled in coin-cell hardware do not cycle as well as in pouch cell hardware. A mechanism for the short coming is currently under investigation. As a result, an investigation into making pouch cells was initiated. In the pouch cells, the anode has 9% more superficial area than the cathodes. Full pouch-cells were made with excess anode capacity of 2.8 %. Cells with excess anode capacity are expected to have less total cell capacity because the side reaction on the anode will require lithium from the cathode, which leads to the premature discharge of the anode than expected from a perfectly balanced cell. (Cells with too little anode capacity risk lithium deposition near the top of charge.)

Figure V- 27 shows the cycling performance of the full cell with just 2.8% more anode capacity than cathode capacity. The cell was cycled between 2.8 and 4.2 V at a C/2 charge and C/1 discharge rate and has reached 700 cycles with a small amount of capacity fade. Figure V- 28 shows the average voltage of the charge and of the discharge during each cycle. The difference between the two is an indication of the resistance rise in the cell. One sees that the difference in average voltage has increased less than 10% from cycle 100 to cycle 600. The capacity fade appears to accelerate after the first 600 cycles even though the difference in average

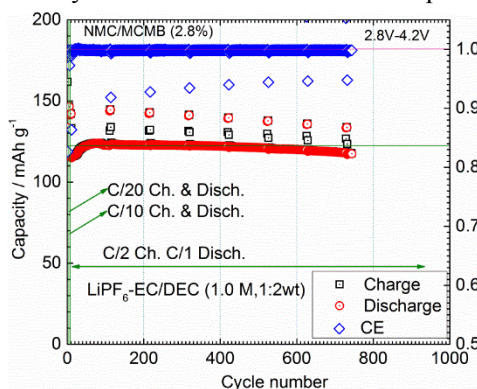


Figure V- 27: Capacity versus cycle number for a Graphite/NCM cell cycled between 2.8 and 4.2 V at different rates

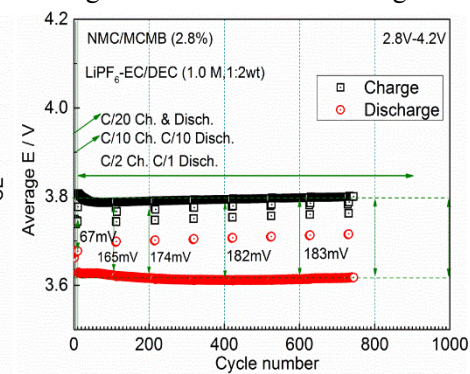


Figure V- 28: Average voltage on charge and discharge plotted versus cycle number

voltage appears to be leveling off. This may be a result of depletion of electrolyte in the cell. Further investigation is needed.

Gas Sampling

The difference in cycleability of three cathode materials: LCO, high-voltage LCO, and NCM is still important to us. Of the three materials, LCO showed the greatest impedance rise. Therefore, a pouch cell of LCO and Li metal was fabricated. A pouch cell was developed that consists of two valves. One valve will allow a sweeping gas in and the other to allow the gas out. To form a gas, the LCO cell was taken to various upper cut-off voltages and held there for 24 hours to see if a gas was generated. At reasonable working voltages, voltages below 4.6 V, no gas generation was evident as the cells did not puff up. The cells were then hooked to a mass spectrometer to measure the composition of any gas that may have been formed, but the mass spec was not of sufficient accuracy to detect a significant change in gas composition. Thus, it appears that the resistance rise in the LCO cell does not generate gas. One cell was pushed to ever increasing cut-off voltages in an effort to generate gas. It finally occurred at around 5.2 V. It is fairly well known that the electrolyte loses stability at this voltage and may form hydrogen gas at the anode. This situation was considered too dangerous to continue. It is believed that there is value in measuring the rate of gas generation in a cell and its composition but not under conditions where the cell voltage is so high that hydrogen is predictably formed. In the meantime a mass spec with slightly better accuracy was acquired.

Fabrication of Thick Electrodes

Preliminary experiments in fabricating thick electrodes was initiated. This will be the focus of our effort for FY16. The first activity was to cast electrodes using a standard formulation of 85% active material, 8% binder, and 7% Super P Li carbon additive to different thicknesses. The binder is Kureha 1100 PVDF. (In the future, PVDF binders from Arkema will be the center of our research: material is expected to arrive early October.) The active material is NCM from a major commercial supplier. The materials are combined with NMP to form a slurry. After an hour of mixing, the viscosity of the slurry was measured at 1810 cp at 6 RPM. This viscosity is one we are familiar with and is adjusted by the amount of NMP added to the slurry. The coating speed for casting the slurry was set at 60 cm/min (about 50 times slower than is found in industry). The table below provides a list of the doctor blade heights and the final thickness of the laminates once the electrodes had dried. One sees that the final thickness is approximately 1/3 the height of the doctor blade. (These are the measured heights before calendaring.)

Table V- 1: Doctor blade heights and final thickness of laminates

Doctor blade gap (μm)	250	300	400	500	600	750
Laminate thickness (μm)	80	95	130	180	205	275

From this preliminary data it was discovered that electrodes cast at 600 microns and greater were difficult to handle as they easily delaminated from the aluminum current collector.

Once electrodes were cast they were taken to the Battery Program SEM for analysis. A method to section electrodes has been developed as can be seen in Figure V- 29. EDS can also be obtained as seen in Figure V- 29.

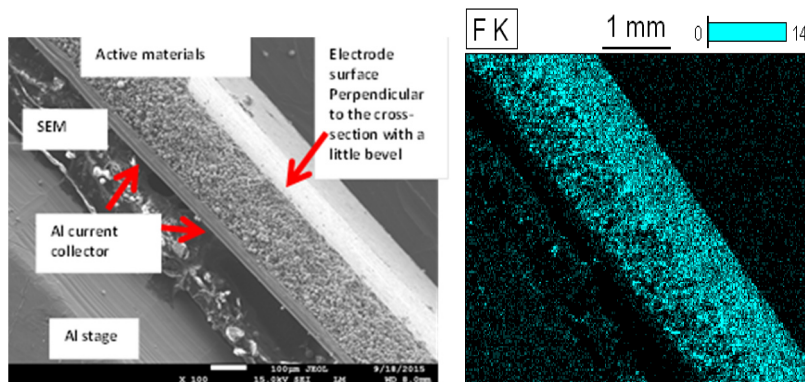


Figure V- 29: Left: SEM of an electrode that has been cross sectioned exposing the current collector, laminate, SEM tape, and Aluminum stage; right: EDS image of the distribution of fluorine in cross sectioned electrode

Conclusions and Future Directions

This fiscal year consisted of the development of a number of methods for fabricating and assessing failure modes of cells. A formulation for fabricating cyclable electrodes of NCM, LCO, and HV-LCO was established. The inability to directly measure the impedance of symmetric cells of cathodes was demonstrated. The ability to make cyclable full cells using pouch cell hardware was established. The ability to make pouch cells with the opportunity for gas analysis was established. Preliminary work on casting thick electrodes was started. Some of the important parameters for casting thick electrodes will be mixing time, coating speed, laminate temperature, and calendaring temperature. Some of these were touched on here.

Future work will focus on methods for fabricating thicker electrodes. Emphasis will be on processing, binder formulation, and material physical properties.

FY 2015 Publications/Presentations

1. "Electrode Fabrication and Performance Benchmarking." ES232_Battaglia_2015_O, U.S. DOE Vehicle Technologies AMR, 2015.
2. This year, there were also over 10 publications from this group, however, the work presented here is just being written-up.

V.C Silicon Anode Research

V.C.1 Development of Si-Based High-Capacity Anodes (PNNL)

Objectives

- Develop high-capacity, low-cost silicon (Si)-based anodes with good cycle stability and rate capability.
- Reduce the first cycle irreversible capacity loss and improve Coulombic efficiencies during cycling.
- Advance the fundamental understanding of the degradation mechanism of Si-based anodes, including the mechanical and electrochemical stability.

Technical Barriers

- Reduced capacity at high loading conditions.
- Large first cycle loss and fast capacity fade.
- High cost associated with preparation of nano-structured Si.

Technical Targets

- Synthesize nanostructured Si with low cost and scalable approaches.
- Achieve >80% capacity retention over 200 cycles of thick electrodes ($\sim 3 \text{ mAh/m}^2$) through optimization of the Si electrode structure and binder.
- Develop pre-lithiation method to reduce the first cycle loss of Si-based anodes
- Develop a 700~1000 mAh/g Si anode (SiNANOdeTM) with a target cycle-life of > 800.
- Synthesize nanostructured Si and lithium oxide nanocomposites by the direct reduction of silicon monoxide to achieve reversible capacities > ~1200 mAh/g.

Accomplishments

- Developed nano-porous Si anode by a low-cost, scalable, and modified magnesiothermic reaction. The sample exhibits good cycling stability at high electrode loadings.
- Developed a low cost approach to prepare nano-Si/hard carbon/graphite composite electrode.
- Demonstrated full cell operation of nano-Si/NCA cell with >80% capacity retention over 100 cycles.
- Generated nano-Si and nano-Si/Li conducting oxide matrix by high-energy mechanochemical reduction (HEMR) of silicon oxides (SiO_x) by reactive reducing agents such as metal and metal alloys. The long term cycling of the nanorods show a capacity of ~1125 mAh/g at a current rate of 1A/g at the end of 100 cycles with a columbic efficiency of ~99.6 %.
- Prepared nano-Si composites by HEMR of metallic silicides using suitable reducing agents.

Project Details

Tien Duong (Program Manager)

Subcontractor: PNNL

Ji-Guang Zhang (Pacific Northwest National Laboratory)

902 Battelle Boulevard, Mail Stop K2-44

Richland, WA 99352

Phone: 509-372-6515; Fax: 509-375-2186

E-mail: Jiguang.Zhang@pnnl.gov

Jun Liu (Pacific Northwest National Laboratory, Co-PI)

902 Battelle Boulevard, Mail Stop K2-44

Richland, WA 99352

Phone: 509-375-4443; Fax: 509-351-6242

E-mail: Jun.Liu@pnnl.gov

Prashant Kumta (University of Pittsburgh)

815C Benedum Hall

3700 O'Hara Street

Pittsburgh, PA 15261

Phone: 412-648-0223; Fax: 412-624-3699

E-mail: pkumta@pitt.edu

Jim Zheng (Florida State University)

Room A346, 2525 Pottsdamer Street

Tallahassee, FL 32310

Phone: 850-410-6464

E-mail: zheng@eng.fsu.edu

Start Date: October 2010

Projected End Date: September 2016

- Developed a low-cost, completely recyclable green abundant template method to prepare high-performance, high-capacity Si nanostructures with an initial capacity of ~2800 mAh/g at a current rate of 50 mA/g and first cycle irreversible loss (FIR) loss of only ~12 to 20%.
- Optimized the SLPMs loaded to anode for high energy and good cycle life and achieved a Coulombic charge efficiency of >95% during the first cycle.
- Apply SLPMs and sacrificial electrode to Li-ion capacitors to achieve a specific energy greater than 30 Wh/kg and the specific power greater than 5 kW/kg, and cycle life greater than 50,000 cycles.

Introduction

Si has a very high theoretical capacity of ~4200 mAh/g and great potential to be used as an anode for next generation Li-ion batteries. However, the large volume expansion that occurs during the lithiation process often leads to a rapid capacity loss. These barriers have hindered the practical applications of Si-based anodes. Although significant progress has been made on the development of the Si-based anodes, there are still many obstacles that prevent their practical application. Long-term cycling stability remains the foremost challenge for Si-based anodes, especially for high loading electrodes ($>3\text{mAh}/\text{cm}^2$) required for many practical applications. The cyclability of full cells using Si-based anodes is also complicated by multiple factors, such as diffusion-induced stress and fracture, loss of electrical contact among Si particles and between Si and current collector, and the breakdown of SEI layers during volume expansion/contraction processes. Several nanostructured Si materials have demonstrated excellent performance, but most of them work well only for low active material loadings. In addition, the electrode performance degrades quickly with the increased loadings required for practical applications. Another barrier in this field is that most high-capacity Si-based electrodes have to be prepared using expensive processes that are difficult to scale up. Therefore, to achieve practical application of this technology, a cost-effective and scalable approach needs to be developed to produce Si-based anodes that can retain excellent performance under highly loaded conditions.

Approach

Innovative Approach:

The main goal of this work is to gain a fundamental understanding on the failure mechanism of the Si-based anode and improve its long-term stability, especially for thick electrodes operated at full cell conditions. The methods described below have been used to reach this goal:

1. Porous Si prepared by a low-cost thermite reaction has been modified for use as Li-ion battery anodes. The as-received material exhibited a low capacity due to its poor electronic conductivity. Therefore, a thin layer of conductive carbon (~10 nm) was coated on the Si surface by chemical vapor deposition. Si anodes with high areal capacity ($>2\text{ mAh}/\text{cm}^2$) will be investigated.
2. A nano-Si-hard carbon-graphite composite was synthesized using a low-cost hydrothermal method. Nano-Si and graphite were dispersed into 1.5 M carbonhydrate solution and hydrothermally treated after stirring for 1 hour. It is a low cost, scalable, one-step synthesis. The ratio of graphite, nano-Si and hard carbon from polymer carbonization can be controlled well. The cycling stability of the thick electrode will be investigated.
3. High-energy mechanical milling of silicon oxides with different reducing agents was carried out to generate nanoparticle a Si– lithium-ion conducting (LIC) matrix composite material by in situ mechanochemical reduction of silicon oxides.
4. The pre-lithiation of the anode electrode was made simply by mixture of anode materials and stabilized Li metal powder (SLMP). When the electrolyte was filled into a complete battery or capacitor cell, The Li will intercalate into anode materials. The more SLMPs that were intercalated into the anode, the lower potential and higher capacity the anode electrode would be.

Results

1. High-loading anodes of mesoporous Si from thermite reaction with surface modifications

Porous Si from thermite reaction (in collaboration with Oregon State University) can have good cycling stability. Figure V- 30a shows the typical cycling performance of a porous Si anode with a loading of $\sim 2 \text{ mAh/cm}^2$. The battery was cycled using the standard BATT (BMR) protocol: 0.005 to 1 V; three formation cycles at 0.06 mA/cm^2 ; and 0.75 mA/cm^2 for delithiation and 0.5 mA/cm^2 for lithiation. The capacity is $\sim 2 \text{ mAh/cm}^2$ at a low current density of $\sim 0.06 \text{ mA/cm}^2$. A capacity of $\sim 1.73 \text{ mAh/cm}^2$ at high rate was observed, and the capacity retention is $\sim 76\%$ over 200 cycles. The porous Si prepared by a modified thermite reaction demonstrated good cycling stability at a high loading of $\sim 3 \text{ mAh/cm}^2$. Figure V- 30b shows cycling stability and Coulombic efficiency of a highly loaded cell ($\sim 3 \text{ mAh/cm}^2$ nano-porous Si prepared by modified thermite method). The capacity retention is $\sim 83.6\%$ over 100 cycles at 0.06 mA/cm^2 charge/discharge current density.

The capacity retention can be $\sim 78\%$ over 150 cycles using the BMR protocol (Figure V- 30c). Porous Si prepared by electrochemical etching was matched with a NCA cathode for full cell demonstration in a coin cell. The NCA-Si full cell was tested between 2 and 4.3 V at a current density of $\sim 0.375 \text{ mA/cm}^2$. The anode capacity is limited in the full cell. The capacity ratio between NCA and Si is $\sim 1.2:1$. The porous Si electrode was pre-cycled in half-cell for two cycles and then re-assembled into the full cell with NCA. The areal capacity of the full cell is $\sim 1.8 \text{ mAh/cm}^2$, and the capacity retention is $\sim 80\%$ after 100 cycles (Figure V- 30d).

A stable window for SEI formation was identified by tuning the charge-discharge voltage window. By lowering the charge voltage from 1 V to 0.6 V, the capacity retention of similarly loaded Si/B₄C/ graphite composite anode can be improved by 20% with slight loss in capacity. This is an indication that the SEI formed on Si anode is stable between 0 to 0.6 V.

2. Nano-Si-hard carbon-graphite composite anode

A new type of ternary core-shell structured graphite-nano Si-hard carbon composite (Figure V- 31A) was synthesized.

By designing spherical graphite/nano-Si coating/hard carbon core-shell structure, we expect to achieve improved cycling stability for highly loaded Si anodes. During the synthesis, nano-Si and graphite were dispersed into 1.5-M carbonhydrate solution and hydrothermally treated after stirring for 1 hour. Scanning electron microscopy (SEM) and transmission electron microscopy (TEM) characterization shows that the designed structure was obtained (Figure V- 31B). Nano-Si is attached to the surface of spherical graphite and coated with a hard carbon layer, while the control samples (blend of graphite/nano-Si and blend of graphite/nano-Si/hard carbon composites) showed phase separation. In the composite, the ratio of graphite, nano-Si, and hard carbon from polymer carbonization can be well controlled. The optimized sample shows good electrochemical performance at a high areal loading of 2.5 mAh/cm^2 . The specific capacity is ~ 800

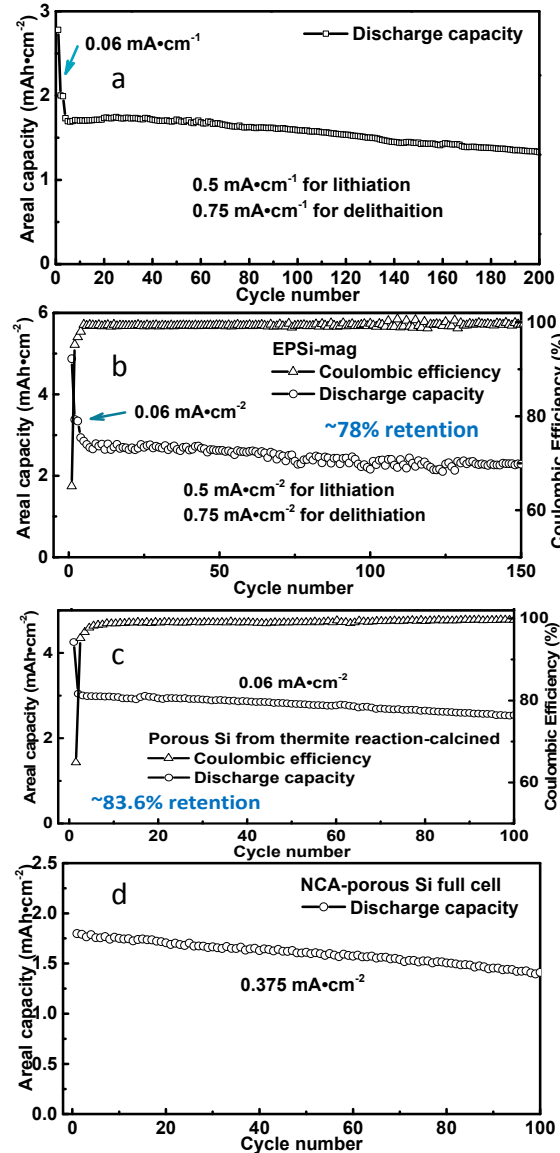


Figure V- 30: a. Cycling stability of a porous Si anode from thermite reaction with a high areal discharge capacity of $\sim 2 \text{ mAh/cm}^2$. b. Cycling stability of a thick porous Si (thermite) anode after modification. c. Cycling stability of a thick porous Si (thermite) anode after modification at low rate of $\sim 0.06 \text{ mA/cm}^2$. d. A full-cell of the NCA cathode and porous Si anode with an areal capacity of $\sim 1.8 \text{ mAh/cm}^2$

mAh/g based on active materials weight at 0.2C rate ($1C = 600$ mA/g). The cell is cycled in the voltage range of ~0.005 to 1.5 V, and the data shown in Figure V- 31C is after three formation cycles at 0.05C ($1C = 600$ mA/g). The designed structure also shows improved rate performance. Further optimization will be done to further improve the cycling stability.

3. Reduction of SiO_x with metals and metal alloys

To validate the formation of amorphous (*a*-Si) or nanocrystalline Si (*nc*-Si) by direct HEMR of SiO_x with reactive agents, SiO was ball milled with the reactive elements under argon atmosphere at room temperature to generate a nano-composite of *a/nc*-Si and by product as follows: $\text{SiO}_x + nxR \rightarrow \text{Si} + x\text{RO}$; R = reductant. The milled powder obtained after 20 hours of ball milling comprised of Si and the by product, has been tested as an anode for Li-ion batteries. The sample ball milled for 20 hours containing the composite containing active Si shows an initial capacity of ~1620 mAh/g, which is close to the theoretical capacity. However, the material undergoes capacity fading of ~1% fade per cycle.

In an alternative approach, direct mechanochemical reduction of SiO with reducing metallic elements was used to validate the generation of *nc*-Si nanocomposite as follows: $\text{SiO} + n\text{M} \rightarrow \text{Si} + \text{M}_n\text{O}$. However, HEMR using reactive reductants is not suitable for large-scale production because of the very reactive nature of the reducing agents under normal atmospheric conditions. Hence, a new stable yet reactive reductant has been identified to reduce SiO to form *nc*-Si and at the same time yield a very soft byproduct matrix. Figure V- 32 shows the X-ray diffraction (XRD) patterns of SiO_x and the reductant mix obtained at different milling times. Si forms even after a short milling time of 5 hours. Increasing the milling time to 20 hours results in a reduction in the the volume fraction of SiO_x ,

whereas the volume fraction of Si increases. To complete the reaction of SiO_x with the reductant, powder milled for 20 hours was heat treated at 700°C. The XRD analysis of the heat-treated sample shows the evolution, and an expected increase, in the intensity of the Si peak, while growth in the peak intensity of the byproduct also occurs. Further washing of the heat-treated powder revealed only broad peaks of Si in the XRD pattern without SiO and the byproduct phase, thus indicating the complete reduction of SiO by HEMR. The heat-treated sample consisting of Si and the byproduct exhibits a first cycle discharge capacity of ~1500 mAh/g, which is close to the theoretical capacity (~1700 mAh/g), although the material shows a capacity fade of $\geq 1\%$ per cycle. Futher studies are ongoing to stabilize the material, thus improving the long term cycling performance and rate capability of the HEMR-derived materials.

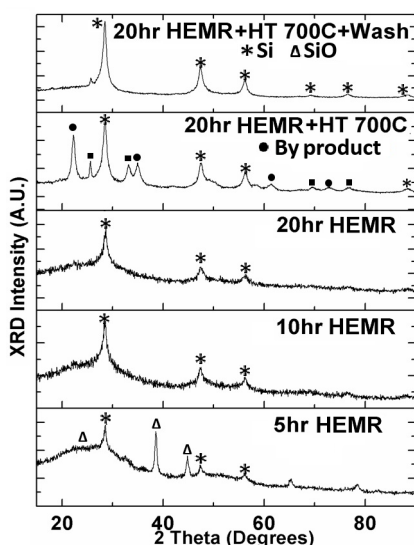


Figure V- 32: XRD patterns of SiO -alloy with milling time, after treatment and etching

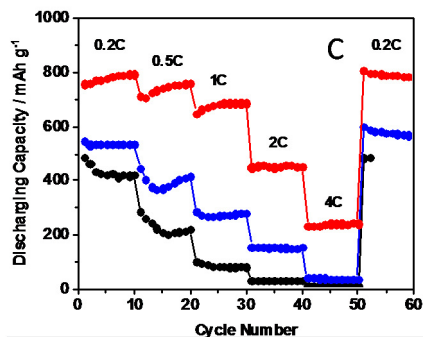
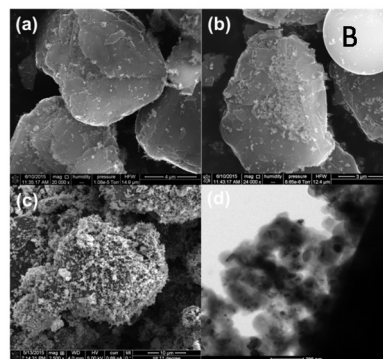
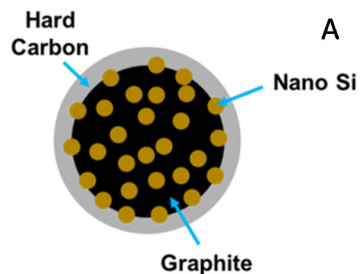


Figure V- 31: A. Schematic view of graphite/Si/graphene shell product. B. (a) SEM images of blend graphite/nano-Si, (b) blend graphite/nano-Si/hard carbon, (c) the product after synthesis and (d) TEM image of the product. C. Cycle retention (full circle) with areal capacity (empty circle) at 0.2C ($1C=600\text{mA/g}$) blend graphite/nano-Si (black), blend graphite/nano-Si/hard carbon (blue), and the product (red) at various C-rate (0.2C fixed for charging test, $1C = 600\text{mA/g}$)

4. Reduction of SiO with Mg₂Si

In another attempt to achieve reduction of SiO, SiO was successively reduced with Mg₂Si using HEMR to obtain Si and MgO. Subsequently, the material was washed and etched with acids to yield nc-Si. The resulting nc-Si was then coated with carbon. SEM images (Figure V- 33a and Figure V- 33b) show micron sized agglomerates consisting of nc-Si. The resulting irregular shaped morphology is consistent with mechanochemical milling reactions. The product obtained at the end of the milling step is accordingly scaled down by the acid etching process yielding a final product with a nonuniform, and a high specific surface area (~190 m²/g). The EDAX spectra shown in Figure V- 33c confirms that the final product is comprised of mostly Si and does not contain any peaks corresponding to Mg/MgO, which were dissolved in the first acid wash step. The presence of oxygen can be attributed to unreacted SiO or presence of an oxide layer formed on the surface of the mechanochemically derived nc-Si. The TEM bright-field image (Figure V- 33d) clearly shows an aggregate of nanosized particles with the particles in the range of few tens of nanometers. The nc-Si/C composite material shows better cycling stability (10 cycles at 50 mA/g plus 90 cycles at 100mA/g, 0.12% per cycle fade rate, ~495 mAh/g at the end of 100 cycles) compared to pure nc-Si material, which shows a very rapid fade rate within the first 20 cycles (Figure V- 34). The high surface area of nc-Si and unreacted SiO are the major contributors to the FIR loss (~55 to 65%) and the initial capacity of ~2000 mAh/g, which will be further improved by increasing the kinetics of the reduction reaction by a combination of milling and thermal activation.

5. Nanostructured silicon using economical water soluble templates

In another study, a low-cost abundant water soluble template-based approach was developed by further exploiting the high-energy mechanical-milling approach followed by low pressure chemical vapor deposition (LPCVD) to develop the Si nanostructures. The template was ball milled for 2 hours and 20 hours to reduce the size of the particles and then coated with Si by thermal decomposition of Si precursors. After washing the template, the Si obtained from 2h milling of the template showed nanoflakes morphology with thickness of ~50-100 nm while the Si obtained from the template milled for 20 hours showed a mixture of nanorods and nanoparticles (Figure V- 35). The XRD analysis shows *no major change in the phase of the water soluble template after mechanical milling and after LPCVD of Si on the milled template*. Because of the highly crystalline nature of the template, the signature of the template dominates the signature in

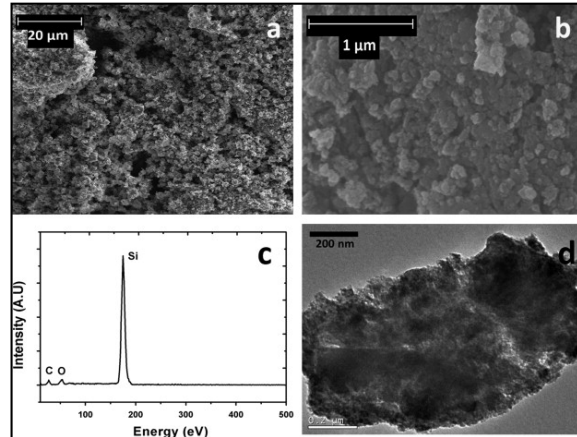


Figure V- 33: (a)&(b) SEM images, (c) EDAX spectra, (d) TEM image of the final nc-Si product

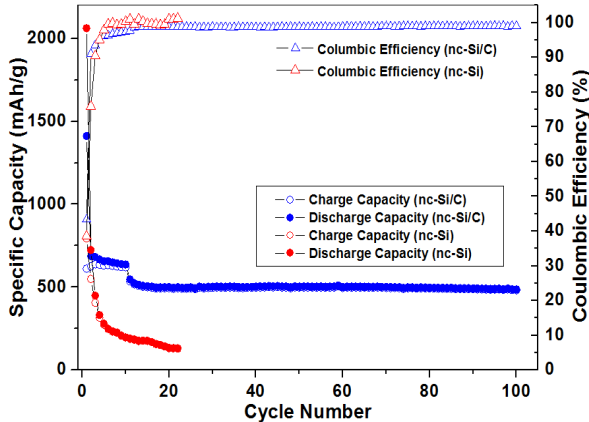


Figure V- 34: Specific charge/discharge capacity/Coulombic efficiency vs. cycles of nc-Si and nc-Si/carbon in Li/Li⁺ system

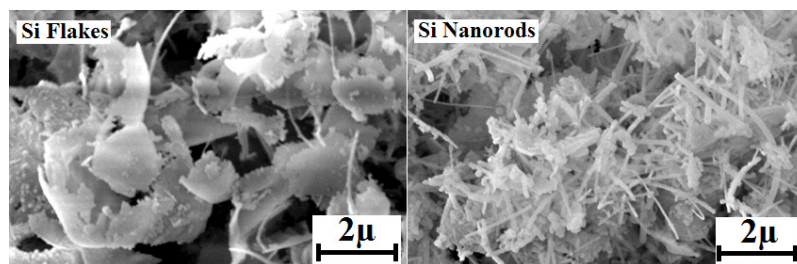


Figure V- 35: Nanoflakes and nanorods obtained by LPCVD of Si on water soluble template

the XRD pattern of Si deposited on the template. However, after complete dissolution of the template in warm deionized water, the XRD pattern reveals an amorphous Si presence very similar to hollow silicon nanotubes (h-SiNTs). The Si obtained from deposition on the template milled for 20 hours shows more crystalline signature as compared to that obtained from the deposition on the template milled for 2 hours.

The long-term performance of the Si with different morphologies of nanoflakes and nanorods is shown in Figure V- 36. The Si nanorod material showed an initial discharge and charge capacity of ~2930 mAh/g and ~2475mAh/g, respectively, with ~12 to 15% FIR loss at a current rate of 50 mA/g. The long-term cycling of the nanorods show a capacity of ~1125 mAh/g at a current rate of 1A/g at the end of 100 cycles with a columbic efficiency of ~99.6% and a fade rate of 0.35% loss per cycle between the 11th cycle and the 120th cycle. The Si nanoflakes showed similar discharge and charge capacities of ~2780 mAh/g and ~2200 mAh/g, respectively, with ~15 to 20% FIR loss at a current rate of 50 mA/g. The long-term cycling of the nanoflakes show a capacity of ~1050 mAh/g at a current rate of 1 A/g at the end of the 150th cycle with a columbic efficiency of ~99.7% and a fade rate 0.21% loss per cycle between the 11th cycle and the 150th cycle. The nanoflakes show a drastic decrease in capacities during the initial cycles followed by stabilization of the capacities, while the nanorod morphology show a gradual drop in capacity with cycling. Currently, studies are being conducted to understand the evolution of the different morphologies and further improve the stability and performance of the system by optimizing the processing parameters. This method indeed demonstrates a completely recyclable, cost-effective, and green method of template processing to develop various Si nano-scale architectures.

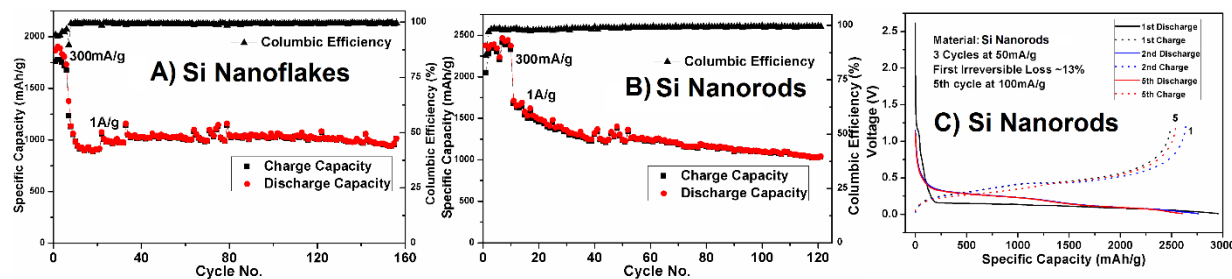


Figure V- 36: Long term cycling of a) Si flakes, b) Si nanorods; and c) voltage vs capacity plot of Si Nanorods showing 13% FIR Loss

6. Si/SLMP anode with first-cycle Coulombic efficiency over 95%

We have applied SLMPs to Si anodes to improve the first roundtrip Coulombic efficiency. Two different anode electrodes were studied in this work. One was porous Si prepared by the anodic etching method, and another one was a mixture of Si powder and carbon nano-tubes (CNT). SLMPs were manually coated on the surface of the electrode, and then pressed under ~50 kg/cm² of pressure to break the surface protection layer of the SLMP. Button cells were assembled with copper foil (current collector), anode electrode, separator paper, Li foil (reference electrode), and stainless steel (current collector). The separator paper was a microporous membrane (Celgard 3501). The electrolyte was 1 M LiPF₆ in ethylene carbonate:dimethyl carbonate at a weight ratio of 1:1. After the potential of the anode was measured, it was discharged to a potential of 0.005 V vs. Li/Li⁺; then charged to 1.0 V vs. Li/Li⁺ under a constant current of 1 mA (0.625 mA/cm²). Figure V- 37 shows the galvanostatic charge-discharge profiles measured from anodes with different SLMP loadings. All electrodes have a diameter of 14.28 mm. The porous Si/C anodes were made with 1.85 mg porous Si and 2.15 mg carbon; the Si powder/CNT anodes were made with 2 mg Si powder and 2 mg CNT. It can be seen that the reversibility of the first charge-discharge cycle is strongly dependent on the SLMP loading. Without the SLMP loading, the ratios of the first discharge and charge capacities were ~50 to 55%; however, when the right amount of SLMP was coated to the surface of anodes, the ratios of the first discharge and charge cycle capacity were nearly 100%.

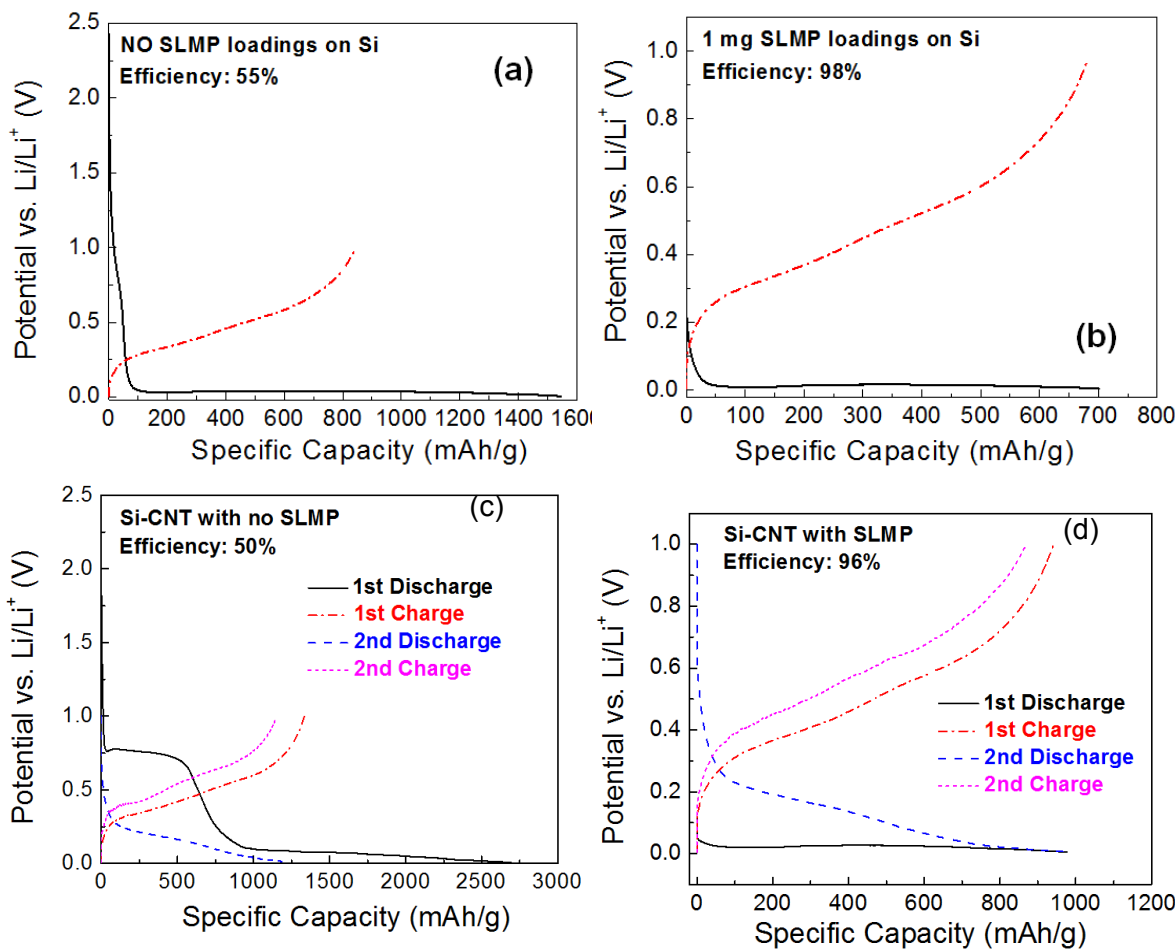


Figure V- 37: Galvanostatic discharge-charge profiles measured from anodes of (a) porous Si/C without SLMP, (b) porous Si/C with 1.0 mg SLMP, (c) Si powder/CNT without SLPM, and (d) Si powder/CNT with 0.91 mg SLMP

7. High energy density Li-ion capacitors based on High surface carbon

The hierarchical porous carbon (HPC) was prepared by ice templating method. The electrode was made with 90% of HPC and 10% binder by weight. A symmetrical button cell supercapacitor was made with HPC electrodes and tested at constant current mode as shown in Figure V- 38a. The specific capacitance was calculated based on the results and was about 107 F/g. We also assembled high energy density Li-ion capacitor (LIC) pouch cell prototypes using an activated anode and a hard-carbon/SLMP cathode. A specific energy and energy density as high as 30 Wh kg^{-1} and 39 Wh L^{-1} were achieved as shown in Figure V- 38b. The pouch cells can deliver over 50% of the maximum stored energy at a discharge rate over the 100C rate. After 100,000 cycles, the LIC pouch cell still has 82.5% of its initial capacitance. The average leakage current is $0.3 \mu\text{A cm}^{-2}$ during the first 72 hours as shown in Figure V- 38c.

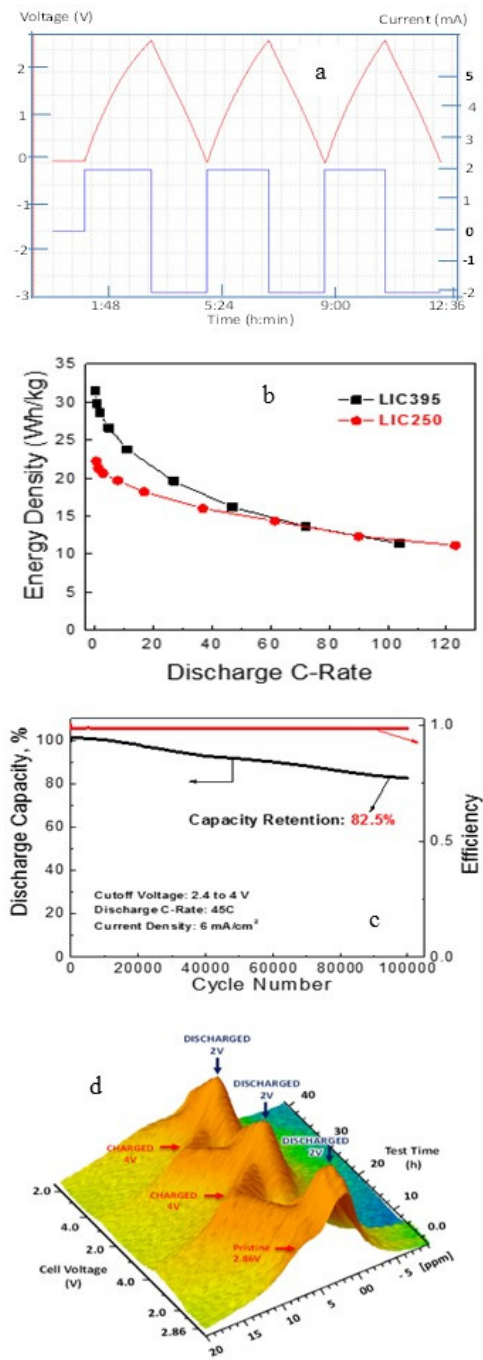


Figure V-38: a. Experimental results from a symmetrical supercapacitor. b. The energy density and power density as a function of the current densities for two pouch cells of LIC250 and LIC395. c. The specific discharge energy as a function of cycle number for the LIC pouch cells. d. Time resolved in situ ${}^7\text{Li}$ NMR spectra of the LIC

This work reveals the importance of surface treatment on nanostructured Si, which will lead to a well-controlled ratio of Si and surface oxide layer and provide guidance on further improvement on Si-based anode materials. In a separate effort, a new type of ternary core-shell structured graphite-nano Si-hard carbon

We performed in situ ${}^7\text{Li}$ nuclear magnetic resonance (NMR) experiments on the LIC by simultaneously cycling an LIC pouch cell in the 2.0 to 4.0 V range. NMR spectra recorded for multiple cycles reveal the ${}^7\text{Li}$ NMR signals arising from different parts of the capacitor. We employed a combination of in situ ${}^7\text{Li}$ NMR, component isolation and Gaussian-Lorentzian peak fitting to investigate the resonances arising from the Li metal from the stabilized Li metal powder (SLMP), free ions in the electrolyte, the SEI layer, intercalated Li in the carbon anode, and Li ions in the electric double-layer on the cathode. The in situ ${}^7\text{Li}$ NMR spectra recorded during galvanostatic cycling of the LICs showed that the charge and discharge processes caused electrochemical reactions that result in considerable repetitive changes in peak intensities and chemical shifts over multiple cycles. Further cycle experiments revealed contributions from the individual electrodes. This series of experiments help us visualize the Li ion transfer mechanisms in LICs.

The time-resolved NMR spectra as shown in Figure V-38d from the series experiments are presented in as a stacked plot for the first two full cycles of an LIC. In the pristine state (first spectrum) at an open-circuit voltage of 2.86 V, we observed the presence of the anode-intercalated Li ions (~ 4.7 ppm), which is a state of partial intercalation caused by the shorting effect upon introduction of electrolyte. The intercalation signal vanishes at the end of the first discharge cycle when a peak emerges at -2.5 ppm, which is confirmed through Gaussian-Lorentzian curve fitting. The reverse process is observed during the next charge with the peak corresponding to lithiation and reaching a maximum at ~ 7 ppm. This trend continues further into the second cycle. These results from the series of experiments confirm the reversibility and repeatability of the electrochemical processes observed. The periodic shifting of the peaks and the simultaneous increase and decrease in the intercalation and double layer peaks clearly follows and confirms the electrochemical behavior of the battery type cathodes and capacitor type anodes of the LICs.

Conclusions and Future Directions

We have engineered the nanoporous Si from a modified magnesiothermic reaction by controlled surface oxidation forming a <5 -nm oxide layer on the 10 to 20 nm nanocrystalline Si. Highly loaded electrodes of ~ 3 mAh/cm 2 demonstrates stable cycling with $\sim 80\%$ capacity retention over 150 cycles. The specific discharge capacity based on the total electrode weight is ~ 1000 mAh/g at the lithiation/delithiation current density of 0.5/0.75 mA/cm 2 .

composite was development using a low-cost, scalable, one-step synthesis approach. The optimized sample shows good electrochemical performance at a high areal loading of 2.5 mAh/cm². The specific capacity is ~800 mAh/g based on active materials weight at the 0.2C rate.

We also made significant progress in Si composite anode (SiNANOdeTM), Mn-rich cathode, and cell performance improvement. The specific capacity of the SiNANOde anode can be controlled in a range of 500 to 1800mAh/g by tuning amounts of engineered Si nanowires on the low cost graphite powders, as needed, using low-cost precursors, which significantly reduces its production cost but still provides high energy density and good cyclability. Initial Coulombic efficiency has been improved up to more than 92% for all the SiNANOde products. Almost 100% utilization of Si capacity has been realized in the cells. By optimizing Si nanowire coverage and distribution on the desired graphite surface and by optimizing electrolyte and binder chemistry as well as by improving the pouch cell formation protocol, cycle life has been significantly improved. We have demonstrated a cycle life of more than 800 cycles at a capacity retention of 79% for the SiNANOde with 700~1000 mAh/g in half cell. We have also demonstrated good cycling performance of >1000 cycles in the full cells combing with NCA cathodes. The improved 1100mAh/g SiNANOde/NCA cell has a slower capacity fading than 600mAh/g SiNANOde/NCA cell.

In a separate effort, we applied SLMPs to Si anodes to improve the first cycle efficiency. When a right amount of SLMP was coated on the surface of anodes, the ratios of the first discharge and charge cycle capacity were close to 100%. We also assembled high-energy-density LIC pouch cell prototypes using an activated anode and a hard carbon/SLMP cathode. A specific energy and energy density as high as 30 Wh kg⁻¹ and 39 Wh L⁻¹, respectively, were achieved. After 100,000 cycles, the LIC pouch cell retained 82.5% of the initial capacitance.

Our future work will focus on the following areas:

- Optimize synthesis parameters for the core-shell structured graphite-nano Si-hard carbon composite using a low-cost, scalable, one-step process. Open spaces will be designed as part of the composite structure to tolerate volume expansion.
- Further improve the performance of SiO_x with different reducing agents to generate a nanoparticle Si-Li conducting matrix composite material by in situ mechanochemical reduction of SiO_x.
- Investigate new binders to improve the cycling stability of high-loading electrodes.

FY 2015 Publications/Presentations

1. "Surface Coating Constraint Induced Self-Discharging of Silicon Nanoparticles as Anodes for Lithium Ion Batteries," Langli Luo, Peng Zhao, Hui Yang, Borui Liu, Ji-Guang Zhang, Yi Cui, Guihua Yu, Sulin Zhang, and Chong-Min Wang, Nano Letters, DOI: 10.1021/acs.nanolett.5b03047.
2. "In-Situ Transmission Electron Microscopy Probing of Native Oxide and Artificial Coating Layer on Silicon Nanoparticles for Lithium Ion Batteries", Yang He, Chunmei Ban, Arda Genc, Lee Pullan, Jun Liu, Ji-Guang Zhang, Scott Mao, and Chongmin Wang, ACS Nano, 8, 11816-11823, 2014.
3. "Surface-Coating Regulated Lithiation Kinetics and Degradation in Silicon Nanowires for Lithium Ion Battery", Langli Luo, Hui Yang, Pengfei Yan, Jonathan J. Travis, Younghlee Lee, Nian Liu, Daniela Molina Piper, Se-Hee Lee, Peng Zhao, Steven M. George, Ji-Guang Zhang, Yi Cui, Sulin Zhang, Chunmei Ban, and Chong-Min Wang, ACS Nano, 9, 5559–5566, 2015.
4. "Scribable multi-walled carbon nanotube-silicon nanocomposites: a viable lithium-ion battery system", Rigved Epur, Madhumati Ramanathan, Moni K. Datta, Dae Ho Hong, Prashanth H. Jampani, Bharat Gattu, Prashant N. Kumta, Nanoscale, 2015, 7, 3504-3510.
5. "A simple and scalable approach to hollow silicon nanotube (h-SiNT) anode architectures of superior electrochemical stability and reversible capacity", Rigved Epur, Prashanth H. Jampani, Moni K. Datta, Dae Ho Hong, , Bharat Gattu, Prashant N. Kumta, J. Mater. Chem. A, 2015, 3, 11117-11129.
6. "High Loading Si Anode for Practical Li-ion Batteries." Xiaolin Li, Sookyoung Jeong, Yulin Chen, Pengfei Yan, Chongmin Wang, Xiulei Ji, Wei Luo, Chunlong Chen, Jun Liu, and Ji-Guang Zhang. Invited talk presented at MRS spring 2015, San Francisco, CA on April 9, 2015.
7. "Porous Silicon as Stable Li-ion Battery Anodes." Li X, SY Hu, P Yan, CM Wang, M Gu, R Kennard, MJ Sailor, W Luo, X Ji, J Zhang, and J Liu. Presented by Xiaolin Li at MRS Fall Meeting, Boston, MA on December 3, 2014.

8. "Nano Silicon (Si_{NP}) Based Carbon Composite: Flexible Anode System in Lithium Ion Batteries", B. Gattu, P. P. Patel, P. Jampani, M. K. Datta and P. N. Kumta, 228th ECS Meeting, Oct 2015; Phoenix, Arizona.
9. "High Performing Hollow Silicon Nanotube Anodes for Lithium Ion Batteries", B. Gattu, P. Jampani, P. P. Patel, M. K. Datta, and P. N. Kumta, 227th ECS Meeting, May 2015; Chicago, Illinois.
10. "The effect of lithium loadings on anode to the voltage drop during charge and discharge of Li-ion capacitors", W.J. Cao, M. Greenleaf, Y.X. Li, D. Adams, M. Hagen, T. Doung, and J.P. Zheng, *J. Power Sources*, **280**, 600 (2015).
11. "Comparative Study of the Power and Cycling Performance for Advanced Lithium-Ion Capacitors with Various Carbon Anodes", W. Cao, J.S. Zheng, D. Adams, T. Doung, and J.P. Zheng, *Journal of The Electrochemical Society*, **161**, A2087 (2014).
12. "Application of physical electric circuit modeling to characterize Li-ion battery electrochemical processes", M. Greenleaf, H. Li, and J.P. Zheng, *Journal of Power Sources*, **270**, 113 (2014).
13. "Strategies to optimize lithium-ion supercapacitors achieving high performance: Cathode configurations, lithium loadings on anode, and types of separator", W. Cao, Y.X. Li, B. Fitch, J. Shih, T. Doung, and J.P. Zheng, *Journal of Power Sources*, **268**, 841(2014).
14. "Development and characterization of Li-ion capacitor pouch cells", W.J. Cao, J. Shih, J.P. Zheng, and T. Doung, *Journal of Power Sources*, **257**, 388 (2014).
15. "Comparative Study of the Power Performance for Advanced Li-Ion Capacitors with Various Carbon Anodes," W.J. Cao, J.S. Zheng, D. Adams, and J.P. Zheng, ECS Trans. 2014 61(18): 37-48.
16. "Catalytic electrode with gradient porosity and catalyst density for fuel cells", J.P. Zheng, Z.Y. Liang, B. Wang, C. Zhang, and W. Zhu, US Patent Number 8,703,355, April 22, 2014.

V.C.2 Pre-Lithiation of Silicon Anode for High Energy Li Ion Batteries (Stanford U)

Objectives

- Design and synthesize lithiated silicon to prelithiate various anode materials.
- Increase first-cycle Coulombic efficiency of various anode materials.
- Increase the stability of lithiated silicon in both dry air and ambient air conditions.
- Design and fabricate fully lithiated Si anodes to pair with high capacity lithium-free cathodes.

Technical Barriers

The high chemical reactivity of prelithiation reagents makes them difficult to synthesize and survive multiple battery fabrication process (exposure to air and solvents, slurry mixing, coating and baking). This fundamental challenge results in the following technical barriers:

- Restrictive synthesis conditions
- Instability in the slurry solvents
- Instability in both dry and ambient air conditions

Technical Targets

- Design various methods to synthesize lithiated silicon with different nanostructures.
- Increase the stability of lithiated silicon in the slurry solvents.
- Increase the stability of lithiated silicon in both dry air and ambient air conditions.

Accomplishments

- Anode materials can be prelithiated by direct contact of Li metal foil to anodes.
- New solvent and binder combination, compatible to lithiated silicon, was developed for slurry processing.
- Anode materials can be prelithiated by $\text{Li}_x\text{Si}-\text{Li}_2\text{O}$ core-shell nanoparticles to increase first-cycle Coulombic efficiency.
- $\text{Li}_x\text{Si}-\text{Li}_2\text{O}$ core-shell nanoparticles exhibit improved dry air stability.
- Artificial-SEI protected Li_xSi nanoparticles exhibit a high capacity $> 2000 \text{ mAh/g}$.
- Anode materials can be prelithiated by artificial-SEI protected Li_xSi nanoparticles to increase first-cycle Coulombic efficiency.
- Artificial-SEI protected Li_xSi nanoparticles exhibit improved stability in both dry air and ambient air conditions.

Introduction

Li-ion batteries have been widely used in portable electronics as the power supply over the last two decades. Higher energy density Li-ion batteries are needed to expand their application towards electric vehicles. The first charging process, in which lithium ions and electrons move from cathode to anode, is critical for lithium-ion battery operation. When the potential of the anode is below $\sim 1 \text{ V}$ versus Li metal, the organic electrolyte is reduced on the anode surface to form a layer of solid electrolyte interphase (SEI) that consists of a complex composition of inorganic and organic lithium compounds. In addition, some lithium may be trapped in the electrode upon lithiation. As a result, the first charging process irreversibly consumes a fraction of the lithium ions, giving rise to a net loss of storage capacity. Such first cycle irreversible capacity loss is usually

Project Details

Tien Duong (DOE BMR Program Manager)

Recipient: Stanford University

Yi Cui (Stanford University, PI)

476 Lomita Mall, McCullough 343

Stanford, CA 94305

Phone: 650-723-4613; Fax: 650-725-4034

E-mail: ycui@stanford.edu

Start Date: August 2013

Projected End Date: July 2017

compensated by additional loading of cathode materials in current lithium-ion batteries. However, lithium metal oxide cathodes have much lower specific capacity (mostly less than ~ 200 mAh g $^{-1}$) than anodes. Excessive loading of cathode material causes appreciable reduction of battery specific energy and energy density. It is therefore attractive to develop an alternative method that suppresses this loss and consequently increases the 1st cycle Coulombic efficiency (1st cycle CE).

Approach

Innovative Approach: The objectives outlined above will be accomplished by synthesizing lithiated silicon with different nanostructures to prelithiate various anode materials. What is more, the synthesized nanoparticles should be processible in a slurry and exhibit high capacity under both dry and ambient air conditions. The major technology innovations will be undertaken to accomplish the objectives of this effort:

1. Improve the capacity of Li_xSi nanoparticles from 1000 mAh/g to > 2000 mAh/g.
2. Achieve improved stability of Li_xSi nanoparticles in the slurry process by developing new solvent-binder combination.
3. Achieve improved stability of Li_xSi nanoparticles in the dry and ambient air condition by exploring different kinds of coatings, such as Li₂O and artificial SEI-coating.

Results

We have achieved the following progress:

The synthesis of artificial-SEI coated Li_xSi nanoparticles

We developed a facile reaction process utilizing the highly reactive nature of Li_xSi NPs to reduce 1-fluorodecane, thereby producing a continuous and dense coating over the NPs as shown in Figure V- 39a. Artificial SEI-protected Li_xSi NPs were prepared via two synthetic steps. Similar to our previous study, crystalline Li_xSi NPs were synthesized by heating a stoichiometric mixture (1:4.4) of Si NPs and Li metal foil at 200 °C under mechanical stirring inside a tantalum crucible at 200 rpm for 3 days in a glove box (Ar-atmosphere, O₂ level < 1.2 ppm and H₂O level < 0.1 ppm). As-synthesized NPs were characterized by transmission electron microscopy (TEM). Care had been taken to limit the electron beam exposure time during image acquisition in order to minimize beam damage to the sample. The TEM image (Figure V- 39b) shows the surface of synthesized Li_xSi NPs is clean.

In step 2, 8 μ L of 1-fluorodecane was dissolved in 5 ml anhydrous cyclohexane, followed by the addition of 50 mg of Li_xSi NPs which is reacted for two hours at room temperature. Dissolved 1-fluorodecane was directly reduced on the surface of these NPs, forming a conformal coating as shown in the TEM images (Figure V- 39c). The selective and self-limiting reaction ensures a uniform and continuous coating on the surface. Both images indicate each individual particle is wrapped in a uniform ~ 13 nm thickness coating. The dispersion of NPs is also improved after coating. By simply doubling the concentration of 1-fluorodecane in cyclohexane, the thickness becomes ~ 30 nm, indicating the tunability of the coating layer thickness.

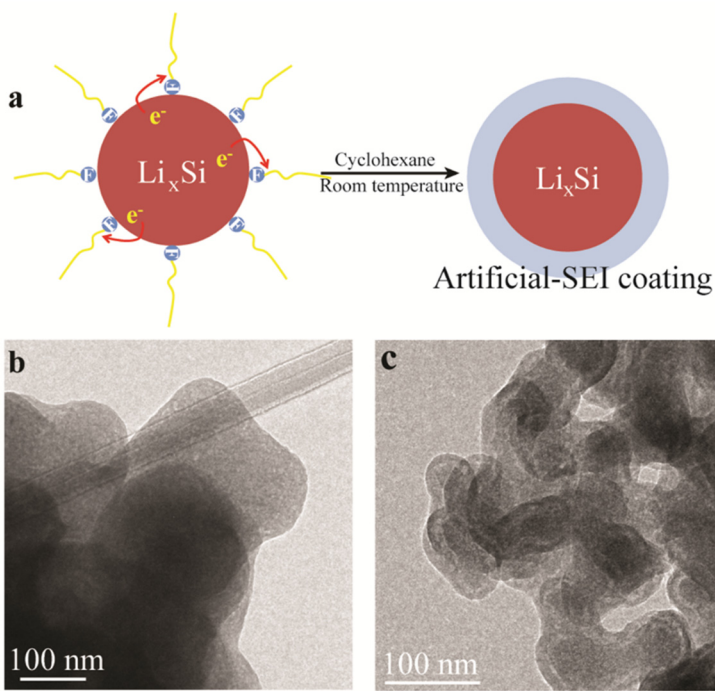


Figure V- 39: (a) Schematic diagram of the artificial-SEI coating formed by reducing 1-fluorodecane on the surface of Li_xSi NPs in cyclohexane. TEM images of Li_xSi NPs (b) before and (c) after coating

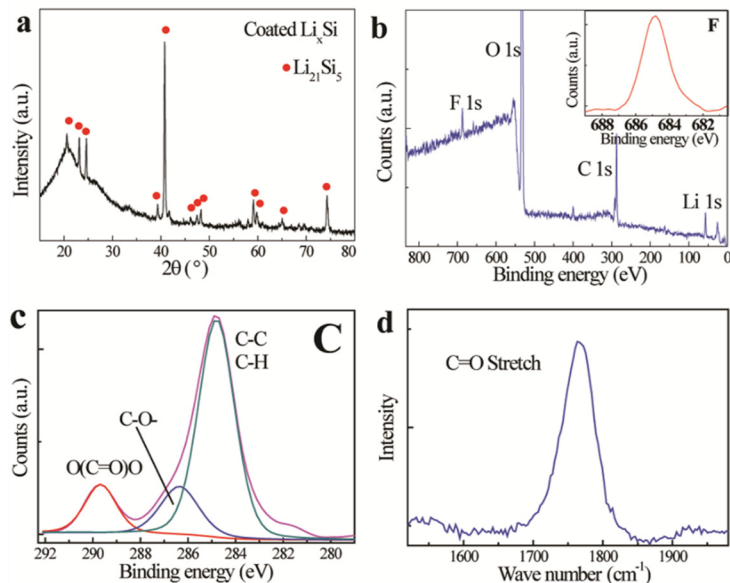


Figure V- 40: (a) XRD pattern of artificial-SEI coated Li_xSi NPs sealed in Kapton tape. (b) XPS of artificial-SEI coated Li_xSi NPs. Corresponding high-resolution XPS spectrum around F 1s peak region is shown in the inset. (c) High-resolution XPS spectra of C 1s. (d) Raman spectrum reveals the peak near 1762 cm^{-1} as the stretching vibration mode of C=O

Compositional analysis of artificial-SEI coated Li_xSi nanoparticles

Compositional analysis of the synthesized core-shell NPs was acquired by X-ray diffraction (XRD), X-ray photoelectron spectroscopy (XPS) and Raman spectroscopy. All peaks in the XRD pattern (Figure V- 40a) are indexed as $\text{Li}_{21}\text{Si}_5$ (PDF# 00-018-747), indicating a crystalline Li_xSi core and an amorphous coating layer. The broad background primarily comes from the Kapton tape used to eliminate possible side reactions with moisture and oxygen in the air. XPS analysis (Figure V- 40b) confirms the chemical composition of the coating layer with the presence of F, O, C and Li. Binding energies of all elements were calibrated with respect to the C 1s peak at 284.8 eV. The Si 2p peak typically observed at around 100 eV, however, is absent in the spectrum, suggesting excellent encapsulation of the coating which masks the NPs from surface-sensitive compositional characterization. As shown in the inset of Figure V- 40b, the F 1s spectrum contains a single peak at 684.9 eV, supporting the presence of LiF. Besides the strong hydrocarbon peak, the XPS of C shows two main peaks at 289.8 eV and 286.4 eV, corresponding to two types of C as in $\text{O}(\text{C}=\text{O})\text{O}-$ and $\text{C}-\text{O}-$, respectively (Figure V- 40c). The peak assignments were further supported by Raman spectroscopy (Figure V- 40d). The Raman spectrum reveals a strong peak at 1762 cm^{-1} which corresponds to the C=O stretching vibration mode, with a similar peak position to that of Li_2CO_3 .

Improved electrochemical performance of artificial-SEI coated Li_xSi nanoparticles

To evaluate the electrochemical performance of artificial-SEI coated Li_xSi NPs, coated Li_xSi NPs were first lithiated to 0.01 V and then delithiated to 1 V, exhibiting a high prelithiation capacity of 2100 mAh/g as shown in Figure V- 41a. Figure V- 41b and c demonstrate, artificial-SEI coated Li_xSi NPs can be mixed with anode materials during slurry processing and serve as an excellent prelithiation reagent for both Si NPs and commercial graphite. The 1st cycle CE is increased from 76.1% to 96.8%, confirming the effective

compensation of the large irreversible capacity loss in conventional Si NP anodes with the extra capacity from coated Li_xSi NPs (Figure V- 41b). The incorporation of a small amount of coated Li_xSi (graphite/coated Li_xSi =85:5 by weight) improves the 1st cycle CE from 87.4% to 99.2% (Figure V- 41c).

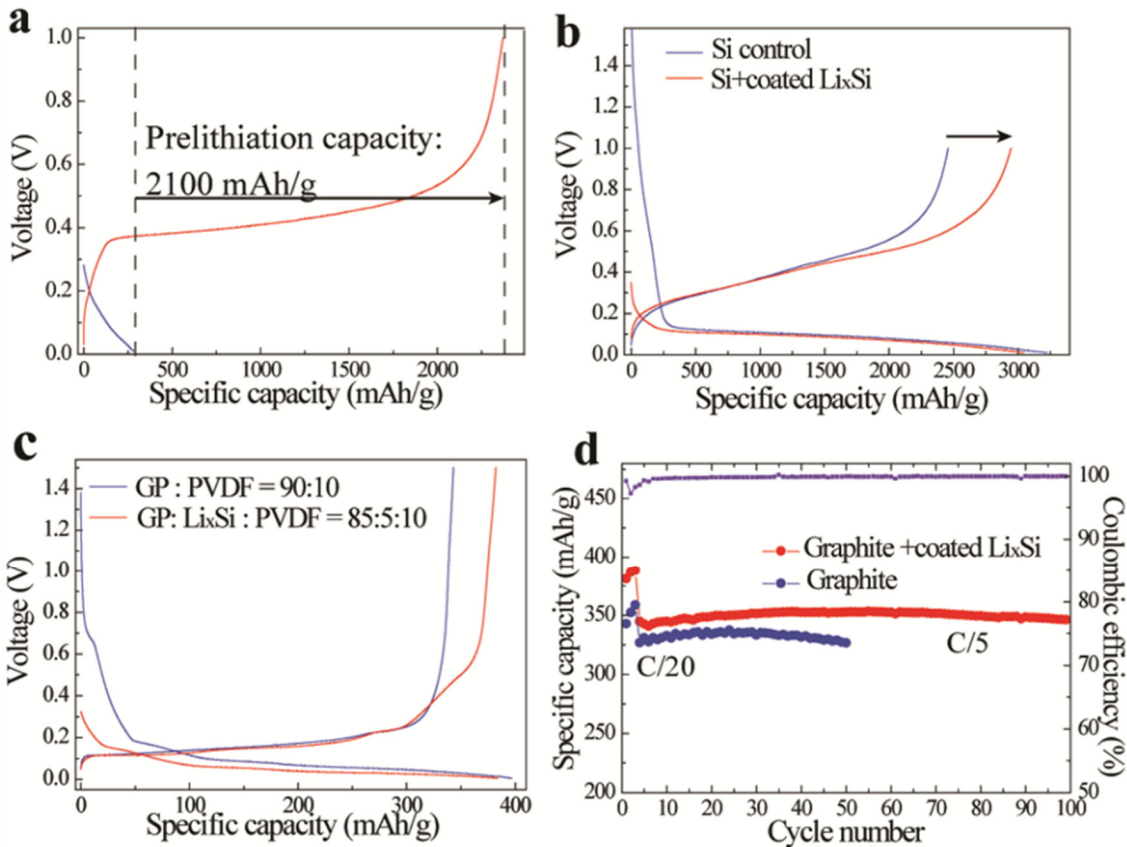


Figure V- 41: (a) 1st cycle galvanostatic discharge/charge profiles of artificial-SEI coated Li_xSi NPs. (b) 1st cycle voltage profiles of Si NPs/coated Li_xSi composite (55:10 by weight) and Si NPs control cells (The capacity is based on the total mass of Si in the electrodes.). (c) 1st cycle voltage profiles of graphite/coated Li_xSi composite (85:5 by weight) and graphite control cells. (d) Cycling performance of graphite/coated Li_xSi composite and graphite control cells at C/20 for the first three cycles and C/5 for the following cycles (1C = 0.372 A/g, the capacity is based on the mass of graphite and Si in coated Li_xSi NPs). The purple line is the Coulombic efficiency of graphite/coated Li_xSi composite

Due to its small size, the added Li_xSi NPs are expected to be embedded in the interstices of graphite microparticles. Since Li_xSi is already in its expanded state, sufficient space has been created during electrode fabrication. The Li_xSi NPs will not squeeze each other during cycling. Accordingly, with the introduction of coated Li_xSi (Figure V- 39d), graphite anodes exhibit consistent higher capacity and good cycling at C/20 for the first three cycles and C/5 for the following cycles (1C = 372 mA/g. The capacity is based on both graphite and Si in Li_xSi).

Improved air stability of artificial-SEI coated Li_xSi nanoparticles

To evaluate the dry air stability, coated Li_xSi NPs were stored in a dry room (dew point = -50 °C) for different days. After in dry air for 5 days, the coated Li_xSi NPs still exhibit a high capacity of 1921 mAh/g, which is only an 8% decay from the initial capacity (Figure V- 42a). In addition, the capacity decay in dry air is much slower for coated NPs than pristine NPs, confirming that the artificial-SEI coating slows down the NPs' side reaction rate in dry air. To further explore the stability in humid air, coated Li_xSi NPs were stored in air with different humidity levels for 6 h. After exposure to humid air with 10% RH, the coated Li_xSi NPs still exhibit a high extraction capacity of 1604 mAh/g (Figure V- 42b). For humidity levels higher than 20% RH, the Li extraction capacity shows a large drop after the 6 h storage period. However, this humidity level is higher than battery electrode fabrication conditions in industry. XRD (Figure V- 42c) demonstrates different reactivity of

coated and uncoated Li_xSi in moisture. Peaks corresponding to LiOH and Li_2O are observed in XRD of uncoated Li_xSi stored in 10% RH air for only 2 h. There is no obvious change in the XRD pattern for coated Li_xSi NPs.

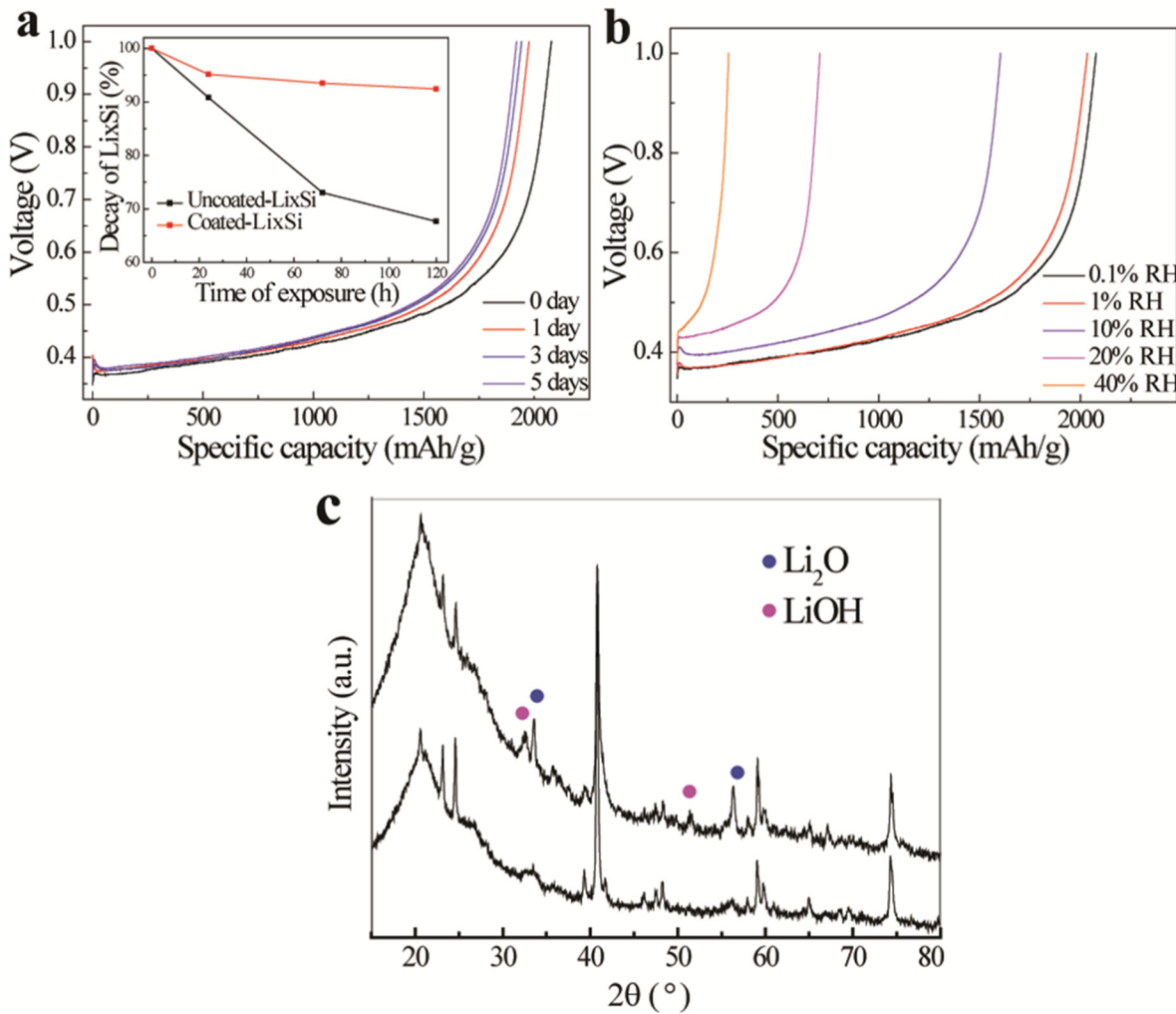


Figure V- 42: (a) The extraction capacity of artificial-SEI coated NPs exposed to dry air for varying periods of time. The inset shows the change of capacity as a function of exposure time. (b) The extraction capacity of artificial-SEI coated NPs exposed to air for 6 hrs at different humidity levels. (c) XRD patterns of uncoated (top) and coated (bottom) Li_xSi NPs in humid air for 2hrs with 10% RH

LiF provides an excellent passivation effect compared to other lithium salts, due to the limited solubility of LiF in water (0.134 g/100 mL at 25 °C). The solubility is about one order lower than that of Li_2CO_3 (1.29 g/100 ml), the coating layer used in SLMP. Some lithium salts such as Li_2O , in contrast, react violently with water. Accordingly, $\text{Li}_x\text{Si}-\text{Li}_2\text{O}$ NPs preserve its capacity only in air with very low moisture levels for a short period of time. LiF , along with Li alkyl carbonate with long hydrophobic carbon chains, slows down the reaction with O_2 and water vapor under ambient environment.

Conclusions and Future Directions

We have developed a two-step process for preparing artificial SEI-protected Li_xSi NPs. The uniform and continuous coating, consisting of LiF and Li decyl carbonate, slows down side reactions under ambient conditions. Therefore, artificial-SEI protected Li_xSi NPs show negligible capacity decay in dry air conditions even after 5 days and exhibits a high capacity of ~1600 mAh/g at 10% RH, indicating that coated Li_xSi NPs are potentially compatible with the industrial battery fabrication environment. It has been shown both alloying and intercalation anode materials can be effectively prelithiated with coated Li_xSi to counteract first cycle capacity loss, and this approach is applicable to other advanced electrode systems involving components of

nanomaterials. Thus, incorporation of coated Li_xSi NPs is a promising approach that may enable the commercial implementation of high-capacity nanostructured materials with large irreversible capacity loss in the first cycle, which is a significant step towards high-energy-density Li-ion batteries.

Due to the cycling performance, lithiated silicon NPs were mixed with intercalation or alloy anode materials during the slurry process and served as prelithiation additives. In the future, we will develop different nanostructures for lithiated silicon to improve the cycling performance. Therefore, lithiated silicon can afford remarkable battery performance as the anode material, and potentially replace Li metal anode in the novel $\text{Li}-\text{O}_2$ and Li-S batteries.

FY 2015 Publications/Presentations

1. J. Zhao *et al.*, Dry-air-stable lithium silicide–lithium oxide core–shell nanoparticles as high-capacity prelithiation reagents. *Nat. Commun.* 5 (2014).
2. J. Zhao *et al.*, Artificial Solid Electrolyte Interphase-Protected Li_xSi Nanoparticles: An Efficient and Stable Prelithiation Reagent for Lithium-Ion Batteries. *J. Am. Chem. Soc.*, 137 (2015).
3. High capacity prelithiation reagents and lithium-rich anode materials. Patent number: 102354-0285 (S14-109).
4. Presentation: Poster at 2015 MRS Spring Meeting & Exhibit.

V.C.3 Atomic Layer Deposition for Stabilization of Silicon Anodes (NREL)

Objectives

- Develop a low-cost, thick and high-capacity silicon (Si) anode with sustainable cycling performance by advanced surface modification
- Synthesize novel stable and elastic coatings for Si anodes using Atomic Layer Deposition (ALD) & Molecular Layer Deposition (MLD)
- Demonstrate durable cycling performance of thick Si anodes by using new ALD/MLD coatings and electrode designs
- Identify the mechanical properties and the impact of the MLD coating material on the electrochemical cycling performance.

Technical Targets

- Stabilize the high-capacity Si anodes by employing the advanced surface coating techniques, ALD and MLD
- Demonstrate the stable high-rate cycling performance of Si anodes
- Relevant to U.S. Advanced Battery Consortium (USABC) goals: 200Wh/kg (EV requirement); 96Wh/kg, 316W/kg, 3,000 cycles (PHEV 40 miles requirement). Calendar life: 15 years. Improve abuse tolerance.

Accomplishments

- Developed a new polymeric hybrid inorganic-organic coating, cross-linked aluminum dioxybenzene, that is covalently bonded to the surface of Si particles via molecular layer deposition
- Resolved the chemistry of the hybrid coating during crosslinking reactions
- Demonstrated a high-performance and high-rate-capable lithium-ion Si anode enabled by this robust, conductive surface coating
- Characterized the morphology and structure evolution of both uncoated and MLD coated Si anodes during cycling.
- What was the capacity and cycle life you achieved, that is important?
- By applying new hybrid coating on conventional Si electrodes, the coated electrode is enabled to provide sustainable cycling with capacities of nearly 1500 mAh g^{-1} after 100 cycles and Coulombic efficiency (CE) in excess of 99%.

Introduction

Major barriers to wider adoption of plug-in electric vehicles include battery cost, performance, life, and safety. Utilization of Si in lithium ion anodes provides a path toward achieving the DOE targets for energy density of batteries for use in plug-in electric vehicles. However, progress towards a commercially viable Si anode has been impeded by Si's rapid capacity fade caused by the large volumetric expansion and complicate interfacial reactions. As part of the U.S. Department of Energy's advanced Battery Material Research (BMR) activity, we addressed the following barriers in this project:

Cost: Inexpensive processing techniques are employed to fabricate conventional thick electrodes

Project Details

Tien Duong (DOE Program Manager)

DOE Agreement Number 16645

Recipient: National Renewable Energy Laboratory

Chunmei Ban (NREL - PI)

15013 Denver West Parkway

Golden, CO, 80401

Phone: 303-384-6504

E-mail: Chunmei.ban@nrel.gov

Steve M. George and Sehee Lee

Department of Chemistry and

Department of Mechanical Engineering

University of Colorado Boulder

914 Broadway

Boulder, CO, 80309

Phone: 303-493-7471

E-mail: steve.george@colorado.edu and

sehee.lee@colorado.edu

Start Date: October 2010

Projected End Date: September 2015

High Capacity: Si is predominantly being explored as a high capacity anode material. There is also a collaborative emphasis to enable high capacity cathode materials

High Rate: Both ALD and MLD coatings are being developed such that high-rate capability is demonstrated for emerging materials

Safety: The ALD/MLD coatings are targeted to improve safety for a variety of electrode materials.

Life: The ALD/MLD coatings are targeted to improve life for a variety of Si anode.

The overall goal of this project is to stabilize the Si anodes with conformal ultrathin coatings. Both ALD and MLD have been developed to fabricate the nanoscale coatings. Unlike cathode materials with negligible volumetric changes, Si particles are enveloped with Si oxide, as well as suffer from the phase and volumetric changes during Li intercalation-deintercalation. Therefore, in addition to the requirement for chemical stability, a functional coating with the control of thickness and mechanical properties is required.

This project has demonstrated success in utilizing MLD to grow mechanically robust and flexible surface coatings to address the challenges associated with Si's dramatic volumetric changes from FY11 to FY14. In FY15, we have concluded this work to investigate the properties of the hybrid coating materials. Most importantly, we have applied the knowledge to develop the materials with desirable elastic properties and good conductivity in order to accommodate the volumetric expansion and protect the surface from the reactive electrolytes.

Approach

An aromatic organic diol, hydroquinone (HQ), was used recently for synthesis of the cross-linked aluminum dioxybenzene coating (AlHQ). The coating integrated aluminum oxides into cross-linked dioxybenzene matrix, resulting in products containing electronically conductive bonding environments. MLD method has been applied to synthesize the hybrid inorganic-organic coatings. Both aluminum glycerol (AlGL) and AlHQ films were grown directly on the nano-Si composite electrodes using a pancake reactor.

The nano-Si based composite electrodes were prepared by spreading nano-Si powder (50 nm, Alpha Aesar), acetylene black (AB), and PVDF (polyvinylidene fluoride, binder) mixed in N-methyl pyrrolidinone solvent (60:20:20 weight ratio) on a piece of copper (Cu) foil. The electrochemical measurements were all normalized based on the mass of nano-Si in each electrode (typically 0.5-0.8 mg/cm²).

The hybrid coating (denoted by AlHQ) was deposited conformally onto the nano-Si anodes using the sequential, self-limiting reaction of trimethyl aluminum (TMA) (Al(CH₃)₃) and hydroquinone (HQ) (C₆H₄(OH)₂) according to:



where asterisks indicate surface species and Si represents the underlying Si electrode. In this work, MLD coating has been applied on the laminated electrode to maintain the original electrode structure. The growth rate of this MLD reaction is measured to be 7.5 Å per AB cycle at a substrate temperature of 150°C.

Results

Mechanical properties have been improved in the cross-linked AlHQ coating. During the MLD reaction, the aluminum oxide was connected with dioxybenzene via a conjugated chain in the form of (Al-O-benzene-O-Al)_n.^[1] Further dehydrogenation occurs when annealing the as-deposited film under both inert and air atmosphere. Dehydrogenation induces a longitudinal crosslinking reaction of the aluminum-dioxybenzene chains. The three-dimensional cross-linked structure leads to improved mechanical properties.

The effect of the crosslinking reaction on the evolution of thickness and density in the MLD film has been evaluated and summarized in Figure V- 43. Results confirm the densification of the AlHQ coating associated with the longitudinal crosslinking of aluminum-dioxybenzene chains. In addition to improving the film's conductive properties, such crosslinking was expected to improve the mechanical properties of the AlHQ

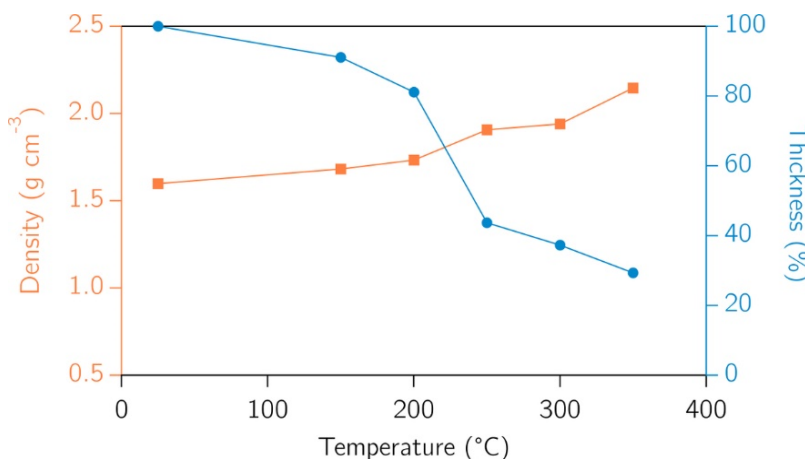


Figure V- 43: Density (orange profile) and percent thickness (blue profile) of the AlHQ films in relation to temperature. Results reveal the densification (thickness reduction) of the AlHQ films with increasing temperature treatments

coating. To study the mechanical effects of heat treatment, we focused our attention on 100-nm-thick AlHQ coatings on Si wafers. The heat treatments were all conducted in air, after the deposition process, for a span of 12 hours. Nanoindentation was used to study the ratio of hardness to Young's modulus (H/E^*), which allows determination of the film's wear resistance as a function of temperature. Results reveal the highest H/E^* for the AlHQ coating heat-treated at 150°C, suggesting a more elastic than plastic deformation under

Table V- 2: Nanoindentation results of AlHQ thin films treated at various temperatures in air revealing the highest H/E^* for the AlHQ coating heat-treated at 150°C

AlHQ Temperature Treatment [°C in air]	Elastic Modulus [E^* , GPa]	Hardness [H, GPa]	H/E^*
25	29.2	1.24	0.0425
150	34.9	1.82	0.0522
200	60.2	2.50	0.0415

contact, with negative returns at 200°C (Table V- 2). Materials with higher H/E^* are expected to have smaller accumulative strains and strain energies; therefore, they are expected to have better wear resistances, which are the indications of the durability of materials under severe mechanical loading. Additionally, the much lower Young's modulus than ALD ceramic coatings (34.9 GPa, compared to 170 GPa for ALD Al_2O_3) makes the coating much more flexible and able to accommodate the volume expansion and contraction of Si nanoparticles. The cross-linked AlHQ coatings show improved mechanical properties that ensure the structural integrity of the nanocomposite electrodes.

Furthermore, the crosslinking structure enabled by the polydentate Lewis acid creates strong covalent bonding to the surface of Si particles, but also provides chemical stability of the coating film.

Chemistry in the crosslinking process of the AlHQ coating has been characterized by using XAS spectra X-ray absorption spectroscopy (XAS). By monitoring the oxygen bonding environments as a function of temperature and atmosphere, we are able to determine the optimal annealing condition for the MLD layer. Figure V- 44 shows the O K-edge XAS spectra for the samples annealed under Ar atmosphere. We note that overall, the O K-edge XAS spectra resemble that of aluminum oxyhydrides (AlO(OH)), with slightly broader features than that of gibbsite ($\text{Al}(\text{OH})_3$), as depicted in Figure V- 44. This indicates that the as-prepared AlHQ-MLD film has a similar electronic structure to both Al-O- and Al-OH functionalities in AlO(OH) . Apart from the σ resonance around 540 eV (associated with the single oxygen bond in Al-O- and Al-O-C, as well as C-O-), there is a relatively well-defined shape resonance near 560 eV in the as-prepared MLD film; this shape resonance closely matches that found for the Al-O- bond in AlO(OH) .^[2] The AlHQ coating was synthesized from the reaction between TMA and HQ, as summarized in reactions A and B. However, the signature of the terminal -OH group from hydroquinone (at about 535 eV) is greatly suppressed in the AlHQ film.

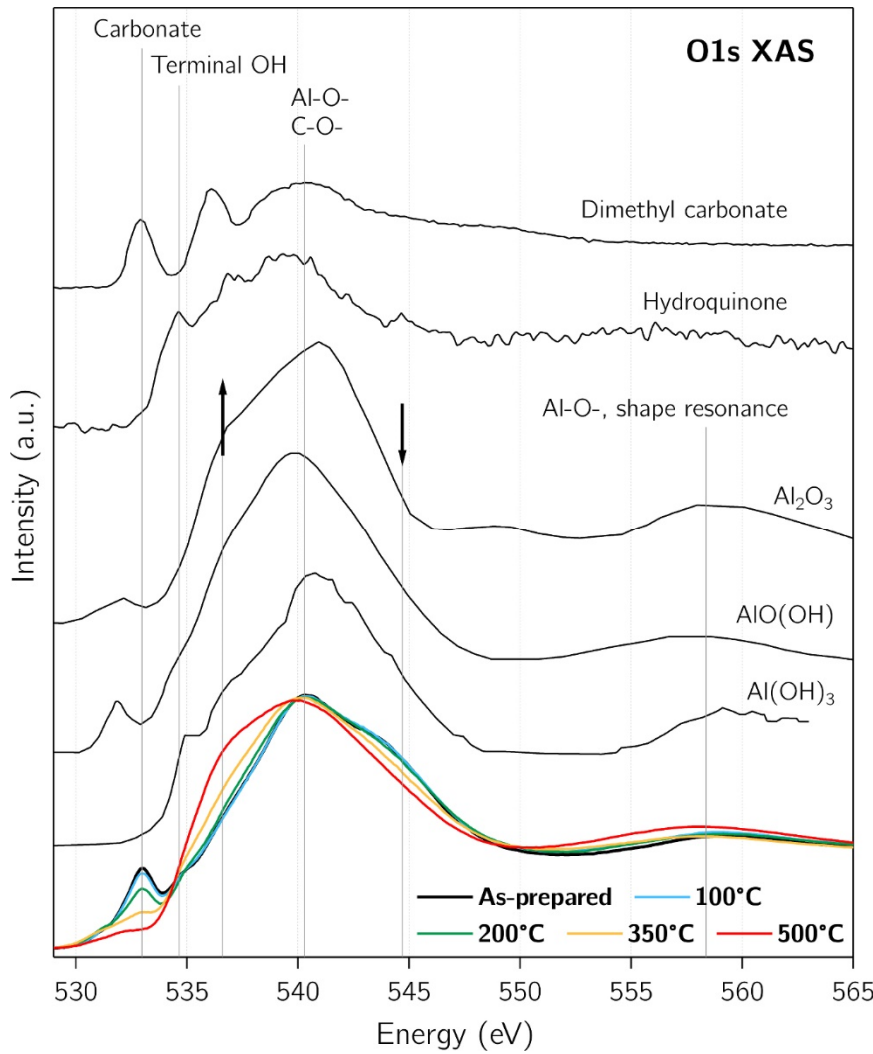


Figure V- 44: XAS spectra of O K-edge (TEY modes) in AlHQ thin films treated at 25, 100, 200, 350, and 500 °C under Ar environment

spans of the O K-edge XAS spectra (535–540 eV, upward arrow, and 542–548 eV, downward arrow in Figure V- 44) to track the transition of AlHQ to Al_2O_3 as a function of annealing temperature. When the annealing temperature is above 200°C, we clearly observed the changes of electronic structure toward Al_2O_3 for the samples heat-treated in both air and argon (Ar) environments. The conversion to Al_2O_3 following pyrolysis is obvious at 350°C. However, a slower transition was observed when using Ar in comparison to the air-annealed sample. The oxygen deficiency in an Ar environment limits oxygen functionalization, resulting in slower kinetics for the crosslinking reaction and the following pyrolysis. Based on these observations, we determined to use a higher temperature, 200°C, for Ar annealing to induce crosslinking reactions in AlHQ coating with no electronic structure changes toward Al_2O_3 . MLD AlHQ coating has improved the cycling performance of the conventional Si-C-PVDF based electrodes, as shown in Figure V- 45a. The Si anodes were prepared by using PVDF as a binder additive. Previous work has confirmed that PVDF fails to accommodate the volumetric changes in Si electrodes. Thus, PVDF has been selected in this work to distinguish the effect of coating on mechanical integrity and electrochemical performance of Si anodes.

The quenched peak confirms the self-limited and sequential reaction between the – OH in HQ and TMA, which is consistent with previous results.^[3] We also notice a low-energy peak around 533 eV that cannot be associated with the saturated bond of the AlHQ framework. Based on careful alignment with the core-excitation database of Hitchcock and co-workers, the resonance lines up with carbonate functionalities. Based on the established reaction pathway of carbonates on an oxygen-covered surface, we speculate that during the processing of the AlHQ film, residual CO_2 reacts with the surface oxide to form carbonates.^[4] As shown in Figure V- 44, the peak (around 533 eV) undergoes gradual decomposition as the annealing temperature rises, indicating that the carbonate species decompose at high temperatures.

In regard to the chemistry evolution of the AlHQ coating upon post-deposition heat treatments, we used two energy

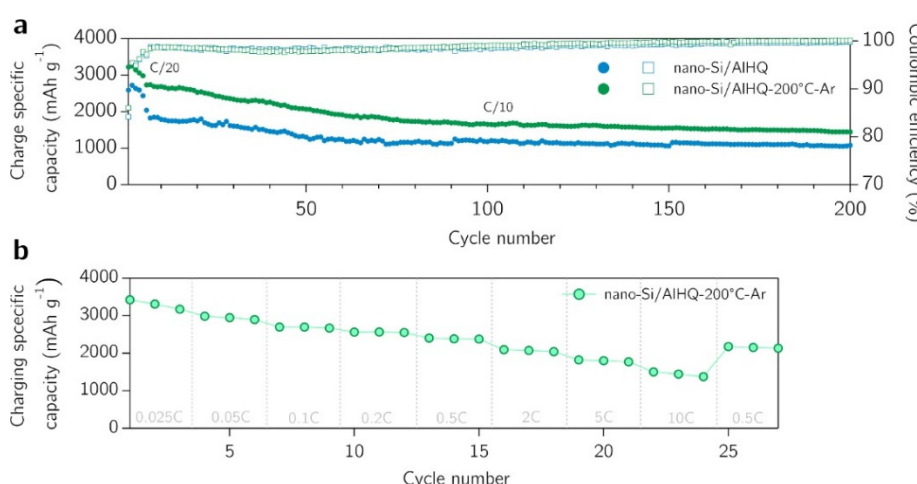


Figure V- 45: (a) Cyclic capacity and CE of a Si anode coated with as-deposit AlHQ (blue symbols) compared to the cyclic capacity and CE of a Si anode coated with Ar-treated AlHQ (green symbols). (b) A rate test demonstrates that the Ar-treated electrode can achieve an average specific charge capacity of 1798 mAh g^{-1} at a rate of 5C and specific charge capacities of about 1500 mAh g^{-1} at a rate of 10C . All the capacities were normalized based on total Si-active material in each electrode

anode corresponds to an electrode areal capacity of $0.581 \text{ mAh cm}^{-2}$ and a volumetric capacity of 1020 mAh cm^{-3} . The Si electrode coated with Ar-treated AlHQ coating, as compared to the non-heat-treated AlHQ coating, has exhibited the improvements. Both of these electrochemical performances significantly outperform the rapid degradation of an uncoated Si electrode, which fails by its 30th cycle. Moreover, the capacity retention of the AlHQ-coated electrode at 200 cycles nearly triples that of previous attempts to use MLD aluminum-glycerol coatings on Si electrodes.^[4]

Electrochemical rate test was performed to study the transport properties of the Ar-treated AlHQ coating, as shown in Figure V- 45b. At a rate of 5C (17.5 A g^{-1}), the AlHQ-coated electrode exhibited an average specific charge capacity of 1798 mAh g^{-1} —more than 750 mAh g^{-1} the capacity of our previous AlGL surface coating. Also, at a rate of 10C (35 A g^{-1}), the AlHQ-coated electrode is still able to deliver specific charge capacities of about 1500 mAh g^{-1} . Returning then to a rate of $\text{C}/2$ (1.75 A g^{-1}), the electrode recovered 91% of its specific charge capacity. This result attests to the maintenance of the electrode's structural integrity but also suggests that the cross-linked AlHQ coating provides very impressive ionic and electronic transport properties.

Conclusions and Future Directions

By applying this new hybrid coating on conventional Si electrodes, the coated electrode is enabled to provide sustainable cycling with capacities of nearly 1500 mAh g^{-1} after 100 cycles and Coulombic efficiency (CE) in excess of 99%. Diagnostic techniques including X-ray absorption spectroscopy, electrochemical impedance, and nanoindentation have been performed to reveal chemical and physical properties of the hybrid coating and its effect on the electrochemical performance of the Si anodes. The MLD-enabled chemistry overcomes many impediments in wet-chemistry fabrication for surface modification and also greatly extends the compositional possibilities of surface modifiers on lithium-ion battery electrodes.

The favorable combination of mechanical and electrochemical properties achieved with AlHQ conformal coatings on Si anode could present a major advancement in lithium-ion battery technology. Surface modification with many chemicals had previously been deemed unsuitable for materials with large volume changes due to the mechanical failure of the coatings under large stresses. However, here we have demonstrated the remarkable capability of the AlHQ electrode coating to not only maintain a reversible Si-based anode structure with stable and high capacities for hundreds of cycles, but to also allow electron and ion exchange at very high rates. At a rate of 10C (35 A g^{-1}), the AlHQ-coated electrode is still able to deliver specific charge capacities of about 1500 mAh g^{-1} . This back-end surface modification process is also compatible with a range of Si-based electrode configurations. While this work has been focused on enhancing

Both electrodes with the as-deposited AlHQ coating and the cross-linked AlHQ coating (treated under Ar) were run at a rate of $\text{C}/20$ (175 mA g^{-1}) for the first five cycles and then at a rate of $\text{C}/10$ (350 mA g^{-1}) for all subsequent cycles, as plotted in Figure V- 45a. At cycle 200, the AlHQ-coated electrode exhibits a specific charge capacity of nearly 1500 mAh g^{-1} and CE values in excess of 99%, whereas the as-deposited AlHQ-coated electrode achieves a stable capacity of about 1000 mAh g^{-1} . The specific charge capacity of 1500 mAh g^{-1} of the coated Si

the electrochemical performance of conventionally prepared Si anode structures with PVDF and conductive additives, the AlHQ surface chemistry is not limited to these structures. Preliminary work on AlHQ coated Si anodes utilizing a carboxymethyl cellulose binder and conductive additives shows great promise. This research may also be adaptable to a range of other high-capacity materials, representing an important advancement in high-energy LIBs applications. Future work, moving to the Applied Battery Research program, will look into an in-depth study of this particular aromatic framework to fully understand its electrochemomechanics, in addition to improving the early cycling coulombic efficiency through electrolyte modifications.

FY 2015 Publications/Presentations

1. D.M. Piper, Y. Lee, S.B. Son, T. Evans, F. Lin, D. Nordlund, X. Xiao, S.M. George, S.H. Lee, C. Ban, "Cross-Linked Aluminum Dioxybenzene Coating for Stabilization of Silicon Electrodes", submitted.
2. Y. Ma, J.M. Marinex de la Hoz, I. Angarita, J.M. Berrio-Sanchez, L. Benitez, J.M. Seminario, S.B. Son, S.H. Lee, S.M. George, C. Ban and P.B. Perla, "Structure and Reactivity of Alucone-Coated Films on Si and Li_xSi_y Surfaces", ACS Appl. Mater. Interfaces, 2015, 7 (22), pp 11948–11955.
3. L. Luo, H. Yang, P. Yan, J. J. Travis, Y. Lee, N. Liu, D.M. Piper, S.H. Lee, P. Zhao, S.M. George, J.G. Zhang, Y. Cui, S. Zhang, C. Ban and C. Wang, "Surface-Coating Regulated Lithiation Kinetics and Degradation in Silicon Nanowires for Lithium Ion", ACS Nano, 2015, 9 (5), pp 5559–5566.
4. D.M. Piper, S.B. Son, J. J. Travis, Y. Lee, S.M. George, S.H. Lee, C. Ban, "Mitigating irreversible capacity losses from carbon agents via surface modification", Journal of Power Sources, 2015 275, 605-611.
5. Y. He, D.M. Piper, M. Gu, J.J. Travis, S.M. George, S.H. Lee, A. Genc, L. Pullian, J. Liu, S.X. Mao, J.G. Zhang, C. Ban and C. Wang, "In Situ Transmission Electron Microscopy Probing of Native Oxide and Artificial Layers on Silicon Nanoparticles for Lithium Ion Batteries" ACS Nano, 2014, 8 (11), pp 11816–11823.
6. S.B. Son, B. Kappes, C. Ban, "Surface Modification of Silicon Anodes for Durable and High-Energy Lithium-Ion Batteries", Israel Journal of Chemistry, 2015, 55 (5), 558-569. (Review paper)
7. 249th ACS National Meeting, Denver, Colorado, 2015: Investigation of atomic/molecular layer deposition coatings for Li-ion electrode. (Invited)
8. International Battery Association and Pacific Power Source Symposium Joint Meeting 2015: Investigation of Molecular Layer Deposition Coatings for Silicon Anodes. (Invited)
9. 40th Annual symposium AVS, East Lansing, Michigan, 2014: Surface modification of silicon anodes for advanced Li-ion batteries. (Invited)

References

1. (a) B. Yoon, Y. Lee, D. Derk, C.B. Musgrave, S.M. George, ECS Trans. 33 (2011) 191-195; (b) Y. Lee and S.M. George, "Molecular Layer Deposition of Alucones and Zincones Using Hydroquinone", AVS 59TH International Symposium & Exhibition, Tampa, FL (Oct. 2012).
2. (a) Y.F. Hu, R.K. Xu, J.J. Dynes, R.I.R. Blyth, G. Yu, L.M. Kozak, P.M. Huang, Geochim. Cosmochim. Acta 72 (2008) 1959-1969; (b) R.K. Xu, Y.F. Hu, J.J. Dynes, A.Z. Zhao, R.I.R. Blyth, L.M. Kozak, P.M. Huang, Geochim. Cosmochim. Acta 74 (2010) 6422-6435.
3. J.T. Francis, A.P. Hitchcock, J. Phys. Chem. 96 (1992) 6598-6610.
4. D. Molina Piper, J.J. Travis, M. Young, S.-B. Son, S.C. Kim, K.H. Oh, S.M. George, C. Ban, S.-H. Lee, Adv. Mater. 26 (2014) 1596-1601.

V.D High Energy Density Cathodes for Advanced Lithium-ion Batteries

V.D.1 Studies on High Capacity Cathodes for Advanced Lithium-Ion (ORNL)

Objectives

In FY 2015 we have a twofold objective: (i) to complete our multiyear investigation on voltage fade & stability of lithium-manganese rich NMC (LMR-NMC) high V cathodes and (ii) develop practical high capacity multivalent cathodes belonging to $\text{Li}_2\text{M}^{\text{I}}_x\text{M}^{\text{II}}_{1-x}\text{O}_2$, where M^{I} and M^{II} are transition metals (TM) that do not include Mn or Co. In 2015 we have focused efforts towards stabilizing high capacity $\text{Li}_2\text{Cu}_{1-x}\text{Ni}_x\text{O}_2$ cathodes. The overall goal is to develop stable high voltage cathodes for EV and PHEV applications that meet and/or exceed the DOE energy density and life cycle targets from the US DRIVE/USABC roadmap (400 Wh/kg & 600 Wh/L)

Project Details

Tien Duong (Program Manager-BMR)

Jagjit Nanda (ORNL-PI)

1, Bethel Valley Road

Oak Ridge, TN 37934

Phone: 865-241-8361; Fax: 865-331-2199

E-mail: nandaj@ornl.gov

Collaborators

Rose Ruther & Frank Delnick (ORNL)

Start Date: October 2011

Projected End Date: Sept 2015

Technical Barriers

- Low gravimetric and volumetric capacity
- Intrinsically lower electronic and/or ionic conductivity leading to poor rate capability
- Structural and phase instability during continuous high voltage ($> 4.5\text{V}$) electrochemistry
- Transition metal dissolution leading to capacity fade and cell failure
- Interfacial stability and compatibility with high capacity anodes such as silicon and metal alloys.

Technical Targets

- Attain reversible capacity $> 250 \text{ mAh/g}$ at C/3 for $\text{Li}_2\text{M}^{\text{I}}_x\text{M}^{\text{II}}_{1-x}\text{O}_2$ cathodes where M^{I} and M^{II} are TMs such as Cu, Ni.
- Attain structural stability under > 1 Li-transfer per TM cation by isovalent or aliovalent substitution
- Suppress or prevent oxygen participation or evolution when charged to higher voltage ($> 4.2\text{V}$) by anionic substitution.

Accomplishments

Our key accomplishments for FY 2015 are in (i) understanding and addressing the voltage fade and capacity limiting mechanisms in high voltage LMR-NMC cathodes and (ii) developing alternative high capacity cathode materials with formula $\text{Li}_2\text{M}^{\text{I}}_x\text{M}^{\text{II}}_{1-x}\text{O}_2$, where M^{I} and M^{II} are transition metals (TM).

- EIS results show that the charge transfer resistance and double layer capacitance of LMR-NMC high-V cathodes are strongly voltage dependent with large hysteresis between charge and discharge. This provides evidence of compositional instability of this material during continuous high V cycling.
- The electrochemical behavior of Li_2MnO_3 thin film and slurry cathodes provides vital clues towards the mechanism of degradation and voltage fade in LMR-NMC cathodes. Delithiated Li_2MnO_3 clearly shows a new Raman signal at 665 cm^{-1} corresponding to MnO_2 , Li-birnessite, and/or LiMn_2O_4 spinel.
- Raman mapping reveals significant heterogeneity in the oxide structure in both thin film and slurry Li_2MnO_3 electrodes. In contrast, earlier work on LMR-NMC electrodes showed the structure was uniform across large areas of the electrode.

- A new 4 V Li-ion cathode material, $\text{Li}_2\text{Cu}_{0.5}\text{Ni}_{0.5}\text{O}_2$, shows initial capacities exceeding 200 mAh/g.
 - Electrochemical stability of high capacity $\text{Li}_2\text{Cu}_{1-x}\text{Ni}_x\text{O}_2$ cathodes can be improved by limiting Cu formation and avoiding gas generation.
-

Introduction

Development of high-energy-density, low-cost, thermally stable, and environmentally safe electrode materials is one of the key enablers for advanced batteries for transportation. High energy density is synonymous with reducing the cost per unit weight or volume. Currently, one of the major technical barriers towards development of high-energy-density lithium-ion batteries (LIBs) is the lack of availability of robust high-capacity cathodes. To give an example, the most commonly used anode material for LIBs is graphite, which has a specific capacity of 372 mAh/g, while even the most advanced cathodes like lithium nickel manganese cobalt oxide (NMC) have a maximum capacity of around 180 mAh/g. This calls for an immediate need for developing high capacity (and voltage) intercalation-type cathodes that have stable reversible capacity in the range of 250 mAh/g and beyond. Alternative high capacity cathode chemistries such as those based on conversion mechanism, Li-S, or metal air chemistries still have fundamental issues that need to be addressed before integration into cells for automotive use. A number of high voltage cathode chemistries have been developed under the BATT (now BMR) program including Li-rich NMC and Ni-Mn spinel. Our current R&D efforts are directed towards understanding the various mechanisms that limit capacity and improving stability (both bulk and interfacial) under high voltage cycling.

Approach

Synthesis and Surface Modification

We synthesize both new and established cathode materials using a variety of methods including solid-state, sol-gel, and solution-based routes. When appropriate, we use ORNL's expertise in thin film batteries to prepare the same materials as thin films. Thin film electrodes do not require polymer binders or conductive carbon additives, and can therefore facilitate our understanding of the intrinsic properties of the cathode material. We also have an active interest in developing coatings that can improve cathode properties such as conductivity or interfacial stability. Recently, we successfully demonstrated coating a nanometer-thick layer of the solid-ion conductor lithium phosphorous oxynitride (LiPON) on high voltage lithium-manganese rich NMC (LMR-NMC). In an ongoing study, we are collaborating with Argonne National Laboratory on ALD coatings to stabilize $\text{Li}_2\text{Cu}_{1-x}\text{Ni}_x\text{O}_2$ cathodes against oxygen evolution.

Diagnostics

We employ a variety of techniques to understand factors that limit cathode performance. One area of specialization is quantitative electrochemical impedance spectroscopy (EIS). For EIS studies, a three-electrode cell (either a pouch cell or commercial cell from EL-Cell) is typically used to separate contributions from the anode and cathode. Temperature-dependent EIS is used to identify different processes that contribute to the overall impedance and measure their activation energy. We also specialize in techniques that offer both high spatial resolution and large field of view. This is critical for understanding the failure mechanisms of cathode materials, since the electrodes can be highly heterogeneous. These methods include (i) micro-Raman spectroscopy and (ii) X-ray spectroscopy and imaging (TXM-XANES). We have integrated a spectroelectrochemical cell with our Raman microscope to study changes in the structure of cathode materials *in operando*. We have applied this technique to both LMR-NMC and $\text{Li}_2\text{Cu}_{1-x}\text{Ni}_x\text{O}_2$ cathodes. We compliment these efforts with electron microscopy, XPS, and ICP studies to monitor transition metal (TM) oxidation state, migration, and dissolution that limit cathode performance. By combining new syntheses with advanced diagnostics, this project aims to develop stable, high-capacity cathode compositions for advanced lithium-ion batteries.

Results

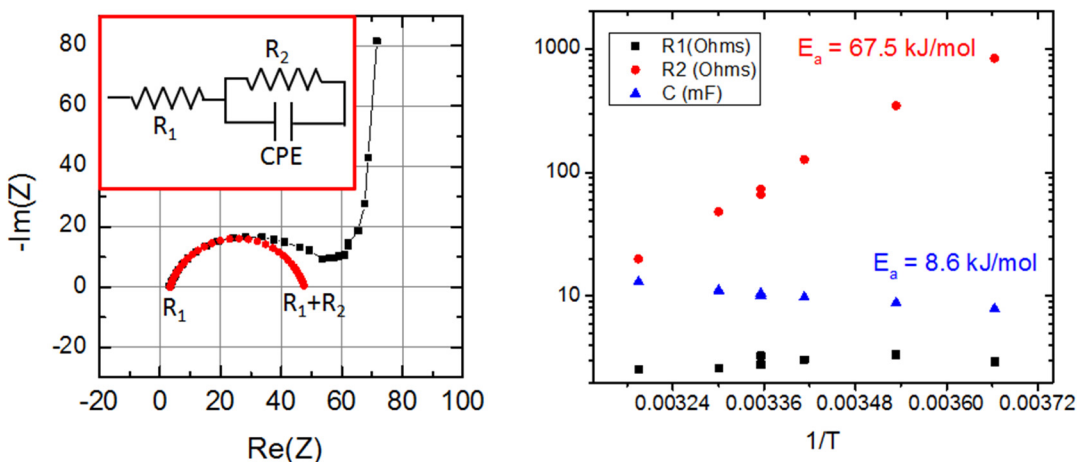


Figure V- 46: (Left) Analysis of EIS spectrum of LMR-NMC cathode at 4 V. (Right) Activation energies extracted from the temperature dependence of different contributions to the cathode impedance

Quantitative Electrochemical Impedance Spectroscopy of LMR-NMC

We undertook EIS studies on LMR-NMC/graphite full cells as a function of state-of-charge (voltage) and temperature. The goal is to extract the charge transfer resistance and bulk lithium-ion diffusivity as a function of lithium concentration. EIS measurements were carried out using a three-electrode cell with a lithium metal reference. HE-5050 cathodes and A12 graphite anodes were obtained from Argonne National Laboratory, and cells were conditioned following the standard ABR protocol. EIS response of the LMR-NMC cathode was studied as a function of voltage and temperature. The EIS response at 4 V (Figure V- 46) can be fit using an equivalent circuit model consisting of an ohmic part (R_1) and a charge transfer resistance (R_2). The charge transfer resistance is in parallel with the double-layer and/or space charge capacitance. The vertical tail at low frequency corresponds to finite diffusion of Li^+ . Unfortunately, due to the slow diffusion of Li in this material, the finite diffusion behavior can only be measured at very low frequencies (<1 mHz). Therefore, for our analysis we focused on the high frequency region. Figure V- 46 right panel shows the charge transfer resistances and double-layer capacitance as a function of temperature. The charge transfer resistance has an activation energy of 67.5 kJ/mol, which agrees well with the energy barrier needed to break-up the solvation sheath of molecules closely coordinated to Li^+ in carbonate electrolytes (Kang Xu, JECS, 2007).

Figure V- 47 shows the variation of the charge transfer resistance and double layer capacitance as a function of voltage. The capacitance and resistance show strong voltage dependence with large hysteresis between charge and discharge, even after considerable rest period (2 h at OCV prior to EIS measurement). The impedance spectra continue to change over a period of several days while resting at OCV, further complicating quantitative analysis. We attribute the evolution of the impedance spectrum to slow phase changes.

Role of Li_2MnO_3 in Capacity and Voltage Fade of LMR-NMC Cathodes

Li_2MnO_3 is a component of the high-capacity Li-rich-manganese-rich oxide materials; however, the mechanism of its electrochemical activity remains controversial. We used Raman spectroscopy and mapping to follow the chemical and structural changes that occur in Li_2MnO_3 during electrochemical cycling and link the findings towards understanding the phase changes and voltage fade in LMR-NMC cathodes. Conventional composite electrodes cast from a slurry and thin film electrodes were studied as a function of the state of charge (voltage) and cycle number. Thin films have similar electrochemical properties as electrodes prepared from slurries, but enable spectroscopy of uniform samples without carbon additives that can obscure the Raman signal of the active material.

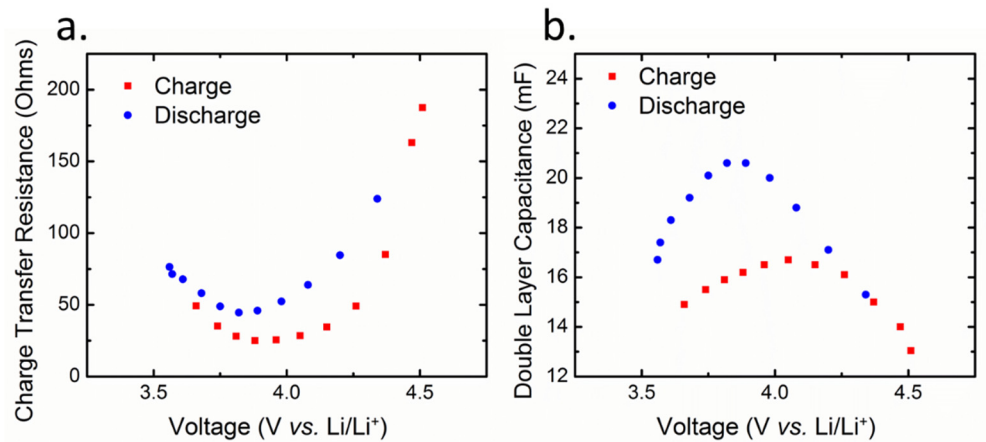


Figure V-47: (a) Charge transfer resistance and (b) double layer capacitance as a function of voltage for LMR-NMC cathodes at RT

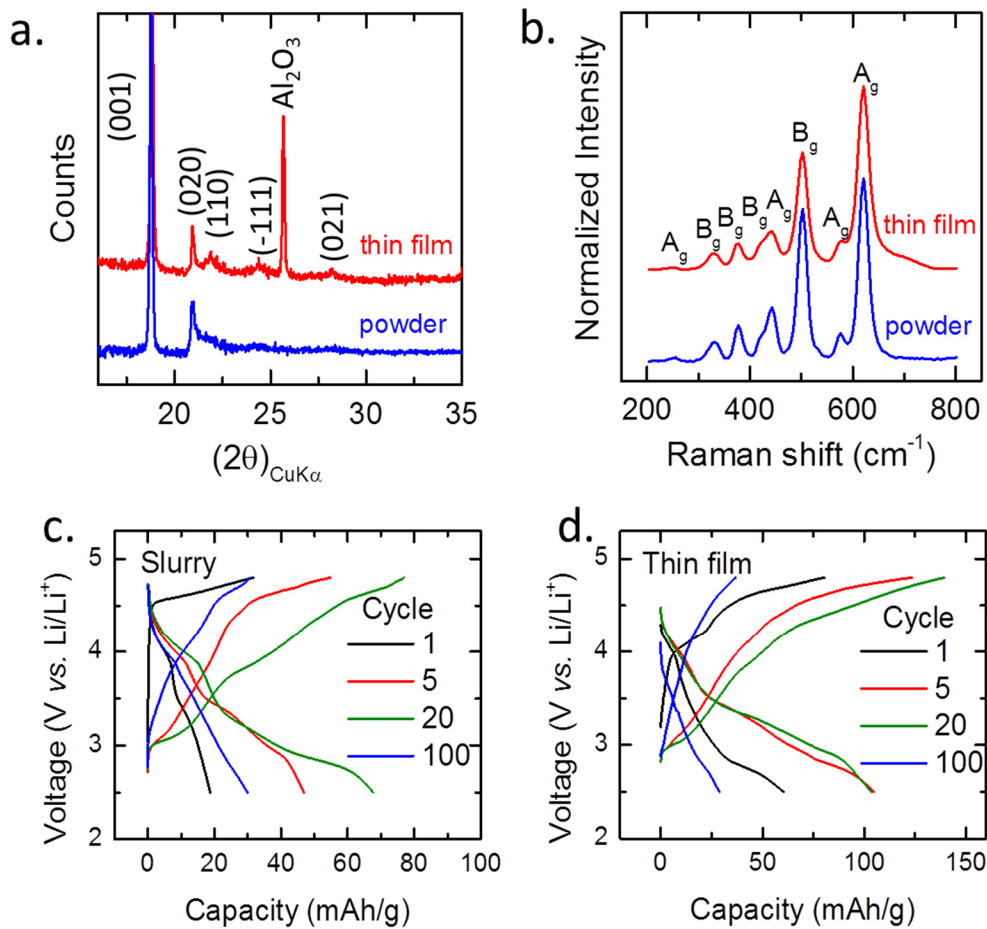


Figure V-48: (a) X-ray diffraction patterns of Li_2MnO_3 thin films and powder. (b) Raman spectra of Li_2MnO_3 thin films and powder. (c) Voltage profiles of Li_2MnO_3 electrodes cast from a slurry. (d) Voltage profiles of Li_2MnO_3 thin film electrodes

Figure V- 48a shows the X-ray diffraction patterns of the Li_2MnO_3 thin film electrodes and the powder used to prepare the slurry for standard tape cast electrodes. The superstructure reflections between 20° and 30° 2θ provide evidence for ordering of the Li and Mn in the transition metal layer. Figure V- 48b shows the Raman spectra for the same samples as in Figure V- 48a. For the first time, the symmetries of the modes were assigned using DFT calculations.

Figure V- 49a shows Raman spectra measured for thin film samples during the first charge and after 10 cycles. No significant changes occur during the first charge, except at the highest charging voltage of 4.8 V when a small shoulder appears near 665 cm^{-1} . This change appears reversible, and a spectrum identical to the pristine material is recovered upon discharge to 2.5 V. Similar behavior was found for the slurry electrodes during the first charge (not shown). The relatively minor changes in the spectrum during the first cycle are consistent with the relatively low initial charge and discharge capacity (Figure V- 48d). After 10 charge/discharge cycles, the shoulder at 665 cm^{-1} is much more pronounced. Figure V- 49b shows pictures of the thin films analyzed in Figure V- 49a. Li_2MnO_3 changes from red to black when charged to 4.8 V.

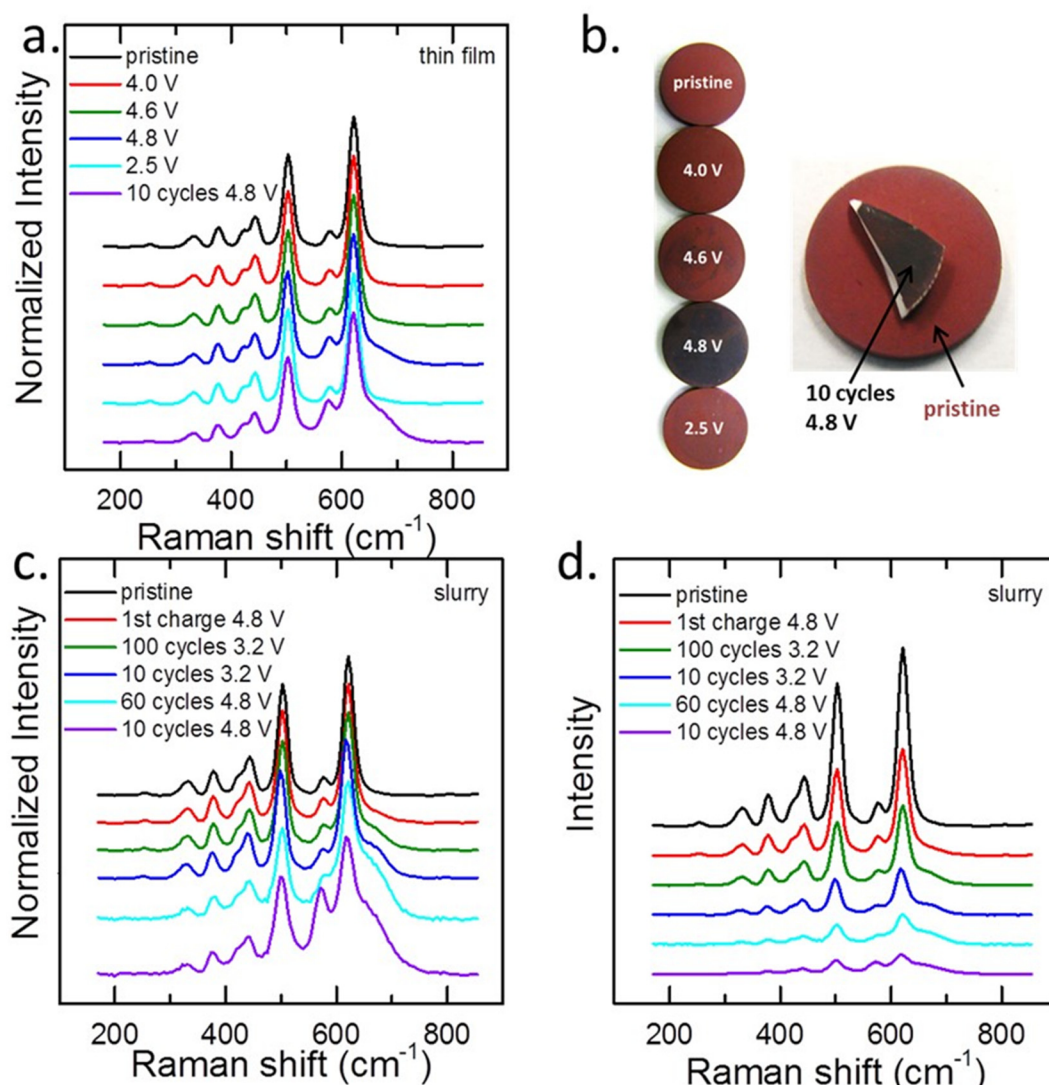


Figure V- 49: Raman spectra of electrodes as a function of the state of charge and history of electrochemical cycling. (a) Normalized spectra of thin films. (b) Photographs of thin films analyzed in panel a. (c) Normalized spectra of slurry electrodes. (d) Same spectra as shown in panel c except the raw (not normalized) intensities are plotted

Figure V- 49c shows Raman spectra for electrodes cast from a slurry. The spectra have been normalized to emphasize changes in the relative intensities of the different vibrational modes. Similar to the thin films, a

shoulder at 665 cm^{-1} emerges with electrochemical cycling and the mode at 574 cm^{-1} becomes more intense. These changes are most pronounced in electrodes charged to 4.8 V after some activation cycles. After discharging to 3.2 V, the shoulder at 665 cm^{-1} is still present, but significantly reduced in intensity. Figure V-49d plots the same data as 4c, but with the raw (not normalized) intensities. The increase in relative intensity of the shoulder at 665 cm^{-1} clearly correlates with a decrease in the absolute intensity. An increase in electronic conductivity, σ , will reduce the optical skin depth and decrease the intensity of the Raman scattering. Therefore, the reduction in the absolute spectral intensity is consistent with the formation of a more electronically conductive phase during charging.

Notably, the frequencies of the Raman active modes shown in Figure V-49 do not show any significant shifts as a function of state of charge (voltage). Rather, at the top of the charge (4.8 V) a new mode appears near 665 cm^{-1} accompanied by changes in the relative intensities of the other modes. This behavior is very characteristic of a two-phase reaction. If delithiation occurs by a single phase pathway, both the frequency and intensity of the bands should change depending on lithium content. The nucleation of new phases is not surprising in light of previous work, which has established that lithium deintercalation does not proceed via a conventional topotactic transition. Analysis of Raman maps provides additional insights into the reaction pathway.

Figure V-50 compares Raman maps of slurry and thin film electrodes. The electrodes were cycled 10 times and charged to 4.8 V prior to analysis. To isolate the spectra of other phases that may be forming, a principal components analysis (PCA) was performed using Witec ProjectPlus software. Figure V-50a shows the first two principal components of spectra from a slurry and thin film sample. Only the first two components are

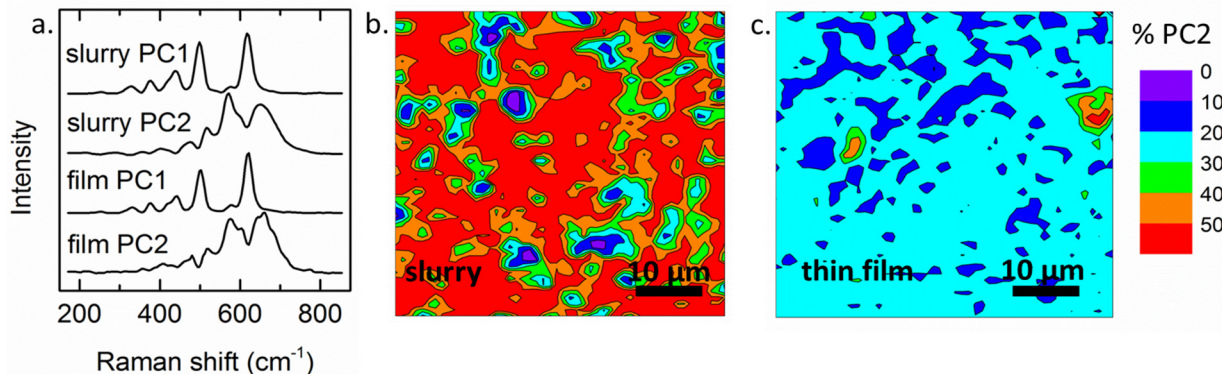


Figure V-50: (a) First and second principal components extracted from Raman maps of slurry and thin film electrodes cycled 10 times and charged to 4.8 V. (b) Raman map of the percent of the second component needed to reproduce the experimental spectra for the slurry sample. (c) Raman map of the percent of the second component needed to reproduce the experimental spectra for the thin film sample

used, since they account for 97% of the variance in the slurry spectra. The first eigenvector is an excellent match for the pristine material, while the second reflects the changes that occur during electrode activation and charging to 4.8 V. The first two principal components of both slurry electrodes and thin films are very similar. Notably, there is a significant increase in intensity at 650 , 570 , and 510 cm^{-1} . Several manganese dioxides have spectra similar to the second component including birnessite ($\delta\text{-MnO}_2$), nsutite ($\gamma\text{-MnO}_2$), and romanechite. The formation of a MnO_2 -like phase is consistent with the loss of both lithium and oxygen from the surface of Li_2MnO_3 as previously proposed.

Figure V-50b and Figure V-50c show Raman maps generated from the PCA analysis. The maps show the percent of the second eigenvector needed to reproduce the experimental spectrum at each point. The slurry electrode is highly heterogeneous: some regions correspond closely to the pristine material and others are rich in the MnO_2 -like phase. The thin film electrode is more uniform, but still shows significant variation in the relative contributions of the two principal components. Interestingly, our own Raman mapping analysis of LMR-NMC cathodes did not reveal any significant heterogeneity in the oxide structure after electrochemical cycling. This is further evidence that the pure phase Li_2MnO_3 shows significantly different structural and electrochemical behavior from the composite lithium-rich cathodes. The physical behavior of each phase is modified by creating an intimate mixture on the nanoscale.

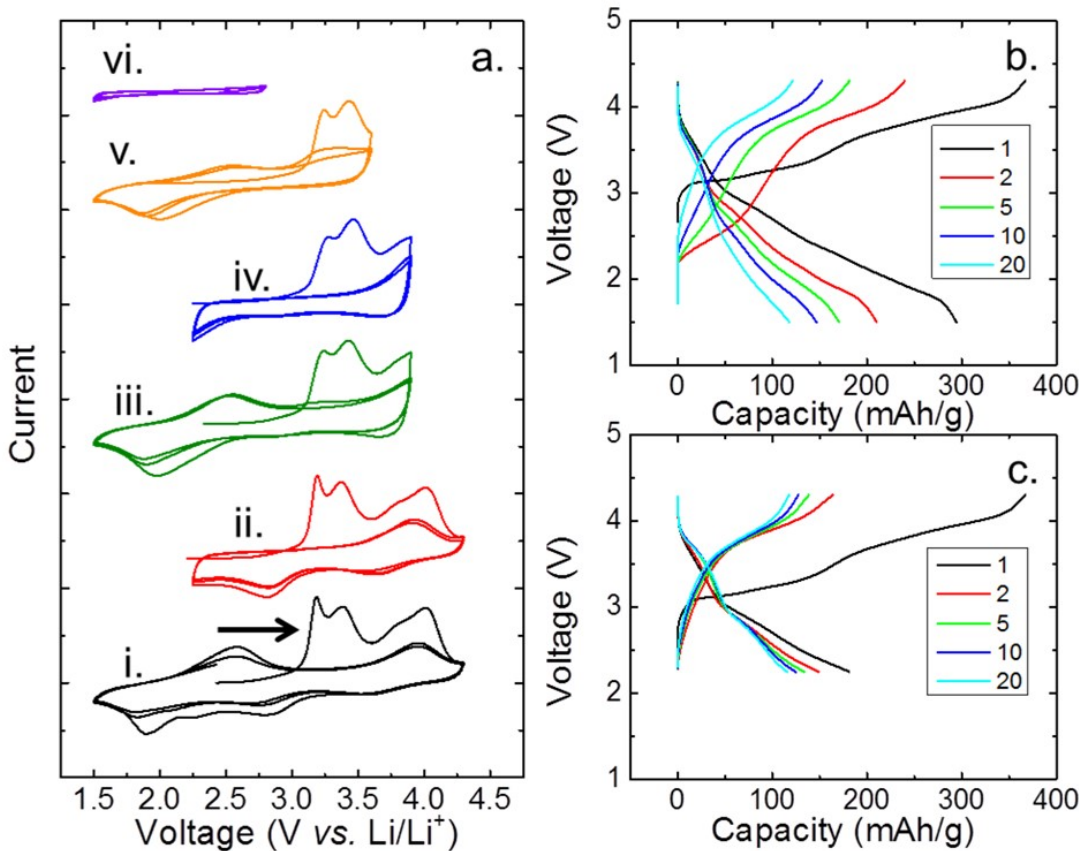


Figure V- 51: (a) Cyclic voltammograms of $\text{Li}_2\text{Cu}_{0.5}\text{Ni}_{0.5}\text{O}_2$ (first three cycles) acquired with a scan rate of 0.1 mV/s over different voltage windows: (i) 4.3 – 1.5 V (ii) 4.3 – 2.25 V (iii) 3.9 – 1.5 V (iv.) 3.9 – 2.25 V (v.) 3.6 – 1.5 V (vi.) 2.8 – 1.5 V. (b) Voltage profiles for cells cycled galvanostatically (50 mA per gram of active material) between 4.3 - 1.5 V. (c) Voltage profiles for cells cycled galvanostatically (50 mA per gram of active material) between 4.3 - 2.25 V. Cycles 1, 2, 5, 10, and 20 are shown

High Capacity $\text{Li}_2\text{Cu}_{0.5}\text{Ni}_{0.5}\text{O}_2$ Cathodes: Investigating the Role of Nickel Substitution

Orthorhombic Li_2NiO_2 , Li_2CuO_2 , and solid solutions thereof have been studied as potential cathode materials for lithium-ion batteries due to their high theoretical capacity and relatively low cost. While neither endmember shows good cycling stability, the intermediate composition, $\text{Li}_2\text{Cu}_{0.5}\text{Ni}_{0.5}\text{O}_2$, yields reasonably high reversible capacities. We synthesized $\text{Li}_2\text{Cu}_{0.5}\text{Ni}_{0.5}\text{O}_2$ by co-precipitation of the transition metal nitrate salts followed by solid state reaction with lithium hydroxide. The crystal structure was rigorously characterized by X-ray and neutron powder diffraction. The electrochemical properties of $\text{Li}_2\text{Cu}_{0.5}\text{Ni}_{0.5}\text{O}_2$ were evaluated by cyclic voltammetry and galvanostatic cycling of coin cells using lithium counter electrodes (half-cells). As shown in Figure V- 51, cyclic voltammetry reveals the redox chemistry occurring when $\text{Li}_2\text{Cu}_{0.5}\text{Ni}_{0.5}\text{O}_2$ was cycled over different voltage windows. The widest voltage window was 4.3-1.5 V (Figure V- 51, trace i). The large differences between the first and subsequent cycles indicate that the structural changes during the first cycle are largely irreversible. Shrinking the voltage window does not improve the reversibility, but it does provide additional insights into the redox reactions. Raising the lower voltage cut-off from 1.5 to 2.25 V (Figure V- 51, trace ii) eliminated the redox couple at 2.6 V (oxidation) and 1.8 V (reduction). The low voltage of this reaction suggests that it is related to the $\text{Cu}^+/\text{Cu}^{2+}$ transition. If the upper voltage cut-off is limited to 3.6 or 3.9 V (Figure V- 51a, traces iii, iv, and v), only the low voltage $\text{Cu}^+/\text{Cu}^{2+}$ redox couple contributes significantly to the reversible capacity. No significant redox reactions occur when the electrochemical cycling is limited to 2.8 – 1.5 V (Figure V- 51, trace vi), suggesting that $\text{Cu}^+/\text{Cu}^{2+}$ transition in $\text{Li}_2\text{Cu}_{0.5}\text{Ni}_{0.5}\text{O}_2$ can only be activated when the electrode is cycled to voltages higher than 3.0 V.

Since only the higher voltage redox reactions are of interest for cathodes, galvanostatic cycling was performed with the higher voltage cut-off of 4.3 V. Figure V- 51b and Figure V- 51c show voltage profiles for cells charged and discharged at 50 mA/g (C/5 rate assuming a nominal capacity of 250 mAh/g). Cells cycled

between 1.5 and 4.3 V have the highest initial capacity (300 mAh/g), but also show the most rapid fade (Figure V- 51b). Raising the lower voltage cut-off to 2.25 V improves the stability (Figure V- 51c), but a large hysteresis (~ 1 V) still exists between charge and discharge during the first and subsequent cycles.

To identify which redox processes contribute to the reversible capacity and which result in irreversible loss, we acquired XAS data at the Cu K- and Ni K-edges *in situ* during charge and discharge over the largest voltage window (1.5-4.3 V) (Figure V- 52). *In situ* XANES provided clear evidence for a reversible $\text{Ni}^{2+}/\text{Ni}^{3+}$ redox couple between 2.0 and 4.0 V. However, the pre-edge feature at 8337 eV present in Ni K-edge spectrum of the pristine sample did not return. This shows permanent structural changes occurred during the charging process, consistent with the cyclic voltammetry. Unlike the Ni K-edge, the Cu K-edge did not show any systematic shift during the first charge up to 4.3 V. The strong pre-edge peak at 8983 eV, however, also disappeared during charging, suggesting a change in symmetry or coordination in the Cu environment. No obvious change was observed in the copper oxidation state during discharge to 1.7 V. Further discharge to 1.5 V resulted in the reappearance of a pre-edge feature that can be assigned to Cu^+ .

The cyclic voltammetry and *in situ* XANES provide clear evidence for an irreversible structural transformation during the first charge. To follow the structural changes that occur in the first cycle in more detail, Raman spectra were acquired *in situ* (not shown). After delithiation, the Raman spectrum of $\text{Li}_2\text{Cu}_{0.5}\text{Ni}_{0.5}\text{O}_2$ changed dramatically from the spectrum of the pristine orthorhombic structure. Instead, the Raman spectrum closely resembled that of other close-packed layered oxides such as LiNiO_2 and $\text{LiNi}_{1-y}\text{Co}_y\text{O}_2$.

From the *in situ* XANES, it is clear that during the first charge of $\text{Li}_2\text{Cu}_{0.5}\text{Ni}_{0.5}\text{O}_2$, significant capacity is extracted at the top of the charge without noticeable changes in the oxidation states of copper or nickel. This strongly suggests that oxygen participates in the redox chemistry, consistent with previous experimental and theoretical work on Li_2CuO_2 and related copper oxides. Since both Li_2CuO_2 and Li_2NiO_2 parent compositions evolve oxygen at high voltage, we undertook quantitative measurements of gas generation in $\text{Li}_2\text{Cu}_{0.5}\text{Ni}_{0.5}\text{O}_2$ pouch cells. Charging the cell from the OCP to 3.9 V did not yield any measurable amount of gas. However, significant amounts of gas were generated when the cell was charged above 3.9 V. In fact, virtually all of the capacity extracted from $\text{Li}_2\text{Cu}_{0.5}\text{Ni}_{0.5}\text{O}_2$ above 3.9 V could be attributed to oxygen evolution. Efforts are underway to limit the participation of oxygen in the redox process and stabilize Cu^{3+} through anionic substitution.

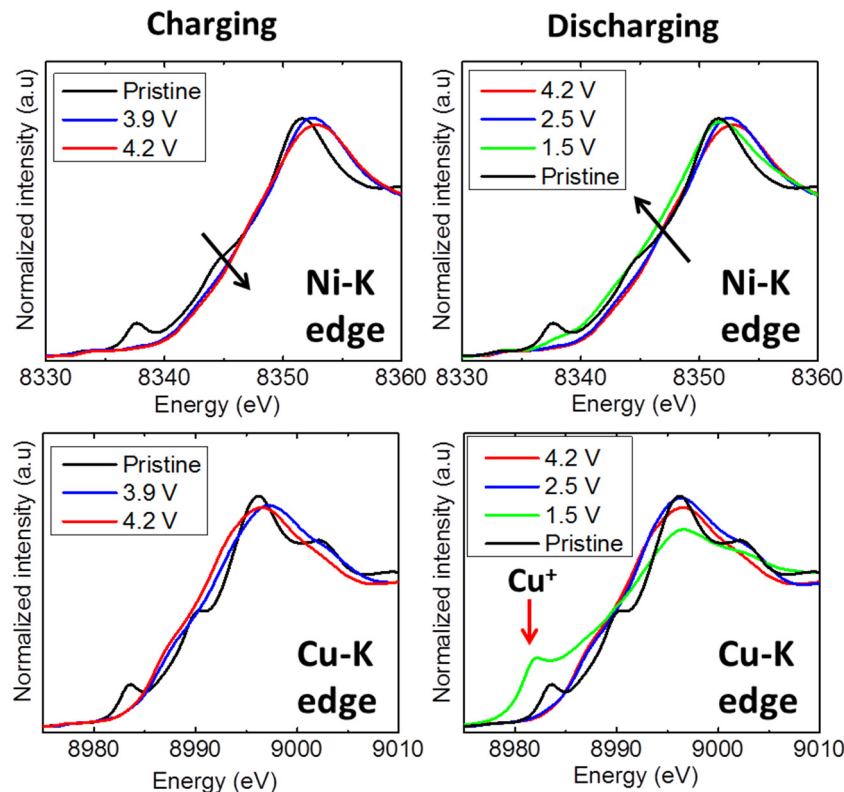


Figure V- 52: XANES data collected at the Cu and Ni K-edges at different states of charge

Conclusions and Future Directions

Using a suite of analytical tools, including various spectroscopies and interface-sensitive techniques, we clarified the fundamental origin of phase instability and voltage fade in high voltage LMR-NMC cathodes. Temperature and SOC dependent EIS results showed that the charge transfer resistance and double layer capacitance of the LMR-NMC high-V cathodes are strongly voltage dependent with large hysteresis between charge and discharge. The capacity degradation in Li_2MnO_3 thin film and slurry cathodes provides vital clues towards the degradation and voltage fade in LMR-NMC cathodes. Upon delithiation, Raman spectra clearly show a new feature at 665 cm^{-1} corresponding to MnO_2 , Li-birnessite, and/or $\text{Li}_{0.52}\text{MnO}_{2.1}$ spinel. Raman mapping reveals significant heterogeneity in the oxide structure in both thin film and slurry Li_2MnO_3 electrodes. In contrast, earlier work on LMR-NMC electrodes showed the structure was highly uniform across large areas of the electrode. Further, we synthesized a new, high-capacity, 4 V Li-ion cathode material, $\text{Li}_2\text{Cu}_{0.5}\text{Ni}_{0.5}\text{O}_2$, with initial capacities exceeding 200 mAh/g. Our results showed that the electrochemical stability could be improved by limiting the voltage window of charge-discharge to prevent Cu^+ formation and gas generation (oxygen evolution). In coming years, we will stabilize the multivalent oxidation states and phase structures of Ni and Cu based cathodes using a number of approaches such as (i) **Isovalent or aliovalent cation substitution:** This stabilizes the lattice by charge compensation as the Li^+ cations are removed. Often the lattice is stabilized against phase transformation when the second cation bonds strongly to neighboring oxides. Zn, Mg, Ga, and Al will be used for this purpose and (ii) **Anion Induction:** For this approach we will substitute polyanionic groups in place of the oxide anions. The 3d orbitals of the TMs have different energies and stability depending on the crystal field and inductive effects of various polyanionic groups. We will first begin with the simplest case of anionic substitution, where we will substitute oxygen with fluorine in $\text{LiCu}_{0.5}\text{Ni}_{0.2}\text{O}_2$.

FY 2015 Publications/Presentations

1. Facet dependent disorder in pristine high-voltage lithium-manganese rich cathode material, H. Dixit, W. Zhou, J-C Idrobo, J. Nanda, V. R. Cooper, ACS Nano, 8 (12), pp 12710, (2014).
2. New Frontiers in Energy Storage: Materials and Systems, J. Nanda, Dow-Chemicals R&D Center, Midland, Michigan, October 2014 (Invited).
3. Raman Microscopy of Lithium-Manganese-Rich Transition Metal Oxide Cathodes , R. E. Ruther, A. F. Callender, H. Zhou, S. K. Martha and J. Nanda, Journal of the Electrochemical Society, 162 (1) A1-A5 (2015).
4. High Voltage (Capacity) Cathodes for Advanced Lithium-Ion Batteries, J. Nanda and R. Ruther *et al.*, ACS Spring Meeting, March 22nd- 26th 2015 Denver (Invited).
5. Quantifying the Chemical and Morphological Heterogeneities in High Capacity Battery Materials Under Electrochemical Cycling, 2015 TMS Meeting, March 15-22nd, Orlando (Invited).
6. Studies on High Capacity Cathodes for Advanced Lithium-Ion Systems, J. Nanda and R. Ruther, Annual Merit Review, DOE Washington DC June 8-12th 2015.
7. New Frontiers in Electrochemical Energy Storage: Materials and Systems, J. Nanda, Indian Institute of Technology, Bhubaneswar (India), June 24th 2015 (Invited).
8. High-Capacity Electrode Materials for Electrochemical Energy Storage: Role of Nanoscale Effects, J. Nanda, S. K. Martha, and R. Kalyanaraman, Pramana- Journal of Physics, 54, 6, 1073 (2015).
9. Synthesis, Structure, and Electrochemical Performance of High Capacity $\text{Li}_2\text{Cu}_{0.5}\text{Ni}_{0.5}\text{O}_2$ Cathodes, R. Ruther, H. Zhou, C. Dhital, K. Saravanan, A. K. Kercher, G. Chen, A. Huq, Frank M. Delnick, and J. Nanda, Chem. Mater. 227, 6746-6754 (2015).
10. Multiscale Modeling and Characterization for Performance and Safety of Lithium-Ion Batteries, S. Pannala, J. A. Turner, S. Allu, W. R. Elwasif, S. Kalnaus, S. Simunovic, A. Kumar, J. J. Billings, H. Wang, and J. Nanda, J. Appl. Phys. 118, 072017 (2015).
11. Modeling the Evolution of Lithium-Ion Particle Contact Distributions Using a Fabric Tensor Approach, A.J. Stershic, S. Simunovic, J. Nanda, J. Power Sources, 297, 540 (2015).

V.D.2 High Energy Density Lithium Battery (Binghamton U)

Objectives

- We propose to develop the anode and cathode materials for high-energy density cells for use in plug-in hybrid electric vehicles (PHEVs) and in electric vehicles (EV) that offer substantially enhanced performance over current batteries used in PHEVs and with reduced cost. Specifically the primary objectives are to:
- Increase the volumetric capacity of the anode by a factor of 1.5 over today's carbons by using a SnFeC composite conversion reaction anode.
- Increase the capacity of the cathode by using a high capacity conversion reaction cathode, CuF₂, and/or using a high capacity 2 Li intercalation cathodes, VOPO₄.
- Enable cells with an energy density exceeding 1 kWh/liter

Project Details

Charles Alsup (NETL Program Manager)

DE-EE0006852 Recipient: RF Binghamton U.

Tien Duong (BMR Program Manager)

Stanley Whittingham (Binghamton U – PD/PI)

85 Murray Hill Road

Vestal, NY 13850

Phone: 607-777-4623

E-mail: stanwhit@binghamton.edu

Subcontractor: None

Start Date: October 2014

Projected End Date: September 2017

Technical Barriers

- In order for PHEVs and EVs to achieve mass adoption, their driving range must be improved and lifetime cost reduced.
Barriers addressed:
 - Higher volumetric energy density
 - Cyclability of conversion electrodes.
 - Lower costs.
 - Abuse-tolerant safer electrodes.

Technical Targets

- Anode Targets: 1.5 times the volumetric energy density of carbon and >500 cycles.
- Cathode Targets: 255 mAh/g and >500 cycles for an intercalation cathode; 400 mAh/g and > 100 cycles for a conversion cathode.
- Cell Targets: Approach 1 kWh/L at end of the project.

Accomplishments

- We have demonstrated more than 100 cycles of the Sn₂Fe/C anode composite at a volumetric capacity exceeding 1.5 times that of carbon.
- We have synthesized and characterized the conversion cathode in the pure state, in composites with carbon, MoO₃ and VOPO₄, and in solid solution with Fe, Cu_{1-y}Fe_yF₂.
- We have achieved more than 10 cycles of the conversion cathode in excess of 200 mAh/g.

Introduction

The project objectives are to develop the anode and cathode materials for high-energy density cells for use in plug-in hybrid electric vehicles (PHEVs) and in electric vehicles (EV) that offer substantially enhanced performance over current batteries used in PHEVs and with reduced cost. Specifically the goal of this project is to enable cells with an energy density exceeding 1 kWh/liter. The carbon anode in today's Lithium-ion cells will be replaced with a tin-based anode with double the volumetric capacity of carbon. Similarly the present intercalation cathodes will be replaced by materials, which are capable of reacting with up to two lithiums per

redox ion. Moreover, these cell reactions will occur within the stability limit of today's electrolytes, leading to longer-lived batteries.

Approach

Innovative Approach: The approach of this "beyond Li-ion" battery concept is (a) to remove the volume intensive intercalation-based carbon anode in todays Li-Ion batteries, and replace it with a conversion reaction based material, and (b) to replace the present cathodes that mostly react with less than one Li ion per transition metal ion with cathode materials that can react with more than one Li ion. This latter is similar to the concept of using the divalent magnesium with its two-electron transfer. However, we believe that moving two of the much more mobile singly charged lithium ions is more viable, and moreover today's electrolytes, SEI additives and cell technology can be used. Attainment of the goals proposed here will lead to a 50-100% increase in the volumetric and gravimetric energy storage capability of both the anode and the cathode, which will allow for the realistic attainment of the next generation batteries for PHEV vehicles. At the same time, the science generated will be applicable to other energy storage systems, such as anodes for Li/S. The anode and cathode components in this approach are:

1. A SnFeC composite for the anode which reacts by a conversion mechanism giving Li_xSn and Fe.
2. A CuF_2 containing material for the cathode which reacts with 2 Li ions by a conversion mechanism giving Cu and LiF .
3. A VOPO_4 containing cathode which reacts with upto 2 Li ions by an intercalation mechanism giving Li_2VOPO_4 .

Results

We have achieved the following progress:

Synthesis of CuF_2 Cathode Materials and Determination of their Discharge Products

Carbon/ CuF_2 and carbon $\text{Cu}_{1-y}\text{Fe}_y\text{F}_2$ composites were synthesized by a mechanochemical approach. They are single phase as shown by x-ray diffraction (Figure V- 53 below). An initial electrochemical discharge reaction shows a capacity between 400 and 500 mAh/g for both compositions. The redox potentials for both Cu and Fe are clearly visible.

The discharge products of $\text{Cu}_{1-y}\text{Fe}_y\text{F}_2$, $y= 0$ and 0.5 , were characterized by ex-situ XRD at different states of discharge. CuF_2 is converted to Cu and LiF as the only discharge products as observed in powder XRD pattern (Figure V- 54). No CuF_2 remains at the end of discharge. Similarly, in the case of $\text{Cu}_{0.5}\text{F}_{0.5}\text{F}_2$, we observe the formation of Cu and LiF . The peaks of Fe phase overlaps with the LiF phase, therefore may not be observed. The reaction however, is observed to continue below 2.4 V where all Cu^{2+} ought to have Cu^0 . The $\text{Cu}_{0.5}\text{F}_{0.5}\text{F}_2$ phase continues to decrease while the LiF phase increases. In addition there is no observable change in the relative intensity of the Cu peaks below this voltage. The reaction of $\text{Cu}_{0.5}\text{F}_{0.5}\text{F}_2$ is not complete even at 1.8 V as evident by the remnant phase of the rutile structure.

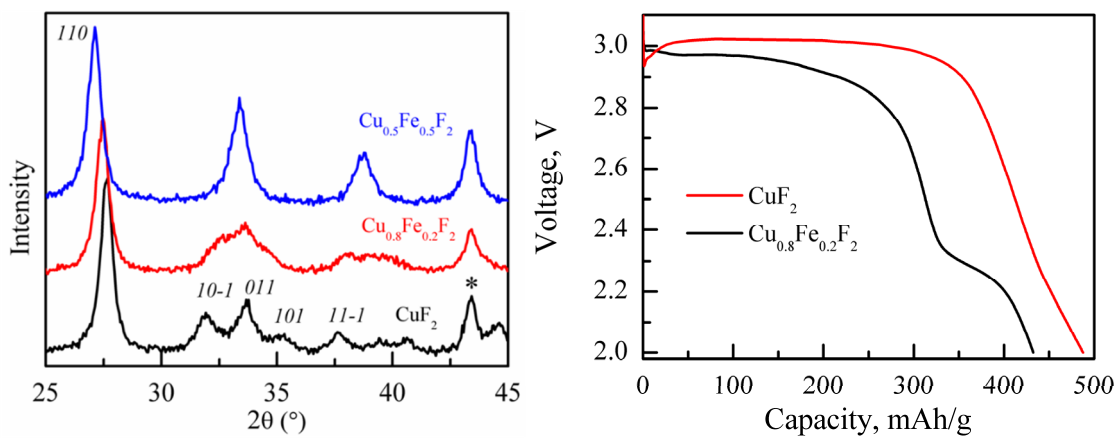


Figure V- 53: (left) x-ray diifraction patterns of $\text{Cu}_{1-y}\text{Fe}_y\text{F}_2$ materials and (right) discharge of CuF_2 and $\text{Cu}_{0.8}\text{Fe}_{0.2}\text{F}_2$

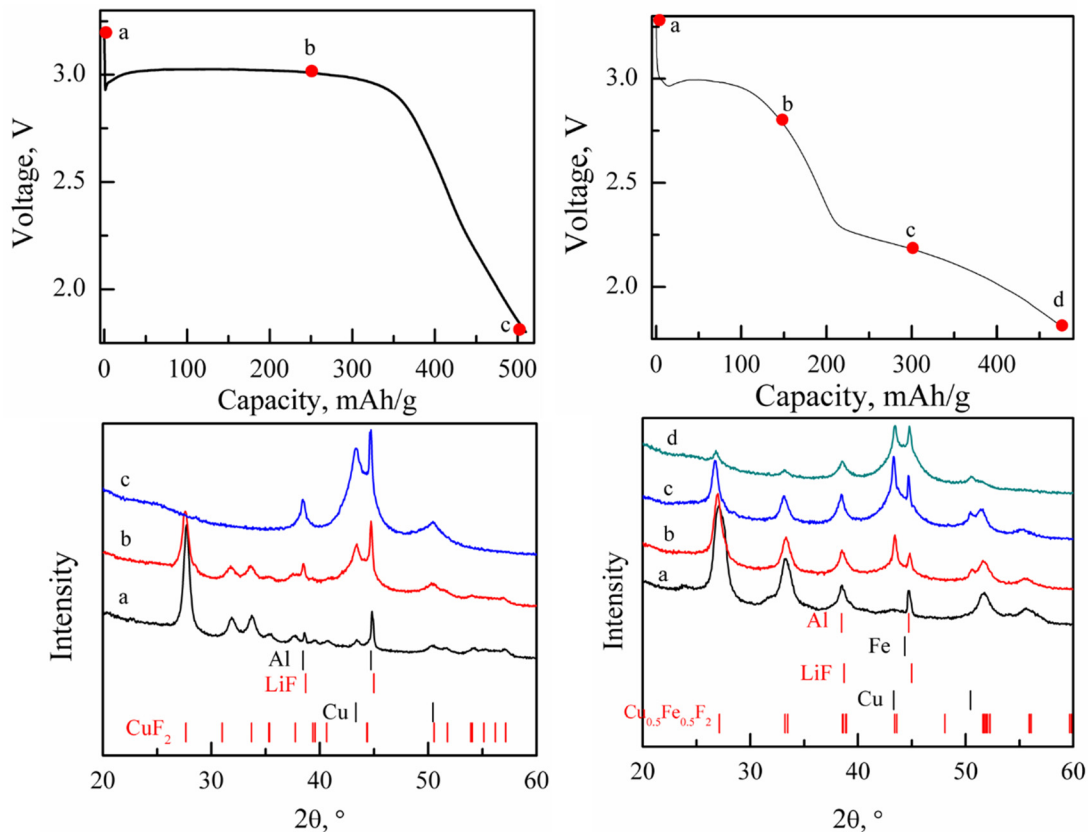


Figure V-54: The powder x-ray diifraction patterns of different discharge states of CuF₂ and Cu_{0.5}Fe_{0.5}F₂. The tick marks are the standard patterns of the different phases. The top shows the discharge curves of the two compounds

Initial Cycling of Copper Fluoride Materials and Choice of Materials for extended Cycling

One of our goals was to determine whether combining CuF₂ with other cathode active material improved the performance as has been reported for primary Li/CuF₂ cells. Composites of CuF₂ with carbon and either MoO₃ or LiVOPO₄ were synthesized; the products of reaction were determined to be merely mixtures of the two materials, no new compounds were formed. The MoO₃ composite was found to exhibit close to the expected theoretical capacity on the first reaction with lithium in electrochemical cells as shown in Figure V- 55; the LiVOPO₄ composite was somewhat lower. However, there was a sharp drop-off in capacity on the second and subsequent discharge cycles for the CuF₂ and CuF₂/MoO₃ composite.

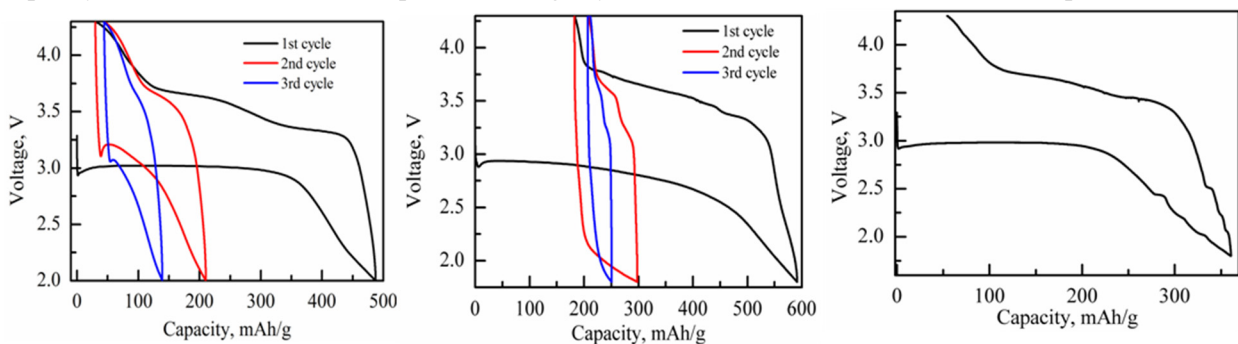
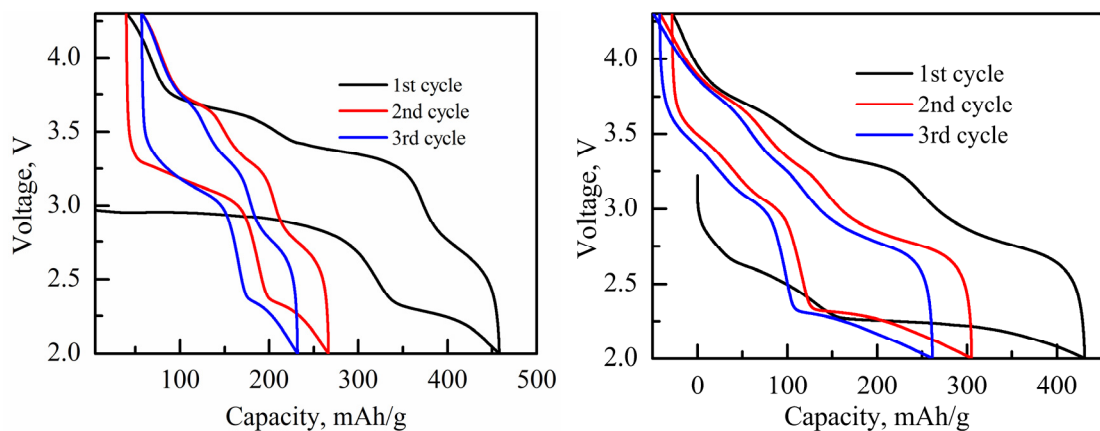


Figure V- 55: Cycling behavior of (left) CuF₂, (middle) CuF₂/MoO₃, and (right) CuF₂/VOPO₄

In contrast, the solid solution Cu_{1-y}Fe_yF₂, retains its capacity for several cycles, and shows superior performance. Therefore major effort was now focused on the solid solution Cu_{1-y}Fe_yF₂ composite with carbon. Initial cycling behavior is showing promising results, as indicated in Figure V- 56.

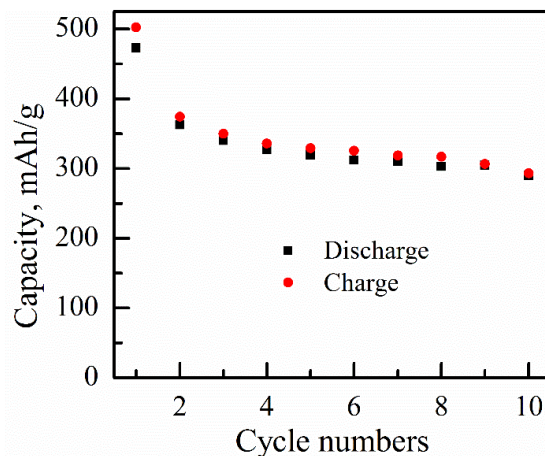
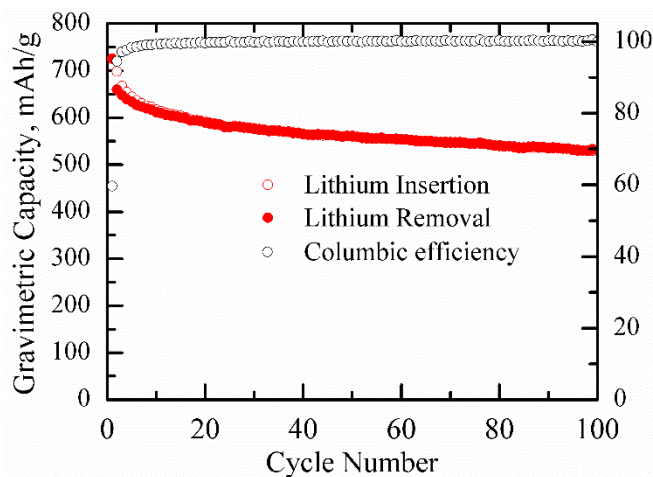
Figure V- 56: The initial cycling behavior of the solid solution $\text{Cu}_{1-y}\text{Fe}_y\text{F}_2$, (left) $y=0.2$, (right) $y=0.5$ cathode

Cell Extended Cycling of the Copper Fluoride Conversion Cathode

Our goal by the end of year 1 was to “Demonstrate cyclability of CuF_2 with a capacity of over 200 mAh/g over 10 cycles.” This was accomplished. For this goal major effort was focused on the solid solution $\text{Cu}_{1-y}\text{Fe}_y\text{F}_2$ composite with carbon. The cycling behavior is showing promising results, as indicated in Figure V- 57, where after 10 cycles the capacity is 290 mAh/g, exceeding the target of 200 mAh/g. In contrast, the solid solution $\text{Cu}_{1-y}\text{Fe}_y\text{F}_2$, retains its capacity for several cycles, and shows superior performance. Therefore major effort was now focused on the solid solution $\text{Cu}_{1-y}\text{Fe}_y\text{F}_2$ composite with carbon. Initial cycling behavior is showing promising results, as indicated in Figure V- 56.

Cycle Behavior and Volumetric Capacity of Sn_2Fe Composite Anode

Our goal was to “Demonstrate more than 100 cycles on Sn_2Fe at 1.5 times the volumetric energy density of carbon.” This goal was accomplished. The extended cyclability of the Sn_2Fe anode composite with carbon is underway, and over 100 cycles have been achieved to date. The tap density of this composite was determined to be around 1.8 g/cc, much higher than that of graphitic carbon which does not exceed 1 g/cc. The calculated actual density of this anode composite is 2.77 g/cc, based on the products in the lithiated electrode. Lithiated carbon, C_6Li , on the same basis is 0.75 g/cc and delivers theoretical capacities of 340 mAh/g and 747 mAh/cc. As Figure V- 58 shows, the Sn_2Fe electrode has a capacity after 100 cycles of around 500 mAh/g, which translates into a volumetric capacity of 1.38 Ah/cc. This is more than 1.5 times that of graphitic carbon.

Figure V- 57: The initial cycling behavior of the solid solution $\text{Cu}_{1-y}\text{Fe}_y\text{F}_2$ cathode, for $y=0.5$ Figure V- 58: Cycling behavior of a Sn_2Fe composite electrode at 0.2 mA/cm^2 . The $\text{Sn}/\text{C}/\text{Ti}$ atom ratio is 1/10/0.25

Comparison of Cyclin Behavior of Sn₂Fe Composite Anode with Carbon Anode

For comparative purposes we compared the cycling behavior of this SnFeC composite with a standard graphitic carbon. This was obtained using both the standard LiPF₆ electrolyte salt and an FSI salt. The latter is reported to be more stable for higher voltage materials. These results are shown in Figure V- 59, and show no deleterious effect on the anode. A slight improvement in the first cycle capacity loss is observed. The higher capacity of the SnFeC composite is clearly apparent.

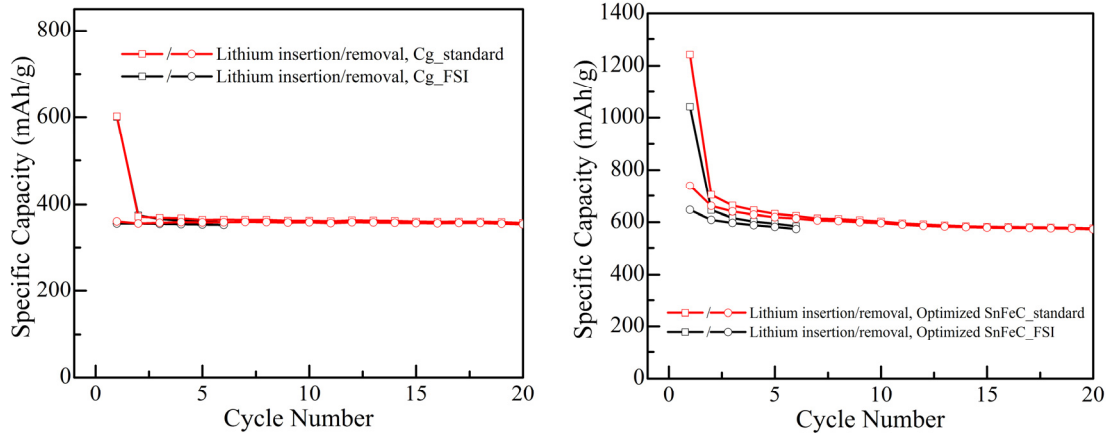


Figure V- 59: Cycling capacity using LiPF₆ and FSI based electrolytes of (left) basleine carbon anode, and (right) advanced SnFeC anode

Conclusions and Future Directions

We have made significant progress in both the cathode and anode conversion materials. The Sn₂Fe/C composite has achieved well over 1.5 times the volumetric capacity of the graphitic anode based on the lithiated product. Next year we will extend the cycling range and determine the capacity behavior over a range of reaction rates (C rates).

We have shown that copper fluoride solid solution electrodes can be cycled vs lithium metal for more than 10 cycles. It appears that mixing CuF₂ with other cathode ctive materials does not enhance the cycling capacity. However, substituting a part of the Copper ions by another metal such as iron enhances the cyclabilility. Next year we will study in depth the reaction mechanism and attain more than 100 cycles vs lithium metal.

We have begun studies of intercalation cathodes based on vanadyl phosphate, VOPO₄, and its analogs. Next year we will determine the optimum starting composition, Li_xVOPO₄, phase, α - ϵ , and synthetic approach. The optimum materials will then be evaluated in electrochemical cells versus Li metal.

These achievements indicate that the proposed technical approach is viable.

FY 2015 Publications/Presentations

1. "High Energy Density Lithium Battery", ES231_Whittingham_2015_p, US DOE Vehicle Technologies AMR, June 10th, 2015.
2. "Cathode: Pushing the Limits of Intercalation Electordes: What is Next? One Option – Two Electron Systems: Two Li Ions as an Alternative to Mg", M. Stanley Whittingham, 10th US-China Workshop, Beijing, China, March 30th 2015.
3. "Tin-Iron Based High Capacity Anodes for Lithium-Ion Batteries", Zhixin Dong, April 28th, 2015, PhD dissertation, Binghamton University, Binghamton, NY.
4. "Synthesis and Characterization of Novel Anode Materials for Lithium Ion Batteries", Tianchan Jiang, March 31st, 20 Annual15, PhD dissertation, Binghamton University, Binghamton, NY.

V.D.3 Development of High-Energy Cathode Materials (PNNL)

Objectives

- Develop high-energy cathode materials with improved safety.
- Develop low-cost synthesis routes for environmentally benign cathode materials with long cycle life.

Technical Barriers

- High cost of materials and synthesis methods.
- Limited energy density, cyclability, and Safety.

Technical Targets

- Understand the phase transition pathway of layered composite $x\text{Li}_2\text{MnO}_3 \cdot (1-x)\text{LiMO}_2$ ($M = \text{Mn, Ni, Co}; 0 \leq x \leq 1$).
- Investigate the roles of lattice Mn^{3+} / oxygen non-stoichiometry on the performances of Li-Mn-rich (LMR) cathode.
- Understand the performance of conventional NMC cathode at high charge cutoff voltage.

Accomplishments

- Identified the transition metal migration pathway in LMR cathode during cycling.
- Identified appropriate synthesis step to enhance homogenous cation distribution in the lattice and demonstrated 200 stable cycles with less than 10% energy loss.
- Developed surface treatment approaches to improve the stability of high-energy cathodes at high voltage conditions.
- Demonstrated high voltage operation of modified NMC cathode with 180 mAh g^{-1} capacity and less than 20% capacity fade for 100 cycles.

Introduction

LMR layered composites, e.g., $\text{Li}[\text{Li}_{0.2}\text{Ni}_{0.2}\text{Mn}_{0.6}]\text{O}_2$, have attracted extensive interest because of their highest energy density among all cathode candidates for Li-ion batteries that could be employed for electric vehicle application. However, fast capacity degradation and voltage fade were usually observed in LMR cathodes due to the layered to spinel-like phase transition. The detailed phase transformation pathway was still elusive and the voltage fade caused by the irreversible phase transformation of the LMR cathode still could not be fully eliminated. Due to the existence of a significant amount of Li_2MnO_3 component, the LMR cathode usually exhibited poor rate capability as compared to conventional NMC cathode materials. In this regard, conventional NMC cathode materials would still be promising if charged to moderately high cut-off voltages to achieve higher accessible capacities without compromising much of their long-term cycling stability.

Approach

1. Use advanced microscopic characterizations to investigate the phase transition pathway of LMR cathodes during cycling.
2. Manipulate oxygen non-stoichiometry to improve the electrical conduction of LMR cathodes.
3. Use charge cutoff voltage to increase discharge capacity of conventional NMC cathode materials.

Project Details

Ji-Guang Zhang (PI)

Pacific Northwest National Laboratory
Energy & Environment Directorate
902 Battelle Boulevard
Richland, WA 99352

Phone: 509-372-6515; Fax: 509-375-2186
E-mail: jiguang.zhang@pnnl.gov

Jie Xiao (Co-PI)

Pacific Northwest National Laboratory
Energy & Environment Directorate
902 Battelle Boulevard
Richland, WA 99352
Phone: 509-372-6515; Fax: 509-375-2186
E-mail: jie.xiao@pnnl.gov

Start Date: October 2011

Projected End Date: September 2015

Results

We have achieved the following progress:

1. Identified the Structural and Chemical Evolution Route of LMR Layered Cathode Materials

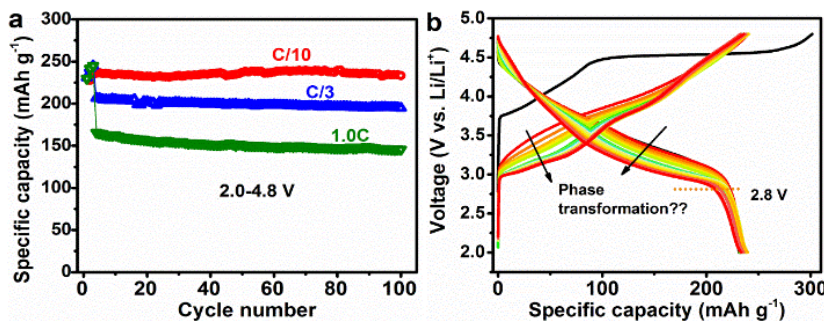


Figure V- 60: (a) Cycling performance at different C rates in the voltage range of 2.0 ~ 4.8 V and (b) charge/discharge profile evolution of LMR cathode at different stages of cycling at C/10 rate

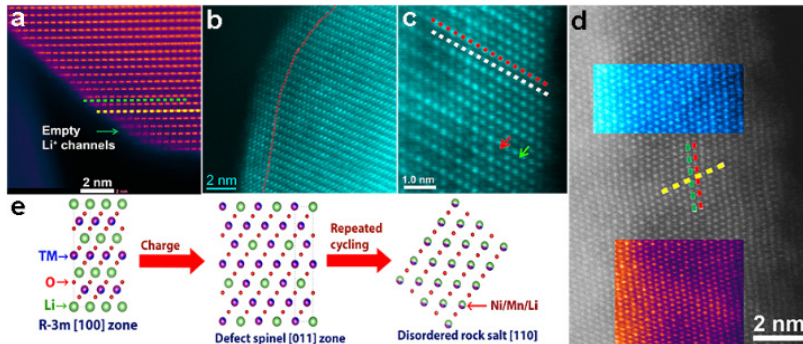


Figure V- 61: Crystal structure of the pristine and cycled LMR cathode. (a) High resolution Z-contrast image of pristine material. (b-d) High resolution STEM image of LMR particles after (b) 1 cycle, (c) 10 cycles and (d) 100 cycles at C/10. (e) Atomic models explaining the structural evolution pathway based on the close observation from the structural changes in cycled materials

electron microscopy (STEM) images at different cycling stages showing the phase transformation of LMR cathode are presented in Figure V- 61. Pristine LMR material is predominantly Li_2MnO_3 type C2/m monoclinic structure with unblocked lithium ion diffusion pathways (Figure V- 61a). After one cycle at C/10, a few atomic layers of transition metal (TM) ions have already been observed in the Li layer at the edge of particles, although this surface reconstruction layer is only about 2 nm (Figure V- 61b). The bulk structure matched well with the atomic model of the R-3m phase in the [100] zone projection. After 10 cycles, more TM ions migrated into the Li layers and the reconstruction layer became thicker (ca. 4 nm) near the crystal edge (Figure V- 61c). There were a few intermediate atomic layers (ca. 2 nm depth) where the Li sites were not occupied by the TM ions, matching well the LT-LiCoO₂-type defect spinel structure (space group Fd-3m) viewed down from the [011] zone axis. In the LT-LiCoO₂-type defect spinel structure, only the 16c octahedral sites are available for reversible Li insertion/de-insertion, while the tetrahedral sites are electrochemically inactive, which not only explains the absence of a 4 V voltage plateau after cycling, but also accounts for the voltage fade as compared to the original layered structure. At the outermost surface layers, some of the 16c octahedral sites of the LT-LiCoO₂-type structure were further occupied by TM ions, converting the defect spinel structure to a disordered rock-salt structure with Fm-3m space group. Further cycling to 100 cycles resulted in the formation of a surface region with a thickness of ca. 10 nm that was transformed to the disordered rock-salt structure (Figure V- 61d).

Figure V- 61e summarizes the phase transition pathway of the LMR material. During cycling, the crystal structure of LMR was transformed from R-3m layered structure (activated from C2/m) to LT-LiCoO₂-type

To date, the voltage fade caused by the intrinsic structural instability of the LMR cathode still cannot be fully eliminated. The detailed phase transformation pathway is not sufficiently understood. In this work, we used the LMR material prepared by a hydrothermally assisted method as a platform to investigate the detailed phase transformation pathway of LMR cathodes during cycling.

The LMR material $\text{Li}[\text{Li}_{0.2}\text{Ni}_{0.2}\text{Mn}_{0.6}]_{\text{O}_2}$ prepared by this method showed decent cycling performance with very limited capacity loss during cycling at different C rates for 100 cycles (See Figure V- 60a), even though the material exhibited continuous voltage decay during cycling (See Figure V- 60b). High resolution scanning transmission

defect spinel-like structure and then further converted to a disordered rock-salt structure, which can be successfully correlated to the voltage fade of the LMR cathode. The reversible Li insertion/removal into/from the disordered rock-salt structure is ascribed to the Li-excess environment that permits Li percolation in the disordered rock-salt structure despite the increased kinetic barrier. Clarification of the phase transformation pathway provides a unique understanding of the voltage-fade and capacity-degradation mechanisms in the LMR cathode.

2. Improved rate performance of the LMR cathode by manipulating the oxygen non-stoichiometry

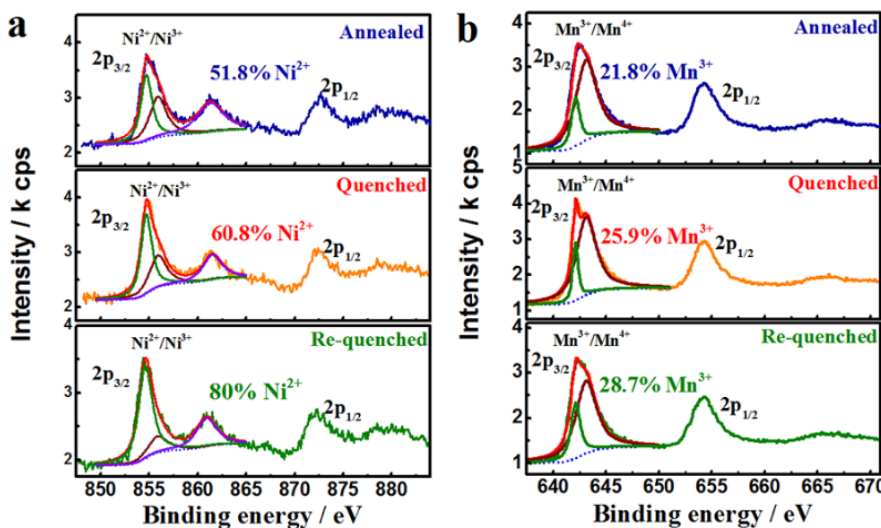


Figure V- 62: (a) Ni 2p and (b) Mn 2p x-ray photoelectron spectroscopy spectra of $\text{Li}[\text{Li}_{0.2}\text{Ni}_{0.2}\text{Mn}_{0.6}]\text{O}_{2-\delta}$ materials

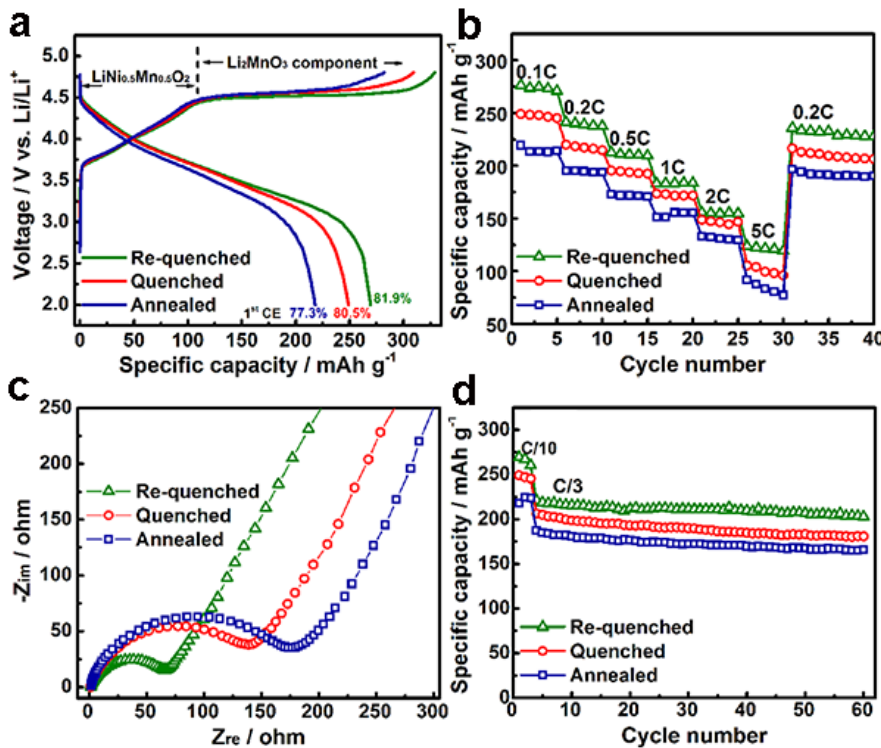


Figure V- 63: (a) Charge/discharge profiles at C/10; (b) rate performance; (c) electrochemical impedance spectra; and (d) cycling performance at C/3 after 3 formation cycles at C/10 of $\text{Li}[\text{Li}_{0.2}\text{Ni}_{0.2}\text{Mn}_{0.6}]\text{O}_{2-\delta}$ materials

It has been proved that the Mn^{3+} content or oxygen non-stoichiometry can enhance the electrical conductivity of a high voltage spinel cathode. Here, LMR cathode $\text{Li}[\text{Li}_{0.2}\text{Ni}_{0.2}\text{Mn}_{0.6}]\text{O}_{2-\delta}$ samples with different Mn^{3+} /oxygen non-stoichiometry have been prepared by different heat treatment processes (anneal, quench and double quench). The re-quenched material showed the highest amount of Mn^{3+} (28.7%), followed by the quenched (25.9%) and annealed (21.8%) counterparts (See Figure V- 62). The LMR material with higher Mn^{3+} content in the original crystal lattice exhibited a considerably prolonged voltage plateau at ~ 4.5 V that is associated with the removal of lithium ions concomitant with an irreversible loss of oxygen from the Li_2MnO_3 component (See Figure V- 63).

During the discharge process, the re-quenched material exhibited the least electrode polarization and the highest discharge capacity of 270 mAh g^{-1} , as compared to quenched material (249 mAh g^{-1}) and annealed material

(218 mAh g⁻¹). The initial Coulombic efficiency increased in the following order: annealed (77.3%) < quenched (80.5%) < re-quenched material (81.9%). The enhanced performance was ascribed to the increase of oxygen non-stoichiometry/Mn³⁺ that provided additional electron hopping pathways and thus enabled the reversible lithium ion de/intercalation. However, increased activation of Li₂Mo₃ resulted in accelerated structural transformation from layered to defect spinel/disordered rock-salt phases, leading to rapid capacity degradation (Figure V- 63d). In this regard, the amount of oxygen non-stoichiometry/Mn³⁺ needs to be manipulated carefully during synthesis of LMR cathode materials in order to reach a reasonable compromise between discharge capacity and long-term cycling stability. The fundamental findings could be widely applied to explain the effects of oxygen non-stoichiometry & Mn³⁺ content on different kinds of LMR cathodes and provide a useful guide for the synthesis of high performance LMR cathodes.

3. Demonstrated high voltage operation of NMC cathode electrodes with different areal capacities

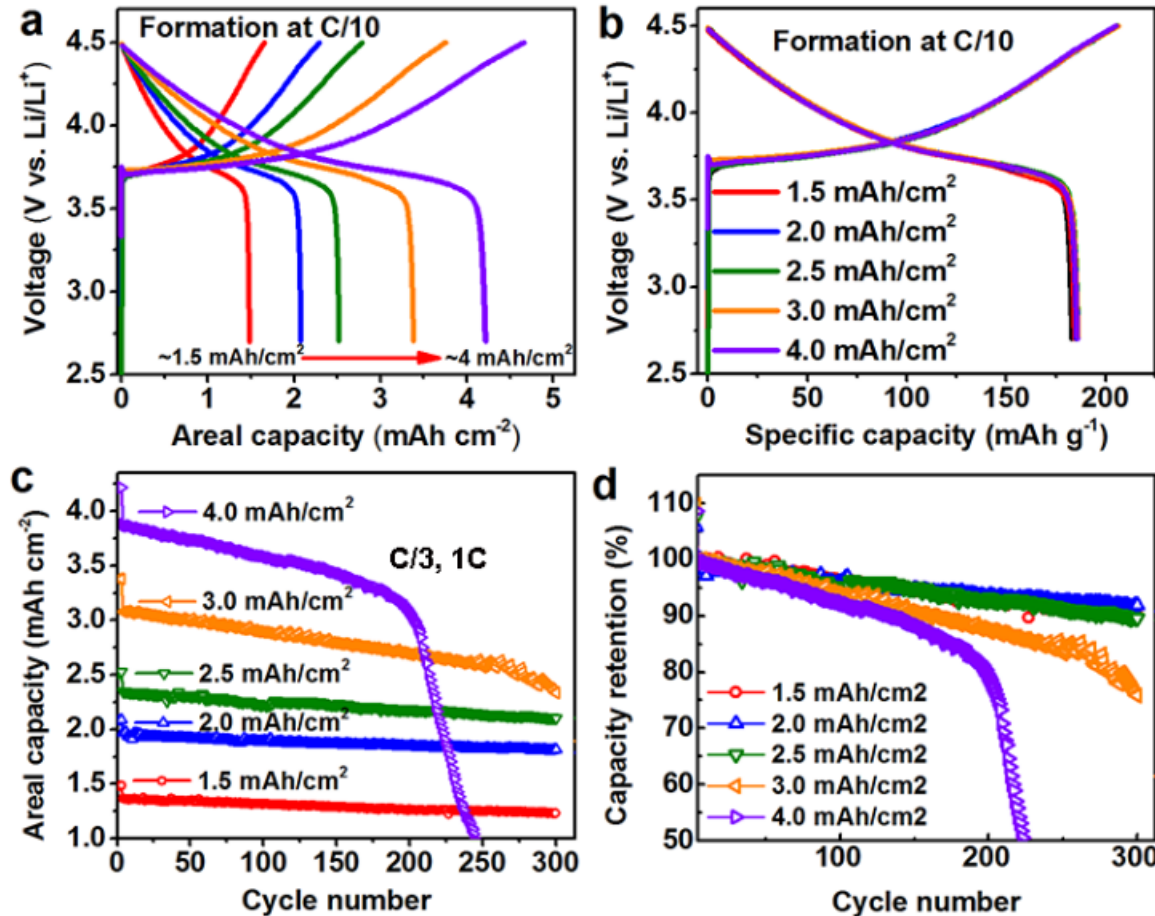


Figure V- 64: (a) Voltage profiles vs. specific capacity, (b) voltage profiles vs. areal capacity, (c) cycling performance and (d) capacity retention of NMC electrodes with different areal capacity loadings

In order to demonstrate the high voltage operation of NMC cathode materials, NMC (LiNi_{1/3}Mn_{1/3}Co_{1/3}O₂) electrodes (92% active material : 4% PVDF : 4% Super P) with different areal capacity loadings have been systematically investigated at a high charge cutoff voltage of 4.5 V (See Figure V- 64). During the formation cycles at C/10, all NMC electrodes delivered similar specific capacity of ca. 185 mAh g⁻¹ regardless of their different loadings, which ranged from ~1.5 to ~4.0 mAh cm⁻², indicating good ionic and electronic conductivity within the loading range. The NMC electrodes showed good cycling stability even with the capacity loading up to ~ 4.0 mAh cm⁻², exhibiting capacity retention above 90% after 100 cycles.

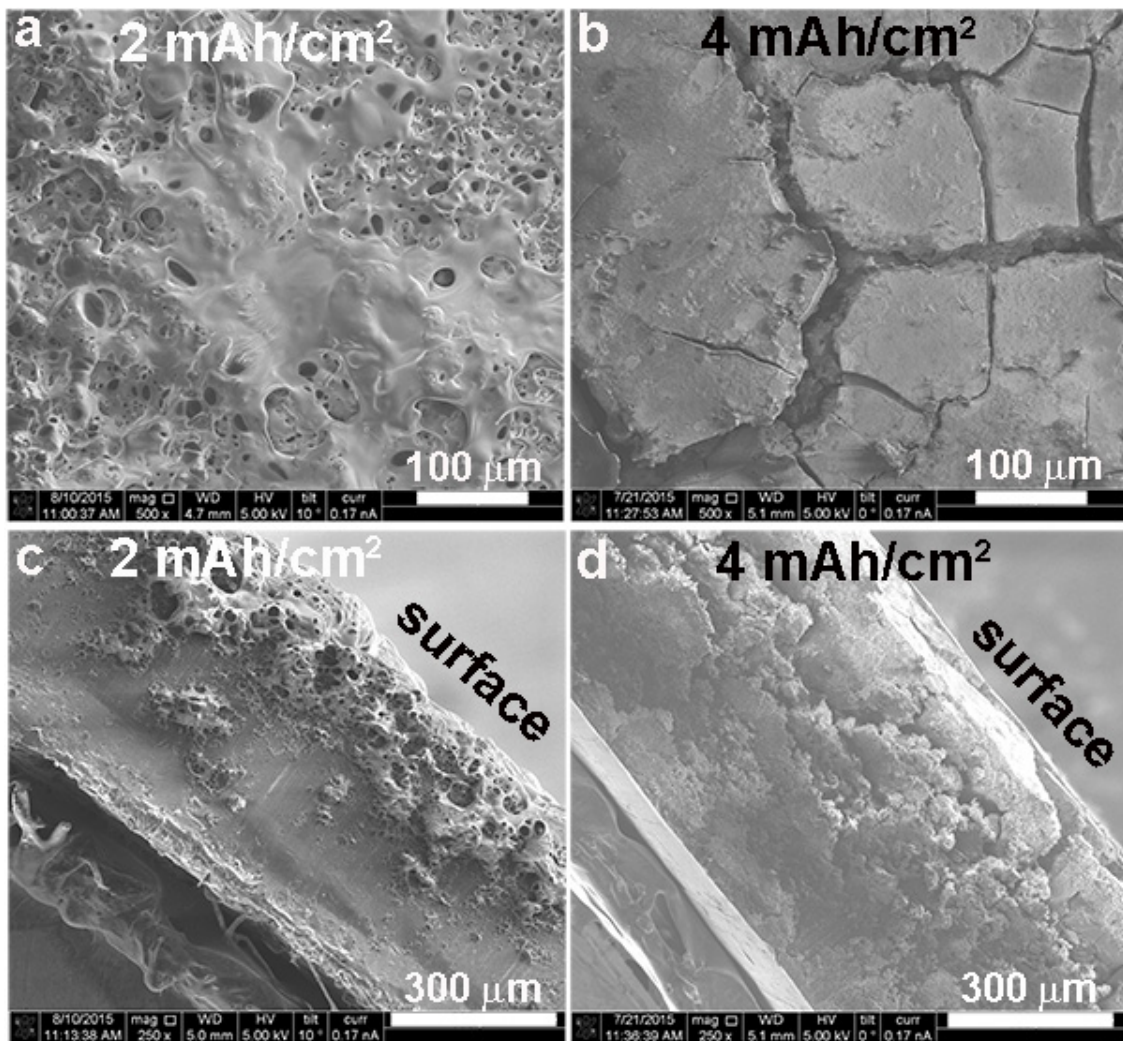


Figure V- 65: SEM images of Li anodes after 300 cycles in cells using (a, c) 2 mAh cm^{-2} NMC counter electrode and (b, d) 4 mAh cm^{-2} counter electrode in terms of (a, b) surface views and (c, d) cross-section views

From 100 to 300 cycles, an obvious difference was observed for NMC electrodes with different capacity loadings (See Figure V- 64c, d). The electrode with moderately high capacity loading of $\sim 2.0 \text{ mAh cm}^{-2}$ still cycled well and retained ca. 90% of its discharge capacity, indicating a decent structural stability of the NMC electrode during cycling at charge cutoff 4.5 V. Further increase of the electrode loading resulted in an accelerated capacity fading, as reflected by the considerably lower capacity retentions of 75.8% and 9.8% for electrodes with ~ 3.0 and $\sim 4.0 \text{ mAh cm}^{-2}$ areal capacity, respectively. However, these tests were performed using half cells. It is suspected that a lithium metal anode, if coupled with a thick cathode, degrades quickly and therefore became the main failure mechanism of the cells.

After cycling, the lithium metal anodes were retrieved and their morphologies were observed using scanning electron microscopy (SEM), which are compared in Figure V- 65. With a moderately loaded ($\sim 2.0 \text{ mAh cm}^{-2}$) NMC cathode, the lithium metal anode was still well maintained, exhibiting a surface covered by a solid electrolyte interface (SEI) layer, which protected the bulk lithium from parasitic reactions with the electrolyte (Figure V- 65a, c). Using a $\sim 4.0 \text{ mAh cm}^{-2}$ NMC cathode, twice the amount of lithium was deposited and stripped in each cycle, which significantly increased the parasitic side reactions among the newly deposited lithium (charge process), the freshly exposed lithium (discharge process), and the electrolyte. The end result was the depletion of electrolyte and the formation of serious cracks and porous/loose lithium after cycling (Figure V- 65b, d), leading to rapid increase of cell resistance and eventual cell failure. The fundamental findings highlighted that the influences from the degradation of the lithium metal anode should be carefully

considered during the operation of high-energy-density cathode materials with high electrode loading in lithium half cells.

Conclusions and Future Directions

In-depth characterization with STEM imaging has revealed that the LMR cathode $\text{Li}[\text{Li}_{0.2}\text{Ni}_{0.2}\text{Mn}_{0.6}]\text{O}_2$ experiences a phase transformation from a layered structure to a LT-LiCoO₂-type defect spinel-like structure and then to a disordered rock-salt structure. The voltage fade can be correlated with Li-ion insertion into the octahedral sites in the defect spinel-like structure and the disordered rock-salt structure. The reversible Li insertion/removal into/from the disordered rock-salt structure is ascribed to the Li-excess environment that can enable the reversible Li percolation in the disordered rock-salt structure despite the increased kinetic barrier.

Increased oxygen non-stoichiometry in the LMR cathode material $\text{Li}[\text{Li}_{0.2}\text{Ni}_{0.2}\text{Mn}_{0.6}]\text{O}_{2-\delta}$ facilitates the activation of the Li_2MnO_3 component, significantly improving the rate capability of the LMR cathode. The superior performance of the material with higher oxygen non-stoichiometry is ascribed to the increase of lattice $\text{Mn}^{3+}/\text{Ni}^{2+}$, which provides additional electron hopping pathways. However, the extensive activation of the Li_2MnO_3 component accelerates the unfavorable phase transformation, thus leading to faster capacity fading.

NMC electrodes with different areal capacity loading have been systematically investigated at a high charge cutoff voltage of 4.5 V. A very decent capacity retention (90% after 300 cycles) could be achieved for an NMC electrode with areal capacity of $\sim 2 \text{ mAh cm}^{-2}$. However, influences from the degradation of the lithium metal anode should be carefully considered with further increase of electrode loading to 3 mAh cm^{-2} or even higher.

Based on the knowledge obtained in FY15, future work will focus on investigation of the structural degradation mechanism of NMC cathode materials with different compositions at high charge cutoff voltages. The fundamental understanding will be used to guide the synthesis of Ni-rich NMC cathode materials. The synthesis conditions and surface treatment will also be optimized to improve the long-term cycling of Ni-rich NMC cathode materials at high charge cutoff voltages.

FY 2015 Publications/Presentations

1. "Structural and Chemical Evolution of Li- and Mn-Rich Layered Cathode Material," J. Zheng, P. Xu, M. Gu, J. Xiao, N. D. Browning, P. Yan, C. Wang and J.-G. Zhang, *Chemistry of Materials* **27**, 1381-1390 (2015).
2. "Effects of structural defects on the electrochemical activation of Li_2MnO_3 ," L. Xiao, J. Xiao, X. Yu, P. Yan, J. Zheng, M. Engelhard, P. Bhattacharya, C. Wang, X.-Q. Yang and J.-G. Zhang, *Nano Energy* **16**, 143-151 (2015).
3. "Evolution of Lattice Structure and Chemical Composition of the Surface Reconstruction Layer in $\text{Li}_{1.2}\text{Ni}_{0.2}\text{Mn}_{0.6}\text{O}_2$ Cathode Material for Lithium Ion Batteries." P. Yan, A. Nie, J. Zheng, Y. Zhou, D. Lu, X. Zhang, R. Xu, I. Belharouak, X. Zu, J. Xiao, K. Amine, J. Liu, F. Gao, R. Shahbazian-Yassar, J.-G. Zhang and C.-M. Wang, *Nano Letters* **15**, 514-522 (2015).
4. "Probing the Degradation Mechanism of Li_2MnO_3 Cathode for Li-Ion Batteries," P. Yan, L. Xiao, J. Zheng, Y. Zhou, Y. He, X. Zu, S. X. Mao, J. Xiao, F. Gao, J.-G. Zhang and C.-M. Wang, *Chemistry of Materials* **27**, 975-982 (2015).
5. "Atomic-Resolution Visualization of Distinctive Chemical Mixing Behavior of Ni, Co, and Mn with Li in Layered Lithium Transition-Metal Oxide Cathode Materials," P. Yan, J. Zheng, D. Lv, Y. Wei, J. Zheng, Z. Wang, S. Kuppan, J. Yu, L. Luo, D. Edwards, M. Olszta, K. Amine, J. Liu, J. Xiao, F. Pan, G. Chen, J.-G. Zhang and C.-M. Wang, *Chemistry of Materials* **27**, 5393-5401 (2015).
6. "Recent Advances on the Understanding of Structural and Composition Evolution of LMR Cathode for Li ion Batteries," P. Yan, J. Zheng, J. Xiao, C. Wang and J.-G. Zhang, *Frontiers in Energy Research* **3**, doi: 10.3389/fenrg.2015.00026 (2015).
7. "Observation of Electron-Beam-Induced Phase Evolution Mimicking the Effect of the Charge–Discharge Cycle in Li-Rich Layered Cathode Materials Used for Li Ion Batteries," P. Lu, P. Yan, E. Romero, E. D. Spoerke, J.-G. Zhang and C.-M. Wang, *Chemistry of Materials* **27**, 1375-1380 (2015).
8. "Probing the failure mechanism of nanoscale LiFePO_4 for Li-ion batteries," M. Gu, W. Shi, J. Zheng, P. Yan, J.-G. Zhang and C. Wang, *Applied Physics Letters* **106**, 203902 (2015).

9. "Visualizing nanoscale 3D compositional fluctuation of lithium in advanced lithium-ion battery cathodes," A. Devaraj, M. Gu, R. Colby, P. Yan, C. M. Wang, J. M. Zheng, J. Xiao, A. Genc, J. G. Zhang, I. Belharouak, D. Wang, K. Amine and S. Thevuthasan, *Nat Commun* 6, 8014 (2015).
10. "Organic Cathode Materials for Rechargeable Batteries," R. Cao, J. Qian, J.-G. Zhang and W. Xu, in *Rechargeable Batteries*, edited by Z. Zhang and S.S. Zhang, pp 637-670.
11. "Development of High-Energy Cathode Materials," J.-G. Zhang and J. Xiao, 2015 DOE Annual Peer Review Meeting Presentation in Washington, DC, June 2015.
12. "Understanding and Mitigation of Voltage Fade in High Energy Cathode Materials," J. Zheng, P. Yan, J. Xiao, C. Wang, and J.-G. Zhang, presented at 2014 Materials Research Society fall meeting, Boston, MA, Dec. 1, 2014.

V.D.4 *In situ* Solvothermal Synthesis of Novel High Capacity Cathodes (BNL)

Objectives

Develop low-cost cathode materials that offer high energy density (>660 Wh/kg) and electrochemical properties (cycle life, power density, safety) consistent with USABC goals.

Technical Barriers

Present day Li-ion batteries are incapable of meeting the 40-mile all-electric-range within the weight and volume constraints established for PHEVs by DOE and the USABC. Higher energy density cathodes are needed for Li-ion batteries to be widely commercialized for PHEV applications.

The development of new, safer lithium batteries requires new tools to better understand the physical and chemical processes that occur during cycling and the ability to predict and ultimately control the key electrochemical properties such as capacity (power and energy density), durability (calendar and cycle life), abuse tolerance (safety characteristics) and cost.

Technical Targets

- High energy density (660 Wh/kg or higher)
- Low cost

Accomplishments

- Determined the reaction pathways and phase evolution during hydrothermal ion exchange synthesis of Li(Na)VPO₅F_x cathodes *via in-situ* studies.
- Optimized ion exchange synthesis for preparing Li(Na)VPO₅F_x with maximized Li content, and characterize its structural and electrochemical properties.
- Developed new reactor design to enable high-throughput synthesis of phase-pure cathode materials.
- Obtained good cycling stability of one high-capacity cathode in a prototype cell with specific capacity higher than 200 mAh/g.

Introduction

Despite considerable interest in developing new cathodes for lithium ion batteries, only a small number of known materials show real promise for achieving significant improvement in capacity and/or a reduction in cost. The preparation of new compounds or materials with unique properties often relies on trial and error as there are a variety of synthesis parameters (precursor concentration, temperature, pressure, *pH* value, cation type and reaction time) that can have a strong influence on the material properties (crystal structure, morphology, particle size) and electrochemical performance (*e.g.*, capacity, rate capability, and durability). Most solution-based reactions are carried out in a sealed autoclave and therefore the reactor is a black box – the inputs and outputs are known, but little is known about intermediate phases and overall reaction pathways. *In-situ, real-time* probes of synthesis reactions can provide the details of reactions, elucidating intermediate phases and how temperature, pressure, time and the precursor concentrations affect the reaction pathways. The results of such studies enable strategies to optimize synthesis reactions, particularly the formation of materials of desired phases and properties. With a more fundamental understanding of the correlation between synthesis

Project Details

J. Patrick Looney

Sustainable Energy Technologies Department
Brookhaven National Laboratory (BNL)
Upton, NY, 11973

Phone: 631-344-3798; Fax: 631-344-7905
E-mail: jlooney@bnl.gov

Feng Wang

Sustainable Energy Technologies Department
Brookhaven National Laboratory (BNL)
Upton, NY, 11973
Phone: 631-344-4388; Fax: 631-344-7905
E-mail: fwang@bnl.gov

Start Date: April 2012

Projected End Date: April 2016

conditions, crystallization processes, and material properties, a more rational design of advanced lithium electrode materials should emerge.

Approach

In this effort, specialized *in-situ* reactors were developed to investigate synthesis reactions in real time using synchrotron X-ray diffraction (XRD) techniques. With these techniques, crystal growth and structural changes can be monitored while leaving the reaction undisturbed. This approach provides a *real-time* measurement of how reaction conditions affect nucleation and crystallization, bonding, particle size, morphology and defect concentration. In addition, *in-situ* measurements reveal the formation of intermediate and short-lived phases formed during the reaction without the need for quenching. These new tools are being used to prepare novel high-energy cathodes with desired properties (*e.g.* structure, stoichiometry).

The structural and electrochemical properties of synthesized materials are evaluated *via* synchrotron X-ray, and various electrochemical methods. The structural/chemical evolution of electrodes during cycling is systematically investigated using *in-situ*, *operando* synchrotron XRD and X-ray absorption near-edge (XANES), extended fine structure (EXAFS) and advanced TEM techniques.

Results

Structure Tracking Aided Design and Synthesis of Li₃V₂(PO₄)₃ Nanocrystals Solvothermal approaches for making monoclinic LVP were explored, starting with investigating the synthesis reactions in making LVP in a solvothermal environment. The local structure and oxidation states of V in the product were examined by a combination of XANES and EXAFS of the V K-edge, along with electron diffraction and high-resolution transmission electron microscopy (TEM). This step led to the formation of an amorphous mixture in which the V-containing phase has a local structural ordering resembling that of the final LVP phase. An extra step of calcination was added to obtain the crystalline LVP, and *in situ* synchrotron XRD was applied to track the phase nucleation and growth from the amorphous mixture in real time. With structure tracking of all of the synthesis reactions, we were able to design a solvothermal-assisted synthesis protocol, through which single-crystalline LVP nanoparticles were obtained under optimized conditions. The electrodes made from the LVP materials in this way were found to have excellent rate capability and cycling stability.

Structure tracking of the reaction intermediates in preparing LVP For the solvothermal synthesis of LVP, the precursors LiH₂PO₄, V₂O₅ and sucrose in an ethylene glycol solution were heated in a sealed autoclave to high temperatures (typically 230°C) for 10 hours. The product was a mixture of amorphous phases and Li₃PO₄ from precursors, identified from the smallest peaks in the XRD pattern shown in Figure V- 66a. TEM images and selected-area electron diffraction (SAED) patterns were also collected from local areas of the powders extracted from the intermediate product. The ill-defined particle morphology and the presence of broadened diffuse rings in the SAED patterns (Figure V- 66b) further confirmed the amorphous nature of the intermediate. The valence state of vanadium and short-range ordering in the intermediate phase were examined *via* X-ray absorption spectroscopy. The oxidation state of vanadium was determined by XANES of V K-edge (with V₂O₅ and V₂O₃ as references; Figure V- 66c). Overall, the energy position of the V K-edge from the intermediate phase is similar to that of V₂O₃, suggesting the reduction of the precursor V₂O₅ to a valence state close to 3+ after solvothermal treatment (with about a 3 eV chemical shift to a lower energy). XANES spectrum of the intermediate has a similar edge position and shape as that of the synthesized VPO₄. The XANES of the final product LVP resembles those of the intermediate and VPO₄ except for a prominent pre-edge peak around 5470 eV. The pre-edge peak originates from the dipole-forbidden transitions from 1s core levels to 3d states, and is an indication of the distorted VO₆ octahedra in the LVP structure. Figure V- 66d is a magnitude plot of the Fourier transformation EXAFS (FT-EXAFS) spectra for the V K-edge (k^3 -weighted in k -space) of the intermediate phase, for comparison to that of the reference materials, including V₂O₃, V₂O₅, synthesized-VPO₄, and the final product LVP. In the FT-EXAFS plot for the LVP, there were two dominant peaks. The peak at approximately 1.5 Å is assigned to the single scattering-path from V to the closest oxygen atoms (the V-O bond in VO₆ octahedra), while the peak at R = ~3.0 Å is attributed to the V-V bonding between two edge-sharing V-O₆ octahedra. The FT-EXAFS plot of the intermediate phase also shows resemblance to that of LVP and synthesized VPO₄, with the 1st peak being present at about 1.5 Å (V-O bond in V-O₆ octahedra) (Figure V- 66d). Therefore, the XAS data confirm that these amorphous intermediates have a similar valence state and local structure to that of VPO₄ (and final LVP as well).

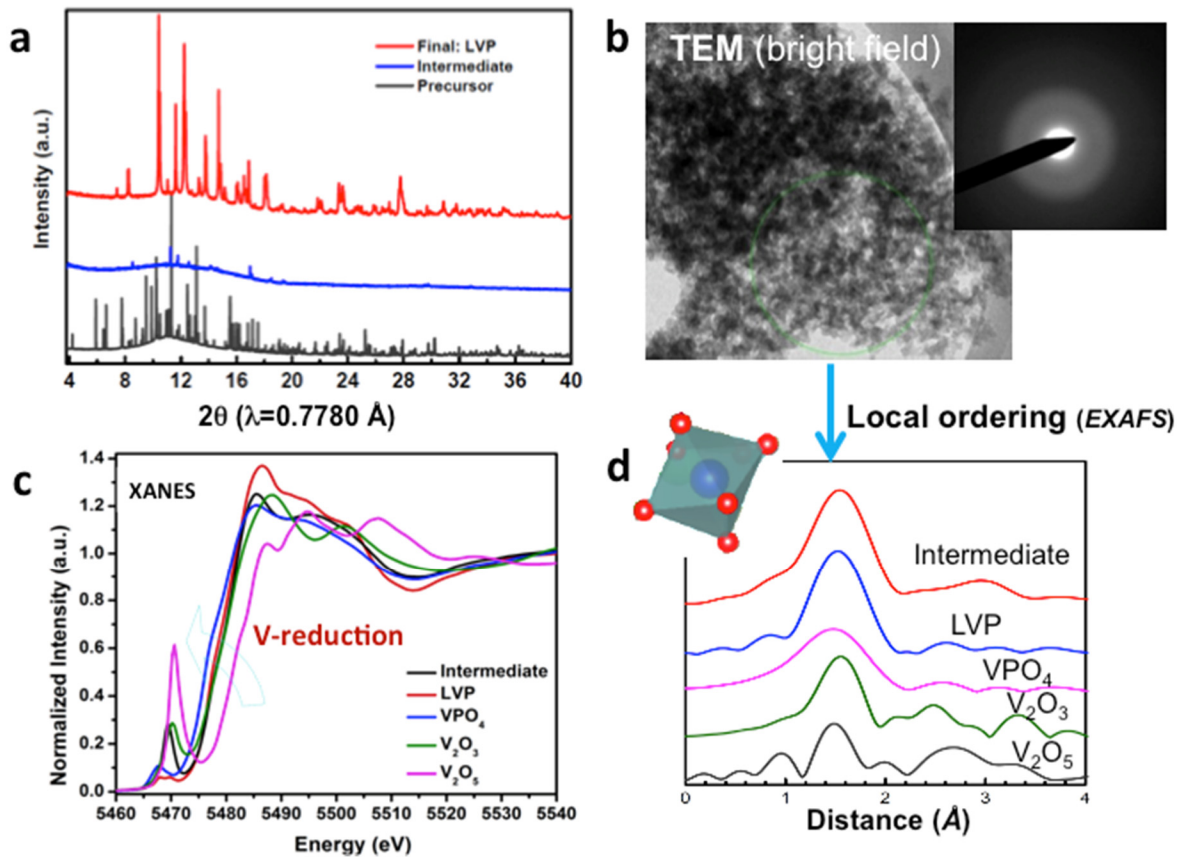


Figure V- 66: Structure tracking of the intermediate and final products in preparing $\text{Li}_3\text{V}_2(\text{PO}_4)_3$ (LVP). (a) X-ray diffraction patterns of the precursor (black), intermediate phase (blue) and final product (red), (b) bright-field TEM image and selected area electron-diffraction pattern (inset; recorded from the areas labeled by the green circle) of the intermediate phase, (c-d) XANES spectra and Fourier transformation magnitude of the EXAFS of V K-edge from intermediate (blue), final LVP (red), precursor V_2O_5 (grey) , and reference compounds of VPO_4 (purple), and V_2O_3 (green)

Attempts were made to obtain the crystalline LVP phase at higher temperatures (up to 260°C), but only amorphous intermediates were obtained, so calcination of amorphous intermediate was undertaken in an argon atmosphere to obtain LVP phase. In order to obtain details of the structural evolution during calcination, *in-situ* time-resolved XRD was performed during heating, with the main results given in Figure V- 67a. In the early stage of heating (Stage I; within the first ~ 3.5 hours), there was no visible change in the Bragg diffraction peaks. It is only when the temperature reached 630°C did the peaks associated with the Li_3PO_4 precursor begin to disappear, and quickly thereafter the new peaks associated with LVP became apparent (at about 666°C ; Stage II). The diffraction peaks were broad and weak due to nanocrystalline nature, and became sharper and stronger with further heating (a trend more obvious in the expanded view in the inset). When the temperature reached 730°C , a pure LVP phase was obtained. In order to track the nucleation and growth processes of the LVP phase, the width of the diffraction peaks was obtained *via* refinements to obtain the particle size, and the peak intensity was integrated to get the concentration of the LVP phase. Figure V- 67b shows the extracted crystal size and concentration as a function of time and temperature. In stage I (below 630°C), no LVP was formed. With a further increase in temperature to about 666°C (in Stage II), LVP particles of about 30 nm formed rapidly, within the time needed to complete a single scan (14 minutes or less) although the concentration of the formed LVP was still low. Interestingly, there was little change in the particle size as the temperature rose from 630°C to 730°C ; while the concentration increased steadily, reaching the maximum value within about one hour. Surprisingly, there is no growth of the particle size, and therefore, the rapid increase in the concentration of the LVP is mostly due to the multiplication of the nucleus of LVP at stage (II). In Stage III with prolonged heating at 730°C (for > 5 hours), LVP concentration stayed almost constant and there was slight increase in particle size to about 40 nm. This indicates that the growth of the LVP particles was largely hindered, mostly likely by the carbon coating on the particle surface.

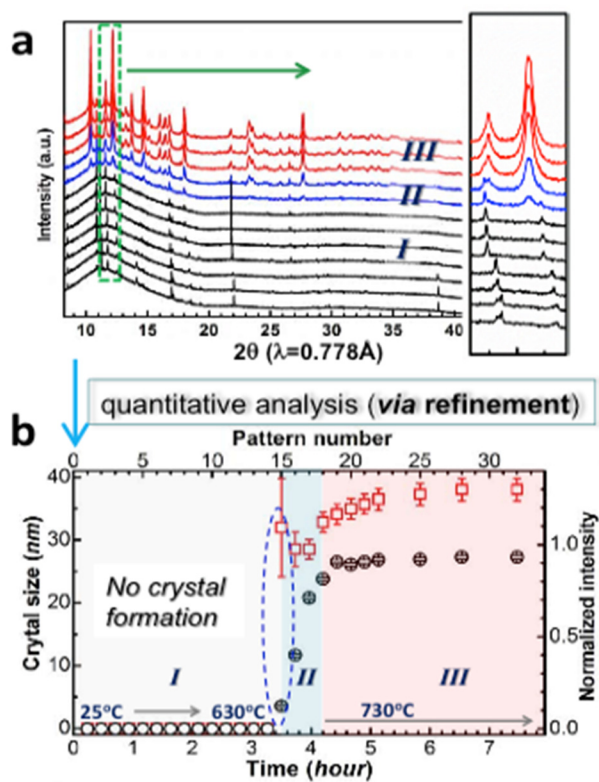


Figure V- 67: Real time tracking of the crystal growth of LVP during calcination by *in-situ* XRD. (a) Time-resolved XRD patterns of the intermediate during heating from RT to 730°C under an Ar atmosphere, (b) evolution of the crystal size (red square) and concentration of LVP (black circle) with time

analyzer (TGA), which was performed by heating the materials in the air from RT to 600°C (Figure V- 68c). This supports the *in-situ* XRD measurements, indicating that the presence of carbon can hinder the agglomeration and growth of the particles under high temperature calcinations, eventually leading to uniformity of the particle sizes.

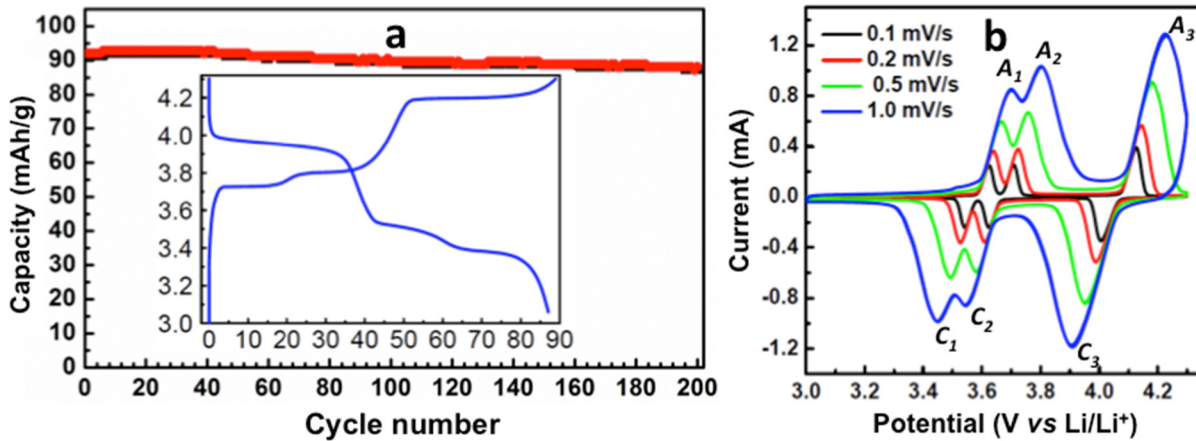


Figure V- 68: Fast rate capability of LVP nanocrystals. (a) cycling performance and charge-discharge curve (inset) at 10 C in the window of 3.0 -4.3 V, (b) evolution of the CV curves of LVP as a function of scan rates (from 0.1 to 10 mV·s⁻¹)

Electrochemical properties of the synthesized LVP nanocrystals The as-obtained carbon-coated LVP material was further tested for use as cathodes in a half cell (with Li as the counter electrode). Figure V- 69a shows the rate performance at a current density of 1.33 A·g⁻¹ (equivalent to 10 C); such a rate performance of this carbon-

Even though the solvothermal treatment does not produce the LVP phase directly, it is an essential step towards forming the VPO₄-like intermediate with a similar local ordering as LVP. The similarity in the local structures between the amorphous intermediate and the LVP phase may play a critical role in the fast nucleation and formation of LVP nanocrystals with uniform size in the calcination step.

Importantly, the solvothermal step not only leads to the amorphous intermediate with desirable local ordering, but also drives the reduction of the vanadium cations and the fine mixture of carbon, which are critical for producing the carbon-coated LVP nanocrystals.

Structural properties of LVP nanocrystals

Using the developed solvothermal-assisted synthetic protocol, *i.e.*, solvothermal treatment followed by calcination at 730°C, we obtained phase-pure LVP powders with a monoclinic structure (cell parameters $a=8.6088(1)$ Å, $b=8.5985(1)$ Å, $c=12.0488(2)$ Å, $\beta=90.546(1)^\circ$; Figure V- 68). The particle size is highly uniform, about 50 nm in diameter (being examined by SEM). These particles are single-crystalline and coated with amorphous carbon according to high-resolution TEM image and Fast Fourier transform (Figure V- 68b). About 6.5 wt% of carbon in the C/LVP composite was also measured using thermos-gravimetric

coated LVP is remarkable, and outperforms the micron-size C/LVP obtained *via* conventional solid-state reactions. On the other hand, the nanosized LVP has a very low polarization in the charge-discharge curves even at such a high rate (inset of Figure V- 69a), which may be due to small charge-transfer resistance. We also applied CV techniques to estimate the lithium diffusion in the LVP electrodes (Figure V- 69b). The variation of peak current (I_p) is linear with the square root of the scanning rate ($v^{1/2}$). The apparent chemical-diffusion coefficient of lithium is about $10^{-10} \text{ cm}^2 \cdot \text{s}^{-1}$ as determined by Randles-Sevik equation. Such high lithium diffusivity may be explained by the three dimensional lithium diffusion pathways, eventually leading to the high rate capacity.

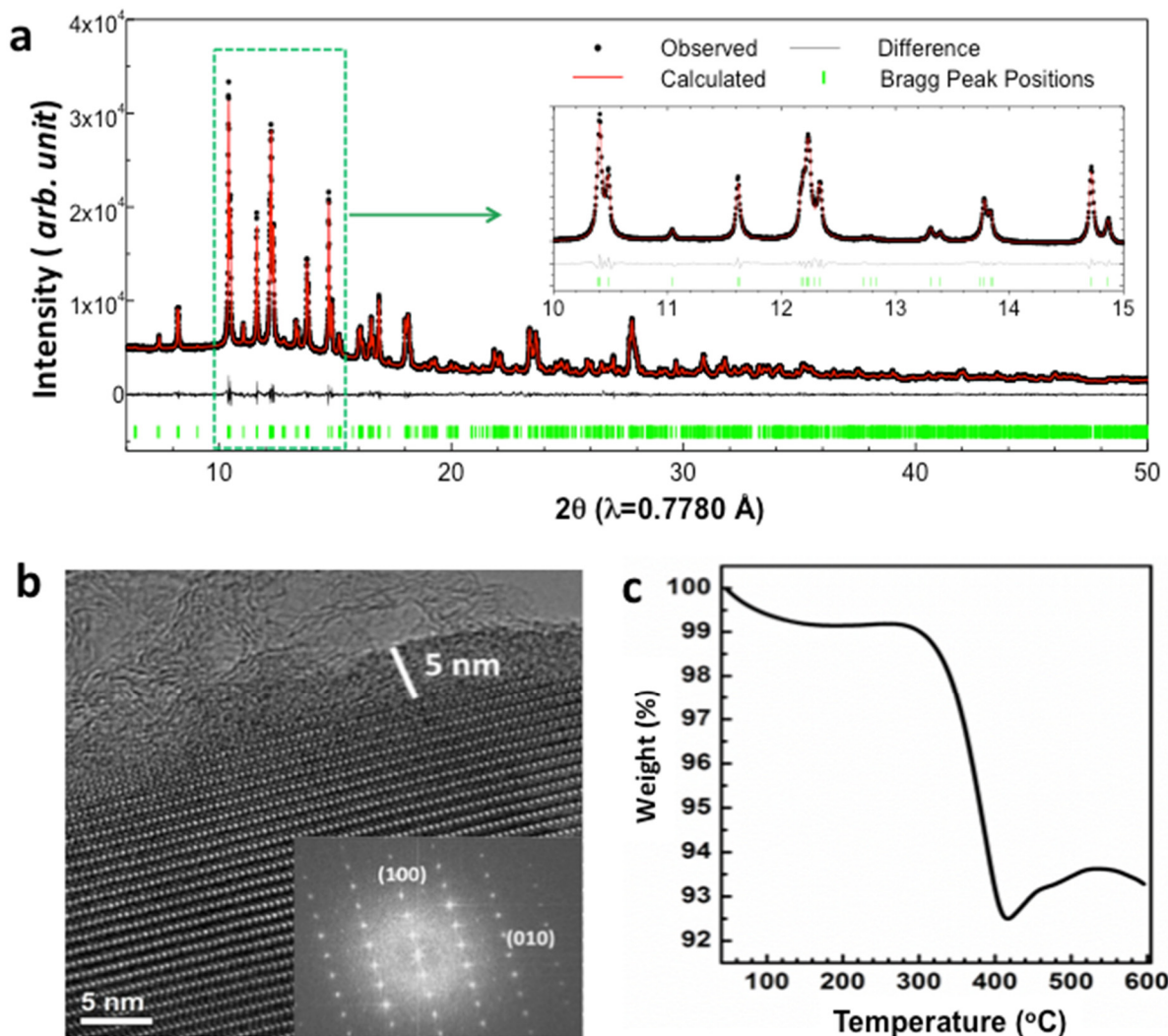


Figure V- 69: Structural properties of the synthesized LVP nanocrystals. (a) Synchrotron XRD pattern and Rietveld refinement with observed data points (red points), calculated data (black line), Bragg positions (green bars) for as-obtained LVP, (b) high- resolution TEM image and corresponding Fourier Transform (inset) of LVP, indicating its single-crystallinity, (c) thermo-gravimetric analyzer (TGA) curve of LVP during heating in air

In summary, aided by the structure tracking investigation of the synthesis reactions, we developed a solvothermal-assisted synthetic protocol for making monoclinic LVP nanocrystals, namely *via* solvothermal treatment, to obtain amorphous VPO₄-like phase and subsequent calcination to get a pure LVP phase. The synthesized single-crystalline LVP nanocrystals deliver excellent cycling retention, with only about 5% capacity decay after 200 cycles. Good rate capability with a discharge capacity of $86 \text{ mAh} \cdot \text{g}^{-1}$ was also obtained in the voltage window 3.0 - 4.3 V at 10 C as a result of the surface carbon coating and nanosize that ensure a low charge-transfer resistance and a high lithium diffusion coefficient.

In situ hydrothermal ion exchange synthesis of Li(Na)VPO₅F_x cathodes

A hydrothermal ion-exchange method was developed for synthesis of Li-containing cathodes from Na counterparts, and utilized to prepare Li(Na)VPO₅F_x (LVOPF), a high-capacity cathode. Systemic studies on synthesis parameters for preparing LVOPF, including temperature, concentration of LiBr solution, Li/Na ratio and heating rate were completed through *in-situ* synthesis. These studies provided insights into the structural evolution and Li⁺/Na⁺ ion exchange pathways, enabling us to optimize the exchange procedures for making LVOPF cathodes of maximized stoichiometry and enhanced cycling stability.

In situ tracking hydrothermal ion exchange synthesis Time-resolved XRD was applied to track the structural change during ion exchange at fixed temperature. The main results are given in Figure V- 70a, showing that, instead of proceeding *via* a single facile solid solution (as commonly believed), the Li substitution into LVOPF is more complicated, involving multiple steps. Among them a 2-phase transformation, from tetragonal to orthorhombic structure (of reduced symmetry), is found to be the rate-limiting step. Raising reaction temperature is one way to accelerate the process, as demonstrated by the 3x reduction in time to complete the phase transition at 120°C (compared to 72°C; Figure V- 70b).

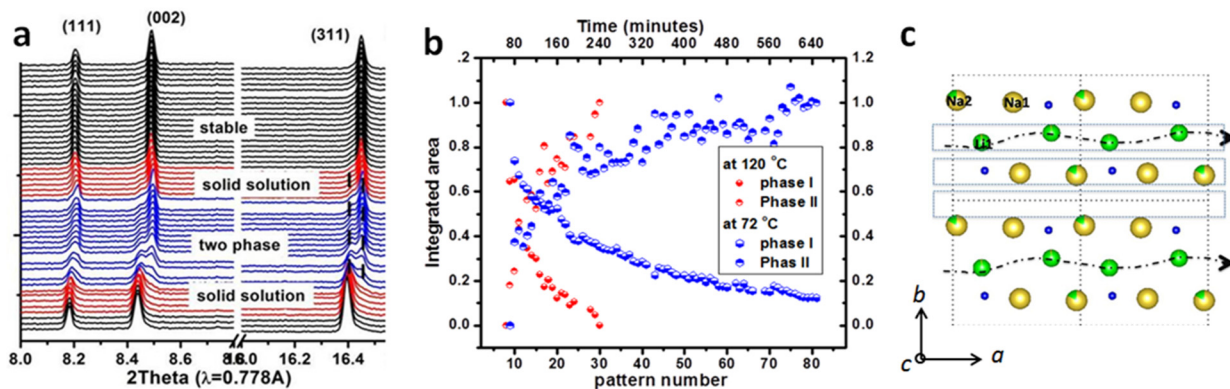


Figure V- 70: *In-situ* studies of ion exchange in Li(Na)VPO₅F_x. (a) Time-resolved XRD patterns, (b) the integrated Bragg peak intensity of (311) of the Na-phase (phase I) and Li-phase (phase II) at fixed temperatures, 72°C and 120°C, (c) illustration of the configuration of Na⁺ ions (golden) and Li⁺ ions (green) in the *ab* plane determined by structure refinement

Complementary to *in-situ* studies, high-resolution synchrotron X-ray and neutron diffraction measurements were performed to identify the positions and occupancies of Li and Na atoms in the intermediate and final products. The local alkali ion and vacancy ordering (determined by structure refinement), along with the possible diffusion pathways, are illustrated in Figure V- 70c. The Li⁺/Na⁺ ion exchange is anisotropic, preferentially going along the *a* direction, which leads to a peculiar Na/Li/vacancy ordering. Those one-dimensional Na, Li, and empty channels are alternatively repeated along *b* direction (as indicated by blue boxes). This is an interesting discovery in that the interdiffusion of ions in the solid is rate-determining step, and the empty channels provide the pathway for the Li/Na interdiffusion, which is essential to the ion-exchange process. These results shed light on the kinetics and thermodynamics of ion exchange in LVOPF that may also be applicable to other polyanionic cathodes (with similar 1D diffusion channel). The dependence of exchange process on the synthesis parameters provides guidance to optimizing the synthesis procedures in obtaining the LVOPF electrodes of maximized lithium capacity and improved cycling stability.

Optimized ion exchange synthesis of Li(Na)VPO₅F_x Through *in-situ* investigation the dependence of exchange process on the synthesis parameters (temperature, concentration of LiBr solution, Li/Na ratio and heating rate) was determined and utilized to obtain a series of LVOPF with varying lithium content. The LVOPF particles are typically micron-sized, and single crystalline as shown by TEM imaging and electron diffraction (Figure V- 71a). The morphology is preserved during the ion-exchange process without particle pulverization. The subtle structural change in the Li_xNa_{1.5-x}VOPO₄F_{0.5} as a function of *x* was determined by high-resolution synchrotron XRD combined with Rietveld refinements, indicating a phase transformation from tetragonal (*P4₂/mm*) to orthorhombic (*Pnnm*) at about *x* = 0.5, with a small volume shrinkage (only about 1% being measured). A maximum of lithium content of *x*=1.34 was obtained by further lithium substitution at a temperature of 160°C *via* a slow solid solution process, with enough exchange time and lithium source.

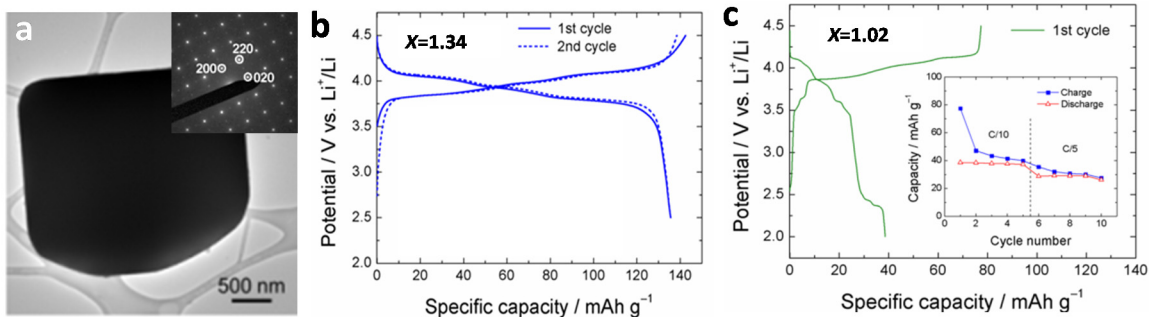


Figure V- 71: Structure and electrochemical properties of the $\text{Li}_x\text{Na}_{(1-x)}\text{VPO}_5\text{F}_{0.5}$ (LVPOF) electrode. (a) typical transmission electron microscopy (bright field) image (inset: electron diffraction recorded from the particle along the zone axis [001]), (b) voltage profiles (at C/10 rate) of the LVPOF electrode ($x=1.34$) for the 1st and 2nd cycles, (c) voltage profile (at C/10 rate) and cycling stability of the LVPOF electrode ($x=1.02$)

The electrochemical properties of $\text{Li}_x\text{Na}_{1.5-x}\text{VOPO}_4\text{F}_{0.5}$ electrodes for different x contents were investigated with Li metal as counter electrode. Some of the results were given in Figure V- 71b, Figure V- 71c, for high lithium contents ($x = 1.34$ and 1.02 respectively). For $x = 1.34$ (maximum Li content), the reversible capacity at a C/10 rate reached 145 mAh g^{-1} . Moreover, a high voltage of $\sim 4 \text{ V}$ (vs. Li^+/Li) was observed, leading to a high energy density of 580 Wh kg^{-1} . This makes it a promising candidate as cathode for Li-ion batteries. In contrast, the electrochemical properties of the $x = 1.02$ electrode were significantly inferior to $x = 1.34$, in terms of capacity (of only 80 mAh/g for the 1st charge) and cycling stability (inset in Figure V- 71c). The electrochemical tests indicate a strong dependence of electrochemical property on the extent of Li^+ exchange, and maximizing lithium ion exchange appears to be essential to the achieving high capacity as well as the long-term cyclability. This is likely due to the enhancement of structural stability with a close-to-complete replacement of Na^+ by Li^+ according to the structural analysis.

Novel ternary metal fluorides as high-energy cathodes

Transition metal fluorides are an appealing alternative to conventional intercalation compounds for use as cathodes in next-generation lithium batteries due to their extremely high capacity (3–4 times greater than the current state-of-the-art). However, issues related to reversibility, energy efficiency and kinetics prevent their practical application. In this study, solid solutions of the ternary metal fluorides $\text{M}^1\text{yM}^2_{1-y}\text{F}_x$ ($\text{M}^1, \text{M}^2 =$ transition metal), were prepared *via* mechanochemical reactions. The structure, stability and electrochemical properties of $\text{Cu}_y\text{Fe}_{1-y}\text{F}_2$ were investigated by density functional theory (DFT) calculations, electrochemical measurements, along with comprehensive structural and chemical analysis using synchrotron XRD, XAS, and ((S)TEM coupled with EELS. Electrochemical measurements indicated a reversible Cu redox reaction in the mixed system, $\text{Cu}_{0.5}\text{Fe}_{0.5}\text{F}_2$, in contrast to irreversible behavior observed in the binary fluoride, CuF_2 .

Synthesis and structural characterization of ternary metal fluorides For the mechanochemical synthesis of the ternary fluorides, as-purchased CuF_2 (Aldrich, 98%), FeF_2 (Aldrich, 98%), NiF_2 (Aldrich, 98%), and CoF_2 (Aldrich, 98%) were used as starting materials without any further purification. The crystal structures of as-synthesized $\text{M}^1\text{yM}^2_{1-y}\text{F}_2$ powders were examined using synchrotron XRD and TEM. Figure V- 72a shows the XRD patterns of the $\text{Cu}_y\text{Fe}_{1-y}\text{F}_2$ system at several different Cu/Fe ratios. The broadened diffraction peaks indicate a loss of long-range order during the mechanochemical synthesis. Interestingly, the milling of CuF_2 and FeF_2 precursors leads to the formation of a single solid solution phase over the entire compositional range. This is not too surprising given the similarity of the CuF_2 and FeF_2 structures. FeF_2 exhibits a tetragonal rutile structure (space group: $\text{P}4_2/mnm$) and is comprised of FeF_6 octahedra, while CuF_2 is monoclinic (space group: $\text{P}2_1/n$), which is essentially a distorted rutile structure due to the strong Jahn-Teller distortion induced by the Cu^{2+} ([Ar]3d⁹) ion. The distorted structure of CuF_2 becomes more symmetric with Fe incorporation as the $\text{Cu}_y\text{Fe}_{1-y}\text{F}_2$ solid solution is formed. The as-synthesized samples are complex agglomerates of small nanocrystallites (Figure V- 72b). The diffusive rings in the electron diffraction pattern (although being broadened due to the nanocrystalline nature of the particles; inset in Figure V- 72b can be assigned to the tetragonal rutile phase, consistent with the XRD measurements (Figure V- 72a).

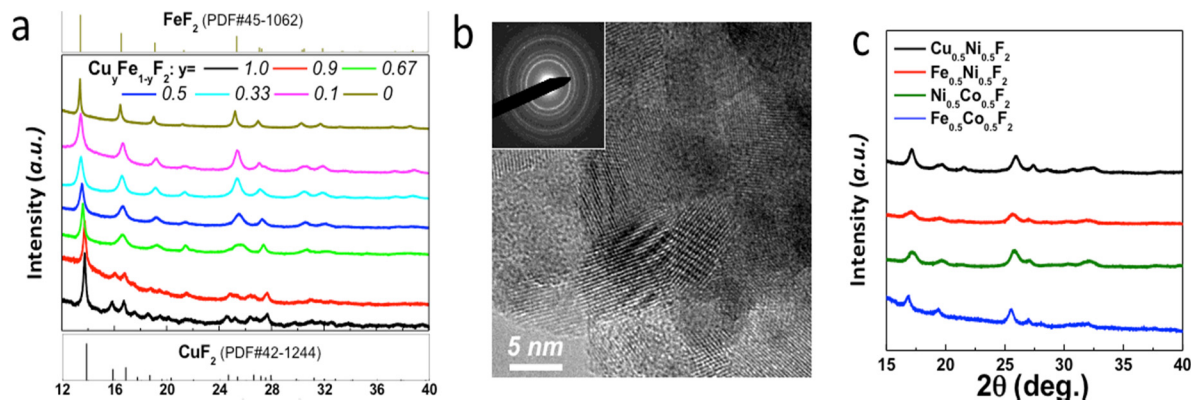


Figure V-72: Structure and stability of novel ternary metal fluorides. (a) Synchrotron XRD patterns from $\text{Cu}_y\text{Fe}_{1-y}\text{F}_2$ along with CuF_2 (PDF#42-1244) and FeF_2 (PDF#45-1062), (b) high-resolution TEM image of as-synthesized $\text{Cu}_{0.5}\text{Fe}_{0.5}\text{F}_2$ nanocrystallites (inset: electron diffraction pattern from a large area), (c) XRD patterns from representative ternary fluorides of varying metal species, $\text{M}^{1.0.5}\text{M}^{2.0.5}\text{F}_2$ ($\text{M}^1, \text{M}^2 = \text{Cu}, \text{Fe}, \text{Ni}, \text{Co}$)

Density functional theory (DFT) calculations were also made to predict the stability of solid solution phases, at all the possible configurations (not shown here), indicating that, regardless of the composition, there exist several $\text{Cu}_y\text{Fe}_{1-y}\text{F}_2$ phases that are energetically more stable (negative energy points) than the simple mixture (zero energy points). The lowest energy points at each composition overlap well with the convex hull (dashed line), indicating that $\text{Cu}_y\text{Fe}_{1-y}\text{F}_2$ can exhibit solid solution behavior over the entire composition range. The structural stability of the solid solution phase was experimentally confirmed by *in situ* XRD (not shown here), which shows no phase decomposition in $\text{Cu}_{0.5}\text{Fe}_{0.5}\text{F}_2$ during dynamic heating up to 250 °C. Since most of the 3d metal binary fluorides (*i.e.* MF_2) have similar structures, either based on the tetragonal rutile or distorted rutile framework, it is expected that they may form a variety of solid solutions. A number of ternary fluoride phases were prepared, including $\text{Cu}_{0.5}\text{Ni}_{0.5}\text{F}_2$, $\text{Fe}_{0.5}\text{Ni}_{0.5}\text{F}_2$, $\text{Ni}_{0.5}\text{Co}_{0.5}\text{F}_2$ and $\text{Fe}_{0.5}\text{Co}_{0.5}\text{F}_2$ (Figure V-72c), which demonstrates the versatility of the mechanochemical synthesis method.

Electrochemical properties of ternary metal fluorides Electrochemical measurements were performed on a series of $\text{Cu}_y\text{Fe}_{1-y}\text{F}_2$ samples to evaluate their electrochemical properties in the presence of two redox centers (Figure V-73). During galvanostatic discharge, $\text{Cu}_y\text{Fe}_{1-y}\text{F}_2$ exhibits a two-step lithiation process as expected, but the voltage profiles are different than those obtained from pure CuF_2 , FeF_2 , or a mixture of the two. In $\text{Cu}_y\text{Fe}_{1-y}\text{F}_2$, the Cu conversion (higher plateau) occurs at similar potentials as CuF_2 , while the Fe conversion (lower plateau) occurs at a much higher potential and does not exhibit the voltage dip typically observed in pure FeF_2 , indicating a more facile Fe conversion. So the electrochemical properties in the ternary system, $\text{Cu}_y\text{Fe}_{1-y}\text{F}_2$, are significantly affected by the cooperative redox of Cu and Fe sitting on the same lattice.

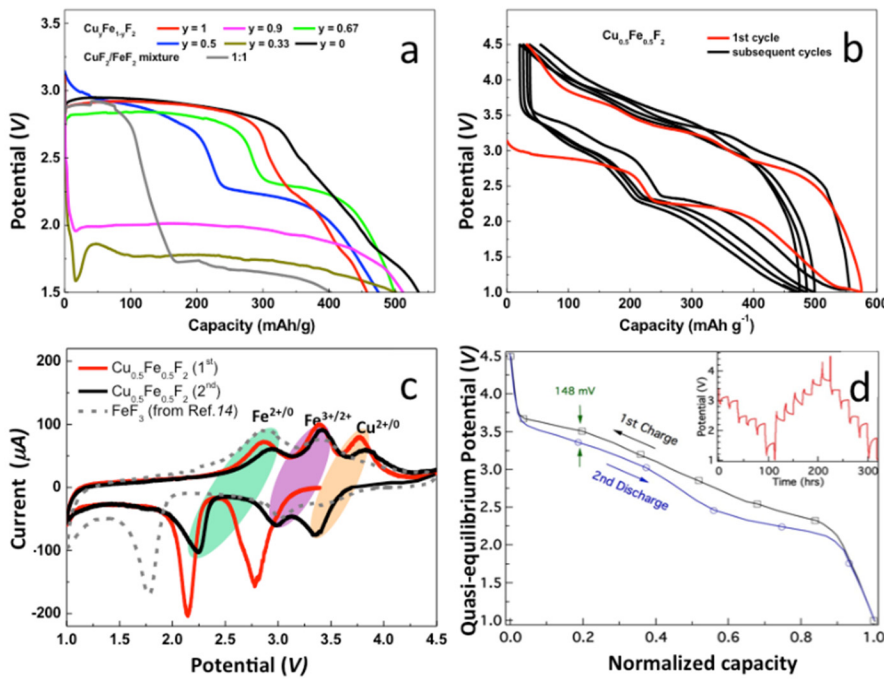


Figure V- 73: Electrochemical properties of $\text{Cu}_y\text{Fe}_{1-y}\text{F}_2$ solid solution. (a) Voltage profiles (first discharge at a current 5 mA g^{-1}) of the $\text{Cu}_y\text{Fe}_{1-y}\text{F}_2$ series along with a simple mixture of CuF_2 and FeF_2 (b) voltage profiles of $\text{Cu}_{0.5}\text{Fe}_{0.5}\text{F}_2$ for the first five cycles (9.2 mA g^{-1}), (c) cyclic voltammetry (CV) curves for the first (red) and second (black) cycles at a rate of $\text{C}/40$, in comparison to that of FeF_3 (adapted from Ref. 14), (d) quasi-equilibrium voltage profile from $\text{Cu}_{0.5}\text{Fe}_{0.5}\text{F}_2$ obtained from GITT measurements (inset; 150 mA g^{-1} for 3.5 hrs followed by a 15 hr rest). All the measurements were performed at room temperature

a high cycling reversibility. The redox reactions in the $\text{Cu}_{0.5}\text{Fe}_{0.5}\text{F}_2$ electrodes were also investigated by cyclic voltammetry (CV), as given in Figure V- 73c, and compared with FeF_3 . During charge, the first peak is attributed to $\text{Fe}^{0/2+}$ oxidation (at $\sim 2.8 \text{ V}$), while the second, located at $\sim 3.4 \text{ V}$ (similar voltage as $\text{Fe}^{2+/3+}$ oxidation), is likely attributed to the further oxidization into trivalent iron (Fe^{3+}). The third peak at higher voltage ($\sim 3.8 \text{ V}$) is noticeably absent in the CV from FeF_3 and must be related to Cu oxidation since there are no other redox centers in this voltage range. There are also 3 peaks in the 2^{nd} discharge, with the first two associated with $\text{Fe}^{2+/0}$ and $\text{Fe}^{3+/2+}$ reduction and a 3^{rd} at $\sim 3.4 \text{ V}$ assigned to $\text{Cu}^{2+/0}$ reduction (with the voltage slightly lower than the theoretical value of 3.5 V). In contrast to pure CuF_2 , which showed no reversible redox Cu peaks, the redox peaks in $\text{Cu}_{0.5}\text{Fe}_{0.5}\text{F}_2$ are present over multiple cycles, indicating different electrochemical behavior in the solid solution ternary phase.

Another striking feature observed in the cycling data is the small voltage hysteresis. Even during conventional galvanostatic cycling (Figure V- 73b), the measured voltage gaps are only $\sim 0.48 \text{ V}$ for $\text{Cu}^{0/2+}$, $\sim 0.63 \text{ V}$ for $\text{Fe}^{0/2+}$ and $\sim 0.43 \text{ V}$ for $\text{Fe}^{2+/3+}$. Those values are significantly less than that of binary fluorides, such as FeF_2 . The voltage hysteresis measured by galvanostatic intermittent titration technique (GITT) is reduced to 148 mV for the $\text{Cu}^{0/2+}$ redox and $\sim 200 \text{ mV}$ for the Fe redox (Figure V- 73d), which is substantially lower than pure FeF_2 (700 mV) and comparable to intercalation-type electrodes. This is the lowest reported hysteresis for conversion reaction in any metal fluoride, indicating the potential for achieving high-energy efficiency in ternary fluoride cathodes.

In summary, novel ternary metal fluorides $\text{M}^1\text{yM}^2_{1-y}\text{F}_x$ ($\text{M}^1, \text{M}^2 = \text{transition metal}$) were prepared by a mechanochemical process. The initial conversion reaction (lithiation) in $\text{Cu}_y\text{Fe}_{1-y}\text{F}_2$ proceeds via a two-stage process, the reduction of Cu to metallic Cu^0 and concomitant formation of disordered FeF_2 , followed by $\text{Fe}^{2+/0}$ reduction. The reformation of the fluoride takes a different path, during which Fe^0 is partially oxidized up to Fe^{3+} , leading to the formation of a rutile framework, which promotes the reconversion of Cu to form a disordered rutile-like Cu-Fe-F final phase (overall similar to the pristine material). However, the formation of trivalent iron limits the full reconversion of Cu^0 back to Cu^{2+} . Although cation dissolution remains a challenge

Electrochemical analysis of $\text{Cu}_{0.5}\text{Fe}_{0.5}\text{F}_2$ over the voltage range of $1.0 - 4.5 \text{ V}$ (Figure V- 73b) revealed an initial high discharge capacity (575 mAh g^{-1}), close to the theoretical value (549 mAh g^{-1} for 2 electron transfer), and a charge capacity 543 mAh g^{-1} ($\sim 94\%$ of the initial discharge capacity), indicating the re-oxidation of both the iron and the copper. The reaction process during the subsequent charge and discharge appear to be different than that during the first discharge, as evidenced by the change from two obvious plateaus (~ 2.9 and $\sim 2.2 \text{ V}$) to three plateaus ($3.4, 3.0, 2.3 \text{ V}$). Upon subsequent cycles the voltage profiles become similar, indicating

for the long-term cyclability, the Cu-based ternary fluorides exhibit unique electrochemical properties - a reversible $\text{Cu}^{2+/0}$ reaction and remarkably low hysteresis (<150 mV), which, along with intrinsically high voltage and capacity, makes them appealing for use in next-generation rechargeable batteries.

New reactor design to enable high-throughput synthesis of phase-pure cathode materials

The development and utilization of *in situ* reactors for *real time* probing of reaction, allow us to gain access to the study of intermediate and short-lived phases, thereby obtaining deep insights as to how temperature, pressure, time, and precursor concentration affect the kinetic reaction pathways. In a recent effort, we developed one new type of micro-reactors of a more flexible design that accommodates different types of synthesis (*e.g.*, solvothermal, ion-exchange, solid-state reactions), and their applications in both *in-situ* and *ex-situ* studies of kinetics and pathways of a particular reaction. These micro-reactors enable combinatorial screening of large number of synthesis parameters – thereby opening new avenues in the search for high capacity cathodes. This approach requires only small amounts of precursor materials for synthesis studies, and fast post-synthesis phase identification by XRD can be undertaken directly to the products within the reactors.

The application of these micro-reactors was demonstrated in the synthesis of Cu-V-O (Figure V- 74). Using *in-situ* XRD to track phase formation in the micro-reactor, we found that the $\alpha\text{-CuVO}_3$ phase started to form at temperatures as low as 240°C and the pure phase was obtained at 430°C within one hour; in contrast to tens of hours of solid-state reaction at ~ 700°C or above (as is commonly done). In addition, *in-situ* studies can now be coupled with combinatorial studies of different reactions by using multiple micro-reactors that contain precursors (Cu_2O and V_2O_5 in this case) of varying concentration, to cover wide composition-temperature space (as illustrated in Figure V- 74).

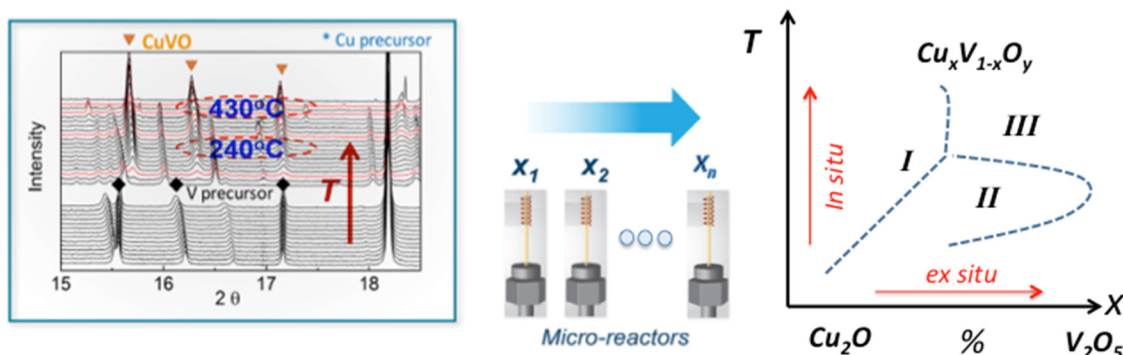


Figure V- 74: Design of micro-reactors for both *in-situ* and *ex-situ* combinatorial studies of synthesis reactions, enabling *high-throughput* synthesis of new cathode materials (an example of $\text{Cu}_x\text{V}_{1-x}\text{O}_y$ being used here)

Conclusions and Future Directions

We have developed micro-reactors of a more flexible design that accommodates different types of synthesis (*e.g.*, solvothermal, ion-exchange, solid-state reactions), and their applications in both *in-situ* and *ex-situ* studies of kinetics and pathways of a particular reaction. These micro-reactors enable combinatorial screening of large number of synthesis parameters – thereby opening new avenues in the search for high capacity cathodes. Built on *in-situ* studies of solvothermal, ion-exchange and solid state reactions, we have developed cost-efficient procedures for making several interesting cathode materials:

- $\text{Li}_3\text{V}_2(\text{PO}_4)_3$ nanocrystals of high power density
- $\text{Li}(\text{Na})\text{PO}_5\text{F}$ of maximized Li content and with enhanced cycling stability
- Cu-V-O with high capacity (> 200 mAh/g) and reasonable cycling stability (patent filed)
- CuFeF_2 cathodes of extremely high capacity (~ 500 mAh/g; patented)

In addition, we have undertaken extensive collaborative research (within BMR and with external partners) on the development and utilization of advanced synchrotron X-ray and TEM techniques for studies of synthesis reactions in preparation of cathodes and Li reactions in electrodes. For example, through collaborations, we have studied the origin of enhanced cycling stability of iron oxyfluorides (FeOF)—a new type cathodes with high capacity (~400 mAh/g), and completed structural analysis of Li-rich $\text{Li}_{1.14}\text{Mn}_{0.54}\text{Ni}_{0.14}\text{Co}_{0.14}\text{O}_2$ cathodes. In the future, we will continue the investigation of polyanionic cathodes, to further improve the

electrochemical performance of Li(Na)VOPO₄F, Li₃V₂(PO₄)₃ and search for new high-capacity Li-V-PO₄-X cathodes. We will develop Ni-Mn based oxides cathodes, through exploring the solid state and hydrothermal based synthesis approaches. New *in-situ* approaches and capabilities will be further developed for studying synthesis reaction in preparing cathode materials. This allows us to develop our understanding of the synthesis reaction pathways and kinetics, and use the knowledge to design and synthesize new high-capacity cathodes.

FY 2015 Publications/Presentations

1. "Structure Stabilization by Mixed Anions in Oxyfluoride Cathodes for High-Energy Lithium Batteries", SW Kim, N Pereira, NA Chernova, F Omenya, P Gao, MS Whittingham, GG Amatucci, D Su, F Wang, ACS nano (ASAP).
2. "Structure Tracking Aided Design and Synthesis of Li₃V₂(PO₄)₃ Nanocrystals as High-Power Cathodes for Lithium Ion Batteries", L Wang, J Bai, P Gao, X Wang, JP Looney, F Wang, *Chem. Mater.* 27, 5712 (2015).
3. "Ternary metal fluorides as high-energy cathodes with low cycling hysteresis", F Wang, SW Kim, DH Seo, K Kang, L Wang, D Su, JJ Vajo, J Wang, J Graetz, *Nat. Commun.* 6: 6668 (2015).
4. "Solvothermal Synthesis of LiMn_{1-x}Fe_xPO₄ Cathode Materials: A Study of Reaction Mechanisms by Time-Resolved In Situ Synchrotron X-ray Diffraction", J Bai, J Hong, H Chen, F Wang, *J. Phys. Chem. C* 119, 2266 (2015).
5. "Eliminating Voltage Decay of Lithium-Rich Li_{1.14}Mn_{0.54}Ni_{0.14}Co_{0.14}O₂ Cathodes by Controlling the Electrochemical Process", Z Wei, W Zhang, F Wang, Q Zhang, B Qiu, S Han, Y Xia, Y Zhu, Z Liu, *Chemistry-A European Journal* 21, 7503 (2015).

Patents

1. "Nanostructured copper vanadium oxides as high-capacity cathodes for lithium ion batteries", F Wang, X. Wang, J Graetz, P Khalifah, US provisional patent (filed).
2. "High-energy cathodes for lithium rechargeable batteries", F Wang, S-W Kim, J Graetz, Patent WO2015109181A1.

Presentations

1. "High-Energy Conversion Cathodes for Rechargeable Lithium Batteries", F Wang et al., TMS 2015 144th Meeting, March 15-19, Orlando, FL. (*invited*)
2. "Tracking the Crystalline Phases in Solution-based Syntheses of Battery Materials with *In Situ* Time-resolved Synchrotron X-ray Powder Diffraction", J Bai, and F Wang, RI 2015, July 6-12, New York.
3. "*In-situ* Solvothermal Synthesis of Novel High Capacity Cathodes", J.P Looney, and F Wang, AMR meeting 2015, June 8-12, 2014, Washington DC.
4. "*In Situ* solvothermal synthesis of High-Energy Cathodes for Lithium-Ion Batteries", J Bai, L Wang, and F Wang, 228th, ECS meeting, Oct. 11-15, Phoenix, AZ.

V.D.5 Novel Cathode Materials and Processing Methods (ANL)

Objectives

- The primary objective of this project is to develop low-cost, high-energy and high-power Mn-oxide-based cathodes for lithium-ion batteries that will meet the performance requirements of PHEV and EV vehicles. A key goal is to improve the design, composition and performance of advanced electrodes with stable architectures and surfaces, facilitated by an atomic-scale understanding of electrochemical and degradation processes.

Technical Barriers

- Low energy density
- Cost
- Abuse tolerance limitations.

Technical Targets (USABC – End of life)

- 142 Wh/kg, 317 W/kg (PHEV 40 mile).
- Cycle life: 5000 cycles.
- Calendar life: 15 years.

Accomplishments

- Exploited the concept of stabilizing composite ‘layered-layered’ structures with a spinel component to achieve electrode capacities approaching 200 mAh/g.
- Explored processing routes with Argonne’s Materials Engineering Research Facility (MERF) to advance the electrochemical properties of composite electrode structures fabricate electrode materials that would improve capacity, power, and cycle life.
- Designed surface structures to protect the underlying metal oxide particles from the electrolyte and to improve their rate capability when charged at high potentials.
- Initiated computational studies to simulate the structural and electrochemical properties of ‘layered-layered-spinel electrodes.

Introduction

Lithium- and manganese-rich $x\text{Li}_2\text{MnO}_3 \bullet (1-x)\text{LiMO}_2$ ($\text{M}=\text{Mn, Ni, Co}$) materials are currently the most promising class of cathodes for next-generation, high energy Li-ion batteries. However, the structural instability of these electrodes at high potentials, that involve both surface and bulk phenomena, has prevented their large-scale use in commercial systems. To advance the technology, more robust electrode structures and surfaces must be designed and fabricated.

Approach

- Advance the performance of high-capacity ‘layered-layered’ $x\text{Li}_2\text{MnO}_3 \bullet (1-x)\text{LiMO}_2$ ($\text{M}=\text{Mn, Ni, Co}$) electrodes by introducing a spinel component to stabilize the structure and minimize or eradicate the voltage-fade phenomenon.

Project Details

Michael Thackeray (Argonne National Lab, PI)
9700 South Cass Avenue
Argonne, IL 60439
Phone: 630-252-9184; Fax: 620-252-4176
E-mail: thackeray@anl.gov

Jason R. Croy (Argonne National Lab, Co-PI)
9700 South Cass Avenue
Argonne, IL 60439
Phone: 630-252-5917; Fax: 620-252-4176
E-mail: croy@anl.gov

Start Date: October 2011
Projected End Date: September 2015

- Explore processing routes in the laboratory and with Argonne's Materials Engineering Research Facility (MERF) to prepare 'layered-layered-spinel' composite electrode materials with acceptable capacity, power and cycle life.
- Design effective surface structures to protect the underlying metal oxide particles from the electrolyte and to improve their rate capability when charged at high potentials.
- Perform complementary computational studies to aid the compositional and structural design of composite electrode structures.

Results

'Layered-Layered-Spinel' (LLS) Electrodes

Recent studies have revealed that the integration of a small amount of spinel into 'layered-layered' (LL) $x\text{Li}_2\text{MnO}_3 \bullet (1-x)\text{LiMO}_2$ ($\text{M}=\text{Mn, Ni, Co}$) electrode structures by slightly reducing the lithium content improves their cycling stability, capacity, first cycle efficiency (FCE) and rate capability [1, 2]. For example, Figure V-75 shows that by reducing the lithium content in a parent $0.25\text{Li}_2\text{MnO}_3 \bullet 0.75\text{LiMn}_{0.375}\text{Ni}_{0.375}\text{Co}_{0.250}\text{O}_2$ electrode, represented by x in the normalized formula $\text{Li}_x\text{Mn}_{0.53}\text{Ni}_{0.28}\text{Co}_{0.19}\text{O}_8$, the capacity reaches a maximum at a targeted 6% spinel content, while the first-cycle efficiency increases continually as x decreases.

The 'layered-layered-spinel' phase space, which is vast and unexplored, offers new approaches for fabricating and designing high capacity cathode structures. Figure V-75(b) shows the first-cycle voltage profiles of a $\text{Li}/0.1\text{Li}_2\text{MnO}_3 \bullet 0.9\text{LiMn}_{0.4}\text{Ni}_{0.55}\text{Co}_{0.5}\text{O}_2$ (LL) half-cell (black profile) and cells with the same cathode after being treated with a cobalt-containing acidic solution to leach lithium from the structure. The cobalt-treated samples were subsequently annealed at 450°C (red profile) and 750°C (blue profile). It was apparent that during these processes cobalt was accommodated in the Li layers of the structure. The time and annealing temperature dictate the amount of cobalt in the Li layers of the final product, strategically yielding Co-based spinel-like regions. The first-cycle discharge reveals that annealing at 750°C results in a predominantly layered structure, whereas the sample annealed at 450°C shows a reaction between 3.6 and 3.3 V, consistent with the electrochemical behavior of a cobalt-rich spinel. Figure V-75 (c) shows the initial charge and discharge capacities of the three cells and their FCEs. The LLS electrode prepared at 450°C shows the highest FCE, consistent with the presence of a spinel component in the structure, and a capacity equivalent to the parent LL electrode.

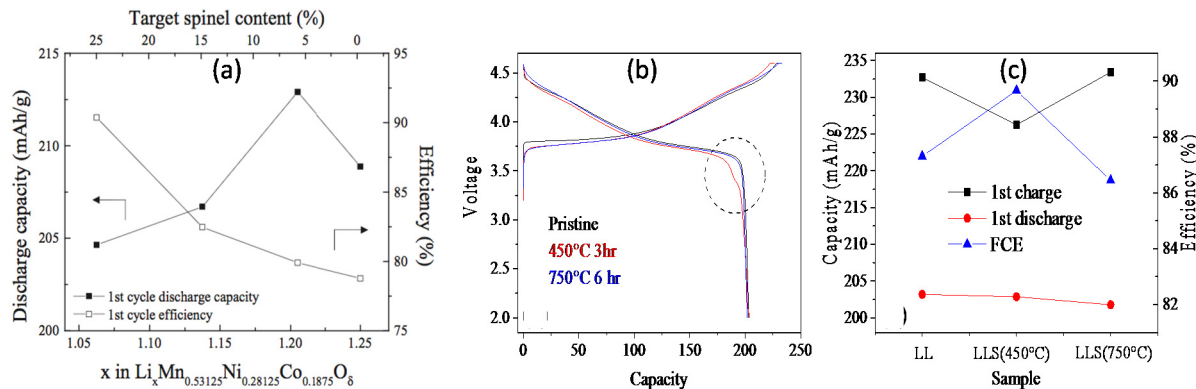


Figure V-75: (a) First cycle discharge capacity and efficiency as a function of x in a $\text{Li}_x\text{Mn}_{0.53}\text{Ni}_{0.28}\text{Co}_{0.19}\text{O}_8$ LLS electrode; (b) First-cycle charge and discharge profiles of cells with a $0.1\text{Li}_2\text{MnO}_3 \bullet 0.9\text{LiMn}_{0.4}\text{Ni}_{0.55}\text{Co}_{0.5}\text{O}_2$ cathode before (black) and after acid treatment and annealing at 450°C (red) and 750°C (blue); (c) First charge (black) and discharge (red) capacity and FCE (blue) of the cathodes in (b)

'Layered-Layered-Spinel' Electrodes Prepared by Argonne's Materials Engineering Research Facility (MERF)

LLS electrode materials prepared at a laboratory bench scale, typically <1g, that gave promising results were scaled to a 10g batch size at Argonne's Materials Engineering Research Facility (MERF). Laboratory scale materials were made from oxalate precursors as this approach provided the most reproducible results but led to products with a relatively low tap density (1.70 g/cc). Materials from MERF that showed the best results were synthesized from carbonate precursors. The electrochemical cycling stability and corresponding dQ/dV plots of a layered-layered-spinel electrode with normalized formula,

$\text{Li}_{1.063}\text{Ni}_{0.265}\text{Mn}_{0.542}\text{Co}_{0.193}\text{O}_y$, prepared from oxalate (bench) and carbonate (MERF) precursors are shown in Figure V- 76, left and right, respectively. The data clearly show the superior quality of the MERF

material prepared by industrial co-precipitation methods. Of particular significance is that the MERF LLS electrode shows little voltage fade when cycled between 4.45 and 2.0 V (average 3.64V) delivering 195 mAh/g at ~15 mA/g for 40 cycles, which corresponds to an energy density of 711 Wh/kg, based on the mass of the oxide electrode.

Surface Protection of 'Layered-Layered-Spinel' Electrodes: Substituted $\text{Li}_{3-2x}\text{Ni}_x\text{PO}_4$ Coatings

Aliovalent substitution of lithium by divalent cations such as Mg^{2+} , Al^{3+} and Ni^{2+} in Li_3PO_4 provides an opportunity to design stable, defect surface structures that may allow fast Li-ion transport at the electrode/electrolyte interface of Li-ion battery electrodes. A study of the structure-property relationships of several substituted Li_3PO_4 materials was therefore undertaken with a particular emphasis on the $\text{Li}_{3-2x}\text{Ni}_x\text{PO}_4$ system that has shown promise as a protective coating for lithium battery cathodes when charged to a high potential. The electrical conductivity of $\text{Li}_{3-2x}\text{Ni}_x\text{PO}_4$ samples was measured by electrochemical impedance spectroscopy. Figure V- 77(a) shows a linear Arrhenius relationship between 400 and 550 °C. The conductivity and activation energy (1.29 eV) values for undoped Li_3PO_4 were in good agreement with previous reports. Electrical conductivities of 1% and 2% Ni doped samples were enhanced, while activation energies for lithium-ion diffusion were reduced, suggesting that the generation of small number of defects enhances lithium ion transport. Room temperature electrical conductivities were extrapolated from the Arrhenius plots; $\text{Li}_{2.98}\text{Ni}_{0.01}\text{PO}_4$ (1% doping), in particular, showed an enhancement in conductivity of almost an order of magnitude (Figure V- 77 (b)). Figure V- 77 (c) emphasizes the improved rate capability of a standard LiCoO_2 electrode when surface-treated with $\text{Li}_{3-2x}\text{Ni}_x\text{PO}_4$ using a low Ni content (1 and 2% Ni).

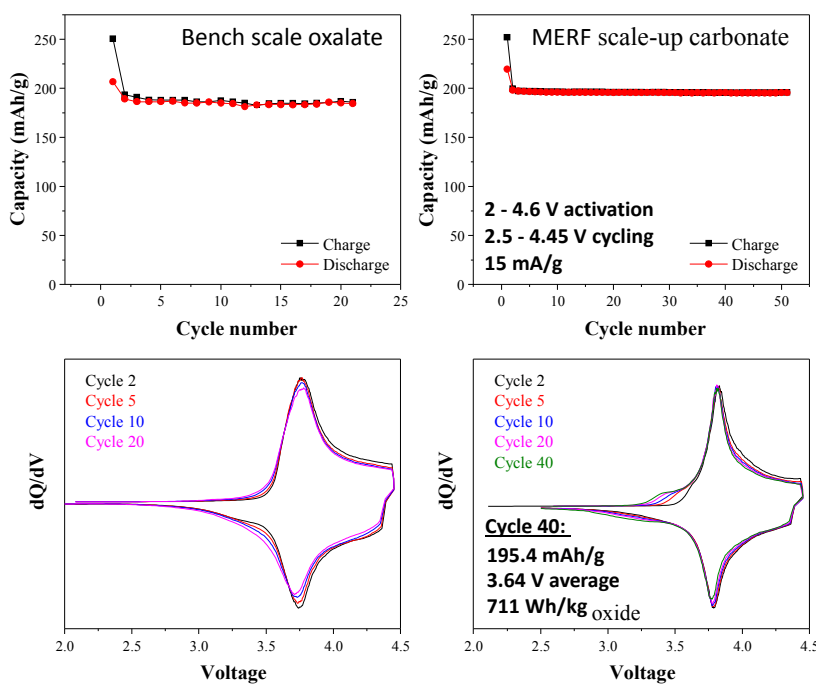


Figure V- 76: A comparison of the electrochemical cycling behavior of a LLS electrode with normalized formula $\text{Li}_{1.063}\text{Ni}_{0.265}\text{Mn}_{0.542}\text{Co}_{0.193}\text{O}_y$, (left) laboratory bench scale; and (right) scaled at Argonne's processing facility, MERF

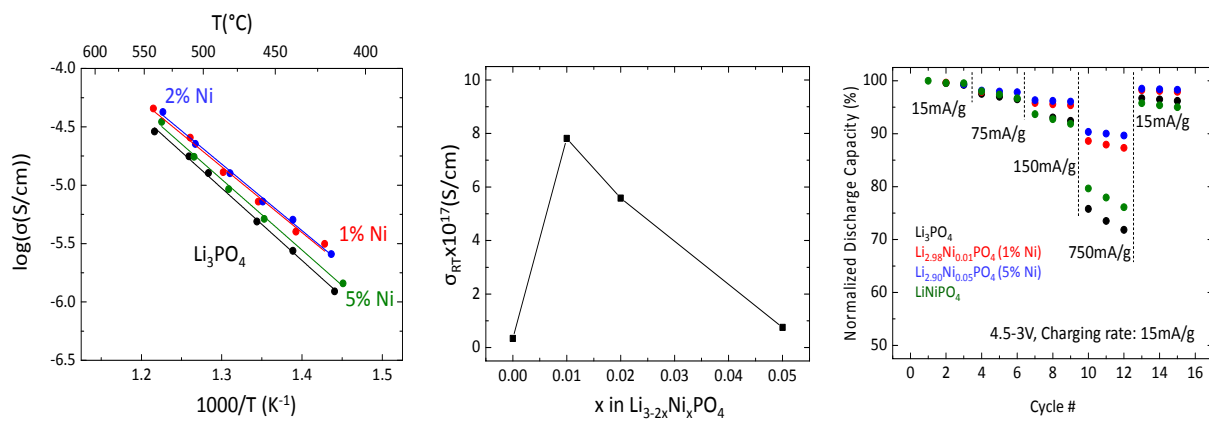


Figure V-77: (a) Arrhenius plots, and (b) conductivity vs. composition plots of substituted Li_{3-2x}Ni_xPO₄ coating materials; (c) capacity vs. cycle number plots of Li_{3-2x}Ni_xPO₄-coated LiCoO₂ electrodes at various current rates

References

1. B. R. Long, J. R. Croy, J. S. Park, J. Wen, D. J. Miller and M. M. Thackeray, *J. Electrochem. Soc.*, **161**, A2160 (2014).
2. D. Kim, G. Sandi, J. R. Croy, K. G. Gallagher, S.-H. Kang, E. Lee, M. D. Slater, C. S. Johnson and M. M. Thackeray, *J. Electrochem. Soc.* **160**, A31-A38 (2013).

Conclusions and Future Directions

'Layered-layered-spinel' (LLS) electrodes show promise for stabilizing high capacity (>200 mAh/g) 'layered-layered' electrodes, arresting voltage fade and improving rate capability. This class of electrode materials provides a vast compositional and phase space to be explored. The project is receiving the interest of industry and will be vigorously pursued in FY2016. In particular, efforts will be continued to exploit the possibility of using cobalt and nickel spinel configurations to stabilize NMC layered structures at low lithium loadings. Computational modeling studies of layered-spinel systems have been instigated to complement experimental findings and to aid and advance the structural and compositional design of these novel cathode materials.

FY 2015 Patents/Publications/Presentations

Patent Applications

1. "Cobalt-Stabilized Lithium Metal Oxide Electrodes for Lithium Batteries", M. M. Thackeray, J. R. Croy and B. R. Long, U.S. Pat. Appl. 20150180032, 25, June 2015.
2. "Metal Fluoride Passivation Coatings Prepared by Atomic Layer Deposition for Li-Ion Batteries", A. U. Mane, J. S. Park, J. R. Croy, J. W. Elam, Filed at USPTO (2015).

Publications

1. "Amorphous Metal Fluoride Passivation Coatings Prepared by Atomic Layer Deposition on LiCoO₂ for Li-Ion Batteries", J. S. Park, A. U. Mane, J. W. Elam, J. R. Croy, *Chem Mater.*, **27** (6), 117 (2015).
2. "Advances in Stabilizing 'Layered-Layered' xLi₂MnO₃•(1-x)LiMO₂ (M=Mn, Ni, Co) Electrodes with a Spinel Component", Brandon R. Long, Jason R. Croy, Joong Sun Park, Jianguo Wen, Dean J. Miller, and Michael M. Thackeray, *J. Electrochem. Soc.*, **161**, A2160 (2014).
3. "Effect of Cooling Rates on Phase Separation in 0.5Li₂MnO₃•0.5LiCoO₂ Electrode Materials for Li-Ion Batteries", B. R. Long, J. R. Croy, F. Dogan, M. R. Suchomel, B. Key, J. G. Wen, D. J. Miller, M. M. Thackeray and M. Balasubramanian, *Chem. Mater.*, **26**, 3565–3572 (2014).

Presentations (6 of 12 provided)

1. "Electrical Energy Storage: Looking Back – Looking Forward", M. M. Thackeray, STFC Global Challenge Network in Batteries and Electrochemical Energy Devices, Abingdon, UK, 30 June – 1 July 2015.
2. "Ultrathin Metal Fluoride Coatings for High Energy Li-Ion Batteries", J. S. Park, A. U. Mane, J. W. Elam, J. R. Croy, MRS Meeting, San Francisco, 6 – 10 April, 2015.
3. "Progress and Challenges in Designing High Capacity Cathodes for Lithium-Ion Cells", M. M. Thackeray, B. R. Long, J. R. Croy, J. S. Park, Y. Shin, G. Krumdick, J. G. Wen and D. Miller, 32nd Annual Battery Seminar & Exhibit, Fort Lauderdale, Florida, 9-12 March 2015.
4. "The Road to Viable Electrical Energy Storage: Challenges and Opportunities in an Evolving Lithium Economy", M. M. Thackeray, IV Congress of the Future – The Crossroads of the XXI Century, Santiago, Chile, 15-17 January 2015.
5. "High-Energy Cathode Research at Argonne National Laboratory", Jason R. Croy, M. Balasubramanian, B.R. Long, J.S. Park, A. Mane, J. Elam, D. Miller, J.G. Wen, M. Suchomel, F. Dogan, B. Key, and M.M. Thackeray, IBA Meeting, Waikoloa Village, Hawaii, 5-9 January 2015.
6. "Designing Advanced High Capacity Electrodes for Lithium Cells", M. M. Thackeray, J. R. Croy, B. R. Long, J. S. Park, C. S. Johnson, L. Trahey, Z. Yang, Y. Ren, D. J. Miller, J. G. Wen, A. Kinaci, M. K. Y. Chan, S. Kirklin and C. Wolverton, MRS Meeting, Boston, 30 November - 5 December, 2014.

V.D.6 Novel Cathode Materials for High-Energy Lithium Batteries (UTA)

Objectives

- Develop high-performance cathodes for lithium-ion batteries and gain a fundamental understanding of their structure-composition-performance relationships.
- Develop a fundamental understanding of the impact of aliovalent doping of V³⁺ and Ti⁴⁺ to improve the performance of polyanion cathodes.
- Develop novel synthesis approaches for phosphate polyanion cathodes that can offer the reversible insertion/extraction of more than one lithium ion per transition-metal ion.

Project Details

Tien Duong (Program Manager-BMR)
Arumugam Manthiram (UT-Austin-PI)
204 E. Dean Keeton Street, Mail Stop C2200
Austin, TX 78712
Phone: 512-471-7394; Fax: 512-475-8482
E-mail: manth@austin.utexas.edu

Collaborators
Craig Bridges (ORNL)

Start Date: January 2012
Projected End Date: December 2015

Technical Barriers

Focusing on the cathode materials, this project addresses the following technical barriers in order for lithium-ion batteries to be employed for vehicle applications: cost, safety, cycle life, energy, and power.

Technical Targets

- Realize high capacity through the reversible insertion/extraction of more than one lithium per transition-metal ion in polyanion cathodes.
- Develop nanostructured polyanion cathodes to overcome the poor ionic and electrical conductivities.
- Develop a fundamental understanding of aliovalent substitutions on the electrochemical performances of polyanion cathodes.

Accomplishments

- Synthesized three polymorphs of LiCoPO₄ and showed their formation dependence on the presence of water during microwave solvothermal (MW-ST) synthesis.
- Synthesized LiCoPO₄ (*Cmcm*) and LiNiPO₄ (*Cmcm*) for the first time at low pressure and LiMnPO₄ (*Cmcm*) for the first time ever.
- Demonstrated that α -LiVOPO₄/PEDOT prepared with a 3-dimensional ordered macroporous (3-DOM) carbon as a hard-template has a capacity of 212 mAh/g.
- Synthesized α -LiVOPO₄ (triclinic) and β -LiVOPO₄ (orthorhombic) /graphene nanocomposites by the MW-ST approach with low-cost solvents of water and ethanol.
- Demonstrated VO₂/rGO nanorods as a potential anode for sodium- and lithium-ion batteries.
- Investigated aliovalent substitution of Ti⁴⁺ for Fe²⁺ in lithium iron phosphate to produce LiFe_{1-2x}Ti_x□_xPO₄.
- Investigated substitution of vanadium for iron in LiFeP₂O₇ and developed a novel low-temperature synthesis method for LiFeP₂O₇.

Introduction

Cost, safety, energy, and power are the major issues that hamper the adoption of lithium-ion technology for vehicle applications. Accordingly, this project focuses on the design and development of high-energy, low-cost, safer polyanion cathodes by addressing the poor electronic and ionic transport in phosphate cathodes. For example, we have shown aliovalent substitution of V³⁺ in LiMPO₄ (M = Mn and Co) enhances the

electrochemical performance. Similarly, novel low-temperature synthesis approaches are able to control the particle-size/morphology, which often enhance the electrochemical utilization and capacity. Accordingly, this project continued to focus on low-temperature synthesis approaches for polyanion phosphate cathodes.

Approach

Most of the phosphate cathodes, such as LiMnPO₄, LiCoPO₄, and LiVOPO₄, suffer from low electronic and ionic conductivities. Accordingly, synthesis and processing conditions play a critical role in realizing the full capacities of these polyanion cathodes. For instance, novel solution-based approaches such as microwave-assisted solvothermal (MW-ST) and template-assisted methods are pursued to control morphologies and particle size to maximize the electrochemical performances. Additionally, the low-temperature microwave synthesis enables high levels of aliovalent substitutions and access to novel polymorphs that are otherwise inaccessible. Finally, template-assisted synthesis is employed to control the particle size and morphology. Synthesized samples are characterized by a variety of techniques including X-ray diffraction (XRD), electron microscopy (SEM, TEM, and STEM), X-ray adsorption spectroscopy (XPS), Fourier transform infrared spectroscopy (FTIR), and in-depth electrochemical measurements. Based on the characterization data gathered, a fundamental understanding of the structure-composition-property-performance relationships is developed, which is then utilized to design better-performing cathodes.

Results

Three Polymorphs of LiCoPO₄

Many investigations have been carried out in the literature on LiMPO₄ (M = Fe, Mn, Co, Ni), but a majority of these were restricted to the olivine polymorph with the *Pnma* space group.

Three orthorhombic polymorphs of LiCoPO₄ belonging to the space groups *Pnma*, *Pn₂1a*, and *Cmcm* have been synthesized with a microwave-assisted solvothermal (MW-ST) synthesis method at a temperature of 260 °C. The XRD patterns and SEM micrographs of the three polymorphs are shown in Figure V- 78.

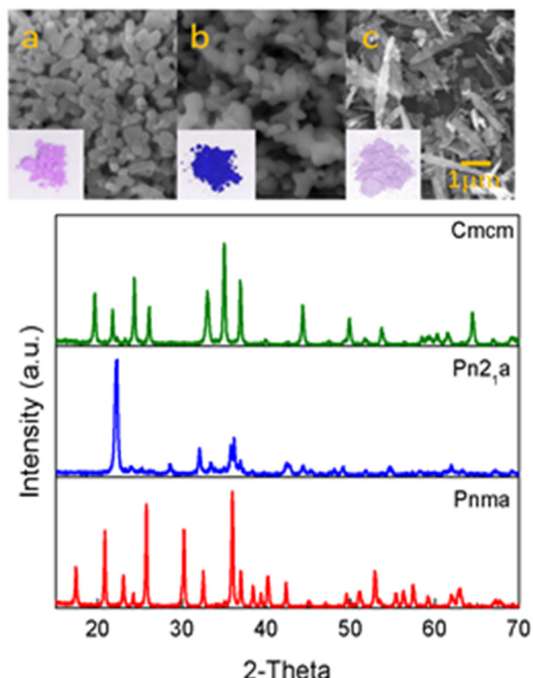


Figure V- 78: SEM of (a) *Pnma*, (b) *Pn₂1a*, and (c) *Cmcm* polymorphs of LiCoPO₄ and corresponding XRD patterns

The production of each of the polymorphs was highly sensitive to the presence of small amounts of water in the solvent, tetraethylene glycol (TEG). The use of anhydrous phosphoric acid and dry TEG during synthesis results in the formation of > 99% *Cmcm* polymorph by weight. The introduction of 2% water by volume results in ~ 22% *Pnma* and 78% *Cmcm* phases by weight. The dependence of the formation of the different *Cmcm* polymorph and *Pnma* polymorph on the presence of water is shown in Figure V- 79.

Our group reported the electrochemical properties of the *Cmcm* polymorph and nano-sized *Pn₂1a* polymorph, shown in Figure V- 80, for the first time. The lithium extraction reaction with the LiCoPO₄ (*Cmcm*) polymorph is presented for the first time, but it is not reversible. The LiCoPO₄ (*Pn₂1a*) polymorph could be a promising candidate for future research due to the high theoretical specific energy capacity and demonstrated electrochemical activity. The water sensitivity of the phases generated has subsequently been shown to translate to the MW-ST synthesis of other LiMPO₄ materials.

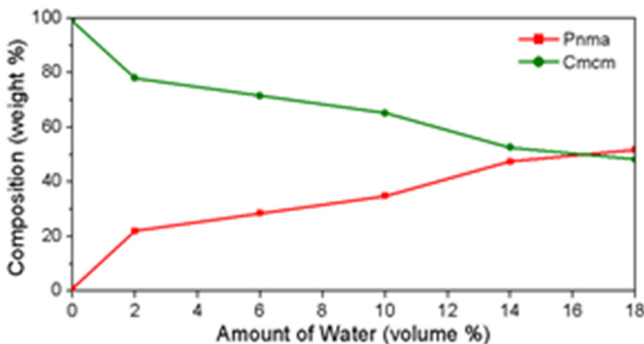


Figure V- 79: SEM of (a) *Pnma*, (b) *Pn₂a*, and (c) *Cmcm* polymorphs of LiCoPO_4 and corresponding XRD patterns

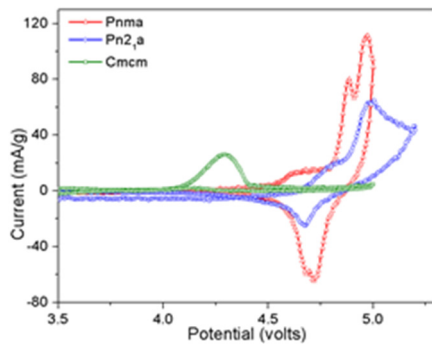


Figure V- 80: Cyclic voltammetry of the three LiCoPO_4 polymorphs

Synthesis of *Cmcm* polymorphs of LiMPO_4

A facile MW-ST synthesis of the *Cmcm* polymorph of all four members of the LiMPO_4 family, *i.e.*, with $\text{M} = \text{Mn, Fe, Co, and Ni}$, has been demonstrated. Unlike many previous studies, our synthesis was carried out at low temperatures ($< 300^\circ\text{C}$) and low pressures (< 30 bar). The protocol did not require the use of special solvents or preparation of the reaction mixture inside a controlled environment, for example, a glove box. The LiMnPO_4 (*Cmcm*) polymorph has been reported for the first time, and the low pressure synthesis of the LiNiPO_4 (*Cmcm*) polymorph has also been reported for the first time.

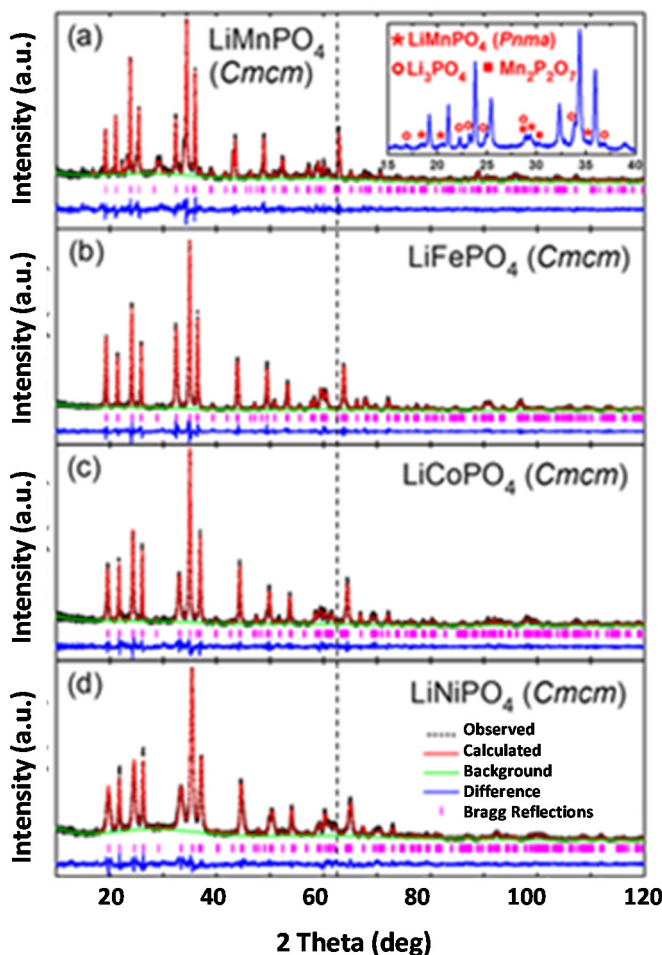


Figure V- 81: XRD patterns of LiMPO_4 (*Cmcm*) with $\text{M} = \text{Mn, Fe, Co, and Ni}$

The XRD patterns of the four *Cmcm* polymorphs are shown in Figure V- 81. Similar to the CV reports in the literature, the LiFePO_4 (*Cmcm*) polymorph shows reversible electrochemical activity at ~ 3.0 V, but the capacity is very small compared to that of the LiFePO_4 (*Pnma*) polymorph. LiMnPO_4 (*Cmcm*), LiCoPO_4 (*Cmcm*), and LiNiPO_4 (*Cmcm*) show, respectively, only a charging peak at 4.2, 4.2, and 4.3 V, but do not show any discharge peak. For $\text{M} = \text{Co and Ni}$, the cathodes were analyzed with *ex-situ* XRD after charging. No evidence was found for peak shifting or structural changes and the XRD patterns matched well with those of the as-synthesized powders. The exact cause of the charging peaks is unknown but could be an irreversible side reaction with the electrolyte. Overall, the *Cmcm* polymorphs perform poorly as cathodes in lithium-ion cells, which may be due to the smaller diffusion pathways in the *Cmcm* polymorph compared to that in the *Pnma* polymorph, caused by the tetrahedral coordination of the lithium ions.

Synthesis of LiVOPO_4 with a hard carbon template

LiVOPO_4 nanoparticles were synthesized by employing a 3-dimensional ordered macroporous (3-DOM) carbon as a hard-

template. The 3-DOM carbon was synthesized with poly(methyl methacrylate) (PMMA) colloidal crystals as the template and glucose as the carbon source, which were fired together at 600°C in argon. LiVOPO₄ was fabricated via a sol-gel process in the presence of the 3-DOM template, followed by firing at 600 °C in argon and air in sequence. The SEM images, Figure V- 82, show that the PMMA crystals are comprised of closed-packed nanospheres, while the 3-DOM carbon has a reverse structure of the PMMA with ordered macropores. The LiVOPO₄ templated from the 3-DOM has a mean particle size of ~ 300 nm due to the confinement by the template. The carbon template was not detected after the sintering process in air.

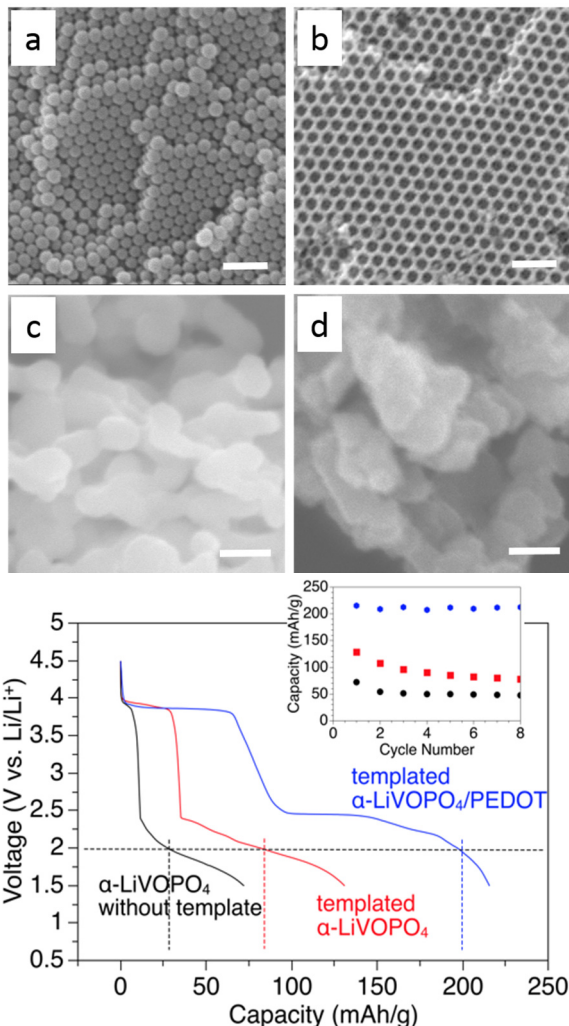


Figure V- 82: SEM images of (a) PMMA colloidal crystal, (b) 3-DOM carbon, (c) α -LiVOPO₄, and (d) α -LiVOPO₄/PEDOT composite. The scale bars in (a, b) and (c) are 1 μ m and 500 nm, respectively. The first discharge curves and cycling performances of three α -LiVOPO₄ samples are also shown

LiVOPO₄/PEDOT cathode shows a high capacity of 212 mAh/g during first discharge, equivalent to the insertion of ~ 1.35 Li per vanadium ion (Figure V- 82). In contrast, the α -LiVOPO₄ prepared without the template and PEDOT coating has a much lower capacity of 70 mAh/g, while the templated α -LiVOPO₄ without PEDOT coating offers a moderate capacity of 140 mAh/g. Additionally, the α -LiVOPO₄/PEDOT exhibits much more improved cycling performance than the other two samples (see the inset in Figure V- 82). These results clearly demonstrate the importance of structural optimization for the LiVOPO₄ cathodes that suffer from low electrical and ionic conductivities.

α -LiVOPO₄ and β -LiVOPO₄ graphene composites

Our previous work on the layered α_1 -LiVOPO₄ (tetragonal) demonstrated the importance of incorporating graphene nano-sheets to enhance the electrical conductivity of the cathodes. This strategy was extended to α -LiVOPO₄ (triclinic) and β -LiVOPO₄ (orthorhombic) by the microwave-assisted solvothermal (MW-ST) method. The bare triclinic α -LiVOPO₄ without graphene was first synthesized via a MW-ST process reported by us before at 230 °C in water/ethanol medium. The α -LiVOPO₄/graphene nanocomposite was then synthesized by the same procedure with the addition of different amounts of graphene oxide (GO) to the

reaction mixture. During the MW-ST process, GO is reduced to graphene. XRD data indicated that phase-pure α -LiVOPO₄ in the composite could be obtained only when the GO concentration is $< 0.4 \text{ mg mL}^{-1}$ in the reaction mixture, which resulted in a rather low graphene content of $< 3 \text{ wt.\%}$ in the α -LiVOPO₄/graphene nanocomposite.

This result differs from that of the tetragonal α_1 -LiVOPO₄/graphene system, where a graphene content of up to 10 wt. % could be realized. On the other hand, no phase-pure β -LiVOPO₄ could be formed at all in the presence of GO. Optimization of the synthesis conditions, such as increasing the reaction temperatures/pressures or varying the water/ethanol ratios, was not successful. These results imply that the known conditions to prepare pure phases of bare α - and β -LiVOPO₄ are not suitable when GO is present. The incorporation of graphene in the α -LiVOPO₄/graphene (3 wt. %) sample was confirmed by SEM, Figure V- 83a, in which LiVOPO₄ spheres are partially wrapped by graphene sheets. This composite cathode shows a high initial discharge capacity of 210 mA h g⁻¹ at C/20 rate (Figure V- 83b), but with some capacity fade.

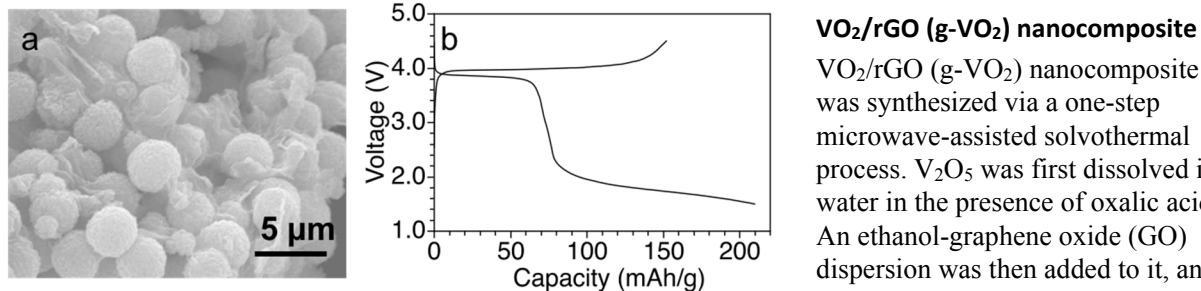


Figure V- 83: (a) SEM image of the α -LiVOPO₄/graphene nanocomposite ($\sim 3 \text{ wt. \%}$ graphene) and (b) its first charge-discharge profiles at C/20 rate

VO₂/rGO (g-VO₂) nanocomposite

VO₂/rGO (g-VO₂) nanocomposite was synthesized via a one-step microwave-assisted solvothermal process. V₂O₅ was first dissolved in water in the presence of oxalic acid. An ethanol-graphene oxide (GO) dispersion was then added to it, and the mixture was sealed and loaded into a rotator for microwave reaction. X-ray diffraction (XRD)

pattern (Figure V- 84a) of the black powder obtained showed good crystallinity without any post heat-treatment, and the diffraction peaks could be indexed to the monoclinic C₂/m VO₂ (B) with cell parameters of $a = 12.07 \text{ \AA}$, $b = 3.71 \text{ \AA}$, $c = 6.43 \text{ \AA}$, and $\beta = 107.0^\circ$.

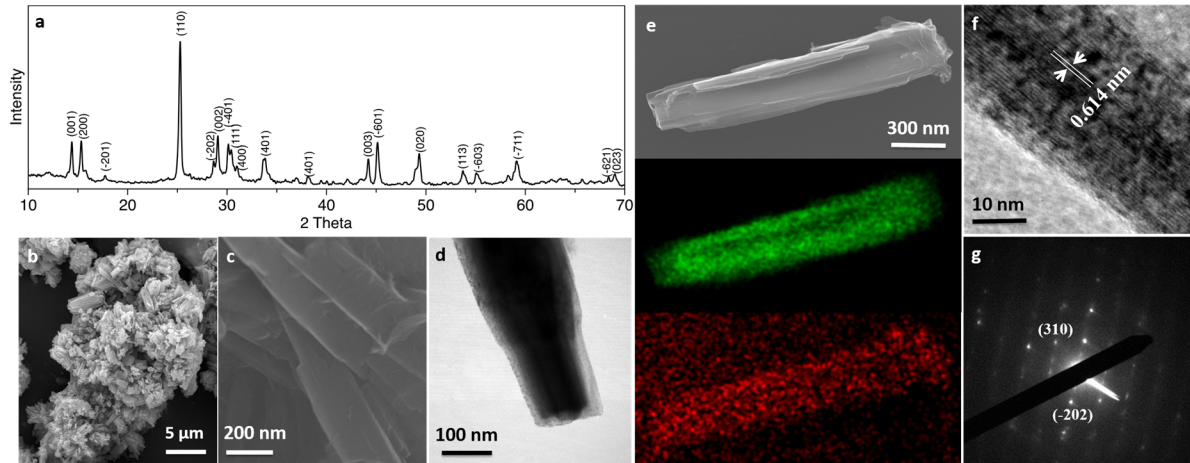


Figure V- 84: Structural analysis of the as-prepared g-VO₂ nanocomposite by microwave-assisted solvothermal method: (a) powder XRD pattern; (b, c) low- and high-magnification SEM images showing a secondary g-VO₂ particle and the detailed VO₂ nanorods and rGO nanosheets; (d) STEM image showing the encapsulation of an individual VO₂ (B) rod by rGO layers; (e) elemental mapping of an individual g-VO₂ nanorod showing the different distribution area of V and C; and (f, g) HR-TEM image and the SAED pattern of a small VO₂ (B) nanorod with good crystallinity

The morphology of the as-prepared sample was examined with high-resolution FE-SEM, STEM, and high-resolution TEM. As shown in Figure V- 84b-d, the VO₂ (B) has a short-nanorod morphology with a mean diameter and length of 200 – 300 nm and 1 – 2 μm , respectively. The VO₂ (B) nanorods are encapsulated by thin layers of rGO, as evidenced in the SEM and STEM images (Figure V- 84c, d). Additionally, elemental maps of an individual nanorod (Figure V- 84e) displays a smaller distribution area for vanadium than for carbon, further confirming the unique structure. A typical HR-TEM image and the corresponding selected-area electron diffraction (SAED) pattern of a small nanorod in Figure V- 84f and 7g suggest single-crystalline

structure of the VO₂ (B). The lattice fringes with a spacing of ~ 0.614 nm are clearly discernable, corresponding to the (001) planes (Figure V- 84f).

The g-VO₂ electrodes were first evaluated in the regular potential window above 1.0 V. Figure V- 85a shows the charge-discharge profiles on various cycles obtained at 100 mA g⁻¹ between 3.3 and 1.5 V. All discharge curves display a slightly sloping plateau from 2.7 to 2.5 V, followed by a well-defined flat plateau at 2.4 V. The initial discharge capacity is 175 mAh g⁻¹, corresponding to the insertion of 0.55 lithium ions per formula unit into the structure. The capacity drops to 162 mAh g⁻¹ on the second cycle, but it then becomes extremely stable over 200 cycles as shown in Figure V- 85b. In contrast, the pristine VO₂ (B) electrode without any rGO exhibits lower initial capacity and relatively fast capacity fade.

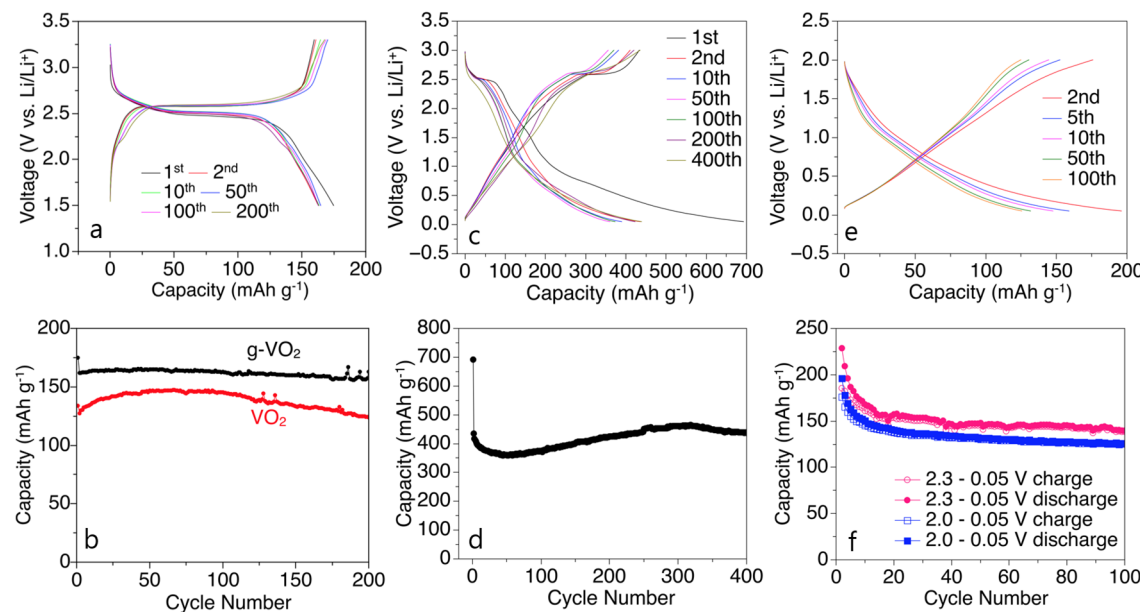


Figure V- 85: Voltage-capacity profiles (a, c, e) and cycling performance (b, d, f) at different voltage windows: (a, b) 3.3 – 1.5 V; (c, d) 3.0 – 0.05 V; (e) 2.0 – 0.05 V; (f) 2.0 – 0.05 V and 2.3 – 0.05 V

The high reversible capacities and stable cycling of the g-VO₂ in the regular window suggest that it is suitable for further studies at lower potentials. In order to avoid any influence from aluminum foils below 1.0 V (vs. Li/Li⁺), copper foils were selected for the cells evaluated at low potentials. As shown in Figure V- 85c , the cell exhibits similar flat plateaus on the initial charge-discharge profiles like in Figure V- 85a, but a large slope is present at the low potential regions on discharge. The total discharge and charge capacities are, respectively, 692 and 433 mAh g⁻¹ at the current density of 100 mA g⁻¹. The large irreversible capacity on the 1st cycle, which has been reported with various anodes, is attributed to the formation of a solid-electrolyte interphase (SEI) at lower potentials. The cell demonstrates stable cycling performance over 400 cycles with an average capacity of ~ 400 mAh g⁻¹ (Figure V- 85d) from the 2nd cycle. The electrochemical performance and XRD patterns of the g-VO₂ suggest that Li-ion intercalation is probably the dominant reaction even at a low discharge potential of 0.05 V.

Conclusions and Future Directions

The dependence of the formation of LiMPO₄ (*Cmcm*) on water during the MW-ST synthesis process has been demonstrated (M = Fe, Mn, Co, and Ni). The electrochemistry of the LiMnPO₄, LiCoPO₄, and LiNiPO₄ *Cmcm* polymorphs were investigated for the first time. Additionally, the reversible extraction of more-than-one lithium per transition-metal ion was demonstrated with α -LiVOPO₄ by employing novel microwave-assisted synthesis and hard-template approaches to control the particle size and morphology.

Our future work will focus on (i) further optimization of the LiVOPO₄ cathodes by microwave and template-assisted approaches, (ii) attempts to enhance the electrochemical properties of non-olivine structures of LiMPO₄ materials, and (iii) continuing the investigation of the substitution of vanadium for M in the LiMP₂O₇ materials.

FY 2015 Publications/Presentations

Publications

1. X. Xiang, J. C. Knight, W. Li, and A. Manthiram, "Understanding the Influence of Composition and Synthesis Temperature on Oxygen Loss, Reversible Capacity, and Electrochemical Behavior of $x\text{Li}_2\text{MnO}_3-(1-x)\text{LiCoO}_2$ Cathodes in the First Cycle," *Journal of Physical Chemistry C* **118**, 23553-23558 (2014).
2. J. C. Knight, P. Nandakumar, and A. Manthiram, "Effect of Ru Substitution on the First Charge-Discharge Cycle of Lithium-rich Layered Oxides," *Journal of Materials Chemistry A* **3**, 2006-2011 (2015).
3. X. Xiang, J. C. Knight, W. Li, and A. Manthiram, "Sensitivity and Intricacy of Cationic Substitutions on the First Charge/Discharge Cycle of Lithium-rich Layered Oxide Cathodes," *Journal of the Electrochemical Society* **162**, A1662-A1666 (2015).
4. G. He, L. Li, and A. Manthiram, "VO₂/rGO Nanorods as a Potential Anode for Sodium- and Lithium-ion Batteries," *Journal of Materials Chemistry A* **3**, 14750-14758 (2015).
5. K. J. Kreder III, G. Assat, and A. Manthiram, "Microwave-assisted Solvothermal Synthesis of Three Polymorphs of LiCoPO₄ and Their Electrochemical Properties," *Chemistry of Materials* **27**, 5543-5549 (2015).
6. G. He, C. A. Bridges, and A. Manthiram, "Crystal Chemistry of Electrochemically and Chemically Lithiated Layered $\alpha_1\text{-LiVOPO}_4$," *Chemistry of Materials* DOI: 10.1021/acs.chemmater.5b02609 (2015).
7. J. C. Knight and A. Manthiram, "Effect of Nickel Oxidation State on the Structural and Electrochemical Characteristics of Lithium-rich Layered Oxide Cathodes," *Journal of Materials Chemistry A* DOI: 10.1039/C5TA05703E (2015).
8. G. Assat and A. Manthiram, "Rapid Microwave-assisted Solvothermal Synthesis of Non-olivine Cmcm Polymorphs of LiMPO₄ (M = Mn, Fe, Co, and Ni) at Low Temperature and Pressure," *Inorganic Chemistry* DOI: 10.1021/acs.inorgchem.5b01787 (2015).
9. G. He, W. H. Kan, and A. Manthiram, "A 3.4 V Layered VOPO₄ Cathode for Na-ion Batteries," *Chemistry of Materials* (submitted).

Presentations

1. A. Manthiram, "Next Generation Rechargeable Battery Chemistries," 2014 Global Innovation Festival, Daegu Gyeongbuk Institute of Science and Technology, Daegu, South Korea, November 20 – 21, 2014 (invited).
2. A. Manthiram, "Next Generation Rechargeable Battery Chemistries," Institute of Chemistry, Beijing, China, June 1, 2015.
3. A. Manthiram, "High-voltage, High-capacity Polyanion Cathodes," 2015 Annual Merit Review Meeting of the Office of Vehicle Technologies, U.S. Department of Energy, Washington, D.C., June 8 – 12, 2015.

V.D.7 Lithium-Bearing Mixed Polyanion Glasses as Cathode Materials (ORNL)

Objectives

- Synthesize mixed polyanion glasses for use as active cathode materials in lithium ion batteries.
- Demonstrate enhanced electrochemical performance and physical properties by tailoring the polyanion content.
- Produce mixed polyanion glasses that undergo multi-valent transitions in the transition metal cations during electrochemical testing.
- Through laboratory-scale testing, demonstrate novel glasses with excellent overall cathode performance that are viable replacements for current cathode materials in electric vehicle applications.

Project Details

Jim Kiggans

Oak Ridge National Laboratory
P.O. Box 2008; MS 6087
Oak Ridge, TN 37831-6087
Phone: 865-574-8863; Fax: 865-574-4357
E-mail: kiggansjojr@ornl.gov

Andrew Kercher

Oak Ridge National Laboratory
P.O. Box 2008; MS 6124
Oak Ridge, TN 37831-6124
Phone: 865-576-5252; Fax: 865-574-4357
E-mail: kercherak@ornl.gov

Start Date: June 2012

Projected End Date: June 2016

Technical Barriers

- Mixed polyanion glasses are being developed to address the following key technical barriers for lithium ion battery cathodes: low energy density, poor high power performance, inadequate cycle life, safety, and high cost.

Technical Targets

- Produce a glass cathode with significantly greater capacity at high discharge rates than crystalline LiFePO₄.
- Develop a glass cathode material with at least 25% greater specific capacity than LiFePO₄.
- Demonstrate multi-valent glass cathodes with specific capacities exceeding 200 mAh/g.

Accomplishments

- Glass-state conversion (GSC) reactions in several metaphosphate/vanadate glasses demonstrated high capacity, large voltage hysteresis, and substantial capacity fade.
- Ex-situ electron microscopy and energy dispersive x-ray spectroscopy of nickel metaphosphate/vanadate cathodes at key states of charge indicated the formation of very fine nickel nanoparticles dispersed throughout intact glass particles as a result of the first cycle of a GSC reaction.
- Molybdate substitution was shown to be an environmentally friendlier alternative to vanadate substitution to produce electrochemically active mixed polyanion glass cathodes.
- Mixed polyanion glasses designed to have improved ionic diffusivity have been produced and may demonstrate reduced voltage hysteresis.
- Initial electrochemical testing of borate and borate/vanadate glass cathodes has provided mixed results.

Introduction

Polyanionic crystalline materials, such as LiFePO₄, are promising cathode materials for lithium ion batteries for electric vehicle applications, because they can have excellent safety and cycling performance due to their rigid covalently bonded structure. However, many polyanionic crystalline materials with theoretically excellent energy densities, such as LiCoPO₄, LiFeBO₃, and Li₂MnSiO₄, have not performed well as cathodes due to low electrical conductivity and/or crystal structure changes during cycling. Oak Ridge National Laboratory has

proposed that mixed polyanion (MP) glasses can be excellent high capacity cathodes that can overcome the limitations of similar polyanionic crystalline materials.

Mixed polyanion glasses have three key advantages over similar polyanionic crystalline materials. First, with the proper choice of polyanion content, MP glasses can have higher electrical conductivities than similar polyanionic crystalline materials. For example, substitutions of molybdate or vanadate for phosphate in iron phosphate glasses have demonstrated increases in electrical conductivity by orders of magnitude. Second, the disordered covalently bonded structure of MP glasses limits the ability of the structure to rearrange, which holds the promise to prevent undesirable microstructural rearrangement during cycling. Third, the glass polyanion content can be tailored to produce cathodes with a maximized redox potential for a given electrolyte system. Changing the polyanion content of a polyanionic cathode material has been shown to change the redox potential due to the inductive effect of the polyanion (Isono, et al., J. Power Sources, 2010, 195: 593-598). Depending on the amount and electronegativity of the polyanion substituted in the glass, the voltage of a glass cathode could be increased or decreased to the desired optimal voltage.

Most polyanionic crystalline materials under consideration as lithium ion battery cathodes are phosphates, borates, or silicates. Phosphates, borates and silicates are renowned glass formers using conventional glass processing methods. Therefore, producing these novel glass cathode materials will not likely require exotic processing methods, but could be produced by low-cost conventional glass processing methods.

Approach

The research into mixed polyanion glass cathode materials involves: (1) computational thermodynamic modeling, (2) glass processing, (3) glass structure & property characterization, and (4) electrochemical testing. Computational thermodynamic modeling of the electrochemical response of prospective glasses is being used to make decisions on the most promising glasses to pursue. Classical heat/quench glass processing has been the primary processing method. Characterization techniques are being used to confirm amorphous structure, to determine transition metal valences, and to measure fundamental glass properties. Electrochemical testing is being performed on coin cells with powdered glass cathodes produced by conventional slurry casting.

Results

Glass-state conversion reactions: cycling performance & microstructural changes

Glass-state conversion (GSC) reactions were unexpectedly found in polyanion glasses in FY2013 of this project. Conversion reactions are well understood in oxide and halide materials and are renowned for a high capacity, low-to-moderate voltages, large voltage hysteresis, and capacity fade. With their amorphous covalently bonded framework that permits wide compositional variation, glasses would not necessarily be expected to have the same electrochemical performance or microstructural changes of a typical conversion cathode.

Cycling tests were performed on cobalt-, nickel-, and silver-bearing metaphosphate/vanadate glasses to obtain a generalized understanding of the capacity fade and voltage hysteresis of GSC reactions (Figure V- 86). Each glass cathode demonstrated first cycle irreversible loss, which has been found by XANES to be associated with electrochemical reduction of V^{5+} to V^{4+} . The subsequent steady capacity fade over tens of cycles was similar to the capacity fade observed in typical conversion cathodes. Although the voltage hysteresis was lower than many typical conversion cathodes, the voltage hysteresis of the GSC reactions was still quite large and progressively worsened during cycling.

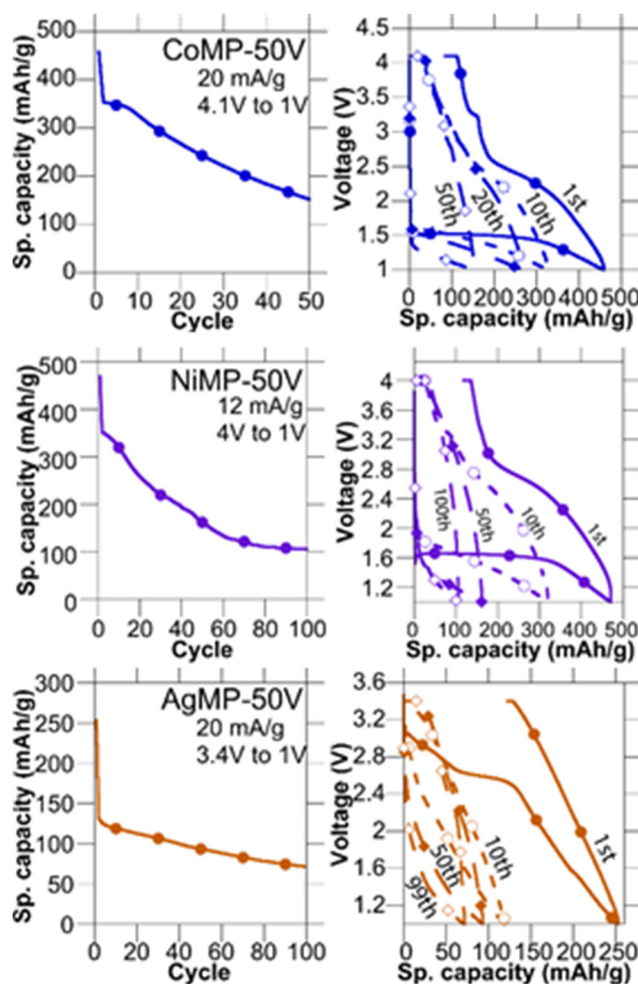


Figure V- 86: Capacity fade and voltage hysteresis were evident in cycle testing of cobalt-, nickel-, and silver-bearing metaphosphate/vanadate glasses (CoMP-50V, NiMP-50V, and AgMP-50V, respectively)

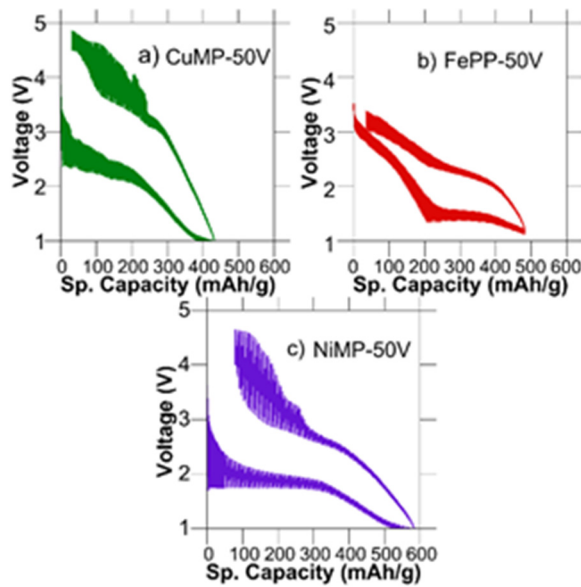


Figure V- 87: GITT testing of metaphosphate/vanadate glass cathodes showed persistent voltage hysteresis

Short 10-cycle tests were also performed on nickel, iron, cobalt, and copper phosphate/vanadate glasses at specific currents ranging from 5 mA/g up to 2,000 mA/g to determine the high power capability of GSC reactions. Nickel and cobalt metaphosphate/vanadate glasses showed excellent capacity retention up to 500 mA/g. Copper metaphosphate/vanadate and iron pyrophosphate/vanadate glasses did not perform as well during high power discharges. However, these were preliminary tests of high rate capability, because the effective particle sizes (180-550 nm) and cathode structure were not optimized.

The particle size and cathode structure for the glass cathodes has not been optimized, so the best electrochemical performance of these materials cannot be inferred from these initial cycling tests. The Galvanostatic Intermittent Titration Technique (GITT) uses capacity doses followed by long dwells to determine the near-equilibrium electrochemical behavior. GITT testing was performed on copper-, iron-, and nickel-bearing phosphate/vanadate glasses to estimate their best achievable performance for optimized cathodes (Figure V- 87). The key finding from GITT testing was that voltage hysteresis was lower for GITT testing than traditional cycle testing, but a fairly large voltage hysteresis did remain in metaphosphate/vanadate glasses.

Ex situ electron microscopy and energy dispersive x-ray spectroscopy were used to study the micro-structural changes occurring in nickel metaphosphate/ vanadate cathodes at states of charge before and after a GSC reaction. The initially charged and first discharged nickel-based glass cathodes both had a uniform distribution of nickel across intact glass particles (Figure V- 88). While XAFS showed the presence of Ni-Ni bonds in discharged cathodes, distinct crystalline nickel particles could not be identified using transmission electron microscopy, which suggested that very fine (< 10 nm) Ni nanoparticles were present. A small number of unidentified crystalline nanoparticles were found at particle surfaces in discharged cathodes, but the electron diffraction pattern indicated a phase with a d-spacing much smaller than Ni. For initial charge and first

discharge, the microstructures from a GSC reaction were similar to what would be expected for a typical conversion reaction.

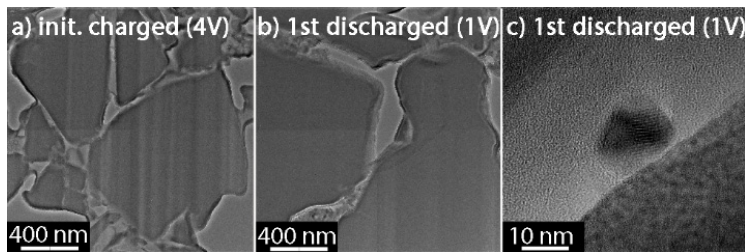


Figure V- 88: TEM images of thin sections from (a) charged and (b) discharged nickel metaphosphate/vanadate glasses both showed intact glass particles. A small number of surface nanoparticles were found in the discharged cathodes (c)

pyrophosphate/vanadate glasses, iron pyrophosphate glasses with molybdate substitution did not exhibit full theoretical capacity for a $\text{Fe}^{3+}/\text{Fe}^{2+}$ intercalation reaction. However, the molybdate-substituted glass did exhibit a GSC reaction at a slightly higher voltage, had a nearly identical total specific capacity, and demonstrated a higher capacity at high specific currents (Figure V- 89). Silver and copper metaphosphate glasses with molybdate substitution were also tested. The silver metaphosphate glass with molybdate substitution had a high capacity GSC reaction similar to silver metaphosphate/ vanadate glass. However, the copper metaphosphate glass with molybdate substitution had negligible capacity unlike the copper metaphosphate/vanadate glass. Thus, initial results suggest that molybdate substitution can be used as an environmentally friendlier alternative in certain glass cathode materials.

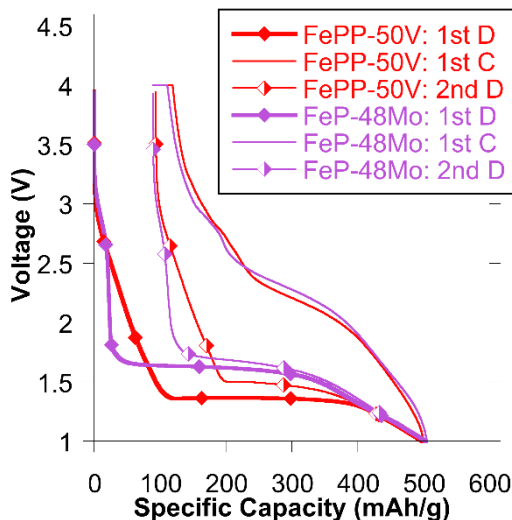


Figure V- 89: Molybdate substitution can be used as an environmentally friendlier alternative to vanadate substitution in certain mixed polyanion glass materials

the additional vanadium reduction reaction and also higher voltage. In cycling, it exhibited some first cycle irreversibility followed by steady capacity fade in subsequent cycles. In comparison with CuMP-50V, the glass with both 10% borate substitution and 50% vanadate (CuMP-10B-50V) had a lower first cycle irreversibility and a reduced voltage hysteresis. Ongoing work is targeted toward confirming that the effects are caused by polyanion substitution, not slight processing variations.

Molybdate: an environmentally friendlier alternative

A program review by US Drive indicated that the US automotive industry found vanadium-bearing compounds undesirable in vehicles due to health and environmental uncertainties. Therefore, molybdate was explored as an alternative polyanion to promote electrical conductivity in mixed polyanion glass cathode materials. Unlike iron

Glass cathodes designed for improved ionic conductivity

A series of copper metaphosphate glasses were made with systematic variations in polyanion content in order to determine the effects of polyanion substitution on the electrochemical performance of glass-state conversion reactions (Figure V- 90). Borate substitution increases the free volume in the glass and would promote higher ionic conductivity. Vanadate substitution increases the electrical conductivity. The baseline copper metaphosphate glass (CuMP) discharged at 5 mA/g was in the first cycle very close to its theoretical capacity for a $\text{Cu}^{2+}/\text{Cu}^{0+}$ GSC reaction (257 mAh/g meas. vs. 242 mAh/g theo.), but subsequent cycles had very low capacity. The glass with 20% borate substitution (CuMP-20B) had slightly higher voltage, but did not improve cycleability. The glass with 50% vanadate substitution (CuMP-50V) was higher capacity due to

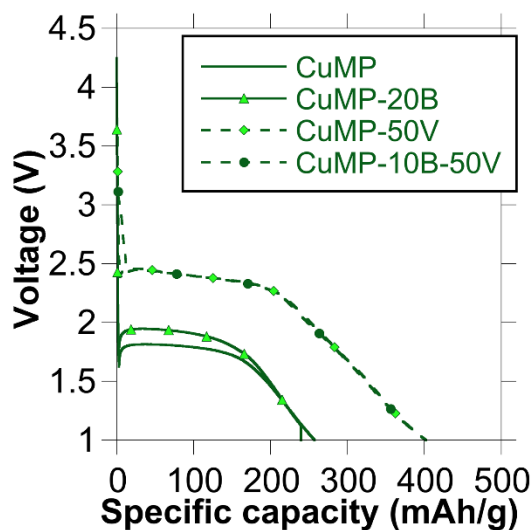


Figure V- 90: Vanadate substitution increased the voltage, capacity, and cycleability of copper metaphosphate glass

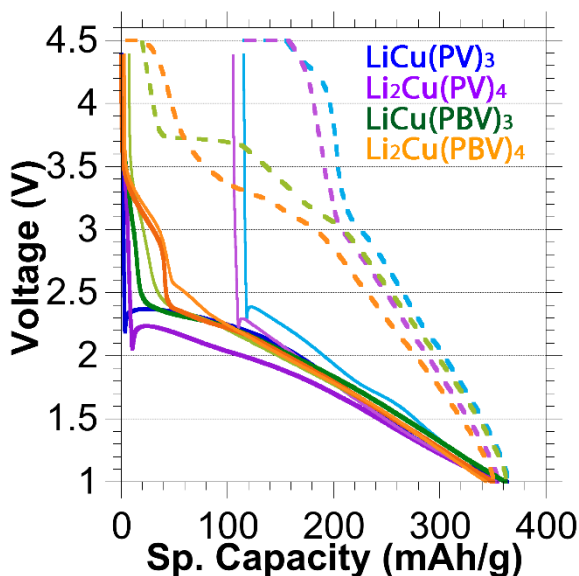


Figure V- 91: Tailoring the polyanion composition was shown capable of reducing the 1st cycle irreversible loss, improving the voltage hysteresis, and increasing the intercalation capacity in a lithium copper phosphate glass (P = phosphate, B=borate, V=vanadate)

hysteresis and substantial capacity fade over the course of tens of cycles, which is similar to the performance of typical crystalline conversion cathodes. GITT testing demonstrated persistent voltage hysteresis, which likely could not be overcome by optimizing the slurry-cast cathode structure. Ex-situ electron microscopy and energy-dispersive x-ray spectroscopy in nickel metaphosphate/vanadate glass cathodes showed that in the first discharge, the GSC reaction forms very fine metal nanoparticles inside intact glass particles. Molybdate substitution was demonstrated as an environmentally friendlier option to vanadate substitution in iron- and silver-based phosphate glasses. Tailoring the polyanion composition in a lithium copper phosphate glass was shown to promote partial intercalation, reduce first cycle irreversible loss, and reduce voltage hysteresis. Preliminary borate glass cathodes have been produced and electrochemically tested.

Ultimately, multi-valent intercalation reactions have the greatest theoretical specific energy and, in principle, could greatly exceed the energy density of commercial cathodes. Thus, the effect of tailoring the polyanion composition was studied on lithium copper phosphate glasses that were theoretically capable of undergoing a multi-valent intercalation reaction (Cu^{3+} to Cu^+) (Figure V- 91). Limited intercalation capacity was observed for a lithium copper phosphate glass with excess lithium & polyanion content and with combined substitution of borate and vanadate ($\text{Li}_2\text{Cu}(\text{PBV})_4$). Thus, tailoring the polyanion composition was shown to improve the intercalation reaction capacity, but substantial further improvement is required to enable utilization of near-theoretical capacity. However, the combined substitution of borate and vanadate into lithium copper phosphate glass ($\text{LiCu}(\text{PBV})_3$ and $\text{Li}_2\text{Cu}(\text{PBV})_4$) nearly eliminated irreversible loss in the first cycle and reduced the voltage hysteresis. While further improvement is needed, this is an important step in correlating glass composition and electrochemical performance.

Borate glass cathodes

Research on this project has focused on phosphate glasses, but other glass formers may have different electrochemical properties. Preliminary borate glasses have been produced and electrochemically tested. A series of lithium manganese borate glasses were produced with 0%, 17%, and 33% vanadate substitution. Unfortunately, similar to a lithium manganese vanadate glass, these glasses exhibited no Mn-based intercalation reaction, no Mn-based conversion reaction, and a low capacity vanadium-based reduction reaction. However, borate glasses can undergo high-capacity electrochemical reactions; a lithium copper borate glass has been produced that undergoes a glass-state conversion reaction.

Conclusions and Future Directions

High-capacity glass-state conversion (GSC) reactions have been demonstrated in cobalt-, copper-, iron-, nickel-, and silver-based phosphate glass cathodes.

Cycle testing of GSC reactions showed large voltage

Future work in FY16 will include: (1) producing borate glass cathodes, (2) tailoring polyanion composition to improve electrochemical performance, (3) casting fully lithiated glasses in a fully charged state, and (4) exploring partially crystallized glasses and exotic glass cathode materials.

FY 2015 Publications/Presentations

1. "Mixed polyanion (MP) glasses as cathode materials", ES184, US DOE Vehicle Technologies Annual Merit Review 2015.
2. Ruther RE, Zhou H, Dhital C, Saravanan K, Kercher AK, Chen G, Huq A, Delnick FM, Nanda J. Synthesis, Structure, and Electrochemical Performance of High Capacity $\text{Li}_2\text{Cu}_{0.5}\text{Ni}_{0.5}\text{O}_2$ Cathodes. *Chem. Mater.* 2015, 27, 6746-67

V.D.8 Design of High Performance, High Energy Cathode Materials (LBNL)

Objectives

- To develop high energy, high performance cathode materials including composites and coated powders, using spray pyrolysis and other synthesis techniques.
- To understand surface and bulk structural properties of Ti-NMCs that lead to enhanced energy densities.

Technical Barriers

- The cost of vehicular batteries is too high and the energy density needs to be improved. Cost on a \$/kWh basis will be lowered if higher energy density can be obtained without adversely affecting cycle life. However, the performance of high-energy high voltage electrode materials needs to be improved by reducing its reactivity with the electrolyte. Alternatively, higher utilization of NMC cathode materials could lead to higher energy density, provided cycling issues can be successfully addressed.

Technical Targets

- Explore feasibility of increasing utilization of NMCs by partial Ti-substitution of Co and using higher voltage cutoffs during cycling.
- Understand origins of Ti-substitution effects in substituted NMCs

Accomplishments

- Demonstrated that aliovalent Ti substitution in NMCs results in better high voltage cycling performance compared to unsubstituted materials, when the same levels of lithium extraction are used.
- Synthesized hierarchically structured NMC particles with tailored Ni-poor and Mn-rich surfaces by spray pyrolysis. These particles show better resistance against surface reconstruction than conventional materials and perform better under high voltage cycling conditions.
- Showed that oxygen on surfaces of NMC particles is easily lost, promoting conversion to rock salt (surface reconstruction)

Introduction

Batteries for vehicular applications need improvements in energy density, ideally without compromising cost or safety. At present, cathodes are the limiting factor preventing achievement of this goal due to their relatively low specific capacities compared to graphite (~370 mAh/g) or silicon anodes (>4000 mAh/g). NMCs, which have the general formula $\text{Li}[\text{Ni}_x\text{Mn}_x\text{Co}_{1-2x}]\text{O}_2$, are a technologically important class of cathodes, but the practical capacities are limited to about 160 mAh/g, slightly more than half of the theoretical (280 mAh/g). While greater capacities can be achieved by cycling to higher voltage limits, this leads to rapid capacity fading. Work on this project is directed towards development of higher capacity NMCs to improve energy density by attempting to understand the phenomena responsible for the capacity fade and using strategies to mitigate it such as partial Ti-substitution.

Project Details

Tien Duong (DOE Program Manager)

Marca Doeffer (Principle Investigator)

Energy Storage and Distributed Resources Division

Lawrence Berkeley National Laboratory

1 Cyclotron Road

Berkeley, CA 94720

Phone: 510-486-5821

E-mail: mmdoeffer@lbl.gov

Start Date: October 2011

Projected End Date: September 2015

Approach

We use a highly collaborative approach to understand what limits high voltage cycling performance in NMC materials. A combination of synchrotron radiation and electron microscopy techniques (in collaboration with A. Mehta, D. Nordlund, T.-C. Weng, and Y. Liu at SSRL and H. L. Xin at BNL) and computational methods (with M. Asta at U.C. Berkeley) are used to understand the surface and bulk characteristics of baseline and Ti-substituted NMCs. Materials are synthesized either by classic co-precipitation methods or by spray pyrolysis.

Electrochemical characterization is carried out in lithium half-cell configurations. Several physical techniques are used to characterize materials before and after electrochemical cycling under a variety of conditions.

Nanotomographic imaging (Transmission x-ray microscopy, TXM) at SSRL is used to determine chemical gradients in particles and correlate this with electrochemical behavior. Soft x-ray absorption spectroscopy (XAS) experiments carried out at SSRL are used to probe oxidation states of transition metals at particle surfaces and in the bulk as a function of their electrochemical history. These results are correlated with scanning transmission electron microscopy (STEM) and electron energy loss spectroscopy (EELS) experiments at Brookhaven National Laboratory to obtain a full understanding of what governs the behavior of NMCs as a function of composition and cycling history.

Results

Background

Our previous work (see 2014 annual report) has been directed towards understanding what limits the high voltage cycling behavior of NMC materials using soft x-ray absorption spectroscopy and electron microscopy. Cycling NMCs to higher voltages than is currently used (4.3V vs. Li⁺/Li) results in higher capacities, and thus potentially higher energy densities in Li-ion cells, but typically results in faster capacity fading. Ensemble-averaged soft XAS experiments, which allow oxidation states of Ni, Co, and Mn to be determined as a function of depth from electrode surfaces show that these metals are reduced on the surface compared to in the bulk, under a variety of cycling and storage conditions. STEM-EELS characterization of specific particles show that there is formation of a rock salt (MO, Fd3_m) structure on surfaces (i.e., surface reconstruction), although the distribution of the rock salt is highly heterogeneous and tends to form more readily on facets through which Li diffuses. The rock salt formation is responsible for the common observation of first cycle inefficiencies and to the apparent capacity fade during high voltage cycling, since no bulk transformation is detected, and nearly all the capacity can be recovered when electrodes are discharged very slowly. Under conditions where metal dissolution does not occur to a great extent (short number of cycles, room temperature or below, materials without a Mn excess), the soft XAS experiments alone can be used as a proxy to determine the extent of surface reconstruction.

FY 2015 Results

Computational results (Markus et al. *J. Phys. Chem. Lett.* **5**, 3649 (2014)) obtained last year indicated that a rock salt structure (Fd3_m) is thermodynamically favored over a layered structure (R3_m) at high states-of-delithiation (at about x=0.35 in Li_xMO₂ depending on exact composition) for NMCs. Ti-substitution stabilizes the layered structure over a wider composition range, although rock salt formation is still predicted to occur in very highly delithiated materials. Results obtained last year, however, indicate that surface reconstruction occurs during conservative lithium removal and even when samples are simply exposed to electrolytic solution for a period of time before they undergo charging (i.e., x=1), although to a lesser extent than during high voltage cycling. These observations can be explained by the prediction that surface oxygen (Figure V- 92) is energetically unstable compared to bulk oxygen, and thus is easily lost, promoting surface reconstruction.

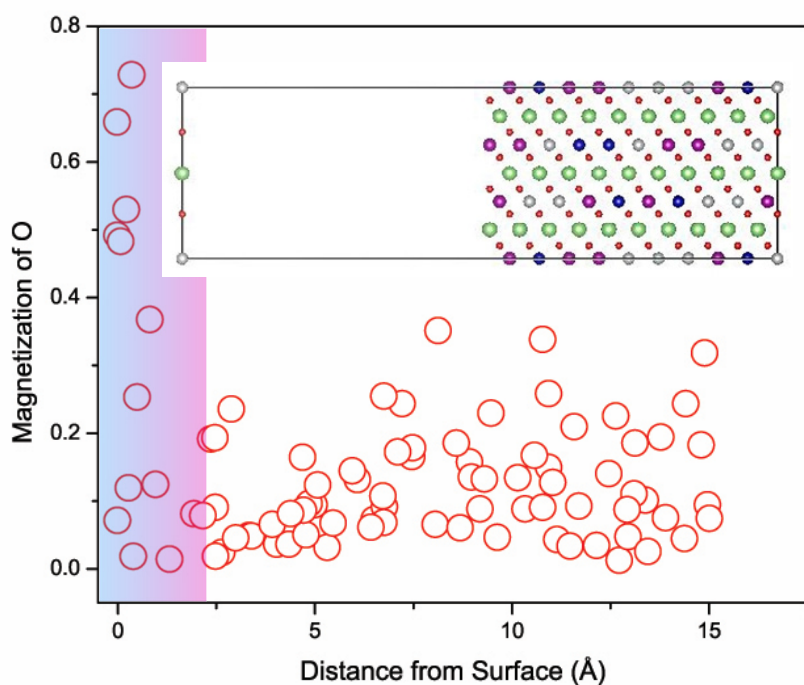


Figure V- 92: Energies of O in NMCs as a function of distance from the surface. The shaded region represents the surface and shows that oxygen will be easily lost

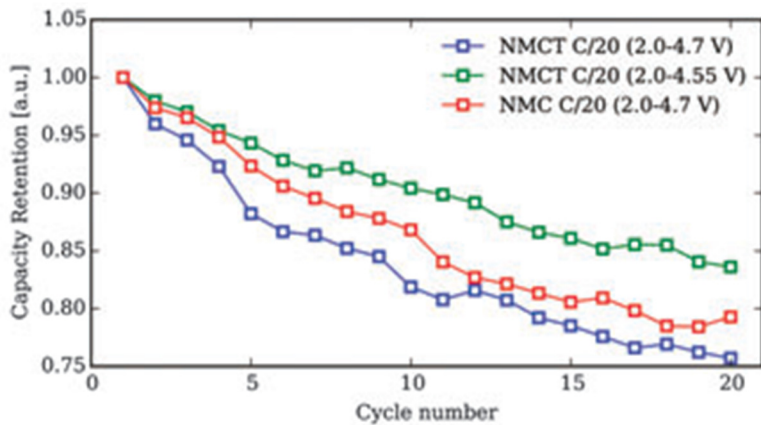


Figure V- 93: Half-cell cycling results for Ti-substituted NMC (NMCT) between 2.0-4.7V or 2.0-4.55V and regular NMC between 2.0-4.7V. The initial extent of lithium extraction is the same for NMCT between 2.0-4.55V and NMC between 2.0-4.7V, but the capacity retention is better for NMCT, as predicted by theory

initial capacity is similar to that of regular NMC cycled to 4.7V (Figure V- 93, see reference 11 below), but the capacity retention is improved, as predicted by theory. Soft XAS experiments also confirm that there is less surface reconstruction for the Ti-substituted NMC cycled to the same degree of lithium extraction as an unsubstituted analog.

Interestingly, spray-pyrolyzed samples of NMC-442 perform as well as conventionally prepared Ti-substituted NMC-442 (Figure V- 94), when cycled to 4.7V. Soft XAS results indicate that there is less surface reconstruction for electrodes consisting of the spray pyrolyzed NMC-442 compared to those made by conventional co-precipitation reactions (Figure V- 95). The spray pyrolyzed samples consist of large (~10 μm) spherical secondary particles

Aliovalent Ti-substitution is also predicted to result in less surface reconstruction during high voltage cycling because of the thermodynamic considerations described above. This should result in better capacity retention during high voltage cycling. However, when results from half cells containing regular NMC and Ti-substituted NMC are compared, this seems not to be the case, although the latter delivers higher capacities when charged to 4.7V. Ti-substitution changes the voltage profile of the NMC, allowing more lithium to be extracted below 4.7V compared to unsubstituted cathodes, which explains the higher capacity that is obtained initially. To accurately determine if the Ti-substituted sample really shows improved cycling performance, it is necessary to cycle it to the same degree of lithium extraction as regular NMC. When an upper voltage limit of 4.55V is used for the Ti-substituted NMC, the

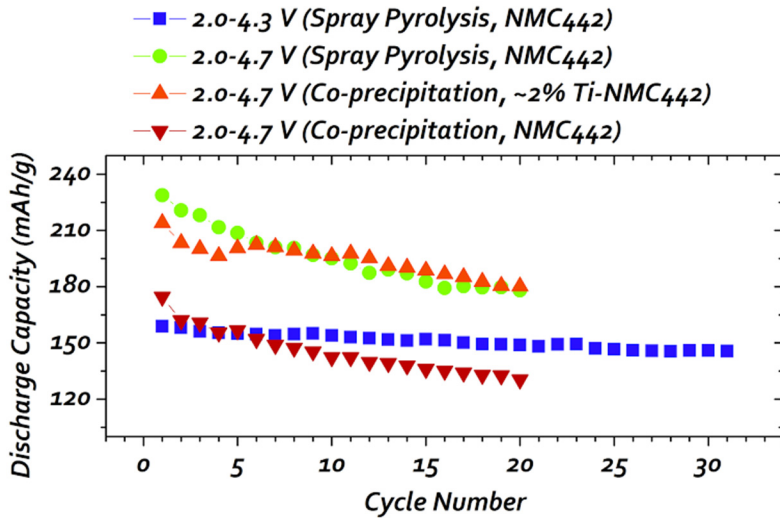


Figure V- 94: Cycling data for NMCs prepared different ways

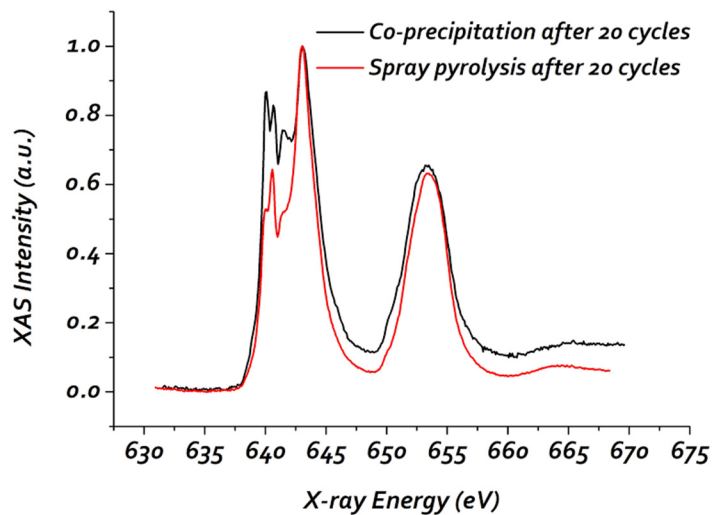


Figure V- 95: Mn L-edge soft x-ray absorption spectra of NMC-442 electrodes cycled to 4.7V, in total electron yield (TEY) mode, which probes the top 5 nm of the surfaces. The low energy shoulder on the L3 edge is a marker for reduced Mn. The co-precipitated sample shows a greater degree of surface reconstruction compared to the spray pyrolyzed sample

comprised of nanometric primary particles fused together, whereas the co-precipitated samples are looser agglomerates of nanometric particles. While the spherical morphology of the spray pyrolyzed particles is favorable for battery performance, it cannot explain the decreased amount of surface reconstruction compared to co-precipitated samples, which results in improved cycling. To investigate this further, nanotomography experiments were carried out at beamline 6.2c at SSRL to map chemical compositions in co-precipitated and spray-pyrolyzed NMC particles. Surprisingly, elemental association maps show a significant degree of compositional heterogeneity in spray pyrolyzed samples (Figure V- 96 and Figure V- 97) compared to the co-precipitated ones (not shown), although XRD patterns are consistent with single phase materials. Notably, surfaces are somewhat poor in Ni content compared to particle interiors, on the secondary particle level (Figure V- 98). The compositional gradient is also present at a nanometric scale, as determined by STEM/EELS mapping of primary particles across a grain boundary (Figure V- 99). Surface reconstruction is most likely associated with the presence of oxidized Ni, which has a tendency to lose oxygen and form rock salt phases. Lowering the Ni content at particle surfaces lessens the tendency towards surface reconstruction during high voltage cycling and improves cycling.

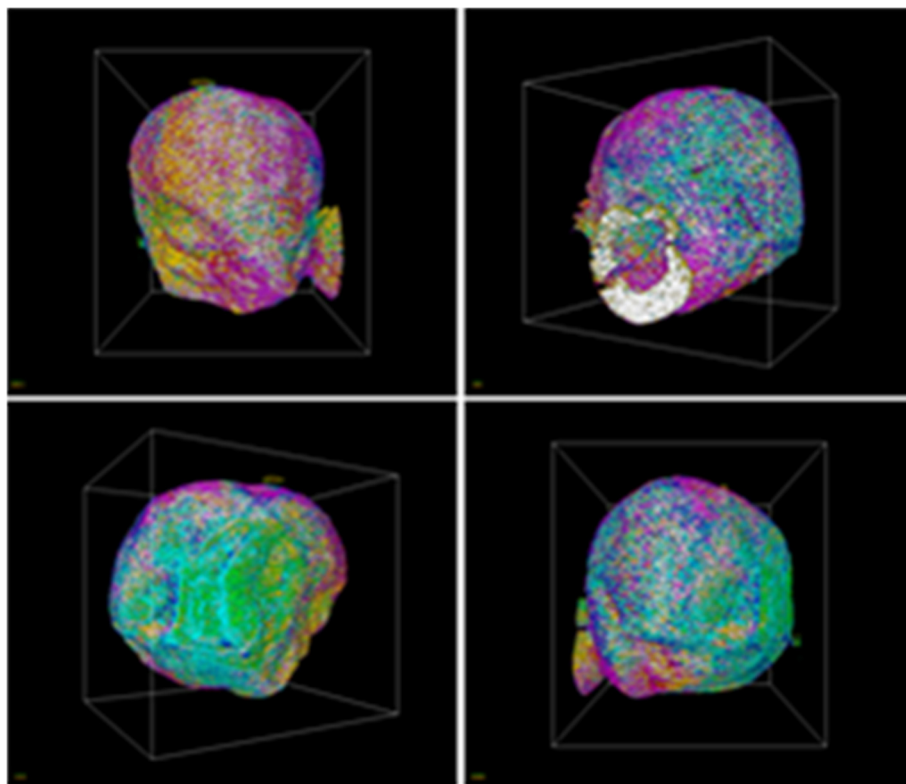


Figure V- 96: Elemental mapping using x-ray transmission microscopy of a spray pyrolyzed NMC-442 particle from different views. Voxel sizes are 32.5nm x32.5 nm x 32.5 nm. See below for color key

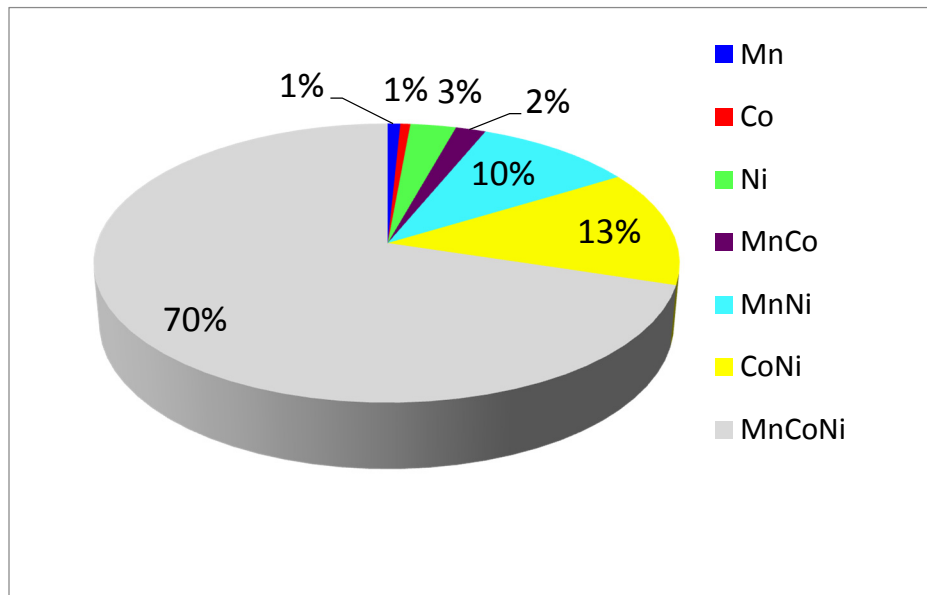


Figure V- 97: Elemental association distributions for the particle shown in the prior figure

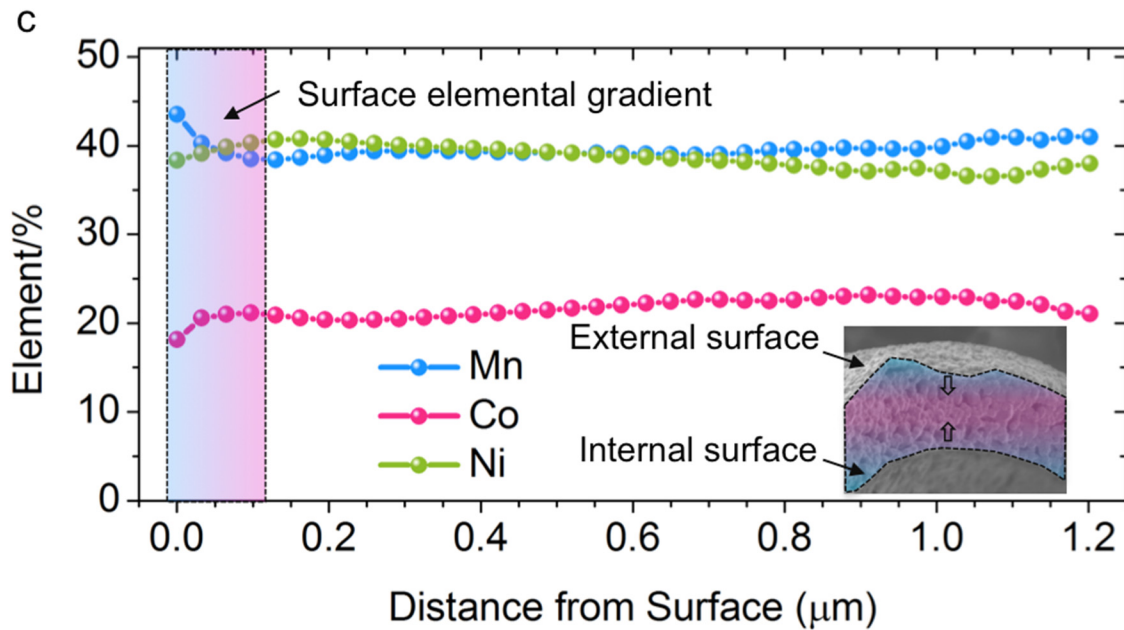


Figure V-98: Elemental distribution as a function of the distance from microsphere surfaces calculated using the TXM data. The shaded region represents surfaces

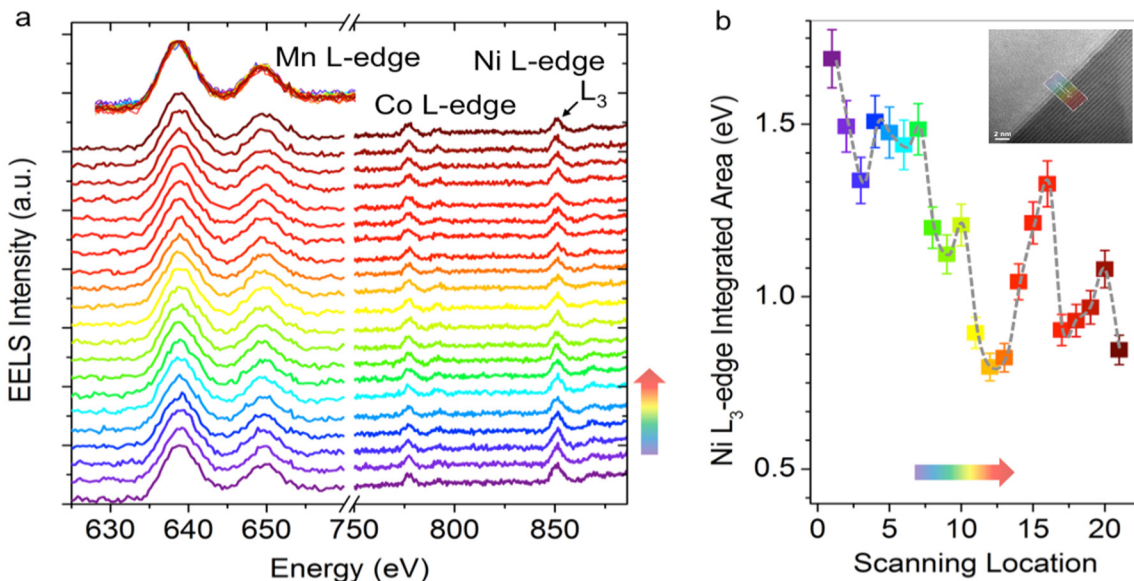


Figure V-99: a) EELS mapping across a grain boundary of two primary particles of an NMC-442 sample made by spray pyrolysis. b) shows the variation in Ni content across the grain boundary shown in the inset

Conclusions and Future Directions

Our research has been designed to determine what limits high voltage cycling performance in NMCs and to take steps to improve it, so that greater energy densities can be obtained in Li-ion cells. We have shown that surface reconstruction occurs under a variety of conditions and is responsible both for the first cycle coulombic inefficiencies that are observed and for capacity fading during high voltage cycling. The surface reconstruction arises as a consequence of the tendency for the Ni-containing particle surfaces to lose oxygen, and the greater thermodynamic stability of the rock salt phase compared to the layered structure at high states of delithiation. Partial aliovalent Ti-substitution for Co in the NMCs delays rock salt formation but does not prevent it

entirely. Ti-substitution modifies the voltage profiles of the NMCs, so that more lithium can be extracted compared to unsubstituted materials. When cycled to the same voltage limit (4.7V), Ti-substituted NMCs and regular NMCs exhibit similar degrees of capacity fading and surface reconstruction, but the former delivers higher capacities and is delithiated to a greater extent during initial charge, so that the comparison is not entirely accurate. When the amount of delithiation is held constant by cycling the Ti-NMC to a somewhat lower voltage limit (4.55V vs. 4.7), the capacity retention is better than that of the unsubstituted analog and the degree of surface reconstruction is less, as predicted by theory. Another method of ameliorating the surface reconstruction is to design materials that have less Ni on particle surfaces than in the bulk, since this phenomenon is mainly associated with high Ni oxidation states. Spray pyrolyzed samples show compositional gradients in which both the secondary and primary particles are Ni-poor on surfaces. This results in less surface reconstruction during cycling and better performance.

While this project has officially ended as of September 30, 2015, this principle investigator will participate in a newly funded multi-investigator project entitled “Advanced Cathode Materials for High Energy Lithium Ion Batteries”. For the new project, we will continue using the synchrotron and microscopy techniques described above to understand functioning of NMC cathode materials, but we will extend our studies to materials with higher Ni contents. Because of concerns with the thermal stability of high Ni-content electrodes, special attention will be paid to the thermal behavior of delithiated materials.

FY 2015 Publications/Presentations

1. “Design of High Performance, High Energy Cathode Materials” Marca M. Doeff 2015 DOE Annual Peer Review Meeting Presentation
2. “Better Cathode Materials for Lithium Batteries by Tailoring Architectural Metal Segregation” F. Lin, D. Nordlund, Y. Li, M. K. Quan, L. Cheng, T.-C. Weng, Y. Liu, H.L. Xin and M. M. Doeff, *Nat. Energy* in press (2015).
3. “Effects of Crystallinity and Impurities on the Electrical Conductivity of Li-La-Zr-O Thin Films” Joong Sun Park, Lei Cheng, Vassilia Zorba, Apurva Mehta, Jordi Cabana, Guoying Chen, Marca M. Doeff, Thomas J. Richardson, Jung Hoon Park, Ji-Won Son and Wan-Shick Hong, *Thin Solid Films* **576**, 55 (2015).
4. “Structural and Chemical Evolution of Amorphous Nickel Iron Complex Hydroxide upon Lithiation/Delithiation” Kai-Yang Niu, Feng Lin, Liang Fang, Dennis Nordlund, Runzhe Tao, Tsu-Chien Weng, Marca Doeff, and Haimei Zheng, *Chem. Mater.*, **27**, 1583 (2015).
5. “Effect of Surface Microstructure on Electrochemical Performance of Garnet Solid Electrolytes” Lei Cheng, Wei Chen, Martin Kunz, Kristin Persson, Nobumichi Tamura, Guoying Chen, and Marca Doeff, *ACS Applied Mater. & Interfaces*, **7**, 2073 (2015).
6. “Effect of Carbon Coating on the Physico-chemical and Electrochemical Properties of Fe₂O₃ Nanoparticles” A. Iturrondobeitia, A. Goñi, I. Oruc, I. Gil de Muro, L. Lezama, M. M. Doeff, and T. Rojo, *Inorg. Chem.*, **54**, 5239 (2015).
7. “High Voltage Cathode Materials for Lithium Ion Batteries: Freeze-dried LiMn_{0.8}Fe_{0.1}M_{0.1}PO₄/C (M=Fe, Co, Ni, Cu) Nanocomposites” Amaia Iturrondobeitia, Aintzane Goñi, Izaskun Gil De Muro, Luis Lezama, Chunjoong Kim, Marca Doeff, Jordi Cabana, and Teofilo Rojo, *Inorg. Chem.* **54**, 2671 (2015).
8. “Transitions from Near-Surface to Interior Redox upon Lithiation in Conversion Electrode Materials”, Kai He, Huolin L. Xin, Kejie Zhao, Xiqian Yu, Dennis Nordlund, Tsu-Chien Weng, Jing Li, Yi Jiang, Christopher A. Cadigan, Ryan M. Richards, Marca M. Doeff, Xiao-Qing Yang, Eric A. Stach, Ju Li, Feng Lin, and Dong Su, *Nano Lett.* **15**, 1437 (2015).
9. “Interrelationships among Grain Size, Surface Composition, Air Stability, and Interfacial Resistance of Al-substituted Li₇La₃Zr₂O₁₂ Solid Electrolytes” Lei Cheng, Cheng Hao Wu, Angelique Jarry, Wei Chen, Yifan Ye, Junfa Zhu, Robert Kostecki, Kristin Persson, Jinghua Guo, Miquel Salmeron, Guoying Chen, and Marca Doeff, *ACS Applied Mater. & Interfaces*, **7**, 17649 (2015).
10. “Sodiation Kinetics of Metal Oxide Conversion Electrodes: A Comparative Study with Lithiation” K. He, F. Lin, Y. Zhu, X. Yu, J. Li, R. Lin, D. Nordlund, T.-C. Weng, R. Ryan, X.-Q. Yang, M. Doeff, E. Stach, Y. Mo, H. Xin, and D. Su, *Nano Lett.*, DOI: 10.1021/acs.nanolett.5b01709 (2015).

11. "Tailoring the Surface Properties of $\text{LiNi}_{0.4}\text{Mn}_{0.4}\text{Co}_{0.2}\text{O}_2$ by Titanium Substitution for Improved High Voltage Cycling Performance" S. Wolff-Goodrich, F. Lin, I. Markus, D. Nordlund, H. Xin, M. Asta, and M. M. Doeff, **Phys. Chem. Chem. Phys.** 17, 21778 (2015).
12. "Three-Dimensional Elemental Imaging of Li-ion Solid-State Electrolytes Using fs-Laser Induced Breakdown Spectroscopy (LIBS)", H. Hou, L. Cheng, T. Richardson, G. Chen, M. Doeff, R. Zheng, R. Russo, and V. Zorba, **J. Anal. Atomic Spectroscopy**, DOI: 10.1039/c5ja00250h (2015).
13. "Overcoming Practical Obstacles to the Use of Garnet LLZO Solid Electrolytes in Lithium Batteries", Marca M. Doeff, Guoying Chen, and Lei Cheng, 2015 International Battery Association and Pacific Power Symposium Joint Meeting, Waikoloa, HI, Jan. 2015.
14. "Layered Cathode Materials Prepared by Spray Pyrolysis for High-Energy Lithium-Ion Batteries" Feng Lin, Yuyi Li, Dennis Nordlund, Tsu-Chien Weng, Huolin Xin, and Marca Doeff, 20th International Conference on Solid State Ionics, June 14-19, 2015, Keystone Colorado.
15. "Probing Interfaces of Garnet Solid Electrolytes in Lithium Batteries" Lei Cheng, Guoying Chen and Marca M. Doeff, 20th International Conference on Solid State Ionics, June 14-19, 2015, Keystone.

V.D.9 Lithium Batteries with higher Capacity and Voltage (UTA)

Objectives

- To increase cell energy density for a given cathode.
- To allow low-cost rechargeable batteries with cathodes other than insertion compounds.

Technical Barriers

- In order to use a metallic anode (lithium or sodium), the safety issue arising from dendrite growth must be resolved.
- Nucleation and growth of alkali metal dendrites should be suppressed. Uniform and smooth growth of alkali metals is preferred in order to (i) reduce irreversible SEI layer formation and (ii) eliminate the chance of short-circuit.
- A separator membrane should block the dendrites to prevent cell short-circuit.
- A separator membrane with liquid catholyte (or anolyte) should also block redox molecule cross-over.

Technical Targets

- To increase cell energy density for a given cathode.
- To allow low-cost, high-capacity rechargeable batteries with cathodes other than insertion compounds.

Accomplishments

- Cross-linked polymer membranes with different chemistries were successfully fabricated via thiol-ene reactions.
- A cross-linked polymer (PETT-FC) and Al₂O₃ composite film that is coated on a glass fiber membrane has been developed for a battery separator.
- For a Li-S battery, highly cross-linked polymer-electrolyte coating layers with electron-donating groups were designed to bind the lithium polysulfides. An ester group with a high spatial density was shown to be a strong candidate to bind the lithium polysulfides.
- Spectroscopic evidence for the presence of lithium bonds between the lithium polysulfides and the electron-donating groups are identified for the first time.
- PETT-Ester coated on a porous PVDF membrane has been developed for a Li battery cell with liquid cathode. The membrane was effective to block the crossover of redox molecules.
- Alkali-metal-free anodes with polymer-coated current collectors have been developed.

Introduction

To develop cells with an alkali-metal anode, we have fully explored the technical potentials of several cross-linked polymer membranes this year. Polymers with different chemical nature (*e.g.* electron donating or withdrawing groups) turned out to have strong interactions with alkali working ions and redox molecules in the electrolyte. By fine tuning the polymer backbone chemistries, we could develop separator membranes for alkali-metal batteries and redox flow cathodes and coating layers for a Li-S battery or an alkali-metal-free anode.

Project Details

John B. Goodenough (UT Austin – PD/PI)
 Department of Mechanical Engineering
 The University of Texas at Austin
 204 East Dean Keeton
 C2201, ETC 9.184
 Austin, Texas 78712
 Phone: 512-471-1646; Fax: 512-471-7681
 E-mail: jgoodenough@mail.utexas.edu

Subcontractor:
 The University of Texas at Austin

Start Date: January 2013
 Projected End Date: December 2016

Approach

The objectives outlined above were accomplished by adopting alkali metal anodes and cross-linked polymer membranes. Cathode materials were chosen from oxide materials, a liquid cathode, and sulfur. Major technology innovations have been undertaken for these milestones:

- Fabricate oxide/polymer composite membrane as a separator in an alkali-ion (Li^+ , Na^+) battery and optimization of pore size, oxide loading, and thickness for blocking anode dendrites with fast alkali-ion transport.
- Investigate membranes that can block a customized soluble redox couple in a flow-through cathode.
- Evaluate Li-ion and Na-ion cells with a metallic Li or Na anode, oxide/polymer membrane as separator, and a flow-through liquid cathode.
- Measure performance of cells with a metallic Li or Na anode, oxide/polymer composite membrane as separator, and an insertion compound as cathode.

Results

We have completed the following investigations:

Fabrication of Li^+/Na^+ conducting cross-linked polymer networks

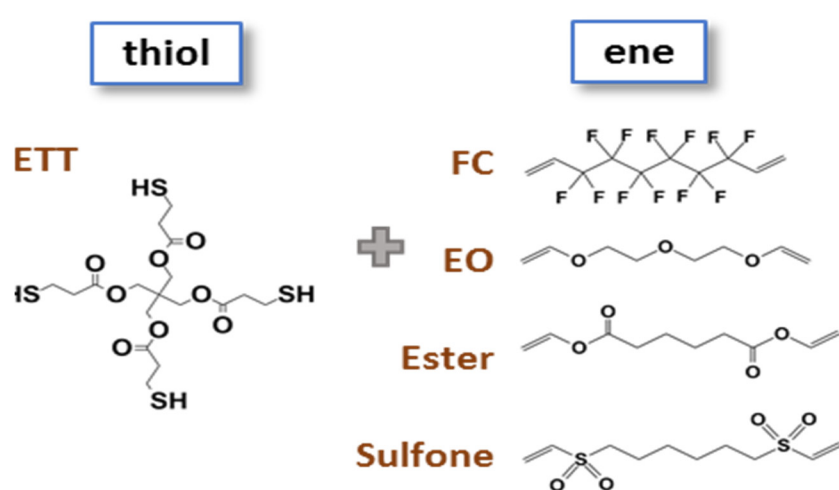


Figure V- 100: Synthesis of cross-linked polymers via thiol-ene chemistry: Schematic representation of the thiol-ene reactions between a tetrathiol crosslinker and difunctional ene monomers to coat sulfur-loaded carbon paper electrodes

Cross-linked polymer membranes were fabricated via thiol-ene chemistry as shown in Figure V- 100. A tetrathiol crosslinker (pentaerythritol tetrakis (3-mercaptopropionate), PETT) was polymerized with four different kinds of difunctional ene monomers with unique functional groups, 1,6-divinylperfluorohexane (FC), di(ethylene glycol) divinyl ether (EO), divinyl adipate (Ester), and 1,6-bis(vinylsulfone)hexane (Sulfone) as shown in

Figure V- 101. They are referred to hereafter as PETT-FC, PETT-EO, PETT-Ester, and PETT-Sulfone,

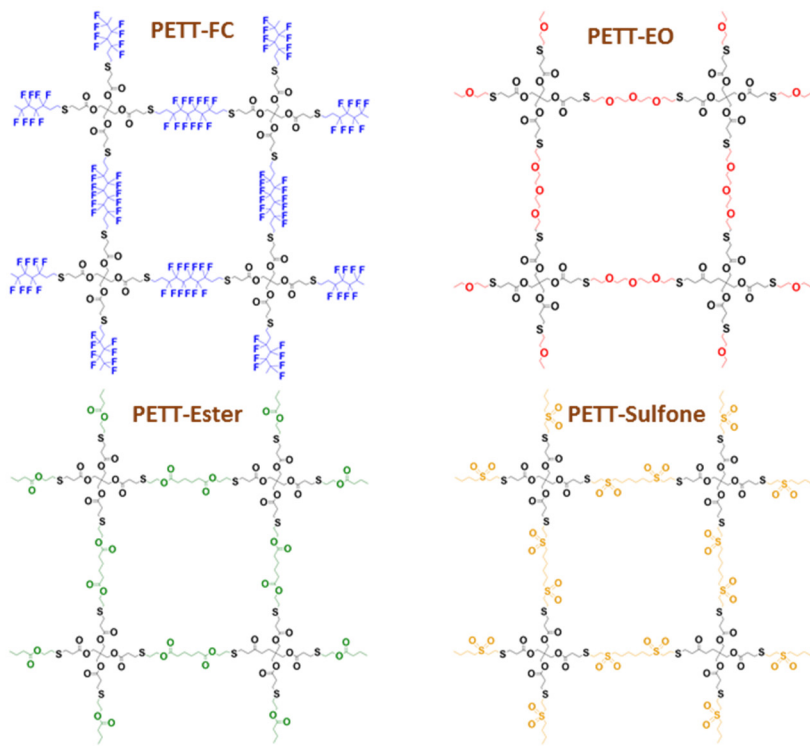


Figure V- 101: Structure of PETT-FC, PETT-EO, PETT-Ester, and PETT-Sulfone

Oxide/polymer composite membrane as a separator in an alkali-ion (Li^+ , Na^+) battery

A cross-linked polymer (PETT-FC) loaded with Al_2O_3 was coated on a glass fiber membrane for a battery separator as shown in Figure V- 102. Al_2O_3 particles in the monomer solution were mostly filtered by the glass-fiber membrane and deposited uniformly on one side of the membrane. The Al_2O_3 layer was shown to suppress sodium dendrite penetration through the porous separator.

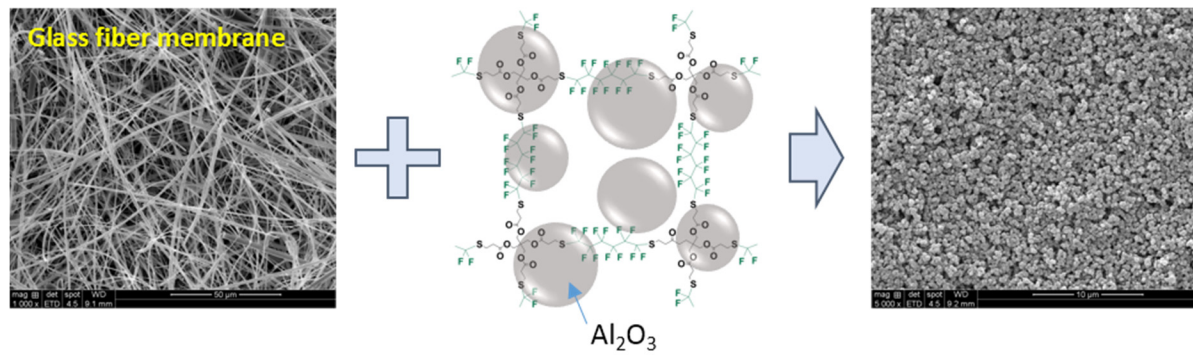


Figure V- 102: Fabrication sheme for the composite separator membrane. A glass fiber membrane was coated with the crosslinked polymer made of tetrathiol crosslinker and divinylperfluorohexane. The monomer solution was originally mixed with Al_2O_3 particles, and they were filtered and mostly present on the surface of the glass fiber membrane in the final composite separator

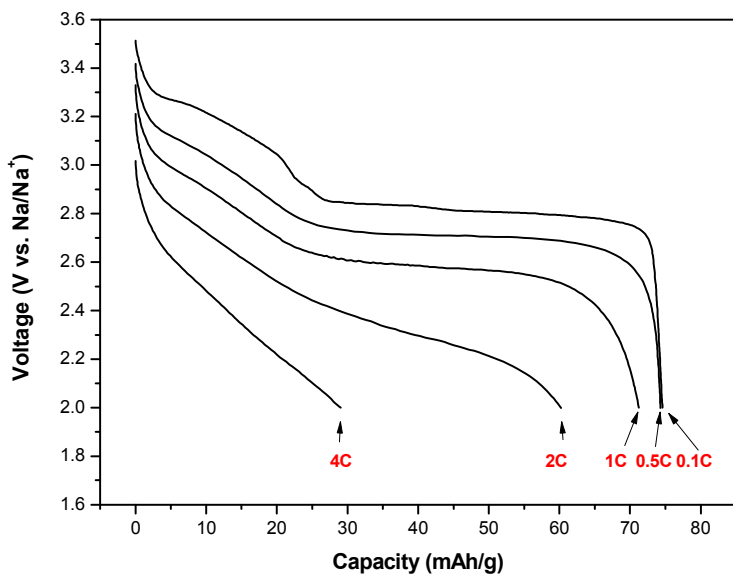


Figure V- 103: Discharge voltage curves of a NaCrO_2 half cell at different current densities cycled between 2.0 and 3.6 V vs. Na/Na^+ . Charging current density was $\text{C}/10$ in each cycle

The fabricated composite separator was tested in a sodium-ion cell with $\text{NaCr}(\text{III})\text{O}_2$ as a cathode material and sodium metal as anode as shown in Figure V- 103. Single-phase NaCrO_2 was synthesized via solid state reaction, and the steps in voltage curves reflect possible Na ordering and phase transitions during charge/discharge. The cell shows good rate capability without significant loss in capacity at high C-rates, which suggests the composite separator has fast Na^+ transport across the membrane.

Trapping lithium polysulfides of a Li-S battery by forming lithium bonds in a polymer matrix

Lithium-sulfur batteries have been extensively studied as a high-capacity alternative to lithium-ion batteries. The electrochemical reactions of sulfur involve several intermediates, lithium polysulfides (Li_2S_n , $4 \leq n \leq 8$) that are soluble in the liquid electrolyte, which induces a continuous loss of active material from a sulfur cathode. To overcome this problem, we trap the soluble lithium polysulfides with a polymer coating layer with electron-donating functional groups that can provide effective binding sites; and the binding performance doesn't depend on surface area, but on the bulk density of the electron donating groups. (See Figure V- 100)

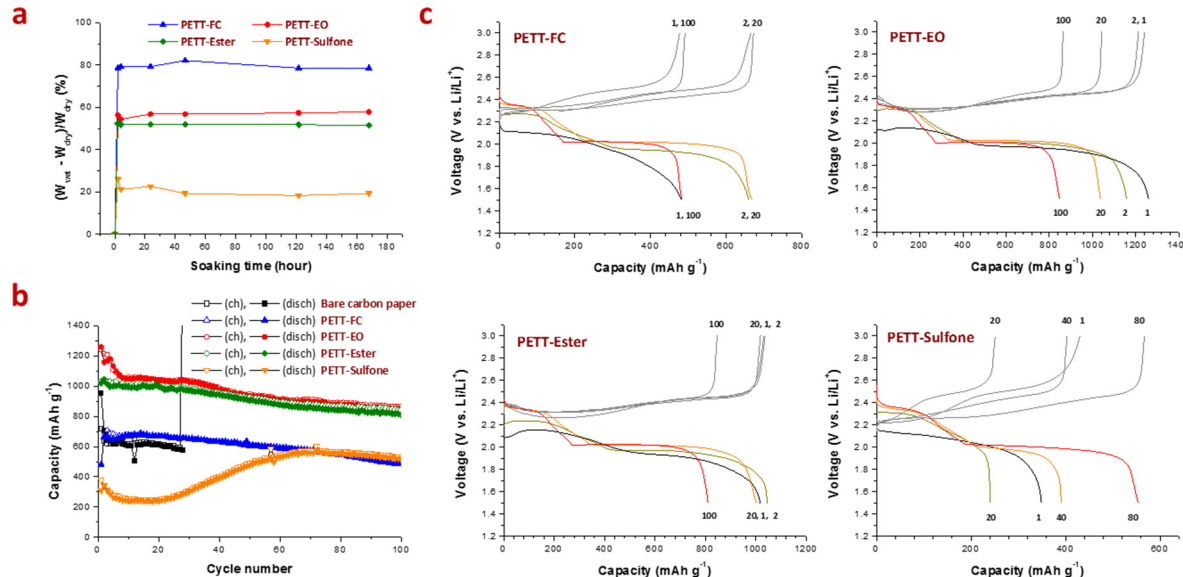


Figure V- 104: Electrochemical characterization of the polymer-coated sulfur electrodes. (a) Time-dependent electrolyte solvent (1:1 DME/DOL) uptake was measured and calculated according to the equation, $(W_{\text{wet}} - W_{\text{dry}})/W_{\text{dry}}$ where W_{dry} is the membrane weight before soaking and W_{wet} is the weight after liquid uptake. (b) Charge/discharge cycle performance and (c) voltage curves of PETT-FC, PETT-EO, PETT-Ester, and PETT-Sulfone electrodes measured between 1.5 and 3.0 V vs. Li/Li^+ at 0.5C-rate

Figure V- 104 shows battery-cell performances of the bare sulfur-loaded carbon-paper electrode, PETT-FC, PETT-EO, PETT-Ester, and PETT-Sulfone. The bare electrode showed a poor initial coulombic efficiency of 75.5% and cycled up to only 28 cycles before the cell was terminated by the endless polysulfide shuttle current. The low cycling capacity indicates that a large amount of active sulfur was lost in the liquid electrolyte during either the electrode soaking in the liquid electrolyte or the cell operation since the carbon paper doesn't provide any geometric structures to hold the soluble polysulfide species. PETT-FC also exhibits similar capacities to those of the bare electrode owing to too large electrolyte uptake, but the cycle stability lasts up to 100 cycles. In contrast to PETT-FC, PETT-Sulfone with the lowest degree of swelling shows even lower initial capacities with a unique cycling performance.

PETT-EO and PETT-Ester show a significant increases in the reversible capacities: the initial discharge capacities are 1260 and 1018 mAh g⁻¹, respectively, with the two distinct voltage regions at 2.4 and 2.0 V. With PETT-Ester, the capacities were remarkably stable throughout the cycle test. This observation signals that the ester group is a more efficient trap of the soluble Li₂S_n.

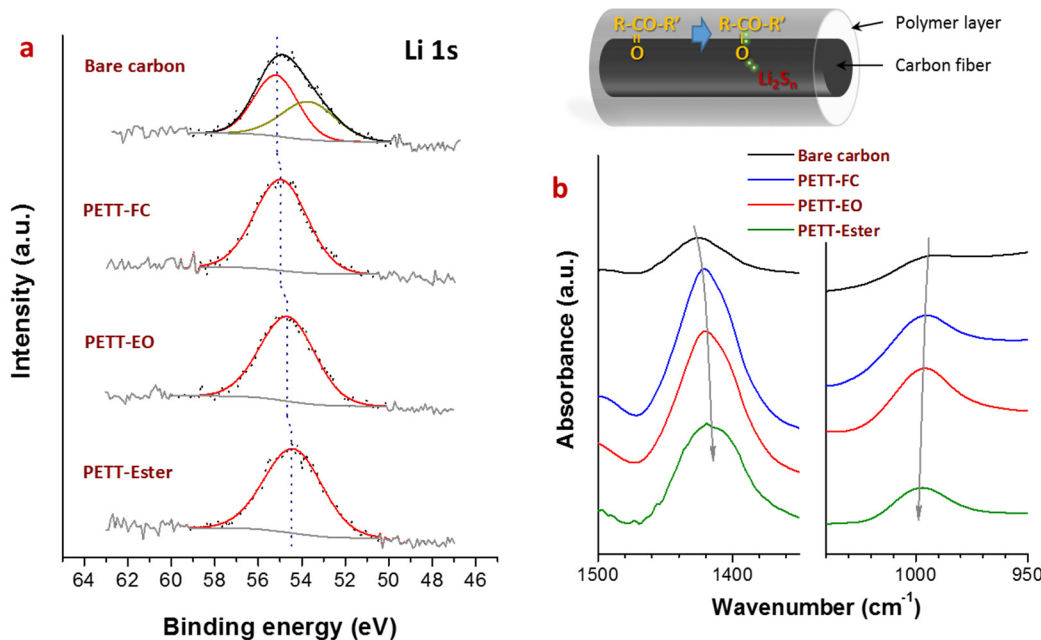


Figure V- 105: Chemical interactions between ester groups in the polymer backbone and lithium polysulfides. (a) Lithium 1s XPS and (b) ATR-FTIR spectra of the bare sulfur-loaded carbon, PETT-FC, PETT-EO, and PETT-Ester electrodes after discharging to 1.5 V. The electrodes were washed with DME and transferred to XPS chamber without any air exposure by using a transfer chamber. Schematic illustration proposes the lithium bond model between the ester group and lithium polysulfides

To probe any chemical interactions between the polymer backbones and the lithium polysulfides, specifically Li₂S, the product of a reduced trapped polysulfides, discharged cells were prepared for XPS and FTIR analyses. We didn't test PETT-Sulfone because it doesn't form Li₂S in the initial cycles as is shown in Figure V- 104. Figure V- 105a shows measured and fitted Li 1s XPS spectra. The bare sulfur/carbon electrode without a polymer coating has an additional peak component at 53.69 eV that can be assigned to Li₂O, an electrolyte decomposition product. The polymer coating remarkably enhances electrolyte stability and only brings a single peak associated with Li₂S. Here we found that the Li 1s XPS peaks of Li₂S in the bare, PETT-FC, PETT-EO and PETT-Ester electrodes were shifted progressively to lower values from 55.19 to 54.95, 54.65, and 54.40 eV, respectively. The lithium in Li₂S is partially reduced in the presence of the polymer layer. To find the corresponding electron donating component, FTIR spectra were analyzed with the same electrode samples as shown in Figure V- 105. The COO stretch vibration shows red shifts from 1425.16 to 1421.3, 1419.37, and 1419.37 cm⁻¹ while the CO vibration exhibits blue shifts from 989.32 to 995.1, 995.1, and 997.03 cm⁻¹ in the bare, PETT-FC, PETT-EO and PETT-Ester electrodes, respectively. The results clearly indicate that the carbonyl double bond in the ester group releases electronic charge to lithium in the lithium

polysulfides to form an asymmetric lithium bond as illustrated in Figure V- 105, which induces the red shifts in the COO vibration and blue shifts in the CO vibration. At the atomic level, pure sulfur S₈ molecules should interact via van der Waals attraction, but after lithiation of the terminated sulfurs in Li₂S_n ($4 \leq n \leq 8$), electrostatic interactions between lithium and sulfur or asymmetric bonding by a covalent component between lithium and surrounding chemical environments become more important. This is the first experimental evidence for forming a lithium bond between Li₂S_n and a host electron-donor site. Our results strongly suggest that forming lithium bonds with functional groups in the polymer backbone that are strong enough to overcome the dissolution interaction of the lithium polysulfides is important to reduce the diffusional loss of the active materials to the liquid electrolyte.

Membranes that can block a customized soluble redox couple in a flow-through cathode

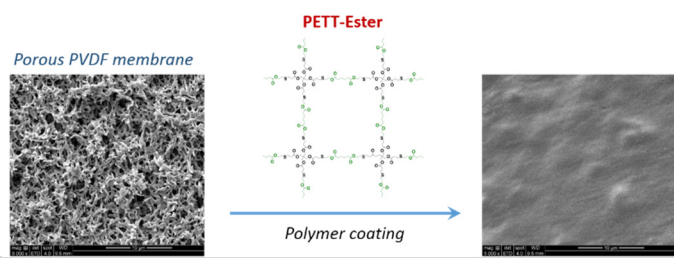


Figure V- 106: Processing scheme for PETT-Ester polymer coating on a porous PVDF membrane

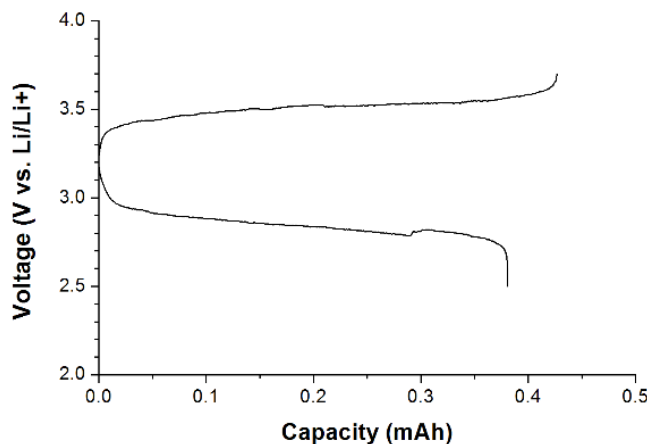


Figure V- 107: Charge/discharge voltage curves of 6-bromohexyl ferrocene catholyte with the PETT-Ester-coated PVDF membrane as a separator

separator. The ester group can transfer electronic charges to Li⁺ to bind, which hinders fast Li⁺ transport through the separator membrane. We could understand from the experiment that controlling the chemical nature of the membrane is also an important factor to control ionic transport kinetics.

Alkali-metal-free Anode

Development of a discharged cell with a bare current collector anode can further increase energy density of a cell. Alkali metal deposition on a metallic current collector was characterized with NaCrO₂ cathode and a stainless-steel current collector as anode. To enhance the mechanical integrity and electrical contact between the deposited alkali metal and current collector, stainless steel was coated with various Li⁺-conducting polymers: PETT-FC, PETT-EO, PETT-Sulfone, and PETT-Ester (See Figure V- 101). For coin cell tests, 1M NaClO₄ in EC/DEC (1/1) was used as electrolyte.

Galvanostatic charge/discharge cycling data are shown in Figure V- 108. The electrochemical performance is disappointing, but several important points were identified in this study. First, with the presence of a liquid electrolyte, there is a voltage plateau at ~ 2 V vs. Na/Na⁺ in all the cells, which corresponds to the formation of the SEI layer. The extent of the plateau directly affects initial coulombic efficiency: for example, PETT-EO

In order to utilize a liquid cathode, we tried to make thin, flexible and mechanically robust membranes that physically or chemically block the crossover of redox-molecules. We adopt a porous PVDF membrane as a support and coated the desired polymer layer on it. Figure V- 106 shows the processing scheme. The PVDF membrane was treated to make its surface hydrophilic, so the PETT-Ester monomer solution could wet the surface homogeneously. In this way, we were able to control the membrane thickness and to eliminate rolling of the membrane after the coating or electrolyte soaking.

The fabricated PETT-Ester on PVDF membrane was used as a separator in a cell with a liquid cathode. The redox molecule in the catholyte is 6-bromohexyl ferrocene and lithium metal was used as the anode. Figure V- 107 shows intial charge/discharge voltage curves of the half-cell. Electrochemical activity of the Fe(III)/Fe(II) redox couple was clearly observed, so the membrane is permeable to the charge carrier, Li⁺-ions. However, the voltage curves show a notable polarization. We attribute the cell impedance to the trapping of the Li⁺ ions by the electron-donating nature of the ester groups in the

and PETT-Sulfone have less SEI formation and higher coulombic efficiencies (>50%) while PETT-FC and PETT-Ester have more pronounced plateaus and lower efficiencies (<40%). Second, cycle performance is poor regardless of the different polymers. The liquid electrolyte reacts with fresh sodium dendrites in each cycle, which robs reversible working ions indefinitely. The formation of sodium dendrites with a liquid electrolyte is prone to rob working ions irreversibly.

Therefore, in order to use a liquid electrolyte, the current collector should have a surface layer that can promote wetting of the current-collector surface by an electrodeposited alkali metal. However, unfortunately it cannot guarantee stable long-term cycle life if the dendrite problems are still present. An alternative method is to use a dry solid electrolyte membrane that can eliminate SEI layer formation and block dendrite penetration.

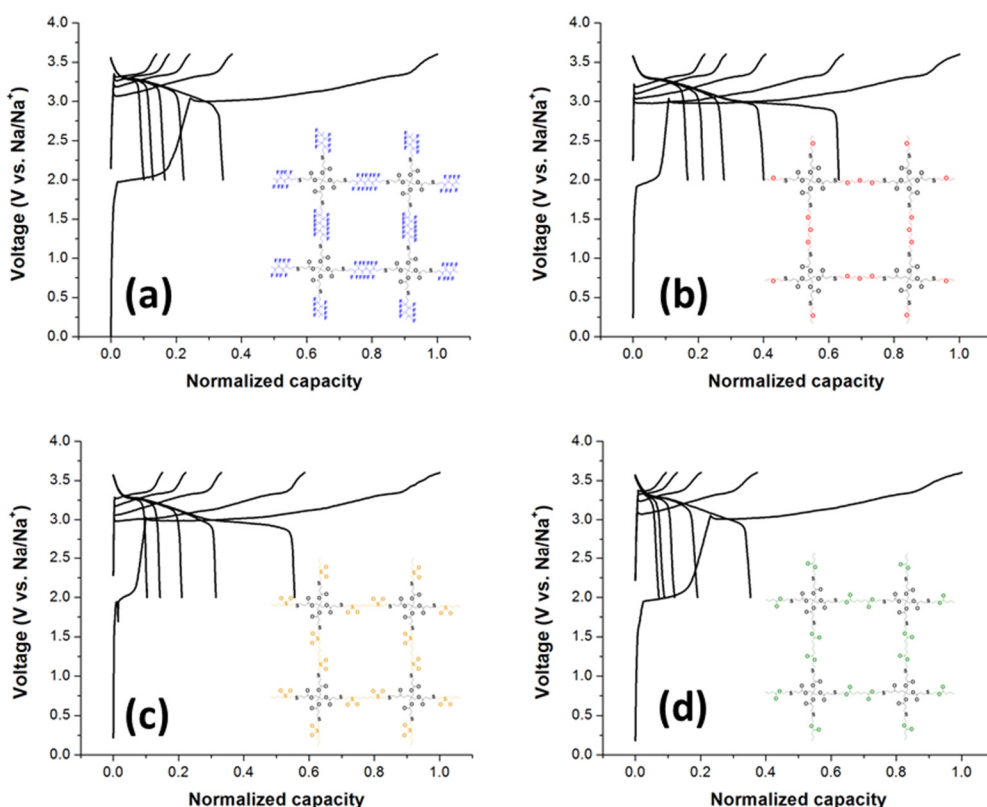


Figure V- 108: Initial 5 charge/discharge voltage curves of NaCrO_2 with bare stainless steel anode current collector coated with various polymers. (a) PETT-FC, (b) PETT-EO, (c) PETT-Sulfone and (d) PETT-Ester

Conclusions and Future Directions

From our studies, it is clear that a membrane separator containing an organic-liquid electrolyte does not solve the problem of an alkali-metal anode even if it blocks dendrites from the anode. It is necessary to develop a dry-polymer or a solid electrolyte that is not reduced on contact with an alkali metals and that prevents formation of alkali-metal dendrites or blocks them. If an alkali-metal anode can be plated reversibly on the anode current collector and is stable in the organic electrolyte, then the small amount of organic liquid electrolyte needed to access the existing cathode strategies, including insertion-compound hosts, flow-through liquid cathodes, and sulfur cathodes can be used without safety problems. We are in the process of testing a glass solid electrolyte to ensure alkali-metal plating through it with a long cycle life. Rechargeable Li and Na batteries will be fabricated and tested to demonstrate cells with an alkali-metal anode.

FY 2015 Publications/Presentations

1. "Trapping lithium polysulfides by forming lithium bonds in polymer electrolytes for a Li-S battery", K. Park, J. H. Cho, J. H. Jang, B. C. Yu, A. T. De La Hoz, K. M. Miller, C. J. Ellison, J. B. Goodenough, *Energy Environ. Sci.* **8**, 2389-2395 (2015).

V.D.10 Exploiting Co and Ni Spinels in Structurally-Integrated Composite Electrodes (ANL)

Objectives

- The goal of this new project is to minimize or eliminate the voltage fade phenomenon in high capacity ‘layered-layered’ cathodes by introducing a stabilizing spinel component into the composite electrode structure with a particular emphasis on employing lithium-cobalt-oxide and lithium-nickel-oxide spinel components that can accommodate lithium at approximately 3.5 V vs. metallic lithium.

Technical Barriers

- Low energy density
- Cost
- Abuse tolerance limitations.

Technical Targets (USABC – End of life)

- 142 Wh/kg, 317 W/kg (PHEV 40 mile).
- Cycle life: 5000 cycles.
- Calendar life: 15 years.

Accomplishments

- Initiated studies of lithium-cobalt-oxide and lithium-cobalt-nickel-oxide spinel structures with the view to using them as stabilizers in high capacity ‘layered-layered-spinel’ cathode structures.
- Initiated collaborations with outside organizations and facilities, such as the Northwestern University Atomic and Nanoscale Experimental Center (NUANCE) and Pacific Northwest National Laboratory’s Environmental Molecular Sciences Laboratory (MSRL) to assist with the characterization of the cathode materials.
- Initiated computational studies to simulate the structural and electrochemical properties of ‘layered-layered-spinel’ compositions relevant to this project.
- Filed three spinel-related patents on materials related to this project at the USPTO.

Introduction

Lithium- and manganese-rich $x\text{Li}_2\text{MnO}_3 \bullet (1-x)\text{LiMO}_2$ ($\text{M}=\text{Mn, Ni, Co}$) ‘layered-layered’ materials provide an opportunity to significantly advance the energy density of state-of-the-art lithium batteries. However, the structural instability of these electrode materials at high potentials both at the surface and within the bulk leads to voltage fade during cycling, which has slowed their entry into the lithium battery market. This project addresses this limitation by embedding a spinel component in the ‘layered-layered’ electrode to create a ‘layered-layered-spinel’ composite structure, thereby placing transition metal ions in the lithium layers to stabilize the structure at low lithium loadings and to prevent the migration of transition metal ions during the electrochemical reactions during both charge and discharge. This is a relatively new area of research, which provides the opportunity to generate intellectual property to protect advances in lithium battery materials and technologies.

Project Details

Michael Thackeray (Argonne National Lab, PI)
9700 South Cass Avenue
Argonne, IL 60439
Phone: 630-252-9184; Fax: 620-252-4176
E-mail: thackeray@anl.gov

Jason R. Croy (Argonne National Lab, Co-PI)
9700 South Cass Avenue
Argonne, IL 60439
Phone: 630-252-5917; Fax: 620-252-4176
E-mail: croy@anl.gov

Start Date: October 2014
Projected End Date: September 2018

Approach

- Design, synthesize and screen spinel compositions and structures comprising cobalt and/or nickel that operate above 3 V and below 4 V and determine their structural and electrochemical properties.
- Evaluate and identify the most promising spinel structures and compositions as stabilizers for high capacity, composite ‘layered-layered-spinel’ cathode materials.
- Generate IP to protect new materials discoveries and developments.
- Interface this project with BMR Task 5.8, *Energy Storage Materials Research using DOE’s User Facilities and Beyond*, to undertake detailed characterization studies of the spinel end-members and corresponding composite ‘layered-layered-spinel’ structures.
- Perform complementary computational studies to aid the compositional and structural design of NMC-based ‘layered-layered-spinel’ structures.

Results

Low-Temperature (LT) Lithium-Cobalt-Nickel-Oxide Spinel

Low-temperature firing of precursor materials such as Li_2CoO_3 , CoCO_3 and NiCO_3 at 400 °C results in complex Li-Co-Ni-O rocksalt structures with lithiated spinel character that can be represented ideally as $\text{Li}_2[\text{Co}_{2-\delta}\text{Ni}_\delta]\text{O}_4$ or simply, $\text{LiCo}_{1-x}\text{Ni}_x\text{O}_2$ [1,2]. These lithiated spinels are attractive cathode materials because they can release and reaccommodate 0.5 Li per transition metal ion at approximately 3.5 V vs. lithium metal. Although these spinels do not cycle particularly well, it has been demonstrated in a parallel Task of the BMR program (Task 3.5) that a spinel-like component, in minor concentration, can stabilize and suppress the voltage fade phenomenon that is observed in high capacity, lithium- and manganese-rich ‘layered-layered’ electrodes. This project is therefore focused on exploiting spinel-related materials in the system $\text{LiCo}_{1-x}\text{Ni}_x\text{O}_2$ as stabilizers for ‘layered-layered’ electrodes. To initiate this project, the structural and electrochemical properties of cobalt- and nickel-containing spinel materials were therefore evaluated to identify the most promising compositions.

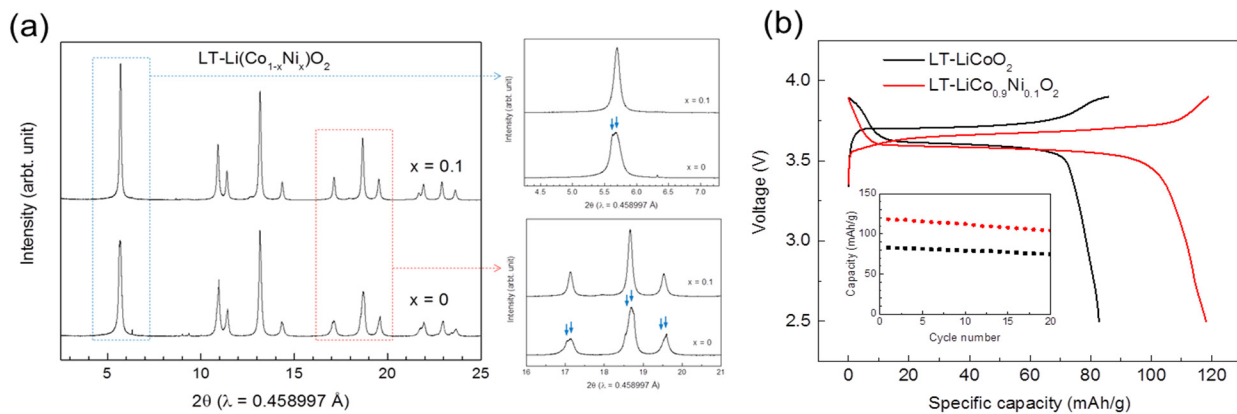


Figure V-109: (a) Synchrotron HR-XRD patterns and (b) initial voltage profiles of Li/LT-Li $\text{Co}_{1-x}\text{Ni}_x\text{O}_2$ ($x = 0$ and 0.1) cells cycled between 2.5 and 3.9 V at the rate of 15 mA/g. The selected 2θ ranges in (a), highlighted in separate panes, show the non-uniform distribution of lattice parameters in LT-Li CoO_2 . Inset in (b) compares the cycling stability of LT-Li CoO_2 and LT-Li $\text{Co}_{0.9}\text{Ni}_{0.1}\text{O}_2$.

Phase pure $\text{LiCo}_{1-x}\text{Ni}_x\text{O}_2$ samples were obtained when synthesized from a carbonate precursors; impurity phases such as Co_3O_4 were detected when oxide or hydroxide precursors were used. Figure V-109(a) shows high-resolution (synchrotron) X-ray diffraction (HR-XRD) patterns obtained at Argonne’s Advanced Photon Source for samples with $x = 0$ and 0.1 . Compared to layered LiCoO_2 , which is typically prepared at higher temperature (e.g., 900 °C), the HR-XRD pattern of LT-Li CoO_2 shows an overlap of the (006) and (012) reflections, and (018) and (110) reflections, indicating a spinel-like arrangement of the cobalt ions. High-resolution data revealed a slight splitting of all the peaks, suggesting a non-uniform distribution of lattice parameters and cobalt ions within the samples. In contrast, the HR-XRD pattern of LT-Li $\text{Co}_{0.9}\text{Ni}_{0.1}\text{O}_2$ revealed a better-defined lithiated spinel lattice. A comparison of the electrochemistry of the LT-Li CoO_2 vs. LT-Li $\text{Co}_{0.9}\text{Ni}_{0.1}\text{O}_2$ electrodes is shown in Figure V-109(b). It is apparent that Ni substitution significantly

improves the capacity and stability of the spinel electrode, the LT-LiCo_{0.9}Ni_{0.1}O₂ electrode initially yielding 120 mAh/g at ~3.6 V, relative to LT-LiCoO₂ (80 mAh/g).

The Conversion of Spinel LT-LiCo_{1-x}Ni_xO₂ to Layered HT-LiCo_{1-x}Ni_xO₂

A systematic study of the effects of synthesis temperature and time on the structure and electrochemical performance of LiCo_{1-x}Ni_xO₂ electrode materials was undertaken. LiCo_{1-x}Ni_xO₂ ($x = 0.1$ and 0.2) compounds were synthesized at various temperatures (400 – 800 °C) and dwell times (days, d). A cubic structure closely resembling a lithiated spinel was obtained for LiCo_{0.9}Ni_{0.1}O₂ at 400 °C (Figure V- 109a). An impurity, Li_xNi_{1-x}O, rock-salt phase was observed in the 400°C-3d sample but disappeared after 6 days of annealing. The XRD patterns of the 500°C-6d and 600°C-4d samples could also be indexed to a spinel phase. However, the 600°C-4d sample showed an asymmetric broadening of the (044) peak, indicating the onset of cobalt/nickel layering. The XRD patterns of the samples synthesized at 700 °C and higher clearly showed the further development of the layered structure, as reflected by the splitting of the cubic (044) peak of the spinel phase into the (018) and (110) peaks of the layered phase. A similar trend was shown by a LiCo_{0.8}Ni_{0.2}O₂ sample.

Electrochemical data of lithium cells with LiCo_{1-x}Ni_xO₂ ($x=0.1$) electrodes, prepared at temperatures between 400 and 800 °C and cycled between 4.2 and 2.5 V, are shown in Figure V- 110b. For the higher synthesis temperatures, the sloping voltage response at ~4.0 V is characteristic of the ‘high-temperature’ (HT) layered LiCoO₂ structure, while for the lower synthesis temperatures the reaction at ~3.5 V is characteristic of the ‘low-temperature’ (LT) spinel LiCoO₂. The electrochemical profiles in Figure V- 110b show unequivocally that a structure with intermediate ‘layered-spinel’ character was generated at 600 °C. This result has important implications for controlling the number of stabilizing cations in the lithium layers of ‘layered-layered-spinel’ electrodes, which is one of the key objectives of this project.

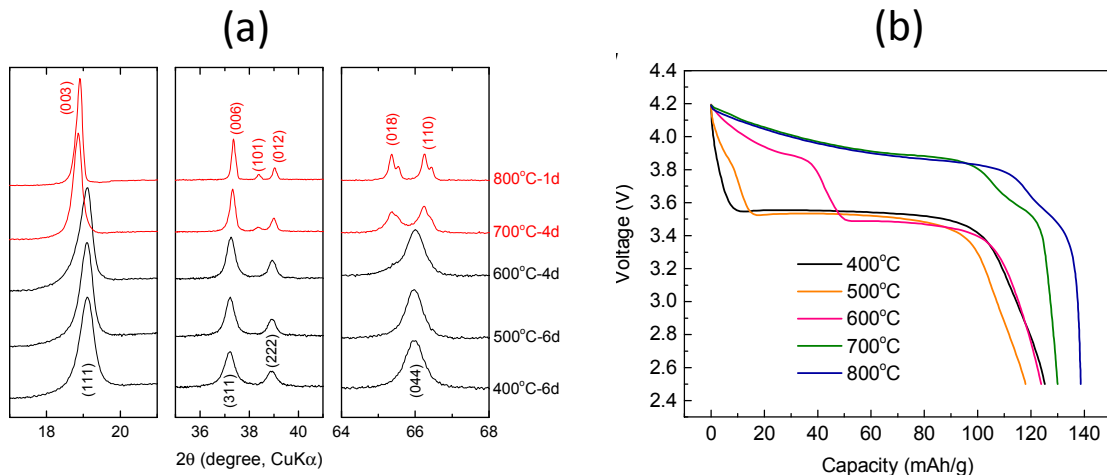


Figure V- 110: (a) XRD patterns and (b) initial discharge profiles of LiCo_{0.9}Ni_{0.1}O₂ samples synthesized at various temperatures (400 and 800 °C)

LT-LiCo_{0.9-y}Ni_{0.1}Mn_yO₂ (NMC) Spins (y = 0, 0.1, and 0.2)

A preliminary study of the effects of Mn substitution on the structure and electrochemistry of LT-LiCo_{0.9}Ni_{0.1}O₂ electrodes was undertaken. Pure LT-LiCo_{1-y}Ni_{0.1}Mn_yO₂ samples ($y=0, 0.1, 0.2$) were prepared without any noticeable impurity phases after extended periods (~7 days) of low-temperature firing of the precursor materials (Figure V- 111a). A comparison of the electrochemistry of lithium cells with LT-LiCo_{0.9}Ni_{0.1}O₂ ($y=0$) and LT-LiCo_{0.9-y}Ni_{0.1}Mn_yO₂ ($y=0.1, 0.2$) electrodes is provided in Figure V- 111b and Figure V- 111c, respectively. It appears that Mn substitution has a negative effect on the capacity of LT-LiCo_{0.9-y}Ni_{0.1}Mn_yO₂ electrodes. When cycled between 3.9 and 2.5 V, the initial discharge capacity decreases with increasing Mn substitution from 120 mAh/g ($y=0$) to 100 mAh/g for $y=0.1$, and to 80 mAh/g for $y=0.2$ (Figure V- 110b). Increasing the upper cut-off voltage to 4.2 V yields slightly higher capacities, but significantly reduces the cycling stability of the electrodes (Figure V- 111b, inset). Efforts to improve the electrochemical stability of LT-LiCo_{1-x}Ni_xO₂ electrodes by compositional control are being continued.

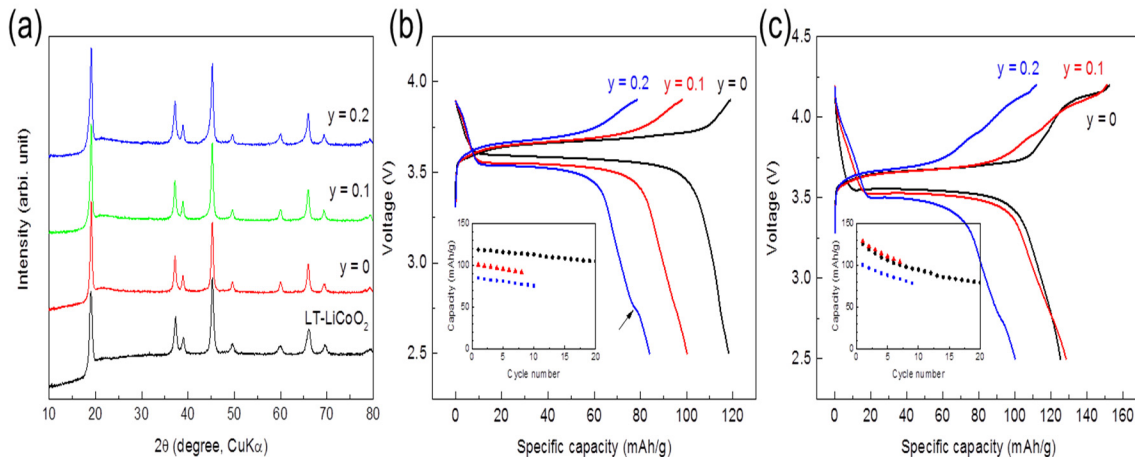


Figure V-111: (a) XRD patterns of LT-LiCoO₂ and LT-LiCo_{0.9-y}Ni_{0.1}Mn_yO₂ samples ($y = 0, 0.1$, and 0.2). Initial voltage profiles of Li/ LT-LiCo_{0.9-y}Ni_{0.1}Mn_yO₂ ($y = 0, 0.1$, and 0.2) cells charged to upper cut-off voltages of (b) 3.9 V and (c) 4.2 V at a rate of 15 mA/g. Capacity vs. cycle number plots are provided as insets in (b) and (c)

Conclusions and Future Directions

The ‘layered-layered-spinel’ (LLS) phase space is vast and largely unexplored. In this respect, the family of Co and Ni spinels that provide unique cation arrangements hold promise for stabilizing high capacity ‘layered-layered’ electrodes that suffer from voltage decay during electrochemical cycling. This approach will be vigorously pursued in FY2016 in the search for advanced cathodes for high energy lithium-ion batteries. Theoretical modeling of LLS composite materials and surfaces will complement experimental efforts.

FY 2015 Patents/Publications/Presentations

Patent Applications

- “Cobalt-Stabilized Lithium Metal Oxide Electrodes for Lithium Batteries”, M. M. Thackeray, J. R. Croy and B. R. Long, U.S. Pat. Appl. 20150180032, 25 June 2015.
- “Lithium Metal Oxide Electrodes for Lithium Batteries”, M. M. Thackeray, J. R. Croy and B. R. Long, U.S. Pat. Appl. 20150180031, 25 June 2015.
- “Lithium Metal Oxide Electrodes for Lithium Batteries”, M. M. Thackeray, J. R. Croy, B. R. Long, J. S. Park and E. Lee, ANL-IN-13-112B, U.S. Pat. Application. Filed 8 June 2015.

Presentations

- “Structure-Property Relationship of 2D Layered Materials for Sodium- and Lithium-ion Batteries”, E. Lee, Invited seminar presentation, Materials Science and Engineering Department, Northwestern University, Evanston, 7 May, 2015.
- “Progress in Designing High Capacity Cathodes for Lithium Cells - Challenges and Opportunities in an Evolving Lithium Economy”, M. M. Thackeray, Perspectives on Catalysis and Energy Workshop, Pontificia Universidad Católica de Chile, Santiago, Chile, 28 – 29 April, 2015.
- “Progress and Challenges in Designing High Capacity Cathodes for Lithium-Ion Cells”, M. M. Thackeray, B. R. Long, J. R. Croy, J. S. Park, Y. Shin, G. Krumdick, J. G. Wen and D. Miller, 32nd Annual Battery Seminar & Exhibit, Fort Lauderdale, Florida, 9-12 March 2015.
- “Designing Advanced High Capacity Electrodes for Lithium Cells”, M. M. Thackeray, J. R. Croy, B. R. Long, J. S. Park, C. S. Johnson, L. Trahey, Z. Yang, Y. Ren, D. J. Miller, J. G. Wen, A. Kinaci, M. K. Y. Chan, S. Kirklin and C. Wolverton, MRS Meeting, Boston, 30 November - 5 December, 2014.

V.E Electrolytes for High Voltage, High Energy Lithium-ion Batteries

V.E.1 Fluorinated Electrolyte for 5-V Li-ion Chemistry (ANL)

Objectives

- To develop a new advanced electrolyte system with outstanding stability at high voltage and high temperature, and improved safety characteristics for an electrochemical couple consisting of a high voltage $\text{LiNi}_{0.5}\text{Mn}_{1.5}\text{O}_4$ (LNMO) cathode and graphite anode.
- To gain a fundamental understanding of the interaction between electrolyte and high voltage electrode materials, the dependence of SEI functionality on electrolyte composition, and the effect of high temperature on full Li-ion cells using the advanced electrolyte system.

Technical Barriers

To meet the energy density requirements for Li-ion batteries established by DOE and the USABC, higher voltage and/or higher capacity cathode materials are needed for these batteries to be widely commercialized for PHEV applications.

However, the state-of-the-art (SOA) electrolytes (originally designed for 4 V Li-ion chemistry) show poor performance in 5 V Li-ion systems due to oxidative decomposition, especially at high temperatures, imposing a barrier to the application of any new cathode chemistry operating beyond 4.5 V, such as next-generation $\text{LiNi}_{0.5}\text{Mn}_{1.5}\text{O}_4$ (LNMO) or Li-Mn-rich high capacity $x\text{Li}_2\text{MnO}_3.(1-x)\text{Li}(\text{Ni}_x\text{Mn}_y\text{Co}_z)\text{O}_2$. Additionally, these electrolytes also incur safety concerns due to their high flammability.

Technical Targets

- New solvents to render intrinsic voltage and thermal stability in the entire electrochemical window of 5 V.
- New additives to enhance the formation of a robust solid electrolyte interphase (SEI), tailored for the new electrolyte.
- Fundamental understanding of the interaction between the electrolyte and the high voltage electrode.

Accomplishments

- Designed and synthesized new fluorinated linear and cyclic carbonates (FEMC, FDEC, TFPC) and a library of fluorinated sulfones.
- Developed a screening method for oxidation stability of the synthesized F-solvents.
- Optimized the ternary F-electrolyte formulations by the oxidation stability, conductivity, electrode/separator wettability, and coulombic efficiency in LNMO/Li cell.
- Achieved good compatibility with graphite anode by dual-function F-carbonates of fluoroethylene carbonate (FEC) and trifluoropropylene carbonate (TFPC) PC acting both the co-solvent and SEI formation additive.

Project Details

Tien Duong (VTO Program Manager)

DOE-EERE-VTO Agreement # 27037

Zhengcheng Zhang (Argonne National Laboratory – PD/PI)

9700 S. Cass Avenue, B200

Argonne, IL 60439

Phone: 650-252-7868; Fax: 630-972-4440

E-mail: zhang@anl.gov

Subcontractor:

US Army Research Laboratory

2800 Powder Mill Road

Adelphi, MD20783

Brookhaven National Laboratory

53 Bell Avenue

Upton, NY 11973-5000

Start Date: October 2013

Projected End Date: September 2015

- Developed two fluorinated electrolyte formulations that not only showed improved oxidation stability with 5-V LNMO, but also stable cycling performance in LNMO/graphite full cells.
- Achieved stable charge/discharge cycling performance with the optimal electrolyte in a LNMO/graphite cells at both room and high temperature (55°C).
- Demonstrated the improved oxidation stability of the F-electrolyte in the layer-structured $\text{LiNi}_{0.5}\text{Co}_{0.2}\text{Mn}_{0.3}$ (NCM523)/graphite cycled at 4.6 V vs Li^+/Li .
- Investigated the Li^+ solvation and Li^+ -F-Solvent interaction by 2D DOSY-NMR spectroscopy.
- Performed the diagnosis analysis of the surface morphology and chemical composition of the cycled LNMO and graphite electrode with fluorinated electrolyte by SEM/TEM, XPS, ICP-MS, FT-IR.
- Demonstrated the presence of extra Li for further extension of the cycle life of LNMO/graphite cells at 55°C.
- Fabricated 100mAh pouch cells with the optimized fluorinated electrolyte and verified the performance from the coin cell data.

Introduction

To meet or exceed the 40-mile electric drive range target for PHEV, it is the most efficient approach to further increase either the capacity or the voltage of the cathode materials on the chemistry level. High-voltage high capacity cathode materials have been developed, such as $\text{LiNi}_{0.5}\text{Mn}_{1.5}\text{O}_4$ (4.8 V), $\text{LiCo}_{0.5}\text{Mn}_{1.5}\text{O}_4$ (5.1 V), and LiCoPO_4 (5.1 V). However, their increased operating voltage presents challenges to conventional electrolytes, whose carbonate-based components tend to oxidatively decompose above 4.5 V. Our recent research on Gen 2 electrolytes with LNMO/graphite couples suggests that the SOA electrolytes are not suitable for high-voltage Li-ion batteries that operate beyond 4.8 V, especially at high temperatures.

In this project, we tried to resolve these issues with new solvents and additives, and used a LNMO/graphite couple as a screening baseline to demonstrate the feasibility of the proposed high voltage electrolytes.

Approach

To achieve the above-mentioned goal, our approach was to explore intrinsically stable fluorinated electrolyte solvents to provide thermodynamic stability that addressed the voltage instability of the current electrolyte. Figure V- 112 illustrated the approach undertaken for this project and will be discussed in detail in the next section. The selection, design, and synthesis of the fluorinated solvents were guided by highly accurate quantum chemistry modeling. Development of the optimal high voltage electrolyte formulation was greatly accelerated by a floating test. To further mitigate the surface reactivity of high voltage cathodes such as LNMO, advanced additives based on highly fluorinated carbonate and phosphates that help in delivering F-alkyls onto cathode surfaces were made, as well as SEI additives tailored for the graphite anode. Extensive material surface and bulk diagnosis using x-ray techniques and atomic force microscopy (AFM) were employed to gain a deep understanding of the success/failure mechanism of the proposed new fluorinated electrolyte under various operating conditions.

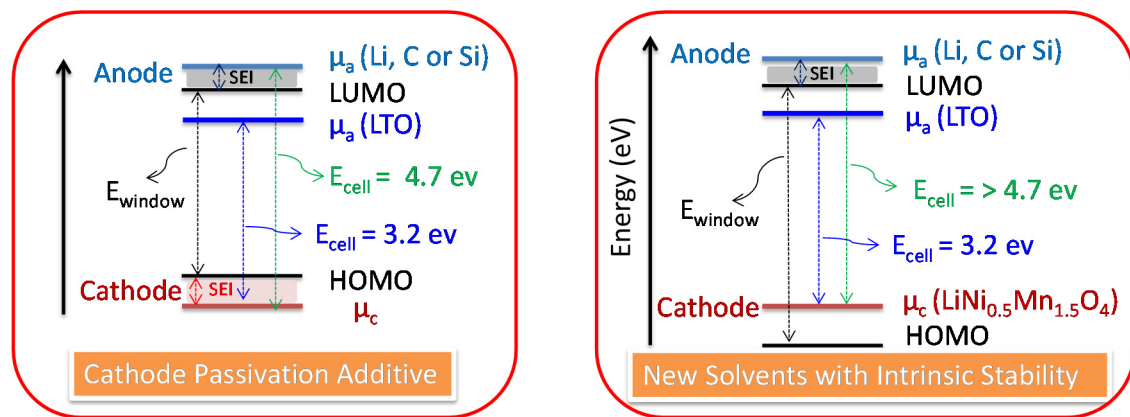


Figure V- 112: Design principle for high voltage electrolytes

Results

We have achieved the following progress in FY15:

Electrolyte Design Principal and Molecular Engineering

An ideal electrolyte must be polar enough to dissociate a salt while remaining thermodynamically stable in a wide potential range (0-5.0V vs Li). These two requirements essentially limit the choice of solvents to only a few families of aprotic organic compounds. Up to date, carbonate solvents are the main stream of electrolyte materials for Li-ion battery in commercial cells and in the R&D labs due to the fact that the skeleton of the solvent provides excellent salt solubility, voltage stability, and super ability to passivate the carbonaceous anode. To further increase its voltage stability, new design should be considered. Fluorination is a commonly used practice to modify electrolyte solvent structure. Generally, introduction of -F group or fluorinated alkyl groups into an carbonate results in the drop of the energy level for both the highest occupied molecular orbital (HOMO) and the lowest unoccupied molecular orbital (LUMO). The former will lead to higher resistance against oxidation, while the latter to lower the resistance against reduction, which might seem to be disadvantage, but as taught by preceding experiences and knowledge about interphasial chemistry, it could also signify better (denser) SEI film as the formation starts at a higher potential. An alternative approach is to employ an electrolyte additive in the state-of-the-art electrolyte to passivate the cathode surface providing kinetic stability on the cathode surface, an idea borrowed right from the SEI formation on the graphite anode. The design diagrams of the solvents with high oxidation stability and new additives for cathode passivation are depicted in Table V- 3.

Table V- 3: HOMO-LUMO energetics of electrolyte solvents and additives

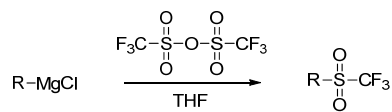
Molecular Structure	Oxidation Potential (P_{ox}/V)	Anion Effect Potential (P_{ox}/V)	Reduction Potential (P_{red}/V)	Stretch Bond Potentials (P_{red}/V)
	7.10 (6.62, EMC)	6.26 (PF_6 ; HF forms) 5.79 (TFSI; H transfer)	0.03	1.40 ($\text{CF}_3\text{CH}_2\text{-O}$) 1.49 ($\text{CH}_3\text{-O}$)
	7.96 (6.46)	7.69 (PF_6) 5.76 (TFSI)	1.29	1.54 ($\text{CF}_3\text{CH}_2\text{-O}$) 2.39 ((CF_3) ₂ CH-O) 1.47 ($\text{CF}_3\text{-O}$)
	7.25 (6.51, DEC)	7.35 (PF_6) -	0.22	1.65 ($\text{CF}_3\text{CH}_2\text{-O}$)
	7.30 (6.80, PC)	6.21 (PF_6) 5.33, 5.44, 5.87 (TFSI)	1.54 (spontaneous C-O bond opening)	
	7.24 (6.95, EC)	6.44 (PF_6) 5.80 (TFSI)	0.33	1.56 (CHF-O)
	6.70 (6.29, MPS)	-	-	1.51 (0.79)
	6.76 (6.34, EMS)	-	-	1.43 (0.80)

oxidation stability depending upon the nature of the substitution. The oxidation voltage of a fully fluorinated methyl isopropyl carbonate is calculated to be 7.96 V, which is 1.5 V higher than methyl isopropyl carbonate. Similarly, fluorination of sulfone can also elevate the voltage stability. Besides, the fluorination of sulfone could lower the melting point and viscosity of the electrolyte, two prerequisite for an ideal electrolyte.

Synthesis of F-Carbonates and F-Sulfones and High Voltage Electrolyte Formulation

The selected fluorinated compounds were synthesized using various routes depending on the structure of the molecule. Figure V- 113 illustrated the organic synthesis of TFP-PC-E by reacting the corresponding fluorinated epoxide and CO_2 gas. The reaction was closely monitored by NMR and GC-MS. Upon completion, pure compound was obtained by fractional distillation (90-100°C/0.2 mmHg) with an isolated yield of 37%. The chemical structure of TFP-PC-E was identified by ¹H (lower left), ¹³C, ¹⁹F NMR and GC-MS (lower right) with a purity level of > 99.8%. The moisture level of these synthesized compounds was determined by Karl Fischer titration and controlled below 20 ppm.

A new class of fluorinated sulfone compounds is also considered for this project. As a widely studied high voltage electrolyte, there are only reports on several sulfones and the F-sulfone is quite rare. Table V- 3 listed the DFT calculation results of the representative F-carbonates and F-sulfones compared with their non-fluorinated counterparts. It revealed that fluorination enhances various degree of



Scheme 1: Synthesis of F-sulfones

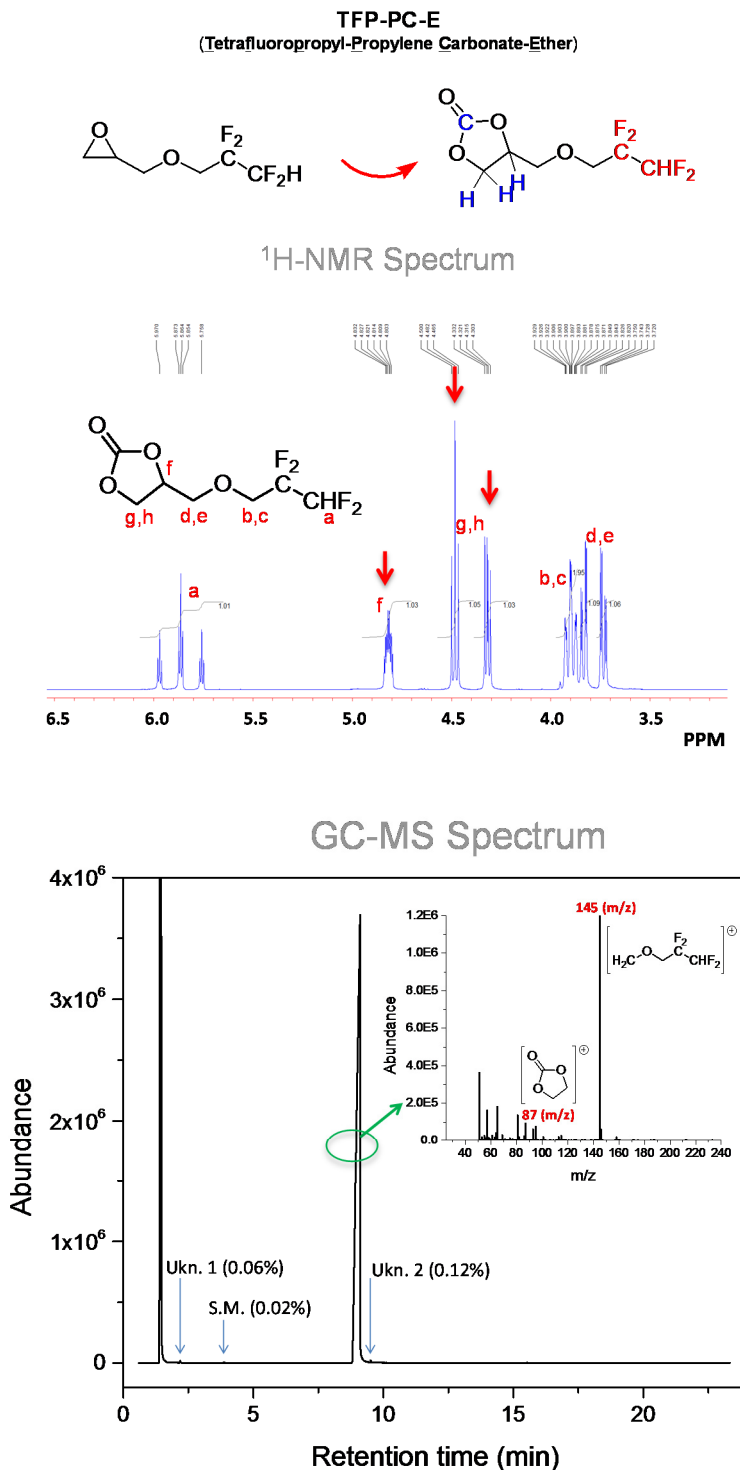


Figure V- 113: Synthesis of F-carbonate and $^1\text{H-NMR}$ and GC-MS spectra

The only reported synthesis of sulfones adopted a route of oxidation of the corresponding thiol ether, a liquid with extremely low b.p. and difficult for handling, purification. Besides, this methodology involves the use of the highly explosive peroxide reagent. We developed a facile one-step synthesis with the corresponding Grignard reagent and trifluoromethanesulfonic anhydride as shown in Scheme 1.

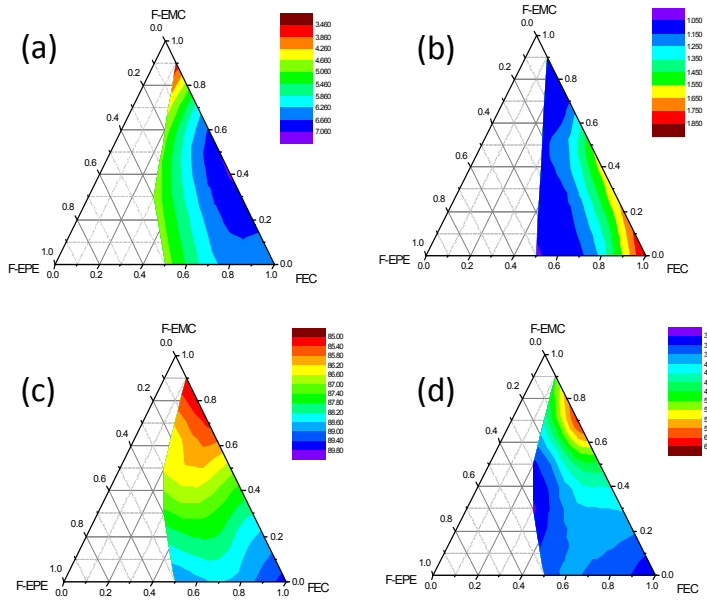


Figure V-114: Optimization of ternary fluorinated electrolytes

surface of electrode, potential polarization during charge and discharge, concentration effect on the voltage stability, the final formulation of this ternary electrolyte has been determined as follows: 30-50% FEC, 20-50% F-EMC and 10-30% F-EPE with 1.0 M LiPF₆.

Li⁺-Solvation and Li⁺-Solvent interaction in F-electrolyte solutions

Ion conductivity is a key electrolyte property, as it quantified how mobile the ions are for the redox reaction, which in part determines the power capability of the cell. Since no single solvent meets all the requirements of an electrolyte (dielectric permittivity, low viscosity, interfacial stability on both cathode and anode), solvents with various properties are usually mixed. 1.0 M LiPF₆ FEC/F-EMC/F-EPE (3/6/2 in volume) is the optimal electrolyte for high voltage application. To understand the ion-solvent interaction, 2-D NMR was performed.

Table V-4: Li salt dissociation in fluorinated electrolyte by 2D-DOSY NMR

T(K)	D _{Li} (m ² /s)	D _{PF6} (m ² /s)	t _{Li+}	Λ _{NMR} (mScm ⁻¹)	Λ _{imp} (mScm ⁻¹)	Λ _{imp} / Λ _{NMR}
283 (10°C)	1.94e-10	1.66e-10	0.54	4.92	1.22	0.25
293	2.37e-10	2.23e-10	0.51	6.08	1.39	0.23
303	3.13e-10	2.83e-10	0.53	7.61	1.55	0.20
313	5.07e-10	3.64e-10	0.58	10.8	1.69	0.16

Nernst-Einstein equation

$$\Lambda_m^0 = c(F^2/RT)(v_+z_+^2D_+ + v_-z_-^2D_-)$$

$$D_{Li} = xD_{ion} + yD_{ion\ pair} + zD_{aggregates}$$

The solvation of lithium salt in fluorinated carbonate electrolytes was characterized by diffusion-ordered spectroscopy (DOSY) NMR. The self-diffusion coefficients of Li⁺, PF₆⁻ and carbonates can be deduced by the measured attenuation curves. The ion dissociation of 1.0 M LiPF₆ FEC/F-EMC/F-EPE (3/6/2 in volume) was evaluated by the 2D DOSY-NMR. The ionic conductivity is calculated by the Nernst-Einstein equation (Scheme 1) after obtaining the self-diffusion coefficients of Li⁺ and PF₆⁻. In the Nernst-Einstein equation, c is the concentration of lithium salt, F is the Faraday constant, R is the gas constant, T is the temperature and D is the diffusion coefficient. However, the ionic conductivity calculated from the diffusion coefficients (Λ_{NMR}) is an overestimation of the actual value since the DOSY-NMR measured self-diffusion coefficients of Li⁺ and

Figure V-114 shows the optimization of the F-carbonate electrolyte formulation for a ternary solvents in terms of conductivity (a), wettability (b), coulombic efficiency (c) and oxidation stability at 4.9 V (d). The physical and electrochemical properties of the ternary electrolyte system with fluoroethylene carbonate (FEC), 2,2,2-trifluoroethylmethyl carbonate (F-EMC) and 1,1,2,2-tetrafluoroethyl-2,2,3,3-tetrafluoropropyl ether (F-EPE) were measured using a.c. impedance method for conductivity and separator wettability and LNMO/Li cells for coulombic efficiency and leakage current (at 4.9 V voltage holding for 10h). All the data were plotted in format of the triangle diagrams in Figure V-114. Combined with other properties such as electrolyte contact angle on the

PF_6^- are the weighted average of the diffusion coefficients of separated ions, ion pairs and aggregates. The DOSY-NMR technique cannot distinguish those species at room temperature because their exchange times are faster than the NMR time. Alternatively, the ionic conductivity measured from impedance spectroscopy (Λ_{IMP}) should only be contributed by the self-diffusion of free ions. Thus, the ratio of $\Lambda_{\text{IMP}}/\Lambda_{\text{NMR}}$ was used to assess the extent of ion dissociation in the electrolyte. Table V- 4 summarized the ratios of $\Lambda_{\text{IMP}}/\Lambda_{\text{NMR}}$ of fluorinated electrolyte at different temperature. The value of $\Lambda_{\text{IMP}}/\Lambda_{\text{NMR}}$ ranges from 0.16 to 0.25 is generally smaller than that of Gen 2 electrolyte (0.6); however, the value of Λ_{IMP} is still much larger than $0.1 \times 10^{-3} \text{ S/cm}$, indicating an ionic conductivity sufficient enough as battery electrolyte.

2D DOSY-NMR technique was also used to assess the relative affinity for lithium between fluorinated and the non-fluorinated carbonates. The peak assignment of EMC and FEMC was first deduced by a series of 1D and 2D NMR techniques including COSY, HSQC and HMBC. After assigning all the peaks, DOSY-NMR was conducted to determine the diffusion coefficients of EMC and FEMC in a 1:1 molar ratio solution with and without the addition of LiPF_6 (0.25 molar ratio to EMC) using benzene- d_6 as external reference. As depicted in Figure V- 115, the diffusion coefficient of FEMC is smaller than that of EMC in a solution without salt, due to the bigger size of FEMC ($F_w=158$) than that of EMC ($F_w=104$). However, the diffusion coefficient of FEMC is larger than that of EMC with the addition of LiPF_6 (1:9 total molar ratio) (Figure V- 116), implying a formation of complex between salt and solvent molecules. It can be perceived that a portion of EMC and FEMC bind with LiPF_6 to form different complexes. As mentioned above, the diffusion coefficient measured by DOSY-NMR at room temperature is the weighted average of all the species presented in the solution, also, the diffusion coefficients of salt-solvent complexes are much smaller than those of free solvent molecules because the complexes have much larger hydrodynamic radii. The fact that EMC diffuses slower than FEMC with the addition of LiPF_6 indicate a significantly larger portion of EMC is complexed with LiPF_6 salt. Therefore, EMC has a significantly higher affinity to Li^+ than FEMC. The result can be explained by the fact that the electronegative fluorinated ethyl group in FEMC reduces the electron density of the carbonyl oxygen, rendering FEMC a lower binding affinity towards Li^+ . Other carbonate couples such as EC/FEC, PC/ TFPC are consistent with EMC/FEMC. Nevertheless, specific details of these interactions remains to be understood and these are not the focus of this project.

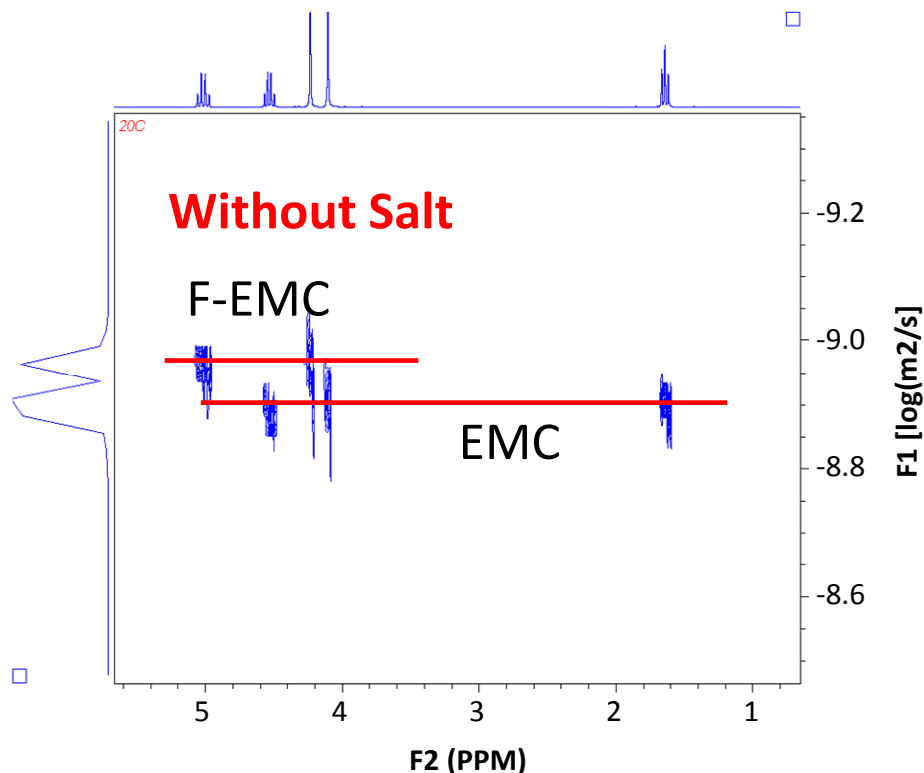
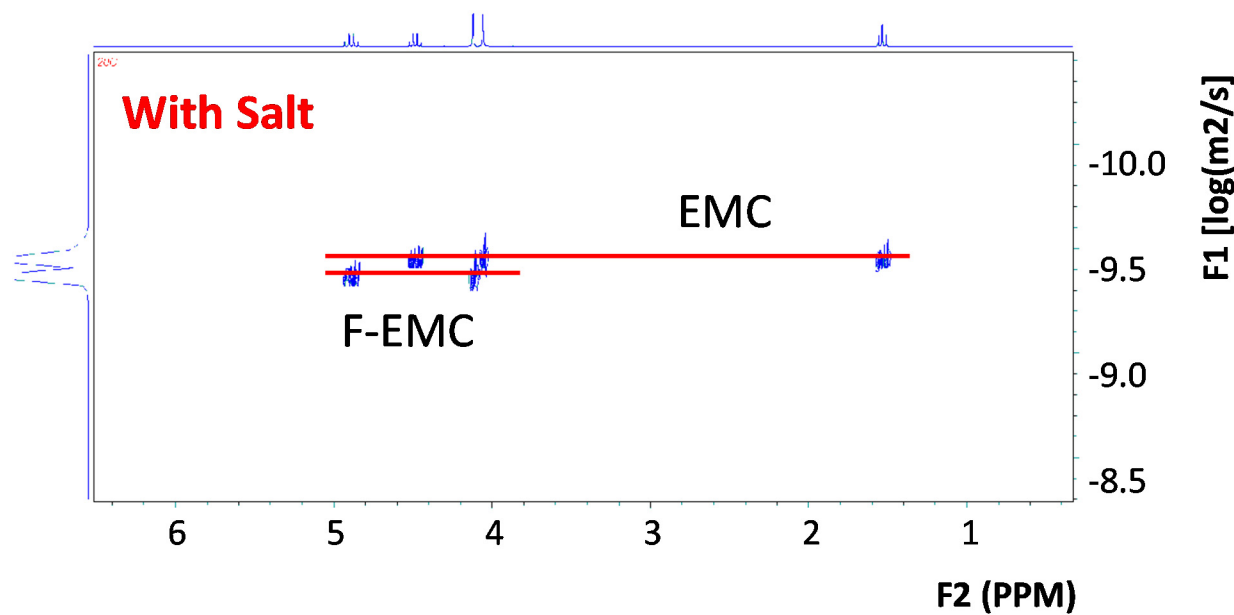


Figure V- 115: Diffusion coefficients of EMC and FEMC in a 1:1 molar ratio solution

Figure V- 116: Diffusion coefficients of EMC and FEMC in a 1:1 molar ratio solution with 0.5 M LiPF₆

Enhanced oxidation stability at 55°C

LNMO/Li cells were assembled with electrolyte containing fluorinated cyclic and linear carbonates (1:1 ratio, 0.5 M LiPF₆) and the cells were then charged and maintained at 4.9 V, 5.0 V, 5.1 V and 5.2 V for 10h, respectively. Figure V- 117 shows the leakage currents. The electrolytes with F-cyclic carbonates showed similar leakage current at RT (data not shown); however, a large increase in current was observed when the temperature was raised to 55°C, with FEC being the most stable and TFE-PC-E being the least stable F-cyclic carbonate. Cycling performance of LNMO/Li cells also confirmed the enhanced stability of the F-electrolyte as shown in Figure V- 118 and Figure V- 119. The electrolytes for this test are 1.0 M LiPF₆ TFPC/F-EMC 3:7 V/V and 1.0 M LiPF₆ FEC/F-EMC/F-EPE 3:5:2 V/V/V.

Improved high voltage stability with LNMO/graphite full cell

It is a fair statement that developing new electrolyte is virtually to fix the interfacial stability on both electrodes. F-carbonate solvents are more oxidatively stable than their non-fluorinated counterparts. However, the incompatibility with graphite anode or lack of surface passivation is a formidable challenge. Developing the magical additive tailored to the specific electrolyte is beyond the capability of theory modeling and experimental practice.

A library of electrolyte formulations was prepared and a few electrolytes have shown surprisingly stability on both LNMO cathode and A12 graphite anode. HVE3 comprises 1.0 M LiPF₆ in FEC/F-EMC/F-EPE=3/5/2 v/v/v with 1% LiDFOB and it improved the capacity retention of the LNMO/A12 cell at 55°C (Figure V- 120). HVE2 (1.0 M LiPF₆ in TFPC/F-EMC/F-EPE=3/5/2 v/v/v with 1% LiDFOB) comprised of TFPC, a trifluoromethyl substituted EC, showed excellent capacity retention; however, the initial capacity is low due to an SEI formation issue on the graphite anode. Other than the cell cycling test, cell self-discharge from a fully charged condition has also been evaluated and the fluorinated electrolyte HVE3 shows at least twice the storage life of the Gen 2 electrolyte. In FY15, tailored additives were designed and synthesized. Initial tests indicate that these additives can sufficiently suppress the co-intercalation of PC-based electrolytes by forming a good SEI on the graphite surface. The sufficiency of these additives for F-electrolytes is under investigation.

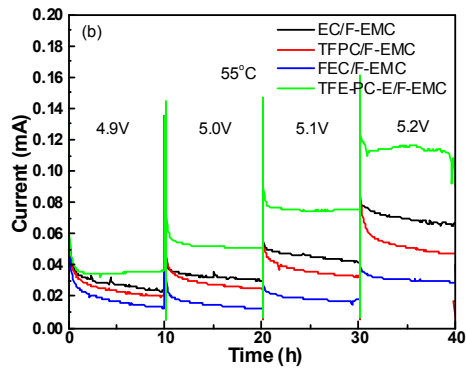


Figure V- 117: Leakage current measured at 55°C

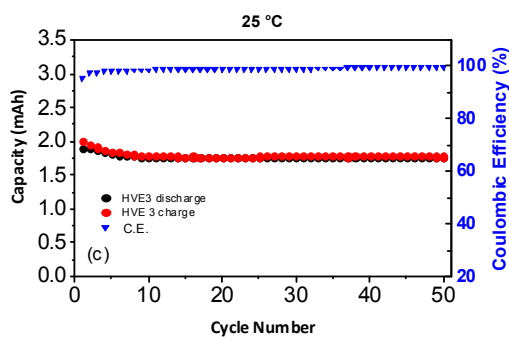


Figure V- 118: Cycling data of LNMO/1.0 M LiPF₆ in TFPC/F-EMC/F-EPE=3/5/2 v/v/v with 1% LiDFOB/Li cells

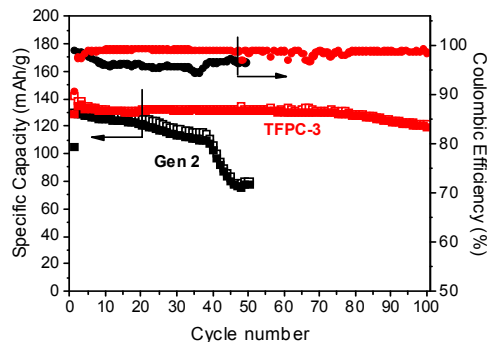


Figure V- 119: Capacity retention of LNMO/graphite cells with 1.0 M LiPF₆ TFPC/F-EMC 3:7 V/V

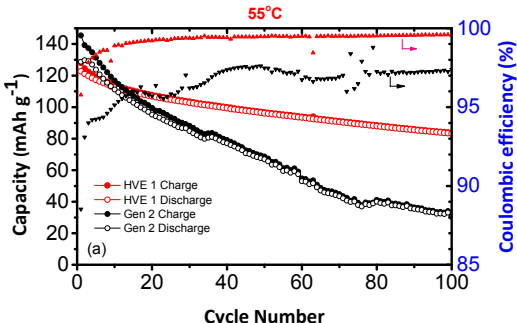


Figure V- 120: Capacity retention of LNMO/graphite cells with 1.0 M LiPF₆ FEC/F-EMC/F-EPE 3:5:2 V/V

Solid Electrolyte Interface Formation Capability on Graphite Anode

The conventional carbonate electrolytes show unique surface chemistries on graphitic anode materials, which provide the key to supporting the reversible intercalation/deintercalation of the Li⁺ with graphite that occurs at the potential far beyond the stability limit of the electrolyte solvents. Low LUMO energies imply that fluorinated solvents are more prone to be reduced at potentials much more positive than that of the Li⁺ intercalation/deintercalation. Our graphite/Li half cells data clearly showed that SEI formation on the graphite anode is dependent on the nature of F-solvents (Figure V- 121). Among all candidates, FEC (Figure V- 121c) and TFPC (Figure V- 121d) are proved to be sufficient to passivate the graphite edge surface and enable the reversible intercalation chemistry. This SEI can be further enhanced by the addition of LiDFOB which reduces at 1.5~1.7 V vs Li, the same range of potential where F-solvents are reduced.

Electrode Post-test Analysis by SEM

TEM images of the harvested LNMO cathodes from the LNMO/graphite cells cycled at 55 °C are shown in Figure V- 122. While the pristine cathode shows mostly clean LNMO crystals, the cycled cathode using Gen 2 electrolyte shows a loose morphology and cracked structure on the LNMO particle surface. In contrast, the HVE3 cathode particles look almost as clean as the pristine cathode. This is a clear demonstration of the stability of the HVE3 against oxidation on the cathode surface. The ultimately decomposed product like H₂O resulted in the etching of LNMO particles in baseline cell due to the oxidative decomposition of EC-EMC solvents and the generation of HF may also lead to Mn and Ni dissolution. ICP-MS data showed that Mn and Ni exist in the cycled baseline electrolyte with much higher concentration. LNMO surface is intact with HVE3 electrolyte, and more integrated when LiDFOB additive was added, indicating the improved chemical and electrochemical stability of F-electrolyte.

On the anode side, significant difference was observed in the morphology of cycled graphite electrode with Gen 2 and fluorinated electrolyte (Figure V- 123). Graphite particles of Gen 2 cycled cell showed significant amount of nanoparticles (a few nm) of transitional M species accumulated in the carbon black region, which could catalyze the parasitic reactions. Anode of HVE3 and HVE3 with LiDFOB additive showed quite different morphology compared with Gen 2 cycled graphite electrode. Less accumulation/agglomeration of the transition particles with larger particle size are observed on the surface of the HVE3 and HVE3 with additive

electrode. The unique morphology of this surface led to less catalytic effect leading to less reductive decomposition of electrolyte.

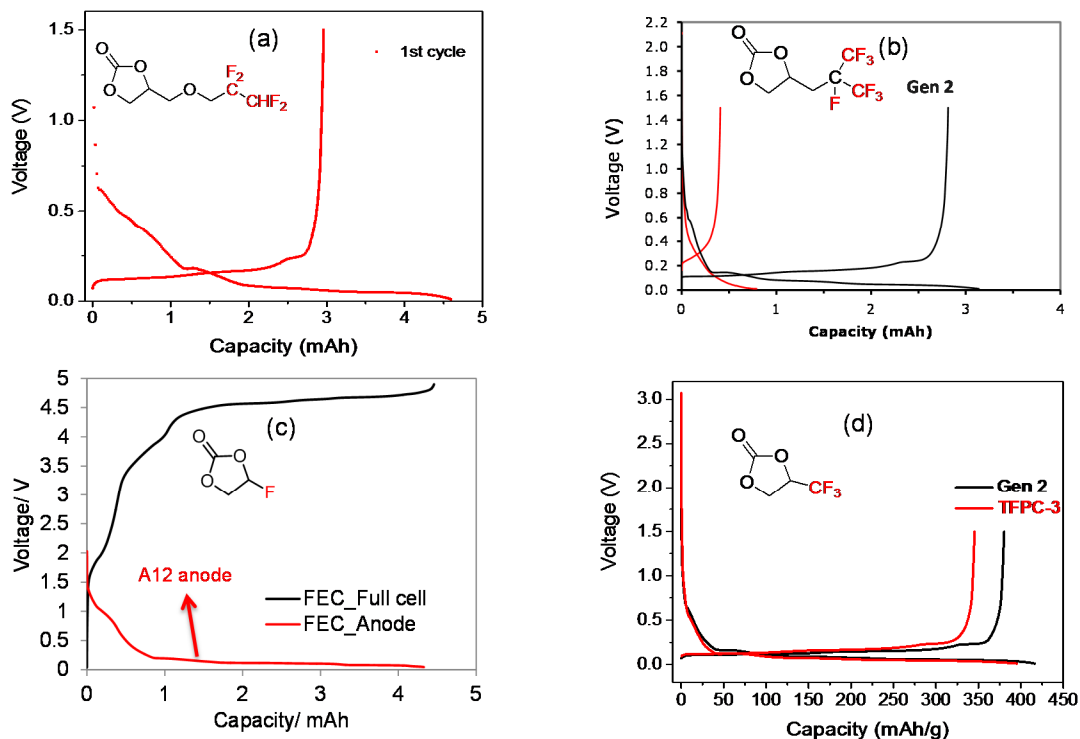


Figure V- 121: Voltage profiles of graphite/Li half cells with (a) TFP-PC-E, (b) HFP-PC, (c) FEC and (d) TFPC

C_{1s}, O_{1s} and F_{1s} XPS spectra of the graphite electrodes taken from LiNi_{0.5}Mn_{1.5}O₄/graphite cells are presented in Figure V- 124. For the C 1s spectra, XPS peaks at 284.3 eV (C-C), 286.0 eV (C-O), 288 eV (C=O) and 289 eV (OC=O, CO₃) are perfectly visible for the electrolyte cycled in the carbonate-based electrolyte. The C-O contribution (286 eV) is more significant when the fluorinated electrolyte is used, instead of carbonate-based. Moreover, the C=O contribution for the fluorinated electrolyte is found to be less compared with the baseline. Finally, C-F bounds are hardly detected when F-EC is present in the electrolyte. O_{1s} spectra reveals that the CO, C=O and CO₃ are perfectly visible for the fluorinated electrolyte. This means that the F-EC, F-EMC and F-EPE compounds participate in the SEI formation on graphite, which confirms the results of graphite/Li half cell data. Finally, despite the high amount of fluorine F_{1s} in the SEI, LiF is present in lower amount compared to baseline electrolyte on graphite (relatively to C-F peak), as already observed by many authors with the use of FEC. Mn_{2p} was not observed at this spot of measurement for graphite with HEV-3 electrolyte due to the transition metal particle accumulation/agglomeration.

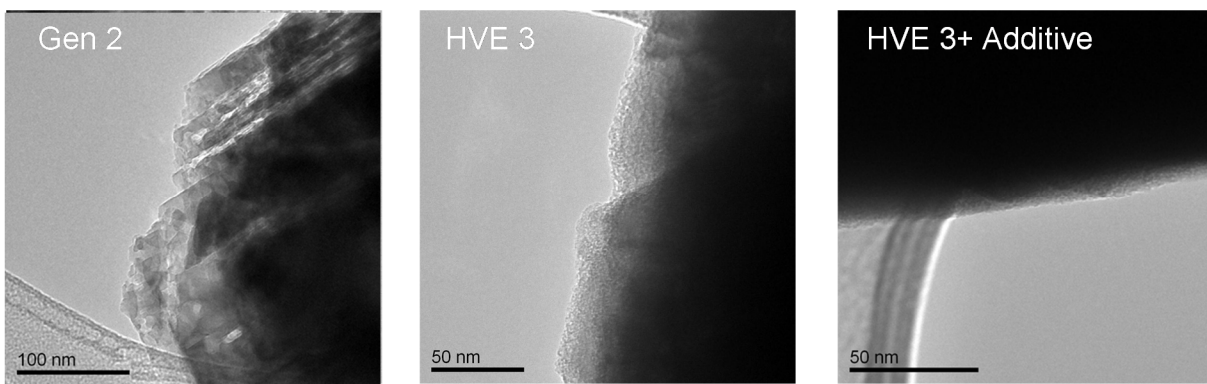


Figure V- 122: TEM image of the cycled graphite electrode with fluorinated electrolyte and Gen 2 electrolyte

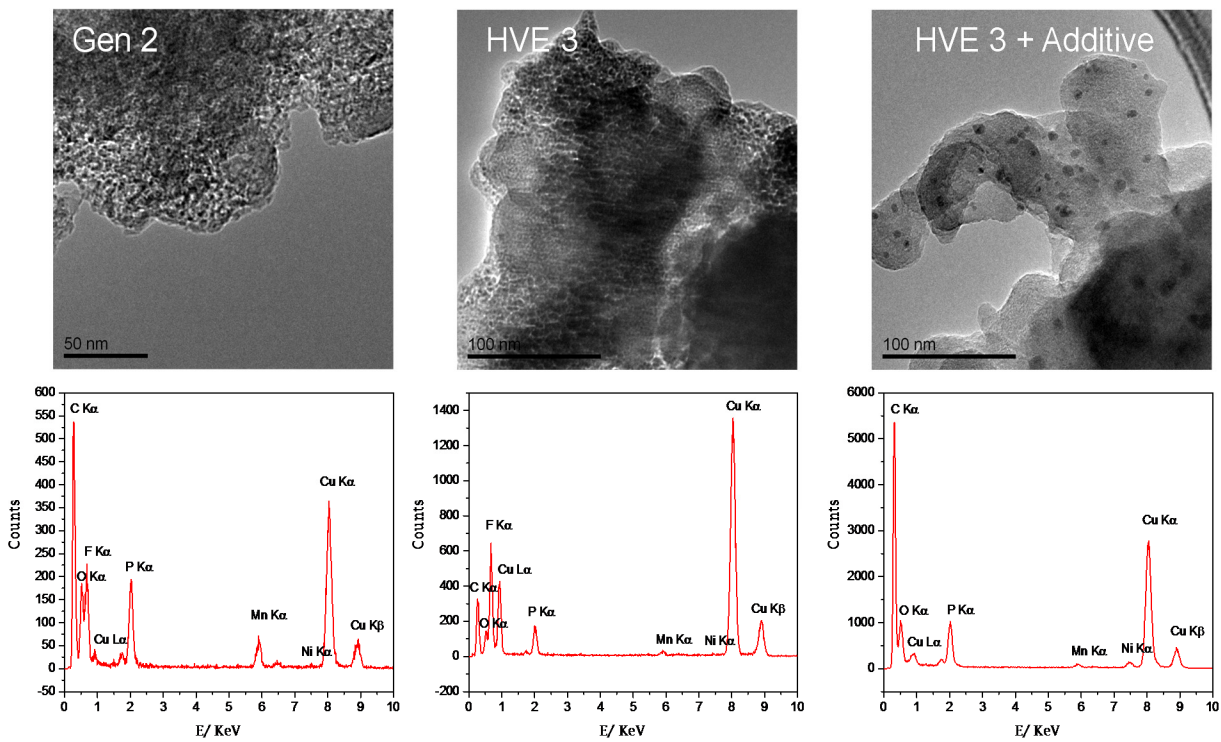


Figure V- 123: SEM image of the cycled graphite electrode with fluorinated electrolyte and Gen 2 electrolyte

Li Reservoir for Extended Cycle Life at 55°C

To further enhance the cycling performance of LNMO/graphite the cell, especially at 55 °C, we examined the effect of an active lithium reservoir introduced by the placement of a lithium foil (Figure V- 125a, Figure V- 125b), SLMP (stabilized lithium metal powder from FMC) (Figure V- 125c) or electrochemically pre-lithiated graphite anode (Figure V- 125d) before assembling the LNMO/graphite cell with fluorinated electrolyte.

Figure V- 126a showed the capacity retention profiles of the cell with lithium foil cycled at C/3 rate with a cut-off voltage of 3.5-4.9 V at 55 °C. The specific capacity of 120 mAh g-1 with a coulombic efficiency of > 99.5% (Figure V- 126b) was maintained even after 100 cycles at 55 °C with no capacity loss, which has never been achieved before. Figure V- 126a also provided the capacity retention profiles of LNMO/graphite cells using HVE3 electrolyte and Gen 2 electrolyte without lithium foil for comparison. The slight fluctuation in capacity retention of the new cell suggests that the lithium compensation might be on and off during the cycling process because of poor contact of the Li metal and the electrolyte, which may be caused by the location where the lithium was incorporated. Post analysis of the disassembled cell indicated that the Li metal was not completely consumed, which means the cycle life of the cell could be extended further.

The voltage profile of LNMO/graphite cells with the Li reservoir strongly resembles that of the LNMO/Li cells instead of LNMO/graphite cells, indicating that at the end of discharge the graphite anode is not fully delithiated and the potential remains low. Nonetheless, this data approved that the introduction of the auxiliary lithium in the LNMO/graphite cell (Figure V- 125a) can compensate the active lithium loss caused by electrolyte decomposition on the LNMO cathode thus enhancing the cell performance.

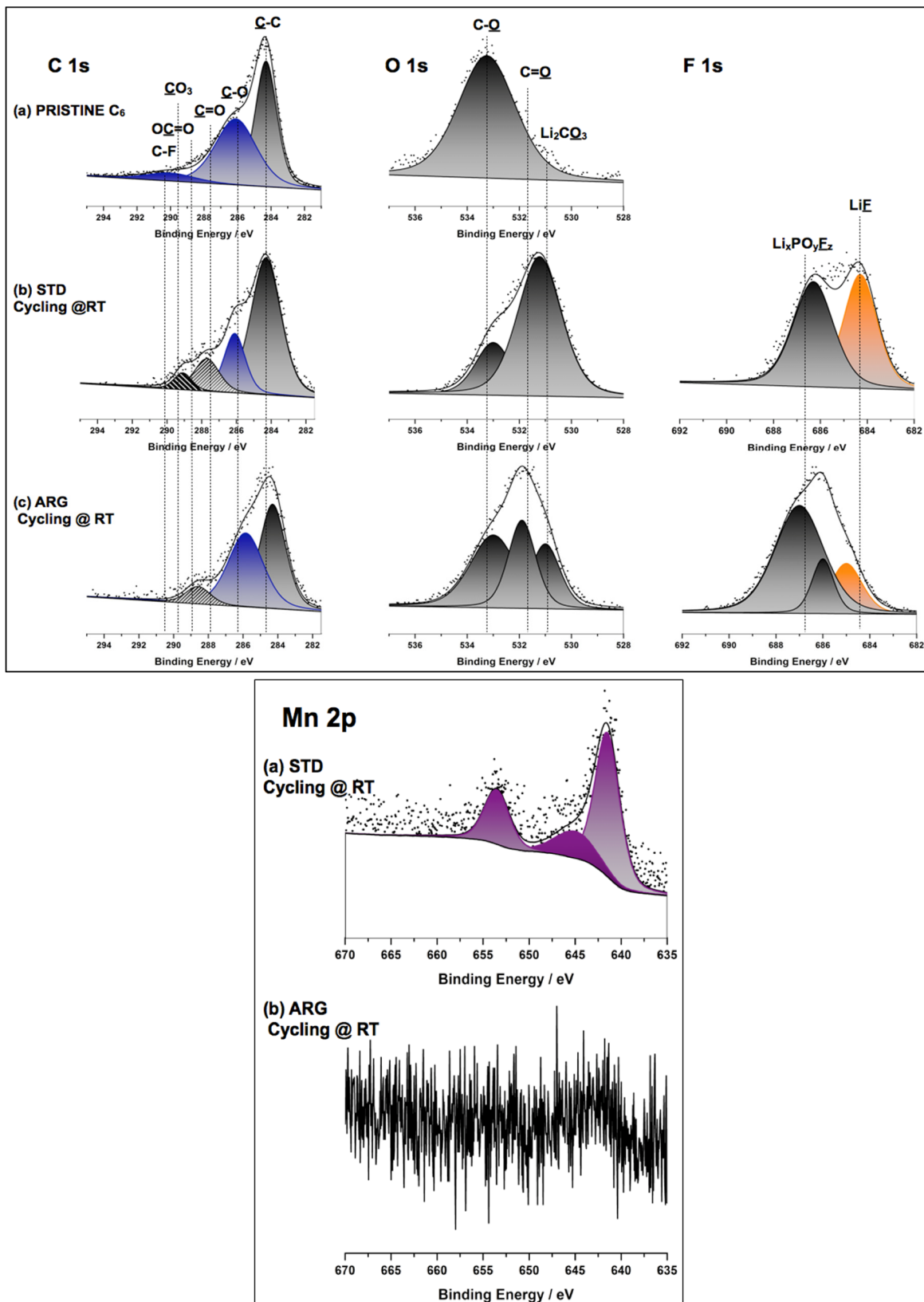


Figure V- 124: XPS profiles of C_{1s} , O_{1s} , and Mn_{2p} from cycled graphite anodes

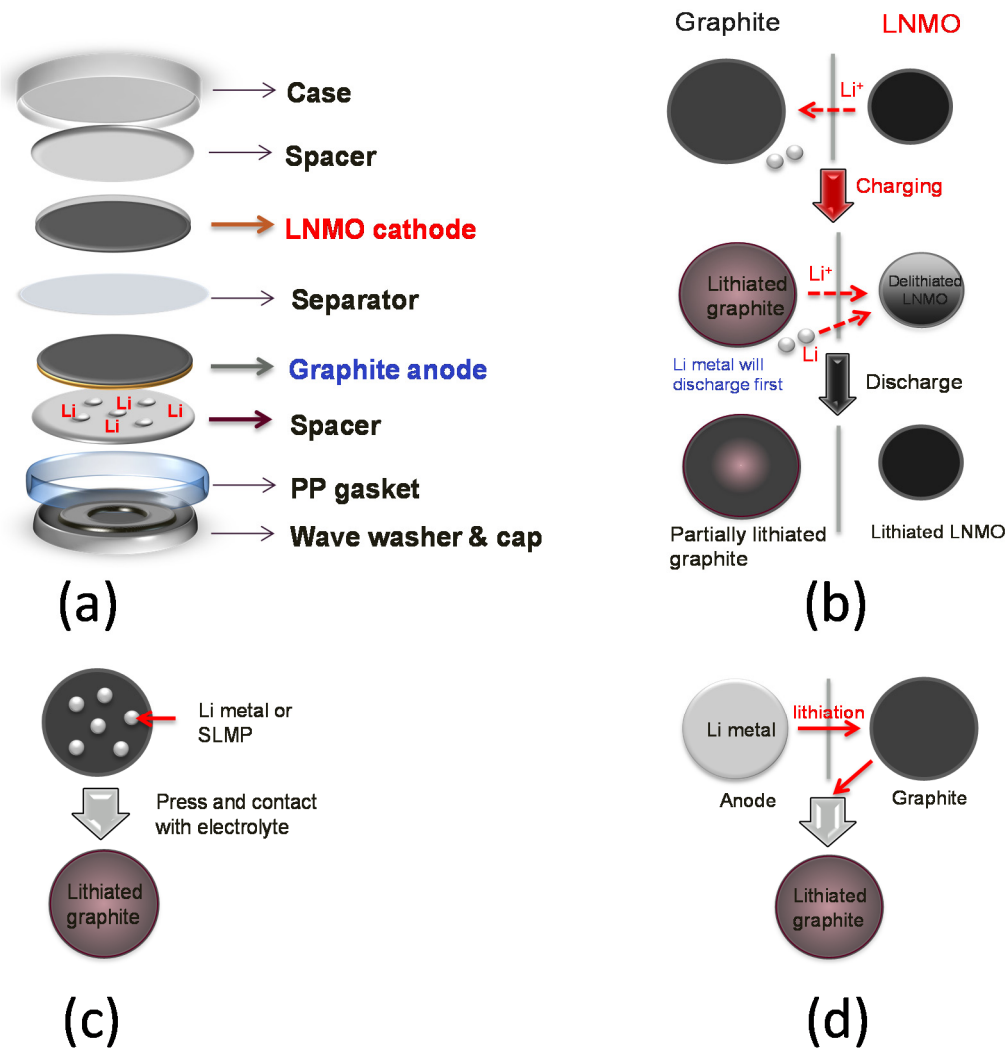


Figure V-125: (a) LNMO/graphite cell assembly with incorporated lithium metal; (b) lithium metal working mechanism at the formation cycles; (c) direct shorting of graphite anode using SLMP; (d) prelithiation of graphite anode using electrochemical method

While the lithium reservoir can also be used in cells with the conventional carbonate electrolytes, our data indicated that it is not a practical solution since the severe oxidative decomposition of the electrolyte on LNMO cathode would lead to faster consumption of the extra lithium and the cell dies quickly. To investigate the effect of the oxidative stability of electrolyte on the performance of the LNMO/graphite cell with lithium reservoir, we carried out the same experiment as described above with Gen 2 electrolyte. As predicted, the improvement of the Gen 2 cell is not as good as the HVE3 cell, the added lithium was fully consumed in 70 cycles upon disassembling the cell, indicating that even with the aid of lithium compensation, a more stable electrolyte is still indispensable for high-voltage cells at high temperature. To further demonstrate the concept of Li compensation is not limited to the delivery method illustrated in Figure V-125, experiments with other methods were also examined using Gen 2 electrolyte. All results provided clear evidence that both methods showed performance improvement over the pristine cells. In addition, we found out that adding extra lithium does not have significant impact in the rate capability of the electrolyte and the rate performance is similar to cells without lithium reservoir.

Conclusions and Future Directions

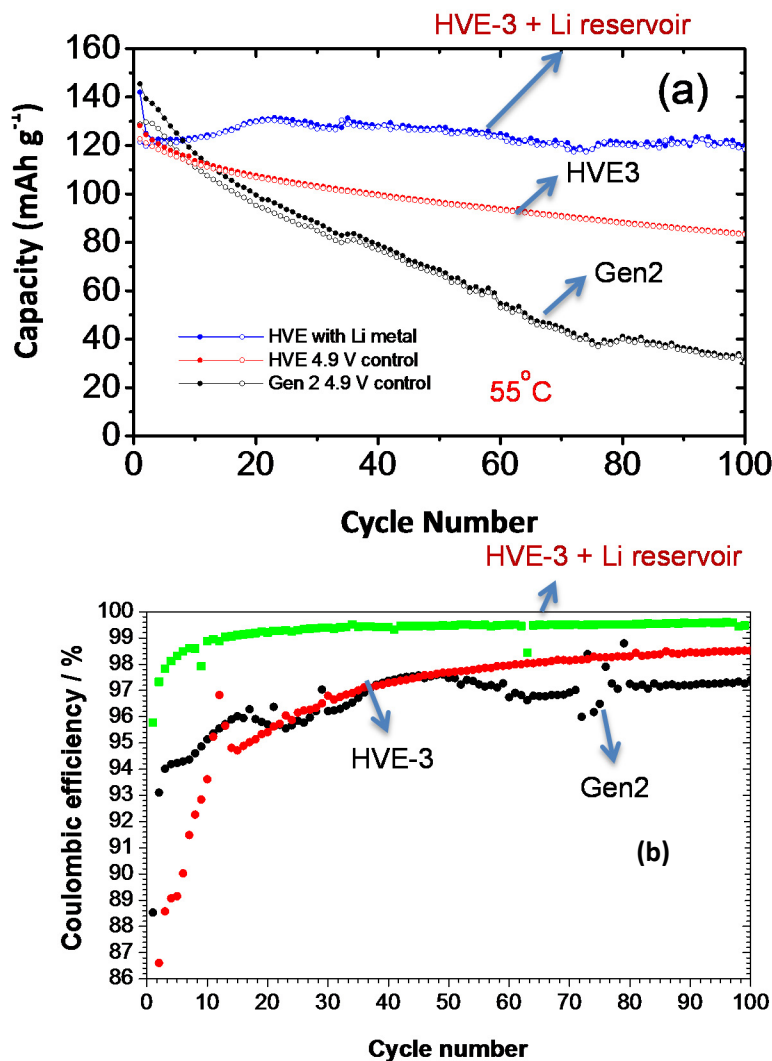


Figure V-126: (a) Capacity retention and (b) coulombic efficiency of LNMO/graphite cells cycled at C/3, 55 °C using HVE3 electrolyte with and without Li compensation (the 1st method), compared with Gen 2 electrolyte without Li compensation, 3.5–4.9 V

C-rate and high power. Also, the new process needs to be developed for the purpose of cost reduction. A couple of the new fluorinated carbonate solvents have scaled up to kg level at Argonne's Material Engineering and Research Facility. The achievements have proved that the proposed technical approach is viable and effective.

FY 2015 Publications/Presentations

1. "A review of fluorinated electrolyte as high voltage electrolyte for lithium-ion battery," Libo Hu, Zheng Xue, Chi Cheung Su, Meinan He, Anthony Burrell, Zhengcheng Zhang*. *J. Electrochem. Soc.*, (2015), to be submitted.
2. "Fluorinated electrolyte for 5-V Lithium-ion battery," Zhengcheng Zhang*, Libo Hu, Zheng Xue, Chi Cheung Su, Meinan He, Arthur von Cresce, Kang Xu Jinhua Huang, Baofei Pan, Lu Zhang, Chen Liao, Anthony Burrell. *Adv. Mater.*, (2015), to be submitted.
3. "The Interplay of Molecular symmetry, Polarity, and Electrochemical Stability in the Redox Shuttle Additives for Overcharge Protection of Batteries," Wei Weng, Jinhua Huang, Baofei Pan, Lu Zhang, Chen Liao, Ilya A. Shkrob, Khalil Amine, Zhengcheng Zhang*. *ChemElectroChem*, (2015), submitted.

The development of new electrolyte with high oxidation stability is a very challenging task. The high voltage electrolyte is first an electrolyte which should meet all the basic properties of an electrolyte, such as dielectric constant, low viscosity, and high conductivity. Another basic property is the passivation capability with the graphite anode, a widely used anode materials for current lithium-ion batteries. In this research, for the first time, we have developed two fluorinated electrolytes which not only showed superior oxidation stability on the high voltage cathode surface, but also stabilized the electrolyte/graphite interface by formation of a robust SEI layer. Both 5-V LNMO/graphite cells and NCM523/graphite cells in coin cell and pouch cell formats clearly demonstrated that the fluorinated electrolyte is a promising as the next generation electrolyte for high voltage high energy lithium ion battery.

Further electrolyte development will be focused on the additive research to further optimization of the performance of the fluorinated electrolyte operated at wide conditions including high temperature, low temperature, high

4. "Anion Solvation in Carbonate-Based Electrolytes," Arthur von Wald Cresce, Mallory Gobet, Oleg Borodin, Jing Peng, Selena M. Russell, Adele Fu, Emily Wikner, Libo Hu, Hong-Xi Lee, Zhengcheng Zhang, Khalil Amine, Xiao-Qing Yang, Steven Greenbaum, Kang Xu. *J. Phys. Chem.*, (2015), submitted.
5. "Fluorinated Electrolytes for 5-V Li-ion Chemistry: Probing Voltage Stability of Electrolytes with Electrochemical Floating Test," Meinan He, Libo Hu, Zheng Xue, Chi-Cheung Su, Paul Redfern, Larry A. Curtiss, Bryant Polzin, Arthur von Cresce, Kang Xu, Zhengcheng Zhang*. *J. Electrochem. Soc.*, (2015), 162(9), A1725-A1729.
6. "Direct Observation of Reversible Magnesium Ion Intercalation into a Spinel Oxide Host," Chunjoong Kim, Patrick J. Phillips, Baris Key, Tanghong Yi, Dennis Nordlund, Young-Sang Yu, Ryan D. Bayliss, Sang-Don Han, Meinan He, Zhengcheng Zhang, Anthony K. Burrell, Robert F. Klie, and Jordi Cabana. *Adv. Mater.* (2015), 27(22), 3377-3384. DOI: 10.1002/adma.201500083.
7. "Molecular Engineering toward Stabilized Interface: An Electrolyte Additive for High-Performance Li-Ion Battery," Lu Zhang, Jinhua Huang, Kyrrilos Youssef, Paul C. Redfern, Larry A. Curtiss, Khalil Amine, Zhengcheng Zhang*. *J. Electrochem. Soc.*, (2014), 161 (14), A2262-A2267.
8. "Next-generation lithium-ion batteries: The promise of near-term advancements," Jason R. Croy, Ali Abouimrane, and Zhengcheng Zhang. *MRS Bulletin*, (2014), 39, 407-415.
9. "Fluorinated Electrolytes for 5-V Li-Ion Chemistry: Synthesis and Evaluation of an Additive for High-Voltage $\text{LiNi}_{0.5}\text{Mn}_{1.5}\text{O}_4$ /Graphite Cell," Libo Hu, Zheng Xue, Khalil Amine, Zhengcheng Zhang*. *J. Electrochem. Soc.*, (2014), 161 (12), A1777-A1781.
10. "Fluorinated Electrolytes for Li-Ion Battery: Dramatic enhancement of $\text{LiNi}_{0.5}\text{Mn}_{1.5}\text{O}_4$ /graphite cell performance by a lithium reservoir," L. Hu, K. Amine, Z. Zhang*. *Electrochem. Commun.*, (2014), 44, 34-37.
11. "Fluorinated electrolyte for high voltage Ni-rich cathode materials," Meinan He, Libo Hu, Zheng Xue, Chi-Cheung Su, Zhengcheng Zhang. 227th ECS Meeting, May/2015, Chicago, IL.
12. "Fluorinated sulfone based electrolytes for high voltage Lithium-ion battery," Chi-Cheung Su, Meinan He, Libo Hu, Zheng Xue, Zhengcheng Zhang. 227th ECS Meeting, May/2015, Chicago, IL.
13. "Fluorinated electrolyte for 5-V Lithium-ion chemistry", ES218, US DOE Vehicle Technologies AMR, June/2015, Washington, DC.

V.F Diagnostics

V.F.1 Design and Synthesis of Advanced High-Energy Cathode Materials (LBNL)

Objectives

- Obtain fundamental understanding on structural, chemical and morphological instabilities during Li extraction/insertion and extended cycling.
- Establish and control the interfacial chemistry between the cathode and the electrolyte at high operating potentials.
- Determine transport limitations at both material and electrode levels.
- Rationally design and develop next-generation electrode materials.

Project Details

Guoying Chen
(Lawrence Berkeley National Laboratory - PI)
 Energy Storage and Distributed Resources Division
 1 Cyclotron Rd, MS 62-203
 Berkeley, CA 94720
 Phone: 510-486-5843
 E-mail: gchen@lbl.gov

Start Date: October 2012

Projected End Date: September 2016

Technical Barriers

- Low energy density, low power density, poor cycle life and poor safety.

Technical Targets

- PHEV40: 96 Wh/kg, 750 W/kg, 5,000 cycles.
- EV: 200 Wh/kg, 1,000 cycles.

Accomplishments

- Demonstrated the effective use of our approach in combining well-formed crystal samples with complementary microscopy and spectroscopy techniques at multi-length scale for controlled diagnostic studies of complex materials.
- Visualized the structure make-up of an entire micron-sized LMR-NMC particle for the first time. Unambiguously revealed a single monoclinic phase in the bulk crystal and a thin layer of defective spinel with reduced transition metals on the pristine surface.
- Revealed the particle-level origins of kinetic barriers, structural and cycling instabilities in LMR-NMC cathodes.
- Obtained critical insights for designing better-performing LMR-NMCs.
- Demonstrated the roles of phase boundaries and phase transformation in the kinetics of materials with first-order transition. Determined the physical properties of Li_xMNO solid solutions.

Introduction

To meet the DOE targets for Li-ion batteries intended for vehicular applications, electrode materials with high-energy density and high stability are needed. Critical performance issues, such as structural and morphological instabilities, side reactions with the electrolyte, and transport limitations, are sensitive to material's chemical compositions, crystal structures, surface facets, and particle sizes. Advances in materials development, therefore, require a better understanding of the relationships between their properties and functions. This project addresses these issues in a systematic way, by synthesizing single-crystal version of the commercially promising yet complex electrode materials, obtaining new insights into the materials by utilizing state-of-the-art analytical techniques that are mostly inapplicable on conventional, aggregated secondary particles, and subsequently establishing the relationships between structure and function. The goal is to use these findings to rationally design and synthesize advanced electrode materials with improved performance.

Approach

Prepare single crystals of Li-rich layered oxides and high-voltage Ni/Mn spinels with well-defined physical attributes. Perform advanced diagnostic and mechanistic studies at both bulk and single-crystal levels. Global properties and performance of the samples will be established from the bulk analyses, while the single-crystal based studies will utilize time- and spatial-resolved analytical techniques to probe material's redox transformation and failure mechanisms.

Results

Li- and Mn-rich Layered Oxides (LMR-NMCs)

In FY15, phase-pure Li- and Mn-rich layered oxide crystals with a composition of $\text{Li}_{1.2}\text{Mn}_{0.13}\text{Mn}_{0.54}\text{Co}_{0.13}\text{O}_2$ were synthesized in six different morphologies, plate, needle, large polyhedron (L-Poly), small polyhedron (S-Poly), box and octahedron, by using the molten-salt method. All samples were micron-sized with a similar surface area of about $0.4 \text{ m}^2/\text{g}$, except that the S-Poly sample had a smaller particle size and 10x more surface area (Figure V- 127). Figure V- 128a to Figure V- 128c show the HAADF STEM images collected on a needle crystal. The bright columns correspond to the transition metals (TMs, Mn, Ni and Co), and the atomic arrangements in the bulk of the crystal can be assigned to [100], [1-10] and [110] directions of monoclinic phase, as shown in the structural models in Figure V- 128e. The study revealed a random distribution of domains of three monoclinic variants in the entire bulk of the $\text{Li}_{1.2}\text{Mn}_{0.13}\text{Mn}_{0.54}\text{Co}_{0.13}\text{O}_2$ crystal (Figure V- 128d) and the lack of composite structure with R-3m and C2/m nano-domains, as typically reported on this class of oxides made by the co-precipitation method. Substantial rearrangement of the TMs was found on the pristine surface, as shown by the STEM image in Figure IV- 129a.

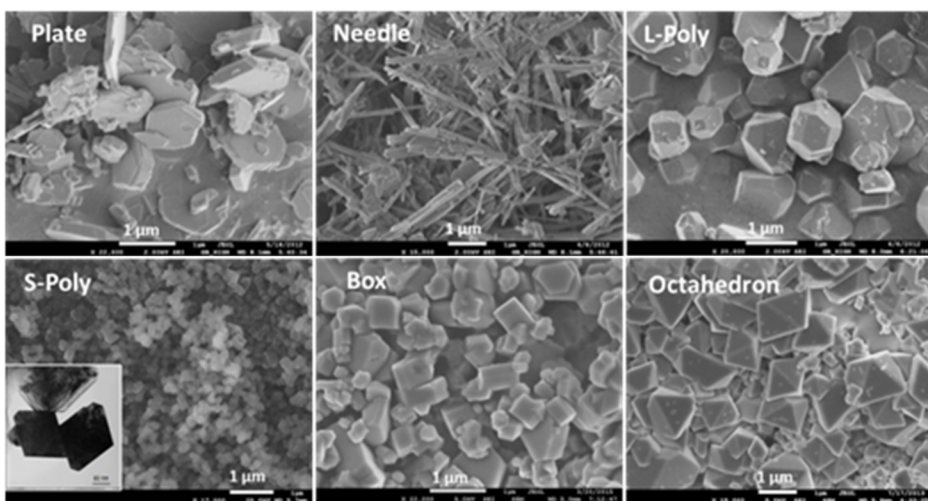


Figure V- 127: SEM images of $\text{Li}_{1.2}\text{Ni}_{0.13}\text{Mn}_{0.54}\text{Co}_{0.13}\text{O}_2$ crystals

gradual chemical reduction of Mn and Co from the bulk to the surface while Ni remains constant at 2+. The reduced surface TMs were found to be in a defective spinel structure, as revealed by careful STEM imaging in multiple zone axes. The change from monoclinic bulk to spinel surface was observed in several orientations but it is directional, with minimal spinel formation in the TM layer stacking direction. Bulk evaluation on surface reduction of TMs was carried out using soft XAS at beamline 10-1 at SSRL. Through depth-resolved probing on a large number of particles using three detection modes, AEY, TEY and FY which probe the top surface of 1-2 nm, 2 to 5 nm, and the bulk of about 50 nm, respectively, Mn and Co reduction from the bulk to the top surface layer of a few nm was confirmed. The thickness of this reduced surface layer depends on morphology, with the least reduction found on plate and L-Poly samples and the most found on the S-Poly and box samples.

A series of spectra covering EELS edges from O to Ni, transitioning from the bulk (bottom) to the surface (top) are also shown in Figure IV- 129b. Compared to the bulk, the Mn and Co L3 edges collected on the surface showed a lower energy loss, indicating a decrease in oxidation state. The L3/L2 ratios for the TMs (Figure IV- 129c) confirms the

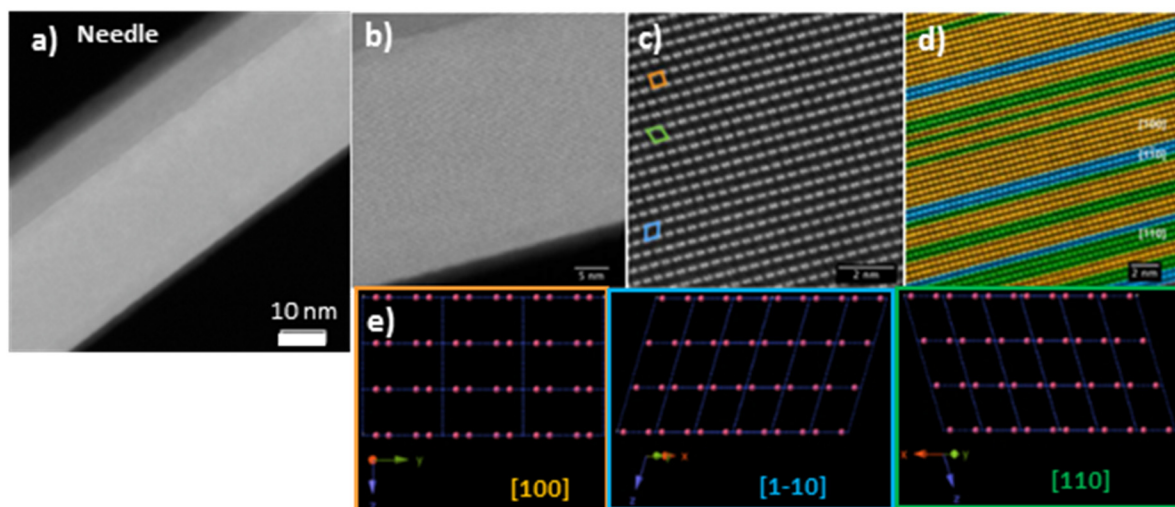


Figure V- 128: HAADF STEM image of a) an entire needle-shaped $\text{Li}_{1.2}\text{Ni}_{0.13}\text{Mn}_{0.54}\text{Co}_{0.13}\text{O}_2$ crystal, b) and c) zoomed in view of the crystal structure, d) color-coded HAADF image showing domains of the monoclinic variants, and e) models showing the monoclinic structure in [100], [1-10] and [110] directions

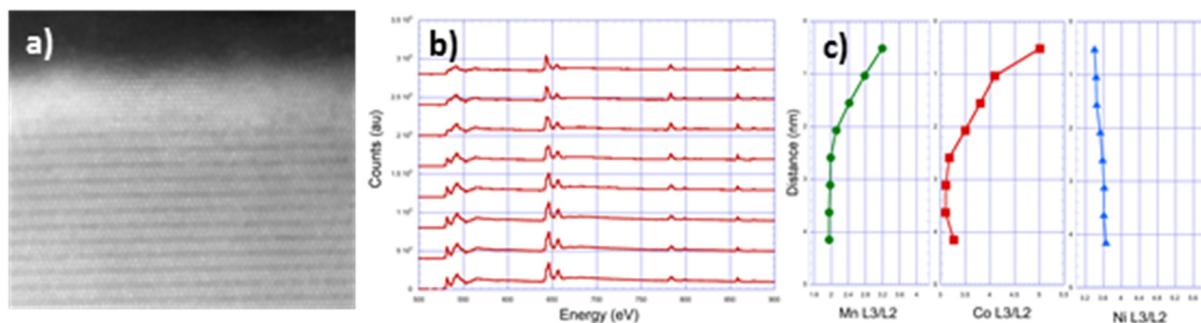


Figure V- 129: a) HAADF STEM image, b) EEL spectra collected from the surface (top) and the bulk (bottom) corresponding to the HAADF image, and c) L3/L2 ratio of Mn, Co and Ni determined from the EELS data

Electrochemical performance of the samples were evaluated by half-cell cycling of composite electrodes, consisting of $\text{Li}_{1.2}\text{Mn}_{0.13}\text{Mn}_{0.54}\text{Co}_{0.13}\text{O}_2$ crystals (80 wt%), a PVDF binder (10 wt%) and carbon (10 wt%), in a 1 M LiPF_6 in EC-DEC (1:1) electrolyte.

Figure V- 130a compares the first-cycle voltage profiles of the cells charged and discharged between 2.5 and 4.8 V at a current density of 10 mA/g. An activation plateau around 4.5 V was observed on all samples, although the actual plateau length varied significantly. Among the micron sized samples, the plate crystals delivered the highest capacity while the box had the lowest, indicating an effect of particle morphology as well as a coupled relationship between the level of activation and discharge capacity. The effects of particle morphology and surface properties were further demonstrated on the rate capability comparison in Figure V- 130b. S-Poly crystals consistently outperformed other samples at all rates tested, suggesting the dominating effect of particle size in kinetic behavior. Long-term cycling is compared in the plots for discharge capacity (Figure V- 130c) and capacity retention (Figure V- 130d), both of which shows the superior cycling stability of L-Poly sample. Figure V- 132 compares the changes in average charge and discharge voltages along cycling. A gradual decrease in the discharge voltage, commonly known as the voltage decay phenomenon in these Li- and Mn-rich oxides, is observed on all samples (Figure V- 132a), but the L-Poly sample experienced a much smaller voltage gap (265 mV at cycle 5) and slowest gap increase during the cycling (165 mV increase from cycle 5 to 85, Figure V- 132b).

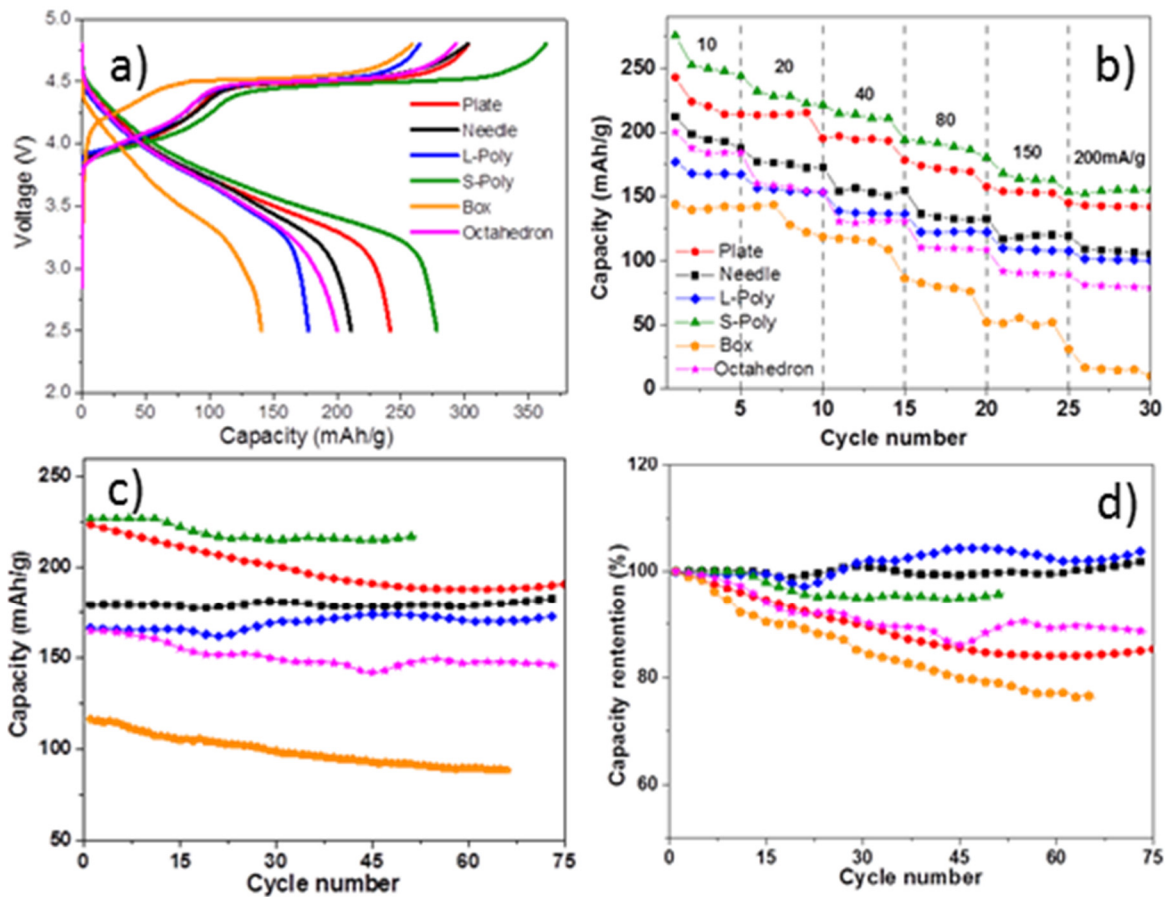


Figure V-130: a) First charge-discharge voltage profiles of the $\text{Li}_{1.2}\text{Ni}_{0.13}\text{Mn}_{0.54}\text{Co}_{0.13}\text{O}_2$ half cells, b) rate capability of the crystal samples, c) and d) long-term cycling and capacity retention of the cells at a current density of 20 mA/g

Soft XAS was then used to investigate the changes in the chemical state of TMs before and after cycling, with the Co *L*-edge spectra shown in Figure V-131a-c. Cycling promoted further Co reduction in all samples, and the monotonous increase in oxidation state from AEY, TEY to FY suggests that Co reduction progressed from the surface to the bulk. Furthermore, the extent of cycling-induced reduction is clearly particle surface dependent, with the most reduction occurred on the box sample and least on L-Poly, following the same trend as the initial Co reduction observed on the pristine oxides. The difference, shown in Figure V-131g, is also consistent with the trend in capacity retention and changes in average charge and discharge voltages. Similar results were also observed on Mn reduction. This demonstrates the correlation in TM reduction and oxide stabilities, and the critical role of particle surface engineering in minimizing cycling-induced structural changes, voltage decay and hysteresis in this class of high-capacity cathode materials.

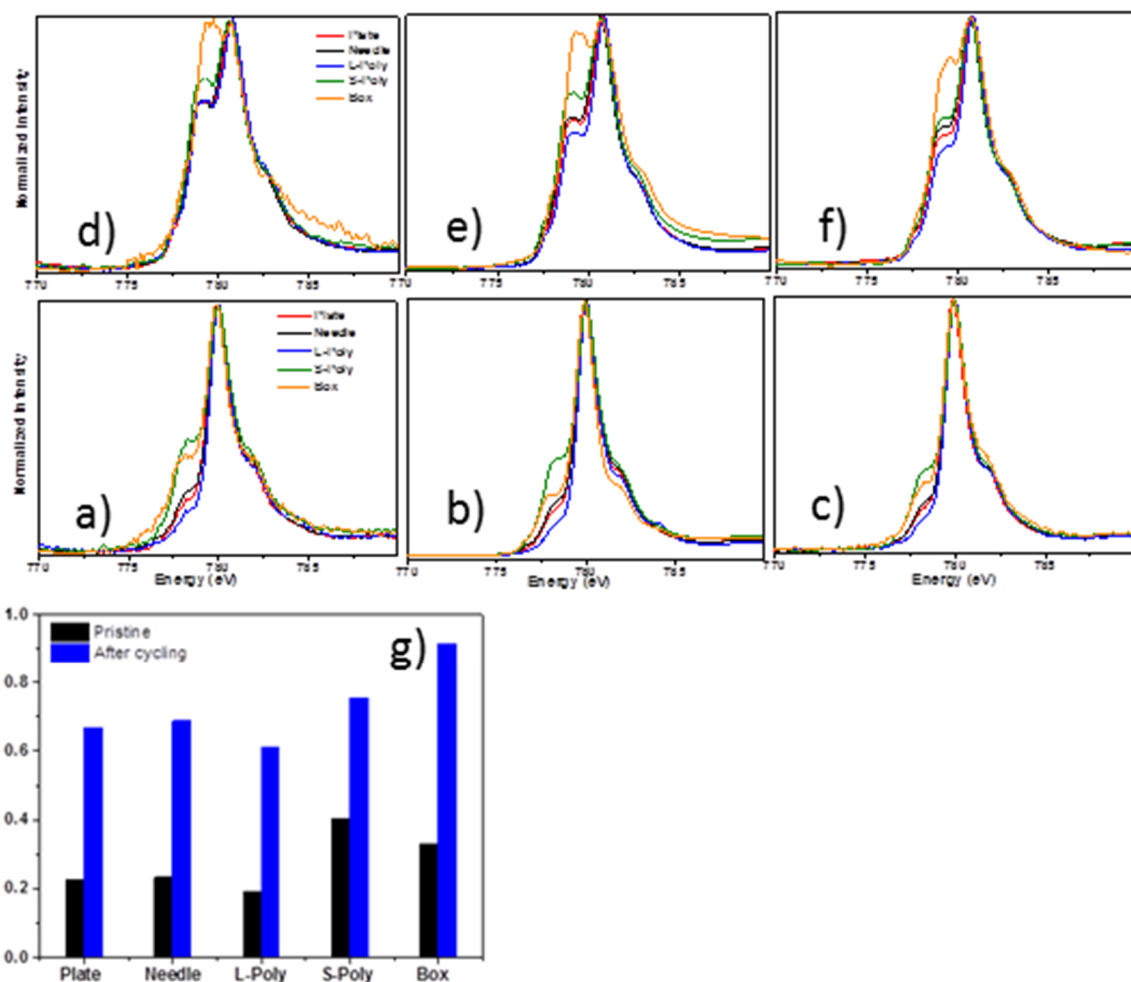


Figure V- 131: Soft XAS spectra of Co L- edge collected in AEY (a and d), TEY (b and e) and FY (c and f) modes on pristine (bottom) and cycled (top) $\text{Li}_{1.2}\text{Ni}_{0.13}\text{Mn}_{0.54}\text{Co}_{0.13}\text{O}_4$ composite electrodes, and g) Co L3 peak ratio of the TEY spectra, with a higher ratio corresponding to a lower oxidation state

Phase Transformation and Rate Capability of Spinel $\text{LiNi}_x\text{Mn}_{2-x}\text{O}_4$

The relationship between the extent of solid solution transformation and rate capability in the intercalation materials was investigated in FY15. Ordered $\text{LiNi}_{0.5}\text{Mn}_{1.5}\text{O}_4$ (LMNO) crystals, previously synthesized by a molten-salt method, was disordered by rapid thermal annealing at 720°C and followed by fast cooling. The dQ/dV profile show a peak separation of about 60 mV at 4.7 V, similar to that observed in $\text{LiNi}_{0.3}\text{Mn}_{1.7}\text{O}_4$ (Figure V- 133a), confirming the disordered nature of both samples. Synchrotron in situ XRD experiments were performed at beamline 11-3 at SSRL, and the phase composition at a given Li content during discharge was obtained from full-pattern Rietveld refinement (Figure V- 133b and c).

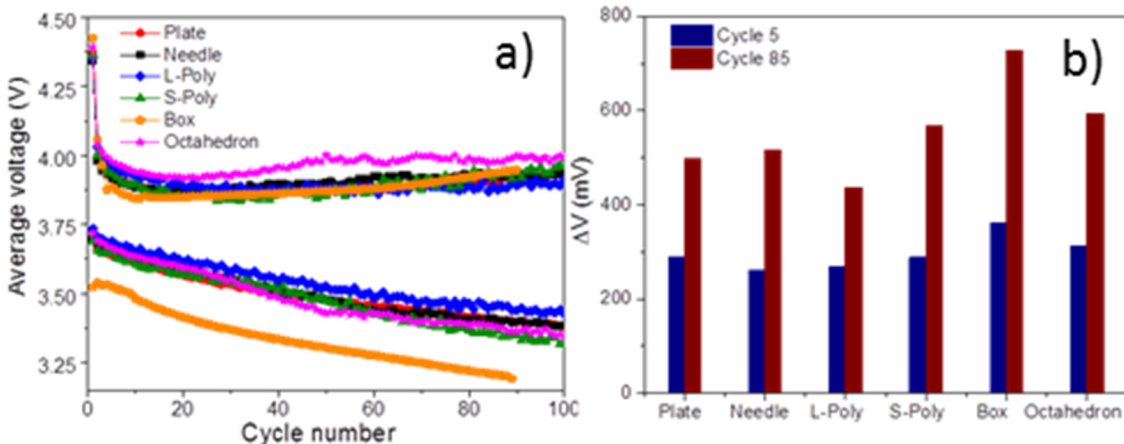


Figure V- 132: a) Average charge and discharge voltages of the $\text{Li}_{1.2}\text{Ni}_{0.13}\text{Mn}_{0.54}\text{Co}_{0.13}\text{O}_2$ half cells and b) comparison of the charge and discharge voltage gaps at cycle 5 and 85

While three cubic phases and two two-phase transitions were involved in $x=0.5$, indicating presence of extensive phase boundaries, the sample with $x=0.3$ transformed through two cubic phases with a large solid solution domain covering nearly 50% of the Li range. The rate capability obtained from varying-rate cycling of half-cells between 3.0 and 5.0 V is compared in Figure V- 133d. At C/22 rate, both spinels delivered a discharge capacity close to the theoretical value of 147 mAh g^{-1} . Compared to the sample with $x=0.3$, slight improvement was observed on $x=0.5$ at all rates, despite a lower Mn^{3+} content and a smaller presence of solid solution in the sample. Contrary to the popular speculation, direct correlation between kinetics and the extent of solid solution transformation was not found in cathodes where two-phase transition is also involved and phase boundaries are present.

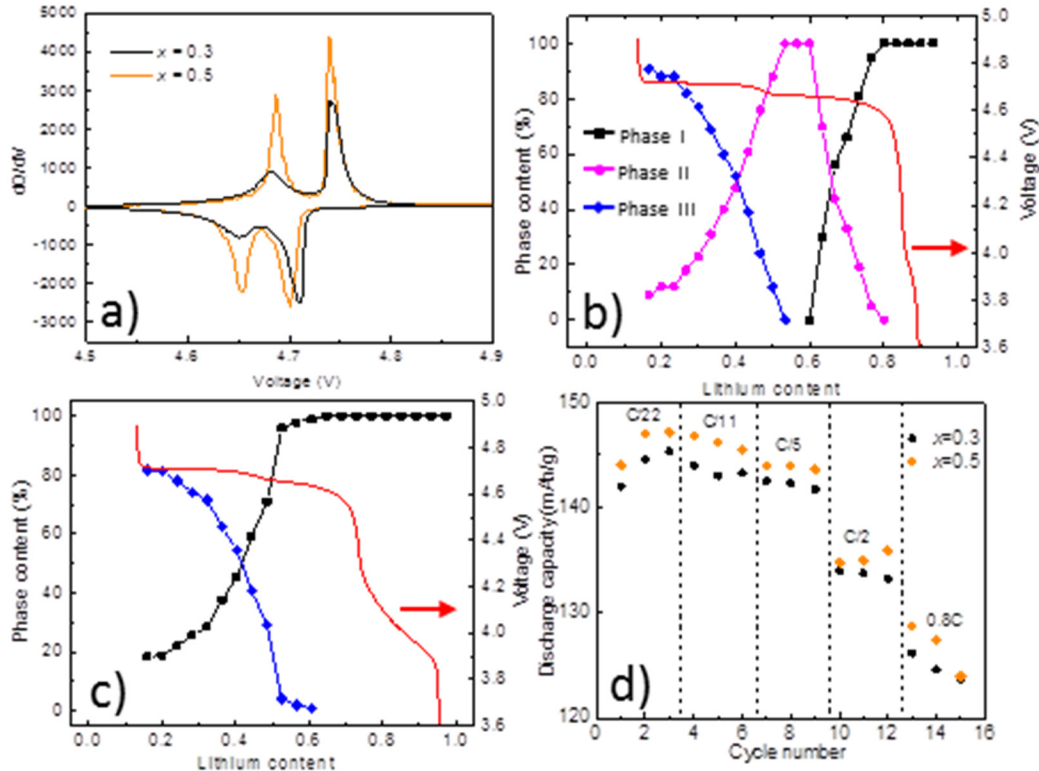


Figure V- 133: a) dQ/dV profiles, b) and c) percentage of the phases present during in situ discharge of $x=0.5$ and $x=0.3$, and d) rate capability of the crystal samples

Physical properties of the room-temperature, phase-pure $\text{Li}_x\text{Ni}_{0.5}\text{Mn}_{1.5}\text{O}_4$ (Li_xMNO , $x \geq 0.71$) solid solutions, previously synthesized through a controlled thermal treatment process, were also characterized in detail to

probe their roles in kinetics. No significant differences were observed when comparing the Raman and FTIR spectra of Li_xMNO ($0.71 \leq x < 1$) solid solution phases, all of which resembled that of pristine LMNO. Neutron profiles obtained from LMNO and $\text{Li}_{0.82}\text{MNO}$ revealed a fully ordered structure with a space group of $P4_332$ in both samples and a nearly identical lattice parameter of $8.1666 \pm 0.0006 \text{ \AA}$.

Conclusions and Future Directions

In conclusion, we demonstrated the use of well-formed crystal samples with complementary microscopy and spectroscopy techniques at multi-length scale for controlled diagnostic studies of LMR-NMCs. By visualizing micron-sized LMR-NMC particle using HAADF SEM and obtaining chemical confirmation from soft XAS, the structure make-up of the crystals, both in the bulk and on the surface, was unambiguously determined. We systematically investigated the intricate relationships in particle surface properties, transition metal redox activities, crystal structural transformation, and the limitations in electrochemical performance, which led to the critical insights for designing better-performing LMR-NMC samples.

Future work will investigate synthesis-structure-electrochemical property relationships in the LMR-NMCs, with the goal of synthesizing oxide particles with desired physical properties. Focus will be placed on surface features that will enable stable cycling, either through surface composition modification or surface coating. We will also monitor chemical evolution and migration of transition metals during cycling, especially the redox behavior and migration of transition metals (both in and out of the active particles) as functions of lithium concentration and cycle number. Development of advanced diagnostic techniques capable of characterizing the reactions and processes at the cathode-electrolyte interface will continue.

FY 2015 Publications/Presentations

1. Shukla, A. K., Q. Ramasse, C. Ophus, H. Duncan, and G. Chen "Unraveling structural ambiguities in Li and Mn rich transition metal oxides," *Nature Communications* (2015), in press.
2. Kuppan, S., H. Duncan, and G. Chen, "Controlling Side Reactions and Self-discharge in High-voltage Spinel Cathodes: Critical Role of Surface Crystallographic Facets," *Physical Chemistry Chemical Physics* 17 (2015): 26471.
3. Kuppan, S., A. Jarry, R. Kostecki, and G. Chen, "A study of room-temperature $\text{Li}_x\text{Mn}_{1.5}\text{Ni}_{0.5}\text{O}_4$ solid solutions," *Scientific Reports* 5 (2015): 8027.
4. Ruther, R., H. Zhou, C. Dhital, S. Kuppan, A. Kercher, G. Chen, A. Huq, F. Delnick, and J. Nanda, "Synthesis, Structure, and Electrochemical Performance of High Capacity $\text{Li}_2\text{Cu}_{0.5}\text{Ni}_{0.5}\text{O}_2$ Cathodes," *Chemistry of Materials* (2015), DOI: 10.1021/acs.chemmater.5b02843.
5. Yan, P., D. Lv, J. Zheng, Z. Wang, S. Kuppan, J. Yu, L. Luo, D. Edwards, M. Olszta, K. Amine, J. Liu, J. Xiao, G. Chen, J.-G. Zhang, and C.-M. Wang, "Atomic-resolution visualization of distinctive chemical mixing behavior of Ni, Co and Mn with Li in layered lithium transition metal oxide cathode materials," *Chemistry of Materials* 27 (2015): 5393.
6. Kuppan, S. and G. Chen, "Surface Facet Dependent Self-discharge in High-voltage Spinel Cathodes," Poster presented at the Industry Day and Open House at Berkeley Lab, Berkeley, CA, April 2015.
7. Kuppan, S. and G. Chen, "Thermal Behavior of $\text{Li}_x\text{Mn}_{1.5}\text{Ni}_{0.5}\text{O}_4$ ($0 \leq x \leq 1$) and Isolation of Room-Temperature Solid Solutions," Presented at the 2015 MRS Spring Meeting & Exhibit, San Francisco, CA, April 2015.
8. Kuppan, S. and G. Chen, "Thermal Behavior of $\text{Li}_x\text{Mn}_{1.5}\text{Ni}_{0.5}\text{O}_4$ ($0 \leq x \leq 1$) and Isolation of Room-Temperature Solid Solutions," Poster presented at the Open House at SLAC National Accelerator Laboratory, Menlo Park, CA, November 2014.
9. Shukla, A. K., Q. Ramasse, C. Ophus, A. Darbal, H. Duncan, and G. Chen, "Unfolding the bulk and defect structure of lithium-rich layered oxides using multi-scale electron microscopy and spectroscopy techniques for high-capacity lithium-ion batteries," Presented at the 2014 BERC Energy Summit, Berkeley, CA, October 2014.
10. Chen, G. "Design and Synthesis of Advanced High-Energy Cathode Materials." ES225_Chen_2015_O, U.S. DOE Vehicle Technologies AMR, 2015.

V.F.2 Interfacial Processes – Diagnostics (LBNL)

Objectives

- This project provides better understanding of the underlying principles that govern the function and operation of battery materials, interfaces and interphases, which is inextricably linked with successful implementation of high energy density materials such as Si and high voltage cathodes in Li-ion cells for PHEVs and EVs:
- Obtain detailed insight into the dynamic behavior of molecules, atoms, and electrons at electrode/electrolyte interfaces of intermetallic anodes (Si) and high voltage Ni/Mn-based materials.
- Establish clear connections between diagnostics, theory/modelling, materials synthesis, and cell development efforts.
- Provide remedies to interface instability e.g., artificial surface layers (e.g., ALD) and/or structures, novel electrode architecture, electrolyte additives, co-intercalation of secondary metals/ions etc.
- Characterize active material/electrode/cell degradation modes, improve long-term stability of high-energy Li-ion systems.
- Develop and deploy novel *in situ* far- and near-field optical multifunctional probes.
- Achieve spatial and temporal resolution that corresponds to the size and rate of basic chemical steps and structural, building blocks.

Project Details

Robert Kostecki (Lawrence Berkeley National Laboratory - PI)
Energy Storage and Distributed Resources Division
1 Cyclotron Road
Berkeley, CA 94720
Phone: 510-486-6002; Fax: 510-486-5454
E-mail: r_kostecki@lbl.gov

Start Date: October 2012

Projected End Date: September 2016

Technical Barriers

This project addresses the following technical barriers related to the battery technology development effort of the DOE Office of Vehicle Technologies:

- Inadequate Li-ion battery energy (related to cost)
- Poor Li battery calendar/cycle lifetime for PHEV and EV applications
- High electrode impedance that limits power density
- Need for new advanced battery materials and composite electrodes with acceptable specific energy, durability, costs, and safety characteristics.

Technical Targets

- Cycle life: 5000 (deep) and 300,000 (shallow) cycles
- Available energy: 200 Wh/kg
- Calendar life: 15 years

Accomplishments

- X-ray absorption, optical fluorescence spectroscopy and imaging experiments demonstrated that electrochemical oxidation of DEC and EC at the $\text{Li}_x\text{Ni}_{0.5}\text{Mn}_{1.5}\text{O}_{4-\delta}$ electrode at potentials > 4.2 V leads to the formation of fluorescent Ni^{II} and $\text{Mn}^{\text{II/III}}$ complexes with β -diketones ligands and Ni^{II} and Mn^{II} oxalates and carbonates.
 - Stepwise and all-concerted proton-coupled electron transfer reaction mechanism, which lead to metal complexes and water formation at the $\text{Li}_x\text{Ni}_{0.5}\text{Mn}_{1.5}\text{O}_{4-\delta}$ surface, are proposed.
 - The rate of these reactions is enhanced by the continuous creation of oxygen vacancies. The adsorption of β -diketone chelate ligands at $\text{Ni}^{\text{IV}}/\text{Mn}^{\text{IV}}$ surface sites greatly facilitates Ni/Mn

- removal from the crystalline lattice and is primarily responsible for the observed Ni/Mn dissolution.
- The postulated heterogeneous catalysis mechanism accurately describes interfacial processes on a larger class of $\text{Li}_x(\text{Ni}_a\text{Mn}_b\text{Co}_c)\text{O}_y$ -type cathodes and links it with the observed failure modes in Li-ion batteries.
 - This study not only determines the mechanism of transition metal dissolution but it can also offer unique insight into the mechanism of Li^+ transport across the solid electrolyte interphases in Li-ion systems
 - *In situ* and *ex situ* characterization studies of the Si electrodes showed that the nature and kinetics of interfacial phenomena are strongly dependent of the electrode surface structure, artificial coatings and electrolyte additives.
 - Alucone coating shifts the composition of the SEI toward higher content of organic compounds (ROCO_2Li), which improve the cycling performance of the Si nano-composite electrode.
 - LiBOB additive promotes early formation of an oligomer-based ($\text{LiB}_2\text{C}_{10}\text{O}_{20}$) surface film at the silicon surface. This “inner” SEI layer inhibits further electrolyte reduction.
 - Feasibility of *in situ* LIBS measurements for elemental depth profiling of the SEI layer on Si wafer electrodes was demonstrated.
 - Near-field IR spectroscopy and imaging of the SEI local composition on Si anodes was demonstrated for the first time.
 - NF-IR images of the SEI layer on Si revealed inhomogeneous distribution of the electrolyte decomposition products at nanoscale.
 - Clear variations in IR contrast correlated to specific features in topography.
 - Preliminary identification of the SEI chemical building blocks was achieved.

Introduction

The main objective of this task is to obtain detailed insight into the dynamic behavior of molecules, atoms, and electrons at electrode/electrolyte interfaces of intermetallic anodes (Si) and high voltage Ni/Mn-based materials at a spatial resolution that corresponds to the size of basic chemical or structural building blocks. The aim of these studies is to unveil the structure and reactivity at hidden or buried interfaces and interphases that determine battery performance and failure modes. To accomplish these goals novel far- and near-field optical multifunctional probes must be developed and deployed *in situ*. The proposed work constitutes an integral part of the concerted effort within the BMR Program and it attempts to establish clear connections between diagnostics, theory/modelling, materials synthesis, and cell development efforts.

This project provides a better understanding of the underlying principles that govern the function and operation of battery materials, interfaces and interphases, which is inextricably linked with successful implementation of high energy density materials such as Si and high voltage cathodes in Li-ion cells for PHEVs and EVs. This task also involves the development and application of novel innovative experimental methodologies to study and understand the basic function and mechanism of operation of materials, composite electrodes, and Li-ion battery systems for PHEV and EV applications.

Approach

Innovative Approach: Design and employment of novel and sophisticated *in situ* analytical methods to address the key problems of the BMR baseline chemistries. The proposed experimental strategies combine imaging with spectroscopy aimed at probing electrodes at an atom, molecular, or nanoparticulate level to unveil structure and reactivity at hidden or buried interfaces and determine electrode performance and failure modes in baseline Li_xSi -anodes and high-voltage LMNO cathodes. The main goal is to gain insight into the mechanism of surface phenomena on thin-film and monocrystal Sn and Si intermetallic anodes and evaluate their impact on the electrode long-term electrochemical behavior. Comprehensive fundamental study of the early stages of SEI layer formation on polycrystalline and single crystal face Sn and Si electrodes will be carried out. *In situ* and *ex situ* far- and near-field scanning probe spectroscopy will be employed to detect and monitor surface phenomena at the intermetallic anodes high-voltage (>4.3 V) model and composite cathodes.

Results

We have achieved the following progress:

The Mechanism of Ni and Mn Dissolution from $\text{LiNi}_{0.5}\text{Mn}_{1.5}\text{O}_4$ and LiMn_2O_4 Spinel Electrodes

The mechanism of Mn and Ni dissolution from $\text{LiNi}_{0.5}\text{Mn}_{1.5}\text{O}_4$ cathode was studied in detail. Previous work in FY2014 revealed the formation of Mn fluorescent species at the $\text{LiNi}_{0.5}\text{Mn}_{1.5}\text{O}_4$ /electrolyte interface by electrochemical oxidation as well as the deposition of a mixture of $\text{Mn}(\text{II})(\text{acac})_2$ and $\text{Mn}(\text{II})$ oxalate at the graphite electrode surface, with $\text{Mn}(\text{II})(\text{acac})_2$ as the major species. Similarly, the presence of $\text{Ni}(\text{II})(\text{acac})_2$ and $\text{Ni}(\text{II})$ carbonates in the SEI were also detected. Metal oxalates and carbonates are commonly formed by decarboxylation reactions of EC and frequently observed in Ni/Mn oxide-based battery system. On the other hand, the mechanism of interaction between the metal site at the $\text{Li}_{x}\text{Ni}_{0.5}\text{Mn}_{1.5}\text{O}_4$ surface and the electrolyte during oxidation, which leads to the formation of metal complexes, is unknown. A plausible formation pathway, presented in Figure V- 134, involves two proton and two electron transfers as well as a propagation mechanism and is accompanied by desorption of water.

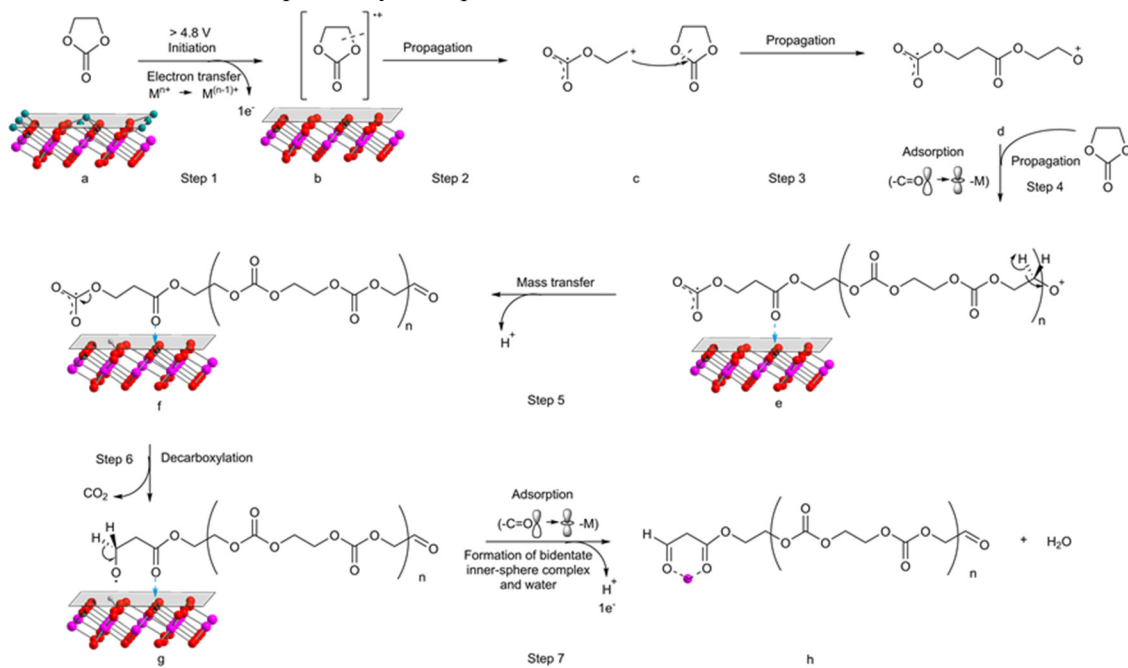


Figure V- 134: Possible formation pathway of the metal complexes upon EC oxidation at the $\text{Li}_{x}\text{Ni}_{0.5}\text{Mn}_{1.5}\text{O}_4$ surface by an electron transfer, propagation, proton transfer and a proton coupled electron transfer (PCET) mechanism

The propagation mechanism results in longer side chains which decrease the solubility of the resultant metal complexes. Therefore a variety of soluble and insoluble fluorescent compounds is observed in aged/cycled Li-ion cells. The M^{II} β -diketone complexes with longer alkoxide side precipitate to form surface films at the cathode side whereas the M^{II} β -diketone complexes with shorter chains diffuse in the electrolyte and get incorporated in the SEI layer on the graphite electrode. These results suggest that the adsorption of β -diketone chelate ligands at $\text{Mn}^{\text{IV}/\text{III}}$ and Ni^{IV} sites is primarily responsible for the observed metal dissolution and that the rate of these reactions is accelerated by the continuous formation of oxygen vacancies. This implies that manganese and nickel diffuse as complex species and not as free $\text{Mn}(\text{II})$ and $\text{Ni}(\text{II})$ ions. This is contrary to the disproportionation mechanism proposed 30 years ago i.e., transition metal dissolution from $\text{LiNi}_{0.5}\text{Mn}_{1.5}\text{O}_4$ occurs via surface oxidation of DEC and EC and formation of $\text{Ni}(\text{II})$ and $\text{Mn}(\text{II})$ coordination complexes at potentials > 4.2 V. This leads to subsequent incorporation of $\text{Mn}(\text{II})(\text{acac})_2$, complexes in the SEI at the graphite electrode.

The influence of the transition metal complexes on the Li^+ transport was tested using graphite symmetric coin cells (prelithiated graphite/graphite) filled with 1 M LiPF_6 , EC/DEC (1:2) electrolyte spiked with 500 ppm $\text{Ni}(\text{II})$ and $\text{Mn}(\text{II})$ compounds. The cells were cycled galvanostatically at C/10 during the initial four cycles and at C/3 for the following 270 cycles. Electrochemical impedance spectra were measured at 50% of state of charge every 10 cycles. To analyze the anode impedance spectra we used a standard equivalent circuit models

consisting of a resistance of the electrolyte (R_1) in series with a second resistance which represents transport processes in the SEI layer and charge transfer resistance (R_2), and constant phase element (CPE_2), which corresponds to the double-layer capacitance. Figure V- 135 shows the dependence of the SEI ionic resistance (R_2) vs. cell cycle number in the baseline electrolyte and electrolyte containing 500 ppm of different transition metal species observed by XANES experiments at the graphite surface in an aged LMNO/graphite cell.

Contrary to the cell cycled with the baseline electrolyte, the presence of transition metal species leads to a rapid increase of the impedance with cycling.

Interestingly, while only a moderate impedance rise is observed in the presence of Mn(II) carbonate and

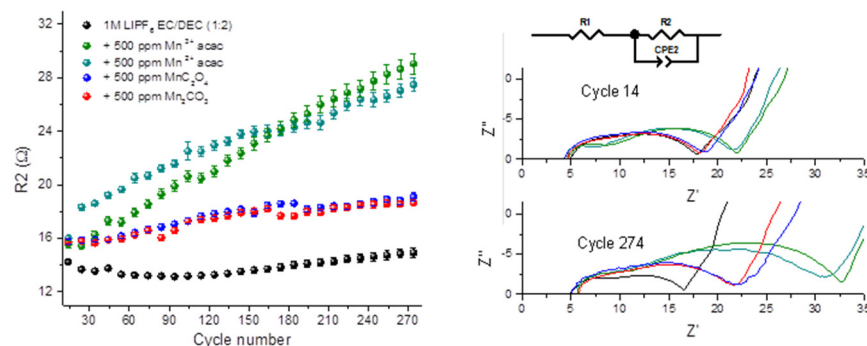


Figure V- 135: Impedance evolution of graphite symmetric cells filled with 1 M LiPF₆, EC/DEC (1:2) spiked with 500 ppm of Mn^{II/III} compounds, measured at 50% of SOC

Mn(II) oxalate, the presence of Mn(II)(acac)₂ and Mn(III)(acac)₃ results in a steep increase of R_2 during cycling. β -diketone complexes are responsible for the observed impedance increase of the graphite anode by inhibiting Li⁺ transport within the SEI. Although the exact mechanism of these Li⁺-Mn(III/II)(acac)₃ interactions in the SEI layer is still unknown, fluorescent β -diketone complexes produced on the cathode may and will be used as a unique probe into the mechanism of Li⁺ transport across the solid electrolyte interphases in Li-ion anodes.

Interfacial Activity of Silicon Anodes

The effect of aluminium alkoxide polymer (alucone) coating on SEI formed on Si anode and its impact on the Li-ion system's long term stability was investigated. 100 nm Si thin films were deposited on copper foil by magnetron sputtering deposition and used as a model electrode for interfacial evaluation. The thin film electrodes were coated with an 8 nm alucone layer by molecular layer deposition. The sample was annealed in Ar at 200°C for 12 hours, assembled in coin cells filled with 1 M LiPF₆, EC/DEC (1:2) electrolyte, and cycled galvanostatically at C/10 for 3 cycles and at 1C for 47 cycles.

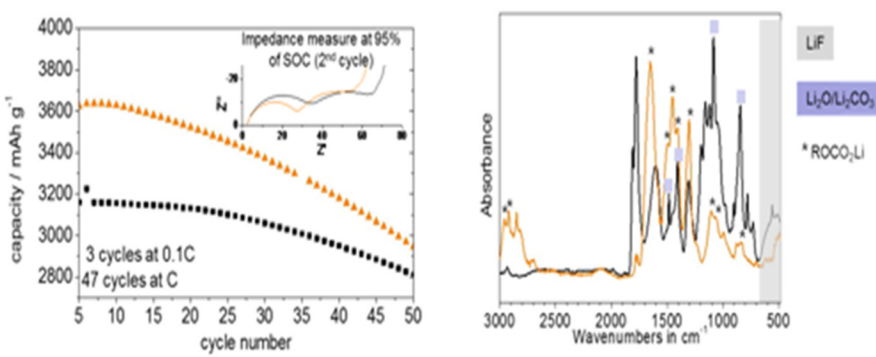


Figure V- 136: SEI layer forms after 50 cycles on 100 nm Si thin film (coated 8 nm Alucone/non coated) in 1M LiPF₆ EC:DEC [1:2] and corresponding impedance spectra

The positive impact of the alucone coating on the cyclability of the Si thin film was confirmed (Figure V- 136). Alucone coating improved the cycling performance of Si thin film and reduced the interfacial resistance. These effects originate from the variation in SEI composition. While the SEI on the non-coated sample consists mainly of inorganic compounds

(LiF, Li₂O/Li₂CO₃), the alucone coating produces improved, ROCO₂Li-enriched SEI. These results are consistent with the literature reports on the behavior of alucone-coated Si composite anodes and they support the general "coating" strategy, indicating that coating of the silicon surface can partially reduce its interfacial instability by changing the nature and/or kinetics of surface reactions. Further advances were also made in

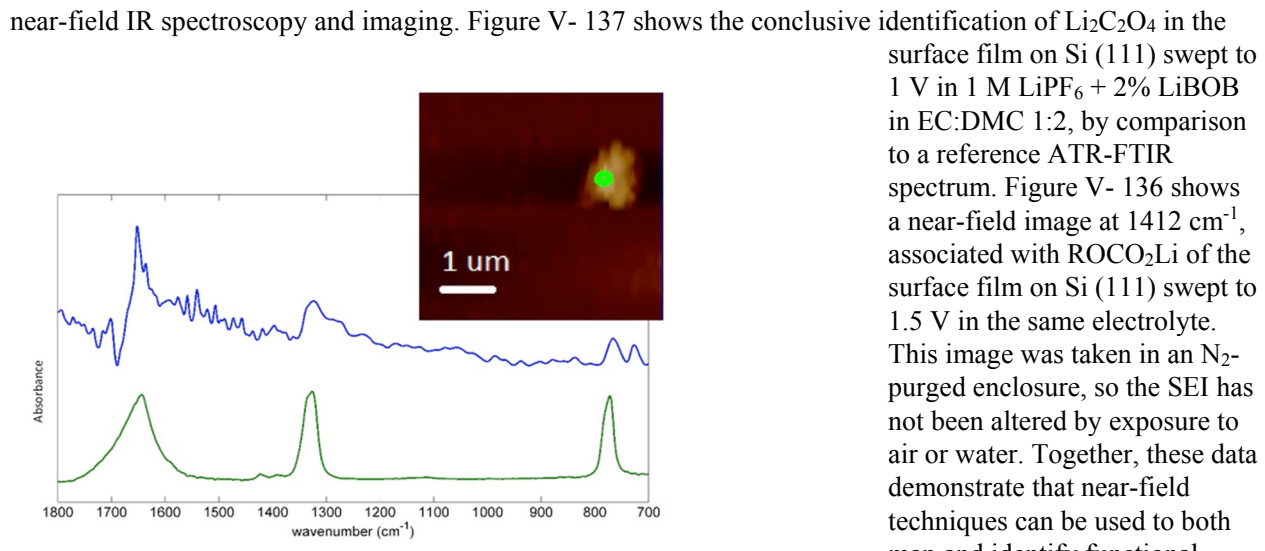


Figure V- 137: (a) Near-field IR (top) spectrum of particle in Si surface film compared to ATR-FTIR spectrum of $\text{Li}_2\text{C}_2\text{O}_4$. Inset: AFM topography with particle marked

Demonstrate Feasibility of *In Situ* Near-Field and LIBS Techniques at Li-ion Electrodes

After switching focus from developing a traditional liquid cell due to technical infeasibility, we focused on the development of graphene electrodes for a transmembrane near-field IR characterization of the growing SEI on a model electrode. This allows *in situ* capability while maintaining a completely sealed cell, avoiding numerous issues associated with liquid immersion. To demonstrate feasibility of this technique, we prepared a sample consisting of CVD graphene on an SiO_2 substrate. The sample was characterized by near-field IR spectroscopy using the Advanced Light Source synchrotron beamline 5.4.1.

The results of this characterization are shown in Figure V- 138. The spectrum shows a characteristic Si-O phonon absorption band in the 1050 cm^{-1} range. This shows that the near-field IR contrast can be resolved through graphene, which is a known Li-ion electrode, demonstrating the feasibility of this approach to *in situ* characterization. We have recently developed and fabricated, in cooperation with the Salmeron group at the LBNL Molecular Foundry, an *in situ* cell using graphene held up by a perforated membrane as a negative electrode. This cell, in combination with the near-field technique demonstrated above, will allow full *in situ* near-field IR characterization of the growing SEI layer on a graphite-like electrode. Experiments using this cell are underway.

To pursue *in situ* LIBS (Laser Induced Breakdown Spectroscopy) for the analysis of SEI layers formed in complex organic carbonate-based electrolytes, we followed two distinct strategies. These strategies address two individual issues that currently limit *in situ* depth-resolved analysis: 1) sensitivity and 2) specificity. In the previous period, we demonstrated that double femtosecond pulse configuration (scheme where collinear fs-laser pulses are temporally separated by hundreds of nanoseconds to microseconds), can provide improved sensitivity through the formation of a rarified atmosphere by the first pulse in the form of cavitation bubbles, exposing the SEI surface directly to the second pulse. Very significant enhancements in sensitivity were observed in organic carbonate-based electrolytes.

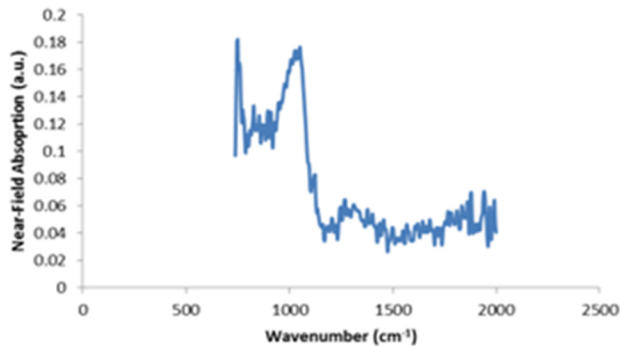


Figure V- 138: Near-field spectroscopic absorption of SiO_2 substrate through graphene membrane

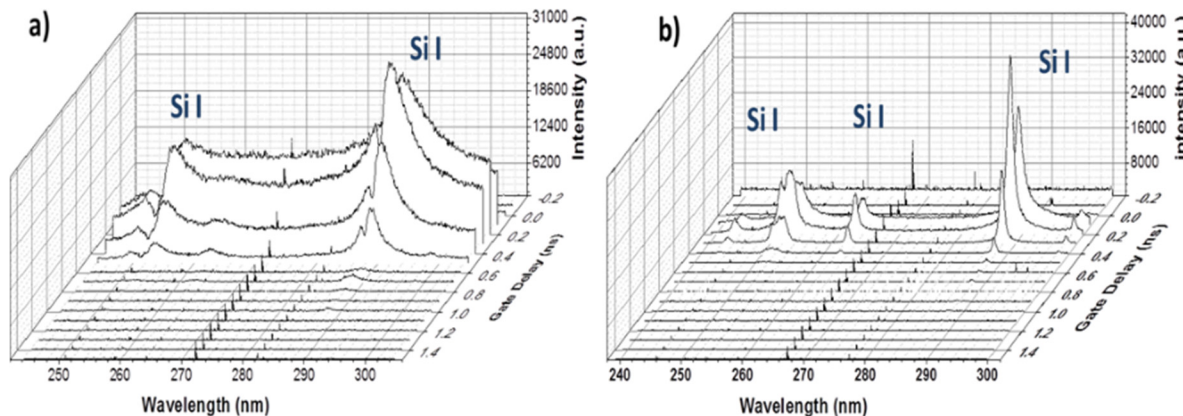


Figure V- 139: Comparison of UV ultrafast LIBS emission from Si (a) in liquid and (b) in air

The second challenge was to de-convolute information originating from the electrolyte and SEI. This period, we addressed this issue by implementing an ultraviolet femtosecond laser excitation, and highly sensitive gated spectrometer/ICCD detection, to study the optical emission characteristics of pre-cycled SEIs and other samples like Si. The samples were submerged in surrogate liquids (such as organic solvents or water) with focus on improving specificity while maintaining high depth resolution. Under ideal conditions, the ultrafast LIBS lines detected in liquids should be very similar to that in air. Figure V- 139 shows the time-resolved emission spectra of Si in the 240-300 nm spectral ranges, where the most prominent Si_I lines are clearly resolved in a) liquid and b) air. We concluded that LIBS has potential to address and elucidate the complex mechanisms leading to the SEI layer formation *in situ*.

Conclusions and Future Directions

- The Li-ion cathode is a major determinant of cost and energy density in lithium-ion batteries. To realize further gains, the specific energies of cathodes must be improved.
- Cathode structural disorder, interfacial instability and the tendency to convert to spinel or rock salt phases during cycling need to be remedied to achieve energy density, lifetime and safety goals.
- These failure modes must be addressed through diagnostic studies to guide development of next generation robust cathode materials.
- Apply advanced characterization techniques to obtain detailed insight into detrimental processes at electrode/electrolyte interfaces of high voltage Ni-rich NMC-type cathode materials.
- Determine and remedy electrochemical performance limiting factors and degradation mechanisms under cycling conditions.
- Determine origins of structural instabilities of the high Ni content electrodes, particularly formation of inert spinel and rock salt phases during cycling, oxygen loss, transition metal dissolution, and formation of resistive interphases and surface films at cathode electrolyte interfaces (CEI).
- Work closely with ABMR PIs to establish clear connections between diagnostics, theory/modelling, materials synthesis, and cell development efforts.
- Develop and apply novel innovative experimental methodologies to study and understand the basic function and mechanism of operation of materials, composite electrodes, and Li-ion cells for PHEV and EV applications.

FY 2015 Publications/Presentations

1. Ayache, Maurice , Simon Franz Lux, and Robert Kostecki, "IR Near-Field Study of the Solid Electrolyte Interphase on a Tin Electrode," *J. Phys. Chem. Lett.* 6 (2015): 1126–1129, DOI: 10.1021/acs.jpclett.5b00263
2. Jarry, Angélique, Sébastien Gottis, Young-Sang Yu, Josep Roque-Rosell, Chunjoong Kim, Jordi Cabana, John Kerr,† and Robert Kostecki, "The Formation Mechanism of Fluorescent Metal

- Complexes at the $\text{Li}_{\text{x}}\text{Ni}_{0.5}\text{Mn}_{1.5}\text{O}_4-\delta$ /Carbonate Ester Electrolyte Interface," *J. Am. Chem. Soc.* (2015), DOI: 10.1021/ja5116698
- 3. Vogl, Ulrike S., Simon F. Lux, Ethan J. Crumlin, Zhi Liu, Lydia Terborg, Martin Winter and Robert Kostecki, "The mechanism of SEI formation on a single crystal Si(100) electrode," *Journal of Electrochemical Society* 62, no. 4 (2015): A603-A607, DOI:10.1149/2.0391504jes
 - 4. Wong, Dominica; Vitale, Alessandra; Devaux, Didier; Taylor, Austria; Pandya, Ashish; Hallinan, Daniel; Thelen, Jacob; Mecham, Sue; Lux, Simon; Lapidès, Alexander; Resnick, Paul; Meyer, Thomas; Kostecki, Robert; Balsara, Nitash; DeSimone, Joseph, "Phase Behavior and Electrochemical Characterization of Blends of Perfluoropolyether, Poly(ethylene glycol) and a Lithium Salt," *Chemistry of Materials* 27, no. 2 (2015): 597–603; DOI: 10.1021/cm504228a
 - 5. Vogl, Ulrike; Das, Prodip K.; Weber, Adam; Winter, Martin; Kostecki, Robert; Lux, Simon, "The mechanism of interactions between CMC binder and Si single crystal facets," *Langumir* 30, no. 34 (2014): 10299–10307.
 - 6. Kuppan, Saravanan, Angelique Jarry, Robert Kostecki, and Guoying Chen, "Thermal Behavior of Chemically-Delithiated $\text{Li}_{\text{x}}\text{Mn}_{1.5}\text{Ni}_{0.5}\text{O}_4$ ($0 \leq \text{x} < 1$) and the Isolation of Room-Temperature Solid Solutions," *Scientific Reports* 5 (2015): 8027, doi:10.1038/srep08027
 - 7. Cheng, Lei , Ethan Crumlin, Wei Chen, Ruimin Qiao, Huaming Hou, Simon Franz Lux, Vassilia Zorba, Richard Russo, Robert Kostecki, Kristin Persson, Wanli Yang, Jordi Cabana, Thomas Richardson, Guoying Chen, and Marca Doeff, "Origin of High Electrolyte-Electrode Interfacial Resistances in Lithium Cells Containing Garnet Type Solid Electrolytes," *Advanced Materials, Phys. Chem. Chem. Phys.* 16 (2014): 18294-18300, DOI:10.1039/c4cp02921f
 - 8. Ayache, M., Jang, D., Syzdek, J., & Kostecki, R. "Near-Field IR Nanoscale Imaging of the Solid Electrolyte Interphase on a HOPG Electrode." *Journal of The Electrochemical Society* 162, no. 13 (2015): A7078-A7082.
 - 9. Ayache, M., J. Syzdek, I. Lucas, N. Norberg and R. Kostecki, "Interfacial Studies of the SEI Layer on a Tin Electrode," Presented at the 2014 ECS and SMEQ Joint International Meeting, Cancun, Mexico, October 2014
 - 10. Ayache, Maurice , Simon Lux, and Robert Kostecki, "Nanoscale Chemical Mapping of the Solid Electrolyte Interphase in Li-ion Systems," Invited talk presented at the SciX Conference, Reno, NV, September 2014.
 - 11. Kostecki, Robert, "Battery Characterization and Diagnostics Across Length and Time Scales," Presented at the 10th China-U.S. Electric Vehicle and Battery Technology Workshop, Beijing, China, March 2015.
 - 12. Kostecki, Robert , Maurice Ayache, Simon Lux, Ivan Lucas, "Near-field optical imaging of the SEI layer on a Sn anode," Presented at the 249th ACS National Meeting & Exposition, March 22-26, 2015, Denver, CO, USA
 - 13. Kostecki, Robert, Maurice Ayache, Angelique Jarry, Ivan Lucas, "Chemical Imaging of Interfaces and Interphases in Li-ion Anodes," Presented at the International Battery Association (IBA) and Pacific Power Source Symposium, Honolulu, HI, January 2015.
 - 14. Kostecki, Robert, Maurice Ayache, Simon Lux, Ivan Lucas, "Near-field optical imaging of the SEI layer on a Sn anode," Presented at the 249th ACS National Meeting & Exposition , Denver, CO, March 2015.
 - 15. Yu, Y. S. , C. Kim, D. Shapiro, M. Farmand, R. Kostecki, D. Qian, S. Meng and J. Cabana, "Advanced X-Ray Transmission Microscopy for Chemical and Fracture Imaging of Single $\text{Li}_{\text{x}}\text{FePO}_4$ Particles at High Resolution," Presented at the 227th ECS Meeting, Chicago, IL, May 2015
 - 16. Kostecki, R., A. Jarry, S. Gottis, and J. B. Kerr, "Mechanism of Formation of Metal Acetylacetones at the $\text{Li}_{\text{x}}\text{Ni}_{0.5}\text{Mn}_{1.5}\text{O}_{4-\delta}$ /Carbonate Ester Electrolyte Interface," Presented at the 227th ECS Meeting, Chicago, IL., May 2015
 - 17. Terborg, L., Y. Park, S. Venkatachalam, P. Hernandez and R. Kostecki, "Interfacial Reactivity of a High Capacity Manganese Rich (HCMRTM) Li-ion Positive Electrode," Presented at the 227th ECS Meeting, Chicago, IL, May 2015
 - 18. Ayache, M., D. Jang, and R. Kostecki, "Nanoscale IR Near-Field Imaging of the SEI Layer on an HOPG Electrode," Presented at the 227th ECS Meeting, Chicago, IL, May 2015

19. Kostecki, Robert, "Challenges and Opportunities in Battery Characterization," Summer Seminar presented at the Westfälische Wilhelms-Universität, MEET Batterieforschungszentrum, Muenster, Germany, August 2015.
20. Jarry, Angélique, Sébastien Gottis, Young-Sang Yu, Josep Roque-Rosell, Chunjoong Kim, Jordi Cabana, John Kerr and Robert Kostecki, "The Mechanism of Mn and Ni Dissolution at the $\text{Li}_x\text{Ni}_{0.5}\text{Mn}_{1.5}\text{O}_{4-\delta}$ / Organic Carbonate Electrolyte Interface," Presented at LiBD-7 2015 – "Electrode materials," Arcachon, France, June 2015.

V.F.3 Advanced in situ Diagnostic Techniques for Battery Materials (BNL)

Objectives

- To determine the contributions of electrode materials changes, interfacial phenomena, and electrolyte decomposition to the cell capacity and power decline.
- To develop and apply synchrotron based in situ X-ray techniques such as x-ray diffraction (XRD) and x-ray absorption spectroscopy (XAS) to study materials in an environment that is close to the real operating conditions.
- To search new approaches on how to improve the thermal stability of cathode materials including doping and surface modification techniques.
- To develop new diagnostic tools for battery studies.

Technical Barriers

- Li-ion and Li-metal batteries with long calendar and cycle life
- Li-ion and Li-metal batteries with superior abuse tolerance
- To reduce the production cost of a PHEV batteries.

Technical Targets

- Complete the In situ XRD studies of the structural evolution of $\text{Li}_{2-x}\text{MoO}_3$ ($0 \leq x \leq 2$) high energy density cathode material during charge-discharge cycling between 2.0 and 4.8 V.
- Complete the x-ray absorption near edge structure (XANES) and extended x-ray absorption fine structure (EXAFS) studies at Mo K-edge of Li_2MoO_3 at different charge-discharge states.
- Complete the preliminary studies of elemental distribution of Fe substituted high voltage spinel cathode materials using transmission x-ray microscopy (TXM).

Accomplishments

- By collaborating with Prof. Zhaoxiang Wang at Institute of Physics, Chinese Academy of Sciences, through a systematic study of lithium molybdenum trioxide (Li_2MoO_3) using synchrotron based XRD and XAS, as well as STEM, a new “unit-cell-breathing” mechanism during charge-discharge was discovered. The cation mixing caused by migration of Mo ions at higher oxidation state provides the benefits of reducing the c expansion range in early stage of charging and suppressing the structure collapse at high voltage charge. These results open a new strategy for designing and engineering layered cathode materials for high-energy-density lithium-ion batteries.
- By designed Fe substitution, the thermal stability optimized high voltage spinel $\text{LiNi}_{1/3}\text{Mn}_{4/3}\text{Fe}_{1/3}\text{O}_4$ was synthesized and characterized, which is thermally stable at temperature as high as 500°C.
- Elemental distribution of Fe substituted high voltage spinel cathode materials was studied using new technique of transmission x-ray microscopy (TXM).

Introduction

The layer structured LiMO_2 has the theoretical capacities $\sim 270 \text{ mAh g}^{-1}$, but only about $140-150 \text{ mAh g}^{-1}$ reversible capacity can be practically utilized with a cutoff voltage about 4.2-4.3 V. If the cells could be

Project Details

Xiao-Qing Yang (Brookhaven National Laboratory – PI)
Chemistry Department
Building 555
Upton, NY 11973
Phone: 631-344-3663; Fax: 631-344-5815
E-mail: xyang@bnl.gov

Xiqian Yu (Brookhaven National Laboratory – co-PI)
Chemistry Department
Building 555
Upton, NY 11973
Phone: 631-344-4142; Fax: 631-344-5815
E-mail: xyu@bnl.gov

Start Date: October 2014

Projected End Date: September 2015

charged to higher voltages without damaging the structure, higher practical energy density (with high capacity and voltage) would be obtained. Unfortunately, when charge voltage limit is increased above 4.3 V, the reversible capacity in subsequent cycles fades seriously due to the structural degradation caused by high voltage charging. Therefore, redesigning the chemical contents and crystal structures to suppress such structural degradation will open a new approach for developing high energy density cathode materials with long cycle life. Some exploratory studies were performed to reach this goal.

$\text{LiNi}_{0.5}\text{Mn}_{1.5}\text{O}_4$ (LNMO) with high operating voltage is a very good candidate as high energy density cathode material for Li-ion batteries. However, In order to be used in EVs, the thermal stability of LNMO needs to be significantly improved. It has been reported that charged LNMO starts oxygen release at around 250°C, showing far worse than its parent material LiMn_2O_4 (LMO). The Fe substituted LNMO designed and synthesized by our group shows dramatic thermal stability improvement but maintains comparable high voltage capacity as the un-substituted LNMO. The structural changes of this new material during cycling and heating were studied.

Approach

1. A combination of time resolved X-ray diffraction (TR-XRD) and mass spectroscopy (MS), together with *in situ* soft and hard X-ray absorption (XAS) during heating and transmission electron microscopy (TEM) to study the thermal stability of the electrode materials.
2. Using *in situ* XRD and XAS, as well as TEM to study a model cathode material Li_2MoO_3 on the lattice breathing of layer structured materials during charge-discharge cycling, aiming to improve the cycle life of Li-ion batteries
3. Using quick x-ray absorption spectroscopy technique to study the kinetic properties of $\text{Li}_{1.2}\text{Ni}_{0.15}\text{Co}_{0.1}\text{Mn}_{0.55}\text{O}_2$ high energy density cathode materials during constant voltage charge for high rate capability of Li-ion batteries.
4. Extended collaboration with other US and international academic institutions and US industrial partners.

Results

We have achieved the following progress:

Tuning Charge-Discharge Induced Unit-Cell-Breathing through Metal-Metal Bonding in Layer-Structured Cathode Materials for Lithium-ion Batteries

Through a systematic study, a new “unit-cell-breathing” mechanism is introduced based on both crystal and electronic structural changes of transition metal oxide cathode materials during charge-discharge: For widely used LiMO_2 ($\text{M} = \text{Co, Ni, Mn}$), lattice parameters, a and b contracts during charge. However, for Li_2MoO_3 , such changes are in opposite directions. Metal-metal bonding is used to explain such “abnormal” behavior and a generalized hypothesis is developed. The expansion of M-M bond becomes the controlling factor for $a(b)$ evolution during charge, in contrast to the shrinking M-O as controlling factor in “normal” materials. The cation mixing caused by migration of Mo ions at higher oxidation state provides the benefits of reducing the c expansion range in early stage of charging and suppressing the structure collapse at high voltage charge. These results open a new strategy for designing and engineering layered cathode materials for high-energy-density lithium-ion batteries. The *in situ* X-ray diffraction patterns of Li_2MoO_3 upon the first charge are shown in Figure V- 140.

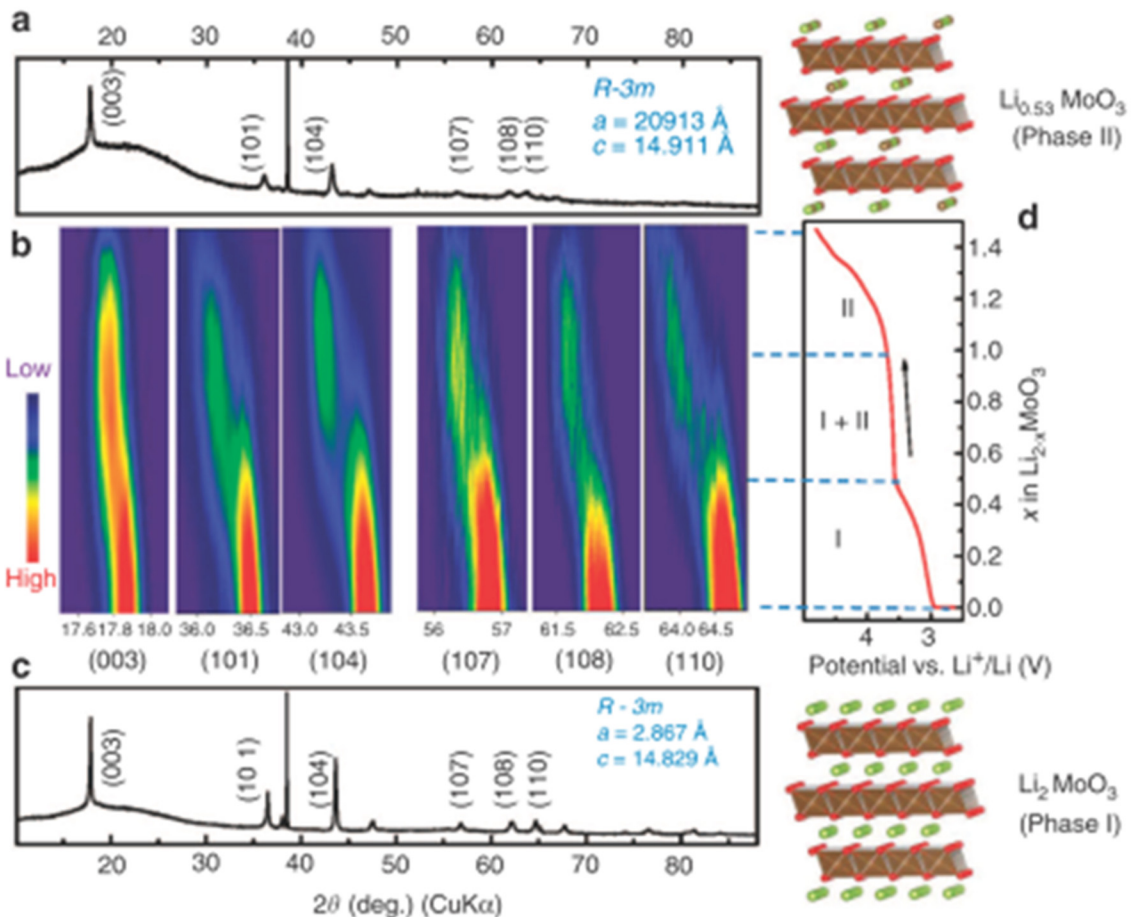


Figure V- 140: *In situ* X-ray diffraction (XRD) of Li_2MoO_3 during the first charge. (a) The XRD pattern of the $\text{Li}_{2-x}\text{MoO}_3$ electrode right after charging to 4.8 V. (b) Contour plot of diffraction peak evolution of (003), (101), (104), (107), (108) and (110) during delithiation. (c) The XRD pattern of the Li_2MoO_3 electrode before charge. (d) Charge curve at a current density of 10 mAg^{-1} from open circuit voltage (OCV) to 4.8 V during XRD data collection

The patterns for fully charged and pristine Li_2MoO_3 are plotted in Figure V- 140a and c, respectively. All the peaks can be indexed by a layered structure with the space group R-3m, except for one strong peak at 38.5° , which is from the Al current collector. To demonstrate the phase transition clearly, the contour plots of peak intensity and position for several main peaks as a function of capacity during charge are presented in Figure V- 140b. It should be noted that the (003), (107) and (108) peaks mainly reflect the evolution along c axis, while the (110) and (101) peaks reflect the evolution along a (and b) axis. The initial charge curves are shown on the right side in Figure V- 140d. In the region of $0 < x < 0.5$, with a voltage slope from 3.0 to 3.6 V, all of these peaks shifted to the lower angles, indicating a solid solution reaction with decreasing d-spacing for Phase I. In the region of $0.5 < x < 1.0$, a new phase (Phase II) started to form and grow at the expense of Phase I. The new phase has the same layered structure as Phase I but larger unit cell with increased lattice parameters in both a (b) and c , migrated Mo ions into the original Li layers, as the number of Li ions decreasing (Structure schematics of Phase I and Phase II are shown in Figure V- 140. The results of this study was published on *Nature Communications* (Publication list 1.)

In order to understand the abnormal structural changes of Li_2MoO_3 during lithium extraction, *in situ* X-ray absorption spectroscopy (XAS) at Mo K-edge was applied to monitor the valence state changes of Mo and local structure changes of Li_2MoO_3 during charge process. Figure V- 141 shows the X-ray absorption near edge structure (XANES) spectra of the Mo K-edge during charge. A continuous increase of the pre-edge intensity indicates the increased distortion of $\text{Mo}-\text{O}_6$ octahedra. Such pre-edge structure is originated from a quadruple excitation, which is forbidden under perfect octahedral symmetry. This $\text{Mo}-\text{O}_6$ octahedra distortion caused pre-edge structure is the typical feature of $a\text{-MoO}_3$ with Mo^{6+} oxidation state. The observation of the increased pre-edge structure and the shifting of white line to higher energy positions suggests that Mo ions are

oxidized to higher than Mo⁴⁺ states upon charging. Compared with the Mo K-edge XANES data of the MoO₂ and α -MoO₃ references, it can be estimated that the Mo ions were oxidized from Mo⁴⁺ to a higher oxidation state between Mo⁵⁺ to Mo⁶⁺. As shown in the enlarged inset of Figure V- 141a, we can see that the intersection is not exactly a “isosbestic point”. It should be due to that the charge process of Li₂MoO₃ is not a simple two-phase reaction, but also including two solid-solution regions. This is confirmed by the *in situ* XRD data. Figure V- 141b shows the magnitude plot of Fourier transformed extended X-ray absorption fine structure (FT-EXAFS) spectra for Mo K-edge (k^3 -weighted in k -space) of pristine ($x = 0$), half charged ($x = 0.75$) and fully charged ($x = 1.47$) in Li_{2-x}MoO₃. The FT magnitudes of MoO₂ and α -MoO₃ are also plotted in the bottom panels as references.

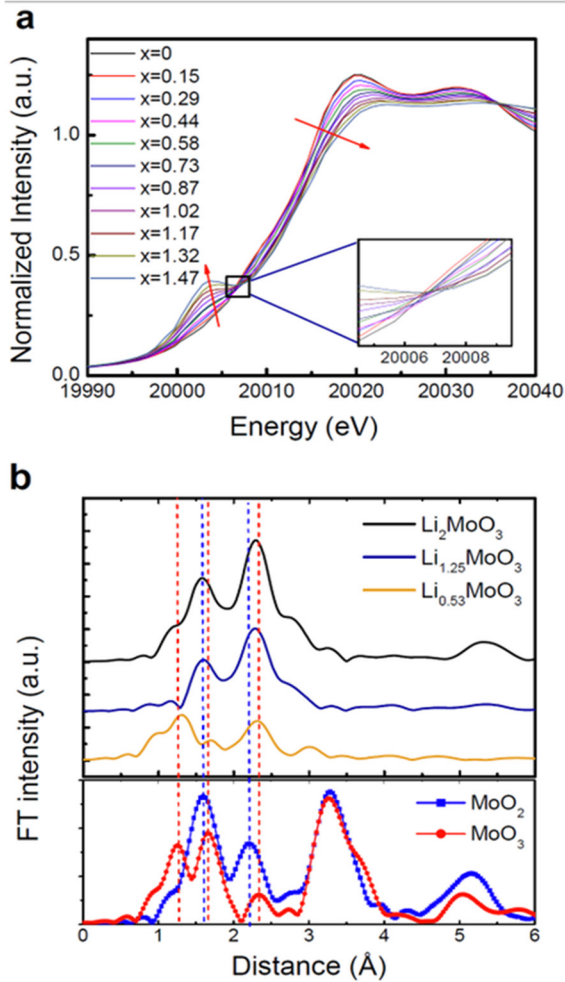


Figure V- 141: XAS spectra of Li₂MoO₃ during the first charge. (a) *In situ* XANES spectra at Mo K-edge during charging to 4.8V. (b) *Ex situ* FT-EXAFS spectra of Li_{2-x}MoO₃ at pristine ($x = 0$), half charged ($x = 0.75$) and fully charged ($x = 1.47$) states. The lower panel shows the FT-EXAFS spectra of MoO₂ and α -MoO₃ references

increases and become clearly observable at $2x=0.5$. Therefore, the solubility limit of Fe in the LiNi_{0.5-x}Mn_{1.5-x}Fe_{2x}O₄ is regarded at around $2x=0.33$. This is supported by the linear relationship between lattice parameter and Fe concentration, following the Vegard's law as shown in Figure V- 142c.

Utilizing High Spin Fe³⁺ in Spinel Structured Cathode Material for Safer High Energy Lithium-ion Batteries

Based on the fundamental understanding of the interplay between oxygen release and crystal structural change which is further related to the electronic structure of transition metal cations, we proposed using Fe as a major component for the high voltage spinel system in designing thermally stable and high-performance cathode. The synthesized LiNi_{0.5-x}Mn_{1.5-x}Fe_{2x}O₄ ($2x = 0.33$) material delivers both satisfactory thermal stability and competitive electrochemical performance. These results highlight the importance of fundamental studies in advancing the battery chemistry. The results of this study was submitted to *Advanced Energy Materials* (under review.)

Since Fe substitution is designed to improve the thermal stability while keep the high energy density of high voltage spinel, higher concentration of Fe is desirable, as long as the structural purity and electrochemical performance is not negatively impacted. LiNi_{0.5-x}Mn_{1.5-x}Fe_{2x}O₄ samples with $2x=0$, 0.2, 0.33, and 0.5 were synthesized and characterized by XRD (Figure V- 142a). It can be seen that the $2x=0$ sample features a pure spinel phase, with all the major peaks indexed by the space group Fd $\bar{3}$ m. The (220) peak, which is very sensitive to the transition metal cations at tetrahedral sites²⁸, is almost invisible, suggesting that tetrahedral sites are almost exclusively occupied by lithium. Therefore, the structure can be described as lithium residing in tetrahedral 8a site, transition metal residing in octahedral 16d site and oxygen in 32e site as shown in the crystal structure in Figure V- 142b. As the Fe concentration increases, some impurity phase starts to emerge and becomes significant in the $2x=0.5$ sample. At the same time, the intensity of (220) peak

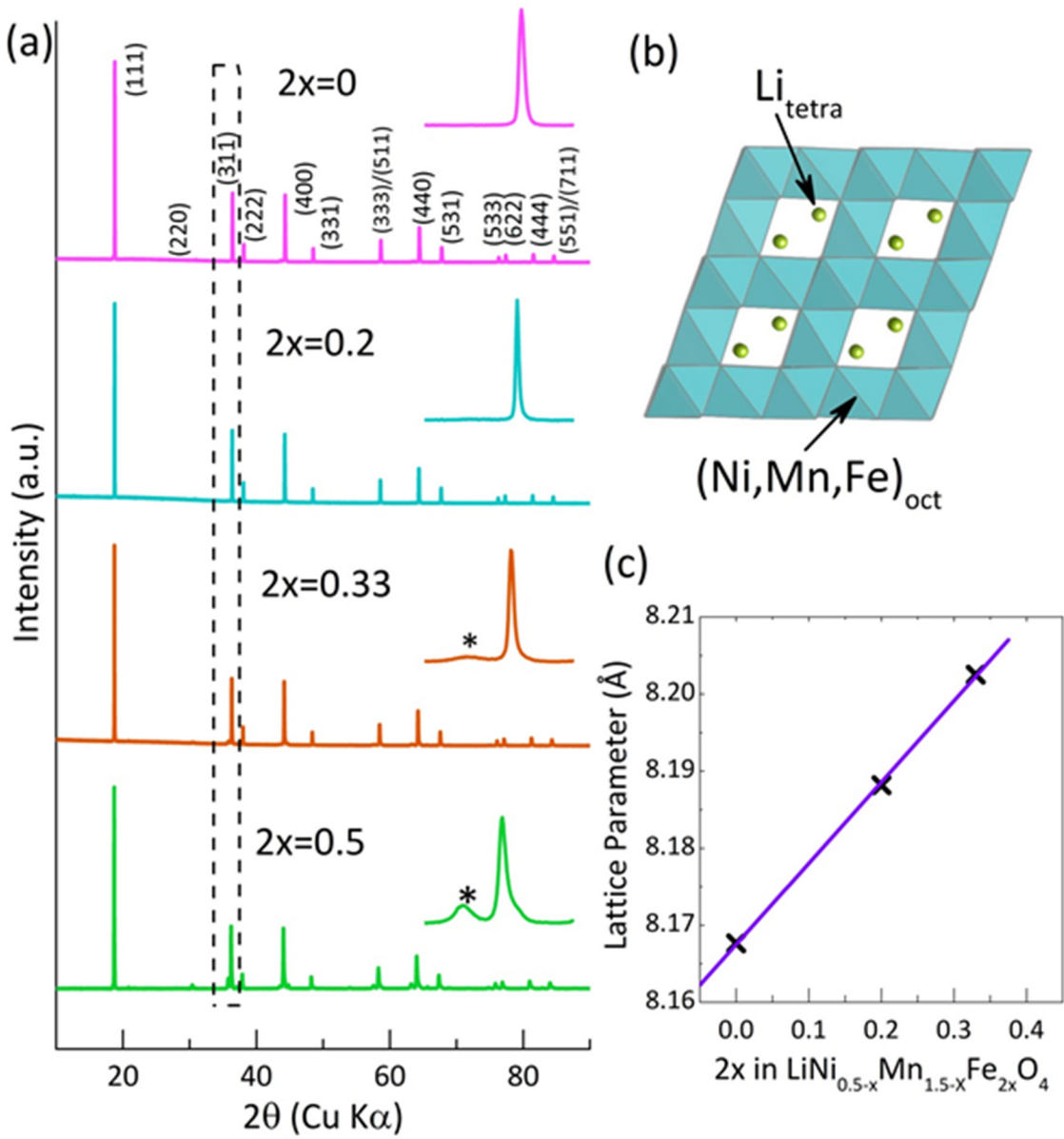


Figure V- 142: (a) XRD patterns for $\text{LiNi}_{0.5-x}\text{Mn}_{1.5-x}\text{Fe}_{2x}\text{O}_4$ ($2x = 0, 0.2, 0.33, 0.5$) with the inset graphs showing the emergence of impurity phase as $2x$ exceeds a certain limit. A pure phase can be indexed by the $\overline{\text{Fd}3\text{m}}$ space group. (b) Illustration of the crystal structure of $\text{LiNi}_{0.5-x}\text{Mn}_{1.5-x}\text{Fe}_{2x}\text{O}_4$. (c) Variation of the lattice parameter as a function of the concentration of Fe. The linear relationship indicates that solid solution is formed in the $\text{LiNi}_{0.5-x}\text{Mn}_{1.5-x}\text{Fe}_{2x}\text{O}_4$ ($2x = 0, 0.2, 0.33$) series

In order to study the elemental distribution of the three transition metal elements cross the sample particles, we also performed nondestructive transmission X-ray microscopic (TXM) investigations. In Figure V- 143, the three dimensional tomographic results (collected at 8380 eV, above the k edges of all the three transition metal elements: Mn, Fe, and Ni) of a ~10-micron-sized particle (Figure V- 143a) and several selected slices through different depth (Figure V- 142, Figure V- 143c-Figure V- 143g) are shown. The three dimensional density distributions within this solid particle are homogeneous. By tuning the x-ray energy, we studied the energy dependency of each single voxels within this volume and quantitatively retrieved the elemental concentration as indicated in Figure V- 143b, in which the elemental concentration over the line path highlighted in Figure V- 142e is plotted. The relative concentration of Mn, Fe, and Ni, shown in Figure V- 143b is in good agreement with the expected elemental composition as designed. These results clearly demonstrated that the new material synthesized has a good degree of homogeneity in the structure and chemical distribution with designed composition.

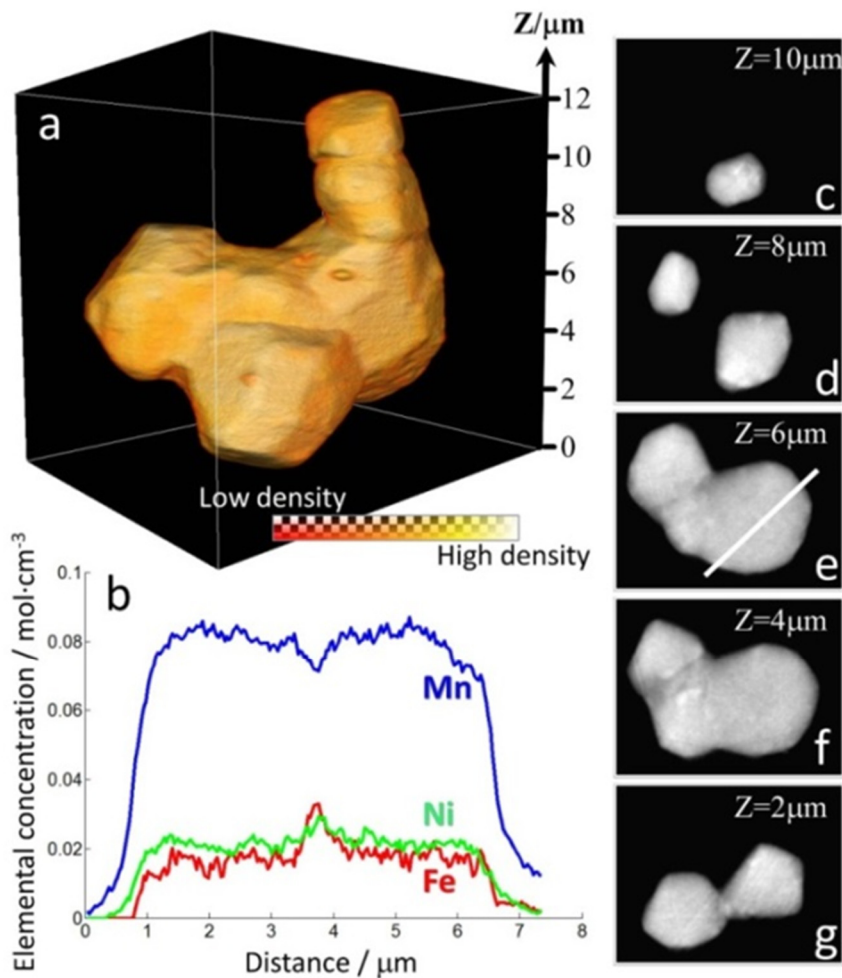


Figure V- 143: Rendering of the 3D structure of a selected $\text{LiNi}_{0.33}\text{Mn}_{1.34}\text{Fe}_{0.33}\text{O}_4$ particle is shown in panel (a) with the scale indicated in the axis and the color legend shown in the inset. Panels (c) through (g) are slices at different depth of the particle showing that it is a solid piece with no internal pores and the density distribution is relatively homogeneous. The elemental concentration over the line path indicated in panel (e) is plotted in panel (b) (the blue, green, and red curves represent the concentration of Mn, Ni, and Fe respectively), which is in good agreement with the elemental composition of the material. Panels (a) and (c) through (g) are reconstructed from nano-tomography data collected at 8380 eV (above the absorption κ edges of all the three transition metal elements), while the data plotted in panel (b) is retrieved from the evaluation of the energy dependency of the absorption coefficient using a method known as Absorption Correlation Tomography

$\text{LiNi}_{0.5}\text{Mn}_{1.5}\text{O}_4$. This phenomenon is also observed previously in Cr-doped $\text{LiNi}_{0.5}\text{Mn}_{1.5}\text{O}_4$. One possible explanation is that Fe substitution reduces the overall size differences among the cations (Ni^{2+} : 0.69 Å, Mn^{4+} : 0.53 Å, Fe^{3+} : 0.645 Å). Therefore, the overall strain is reduced in the system and the system is more tolerant to the variation of lithium concentration. In other words, the strain introduced by lithium extraction/insertion is no longer large enough to induce the phase separation. More accurate explanation may require detailed theoretical studies which will be planned for future studies.

Since our goal is to design cathode material with improved thermal stability while keeping the good electrochemical performance, it is important to make sure that the intrinsic good electrochemical performance of $\text{LiNi}_{0.5}\text{Mn}_{1.5}\text{O}_4$ is not scarified by Fe substitution. Detailed electrochemical studies (Figure V- 144) were carried out for the $2x=0.33$ sample as this material showed the greatest improvement in thermal stability. Upon Fe substitution, capacity (Figure V- 144), cyclability and rate capability (Figure V- 144) are well preserved. In fact, the $2x=0.33$ sample showed even slightly better rate capability. It is also interesting to note that Fe substitution leads to a slopy discharging curve compared with the flat one for $\text{LiNi}_{0.5}\text{Mn}_{1.5}\text{O}_4$. *In situ* XRD results showed that the reaction proceeds in a solid-solution fashion for the Fe-substituted sample, compared with the two-phase reaction for

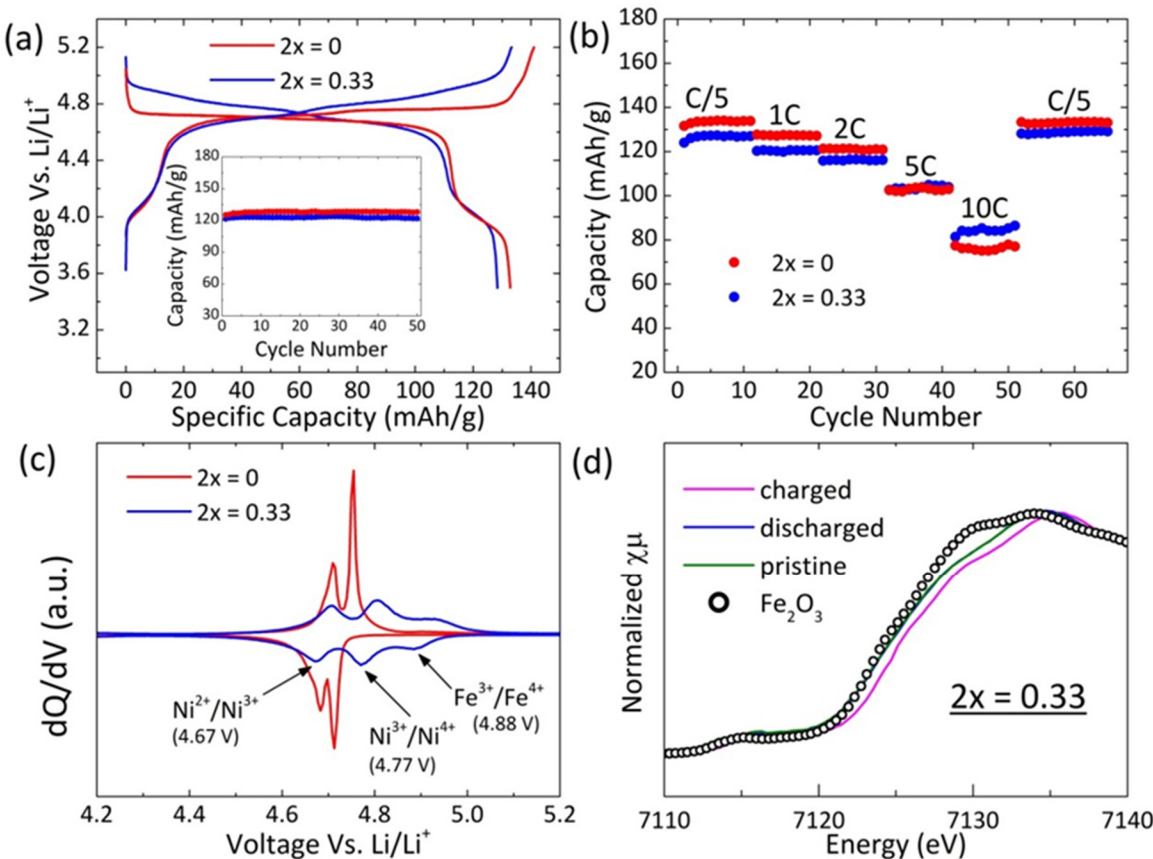


Figure V- 144: Electrochemical performance and XANES spectra. (a) Charge and discharge profiles together with capacity retention (inset graph) of $\text{LiNi}_{0.5-x}\text{Mn}_{1.5-x}\text{Fe}_{2x}\text{O}_4$ ($2x = 0, 0.33$). Cells were cycled at C/5 which corresponds to current density of $0.11 \text{ mA}/\text{cm}^2$. (b) Rate capability of $\text{LiNi}_{0.5-x}\text{Mn}_{1.5-x}\text{Fe}_{2x}\text{O}_4$ ($2x = 0, 0.33$). (c) dQ/dV plot of $\text{LiNi}_{0.5-x}\text{Mn}_{1.5-x}\text{Fe}_{2x}\text{O}_4$ ($2x = 0.33$). (d) Fe K-edge XANES spectra of pristine, charged and discharged samples of $\text{LiNi}_{0.5-x}\text{Mn}_{1.5-x}\text{Fe}_{2x}\text{O}_4$ ($2x = 0.33$)

The origin of undiminished capacity upon Fe substitution can be understood from the dQ/dV plot in Figure V - 5c. It can be seen that there are three redox couples in the Fe-substituted sample, corresponding to $\text{Ni}^{2+}/\text{Ni}^{3+}$, $\text{Ni}^{3+}/\text{Ni}^{4+}$ and $\text{Fe}^{3+}/\text{Fe}^{4+}$. The third one is assigned to $\text{Fe}^{3+}/\text{Fe}^{4+}$ on the basis of Fe K-edge x-ray absorption results shown in Figure V - 5d indicating the capacity lost due to reduced Ni content is compensated by the $\text{Fe}^{3+}/\text{Fe}^{4+}$ contribution.

FY 2015 Publications/Presentations

- He, Kai, Huolin L. Xin, Kejie Zhao, Xiqian Yu, Dennis Nordlund, Tsu-Chien Weng, Jing Li, Yi Jiang, Christopher, A. Cadigan, Ryan M. Richards, Marca Doeff, Xiao-Qing Yang, Eric A. Stach, Ju Li, Feng Lin, and Dong Su, "Transitions from Near-Surface to Interior Redox upon Lithiation in Conversion Electrode Materials," *Nano Lett.* 15, no. 2 (2015): 1437–1444, DOI: 10.1021/nl5049884
- Yue, Ji-Li, Yong-Ning Zhou, Si-Qi Shi, Zulipiya Shadike, Xuan-Qi Huang, Jun Luo, Zhen-Zhong Yang, Hong Li, Lin Gu, Xiao-Qing Yang, Zheng-Wen Fu, "Discrete Li-occupation versus pseudo-continuous Na-occupation and their relationship with structural change behaviors in $\text{Fe}_2(\text{MoO}_4)_3$," *Scientific Reports* 5 (2015): Article Number: 8810.
- Hu, Enyuan, Seong Min Bak, Sanjaya D. Senanayake, Xiao-Qing Yang, Kyung-Wan Nam, Lulu Zhang, Minhua Shao, "Thermal stability in the blended lithium manganese oxide – Lithium nickel cobalt manganese oxide cathode materials: An in situ time-resolved X-Ray diffraction and mass spectroscopy study," *Journal of Power Sources* 277 (2015): 193–197.
- Mahmood, Q., M.G. Kim, S. Yun, S. Bak, X.-Q. Yang, H.S. Shin, W.S. Kim, P.V Braun, H. S. Park, "Unveiling surface redox charge storage of interacting two-dimensional heteronanosheets in hierarchical Architectures," *Nano Lett.* 15 (2015): 2269.

5. Youn, H.-C., S. Bak, M.S. Kim, C. Jaye, D.A. Fischer, C.W. Lee, X.-Q. Yang, K.C. Roh, K.B. Kim, "High-surface-area nitrogen-doped reduced graphene oxide for electric double-layer capacitors," *ChemSusChem* 8 (2015): 1875.
6. Lyu, Y., N. Zhao, E. Hu, R. Xiao, X. Yu, L. Gu, X.Q. Yang, H. Li, "Probing reversible multi-electron transfer and structure evolution of $\text{Li}_{1.2}\text{Cr}_{0.4}\text{Mn}_{0.4}\text{O}_2$ cathode material for Li-ion batteries in a voltage range of 1.0-4.8 V," *Chem. Mater.* 27 (2015): 5238.
7. Xiao, L., J. Xiao, X. Yu, P. Yan, J. Zheng, M. Engelhard, P. Bhattacharya, C. Wang, X.-Q. Yang, J.-G. Zhang, "Effects of structural defects on the electrochemical activation of Li_2MnO_3 ," *Nano energy* 16 (2015): 143.
8. Zhou, Yong-Ning, Enyuan Hu, Xiqian Yu, Seongmin Bak, Xiao-Qing Yang, Hung-Sui Lee, Jun Ma, Zhaoxiang Wang, Lin Gu and Liquan Chen, Kyung-Wan Nam, and Yijin Liu. "Using synchrotron based advanced characterization techniques to study new electrode materials for lithium-ion batteries." Invited presentation, 2014 MRS Fall Meeting, Boston, MA, November 2014.
9. Yu, Xiqian, Yongning Zhou, Enyuan Hu, Seongmin Bak, Xiao-Qing Yang, Hung Sui Lee, Jun Ma, Zhaoxiang Wang, Hong Li, Xuejie Huang, Liquan Chen, Kyung-Wan Nam, Yijin Liu, Huilin Pan, Jie Xiao, and Jun Liu. "Using Synchrotron Based X-ray Diffraction and Absorption and TXM to Study the New Electrode Materials for Next Generation of Batteries." Invited presentation, International Battery Association (IBA) and Pacific Power Source Symposium Joint Meeting 2015, Honolulu, HI, January 2015.
10. Nam, Kyung-Wan, Seongmin Bak, Enyuan Hu, Yongning Zou, Xiqian Yu, Xiao-Qing Yang, Huiming Wu, and Khalil Amine, "Combined In Situ Synchrotron-based X-ray and Mass Spectroscopy Study on Thermal Stability of Cathode Materials for Li-ion Batteries during Heating", Invited presentation, 2015 MRS Spring Meeting, San Francisco, CA, April 2015.
11. Bak, Seongmin, Yongning Zou, Enyuan Hu, Xiqian Yu, Kyung-Wan Nam, and Xiao-Qing Yang, "Synchrotron-Based X-Ray Characterization on the Thermal Decomposition Mechanism of Charged Cathode Materials for Na-Ion Batteries." Presented at the 2015 MRS Spring Meeting, San Francisco, CA, April 2015.

V.F.4 NMR and Pulse Field Gradient Studies of SEI and Electrode Structure (U Cambridge)

Objectives

- Identify major SEI components, and their spatial proximity, and how they change with cycling.
- Contrast SEI formation on Si vs. graphite and high voltage cathodes
- Correlate Li⁺ diffusivity in particles and composite electrodes with rate.
- Explore how additives modify the SEI.
- Develop new NMR based methods for identifying different components in the SEI and their spatial proximities within the SEI, which will be broadly applicable to the study SEI formation on a much wider range of electrodes.
- Investigate local structural changes of high voltage/high capacity electrodes on cycling.

Project Details

Clare Grey (University of Cambridge – PI)
Department of Chemistry
Lensfield Road
Cambridge, CB2 1EW
Phone: +44(1223)336509; Fax: +44(1223)336362
E-mail: cpg27@cam.ac.uk

Start Date: October 2011
Projected End Date: March 2015

Technical Barriers

- Capacity fade due to significant surface electrode interphase (SEI) formation (focusing on Si)
- Reduced rate performance due to SEI formation
- High-energy density
- High power

Technical Targets

- Specific power 300 W/kg
- 10 year life
- < 20% capacity fade

Accomplishments

- Detailed ¹³C NMR study of the Si SEI has been performed to identify major organic components.
- Major species in reduced VC and FEC have been identified by ¹³C NMR
- *In situ* NMR methods for paramagnetic materials have been used to study Li dynamics and electrode reaction methods
- Extended methodologies developed to study Li dendrites to study Na-dendrite formation in Na-batteries.
- High efficiency Li-oxygen battery chemistry has been developed that involves LiOH formation via the redox mediator LiI. The battery can be cycled for multiple cycles.

Introduction

The formation of a stable surface electrode interphase (SEI) is critical to the long-term performance of a battery, since the continued growth of the SEI on cycling/aging results in capacity fade (due to Li consumption) and reduced rate performance due to increased interfacial resistance. Although arguably a (largely) solved problem with graphitic anodes/lower voltage cathodes, this is not the case for newer, much higher capacity anodes such as silicon, which suffer from large volume expansions on lithiation, and for cathodes operating above 4.3 V. Thus it is essential to identify how to design a stable SEI.

The major technique used in this work is NMR and our surface (SEI) studies are complemented by studies that focus on elucidating the short range changes that occur within the electrodes themselves.

Approach

Perform multinuclear nuclear magnetic resonance (NMR) studies of local structure; *in situ* NMR studies of Li⁺ transport. Pulse Field Gradient (PFG) measurements of electrolyte diffusivity and tortuosity; SIMS and XPS of SEI composition.

Results

Using *In Situ* NMR Spectroscopy to Measure Li⁺ Dynamics on the Fly: Application to Spinel

Detailed *in* and *ex situ* NMR studies of spinels have been performed to determine ionic motion during battery cycling, making use of new NMR metrology. Figure V- 145 shows the *ex situ* ⁷Li MAS NMR experiment performed for a sample of nominal stoichiometry Li_{1.08}Mn_{1.92}O₄. Interestingly, the partially charged samples show weak resonances at 1475 and 717 ppm, which are clear signatures for trace Li₂MnO₃ impurities, indicating that the Li content of the spinel sample is lower than implied by the nominal composition. The second observation is the clear collapse of the fine structure between 500 – 750 ppm, assigned to Li-ions in tetrahedral regions, as lithium is removed from the sample (as has been discussed extensively in our prior publications). This collapse is indicative of motion on a timescale that is faster than the separation between the various resonances. Assuming a separation of chemical shifts of approx. 150 ppm, this implies a Li hopping time scale of < 10⁻⁵ s. The increase in Li⁺ ion motion is facilitated by the presence of Li⁺ vacancies, created by charging.

Rapid Li⁺ mobility is observed until approximately 73% SOC, although weaker peaks suggest that there are trapped Li⁺ sites in the structure in addition to the mobile components. Mobility has been explored by performing T2' (spin-spin relaxation) measurements *in situ* during battery cycling (Figure V- 146), the T2' providing an indirect measurement of motion on the 10⁻³ s timescale. (Note that T2' rather than T2 is used here to indicate that the relaxation time has been measured using a Hahn-echo experiment, and is not the true “T2”).

The *in situ* data reveal distinct mobility regimes. A dramatic reduction in T2' is seen initially which correlates with the mobility seen *ex situ*, simulations showing that this is consistent with Li hop rates on the order of 10 kHz. Interestingly, the T2' increases again, the increase increasing with increased temperature. This provides evidence for motion approaching the fast regime. Again simulations suggest motion much faster than 100 s⁻¹. Motion slows down at 50% SOC, a phenomenon that is more clearly observed at lower temperatures, consistent with at least partial ordering at this composition. The approach provides a simple method for tracking Li-ion transport during cycling and for investigating the nature of the phase transformation. For example, the continuous variation in the T2' during the 4.0 V plateau is consistent with a solid solution mechanism, while the behavior on the 4.2 V process is closer to that expected for a two-phase reaction.

SEI Studies: NMR Studies of Composition and the Role of Additives

We have now completed a comprehensive multinuclear ssNMR study of the organic components contained within the SEI formed on the surface of the anode material silicon. A standard battery electrolyte (1M LiPF₆ in ethylene carbonate (EC) and dimethyl carbonate (DMC)) was used with either complete ¹³C enrichment of either EC or DMC or partial enrichment of EC. Anodes were prepared without any binder (so as to remove the

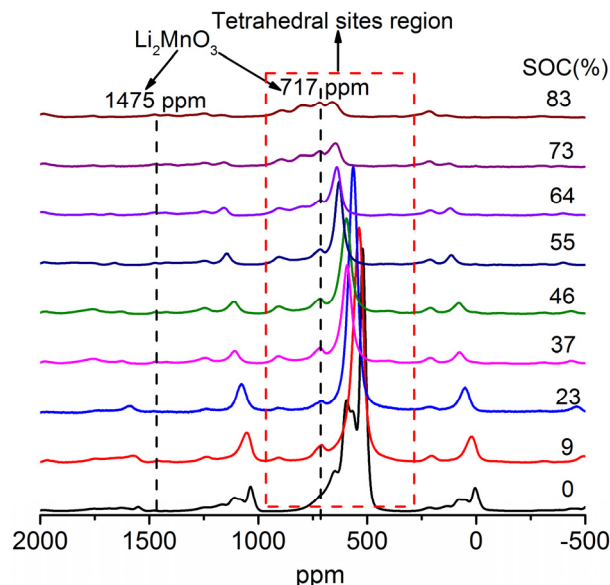


Figure V- 145: ⁷Li MAS NMR spectra of Li_{1.08}Mn_{1.92}O₄ electrodes at different state of charge (SOC). The spectra were acquired at 4.7 T with a MAS frequency of 40 kHz. The impurity Li₂MnO₃ (marked on the spectra) is electrochemically inactive upon charging. The isotropic shift regions are marked with a red dashed square. The other spectral regions are dominated by spinning sidebands

complication of the ^{13}C signal from the binder) and were then cycled using ^{13}C -enriched electrolytes. Assignments of the resulting ^{13}C spectra were performed with the help of two-dimensional NMR studies and by calculating the shifts with DFT methods. A voltage-dependent formation of the SEI was observed by ^1H NMR, with SEI growth correlating with increasing irreversible capacity. A series of PEO-type oligomer species and semicarbonates are observed, with ssNMR enabling the detection of amorphous environments. Future studies will focus on the change in SEI following multiple charge-discharge cycles.

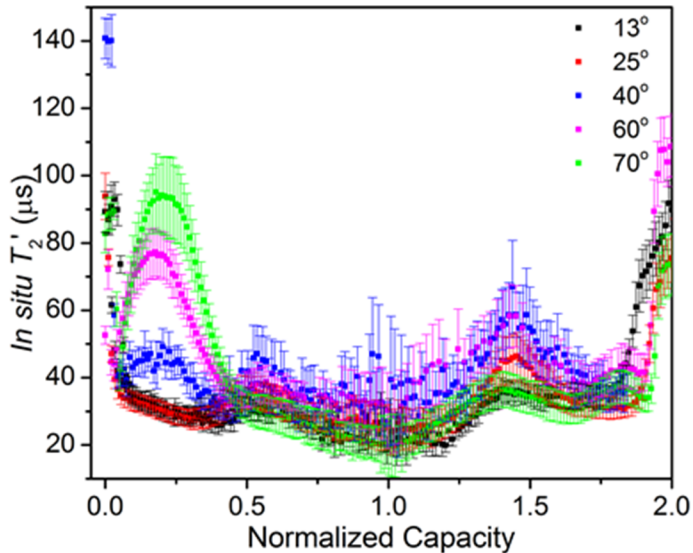


Figure V- 146: ^7Li NMR T_2' measurements of $\text{Li}_{1.08}\text{Mn}_{1.92}\text{O}_4$ measured during battery cycling. (1st charge 0 – 1; 1st discharge, 1 – 2). The measurements were performed at 13, 25, 40, 60 and 70° C

In a collaborative project with Prof. B. Lucht (U. Rhode Island) we have explored the products formed on reducing the electrolyte additives, fluoroethylene carbonate (FEC) and vinylene carbonate (VC), both additives having been shown to reduce the initial irreversible capacity loss, particularly on silicon anodes. These additives are believed to improve the stability of the solid electrolyte interphase (SEI) by forming a series of organic species, possibly cross-linking with solvent molecules such ethylene carbonate. As a first step towards characterising the FEC/VC decomposition products in the SEI, we have examined chemically reduced species, formed with the reducing agent lithium naphthalenide, by using multinuclear NMR spectroscopy. ^{19}F NMR spectroscopy of reduced FEC shows the expected resonance from LiF (Figure

V- 147). No other signals from fluorinated products are seen. By contrast, the ^1H NMR spectra show resonances from ether CH_2O protons and saturated carbons in addition to a higher frequency signal at 6.1 ppm. While it was initially tempting to assign this to an unsaturated product such as lithium vinylene dicarbonate (LiVD) (Figure V- 148), a spectrum acquired from a sample prepared using the deuterated Li naphthalenide did not contain this resonance, indicating that the signal arises from lithium naphthalenide trapped in the solid reduction product. The ^{13}C NMR spectra of the same compounds confirmed this assignment and no signals that could be assigned to LiVD or any other products containing unsaturated C=C double bonds were observed.

Similar ^1H NMR spectra were recorded from reduced VC, except that an additional signal due to formate was observed. A number of different signals were observed in the ^{13}C NMR spectra of FEC and VC, which could be assigned to the species such as those expected from the polymer shown in Figure V- 148, but also to carbonate species including Li_2CO_3 and $(\text{LiOCO}_2\text{CH}_2)_2$.

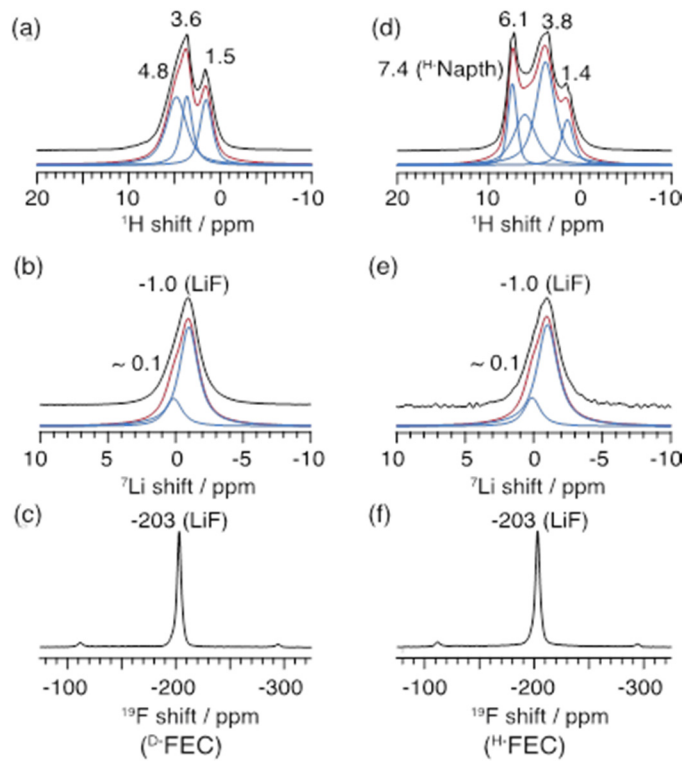


Figure V- 147: ^1H , ^7Li and ^{19}F MAS NMR spectra of reduced protonated (^1H -FEC) and deuterated (^2H -FEC)

high surface area. In the case of galvanostatic cycling, the Na deposits are formed, with a morphology associated with an extremely high surface area. In the case of galvanostatic cycling, the Na deposits are formed, with a morphology associated with an extremely high surface area.

High currents show a significantly greater accumulation of deposits during cycling, indicating a much lower efficiency of removal of these structures when the current is reversed (Figure V- 150). Applying the Scarifker and Hills model,² analysis of chronoamperometry and NMR results can be interpreted as showing a change from progressive to instantaneous nucleation of new Na deposits as the current density is increased.

Measurement of the ^{23}Na and ^{19}F diffusion coefficients in the electrolyte by the pulsed field-gradient NMR method reveal a surprisingly high mobility for the Na^+ cation (compared to dilute NaCl and lithium electrolytes) in the NaTFSI/PC electrolyte used here. Furthermore, analysis of the diffusion data within the context of the Chazalviel model³ for lithium dendrite formation suggests that this Na system is operating well away from this regime.

In Situ ^{23}Na NMR of Sodium Metal Electrodes

^{23}Na *in situ* NMR has been used to study sodium-ion batteries, focusing initially on Na metal anodes and Na anode symmetrical cells. By analogy to Li-anodes and $^{6,7}\text{Li}$ NMR¹ the limited penetration of the radio frequency field (quantified via the “skin-depth”: $12.3 \mu\text{m}$ under the conditions used here) used to excite the Na-spins means that we are sensitive to only the surface and 1st few microns below the surface of the Na-metal anode. By contrast, Na-metal dendrites can be detected in their entirety as their thickness is less than the skin-depth. On galvanostatic plating (Figure V- 149) the ^{23}Na NMR resonance assigned to Na metal grows steadily and linearly with time. Since the total mass of Na metal is constant in a symmetric Na-Na cell, this intensity increase is associated with an increase in Na metal surface (and thus volume of Na excited); this indicates that Na microstructures are formed even at the lowest current studied.

Quantification of the NMR signal shows that Na metal deposits are formed, with a morphology associated with an extremely high surface area.

Na deposits are partially removed at low currents, on

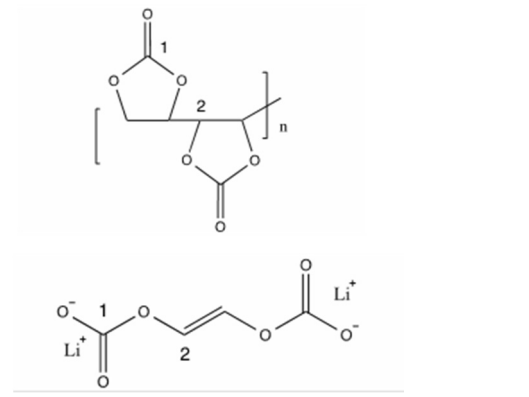


Figure V- 148: Two proposed reduction products of FEC/VC, LiVD (top) and the carbonate polymer (bottom)

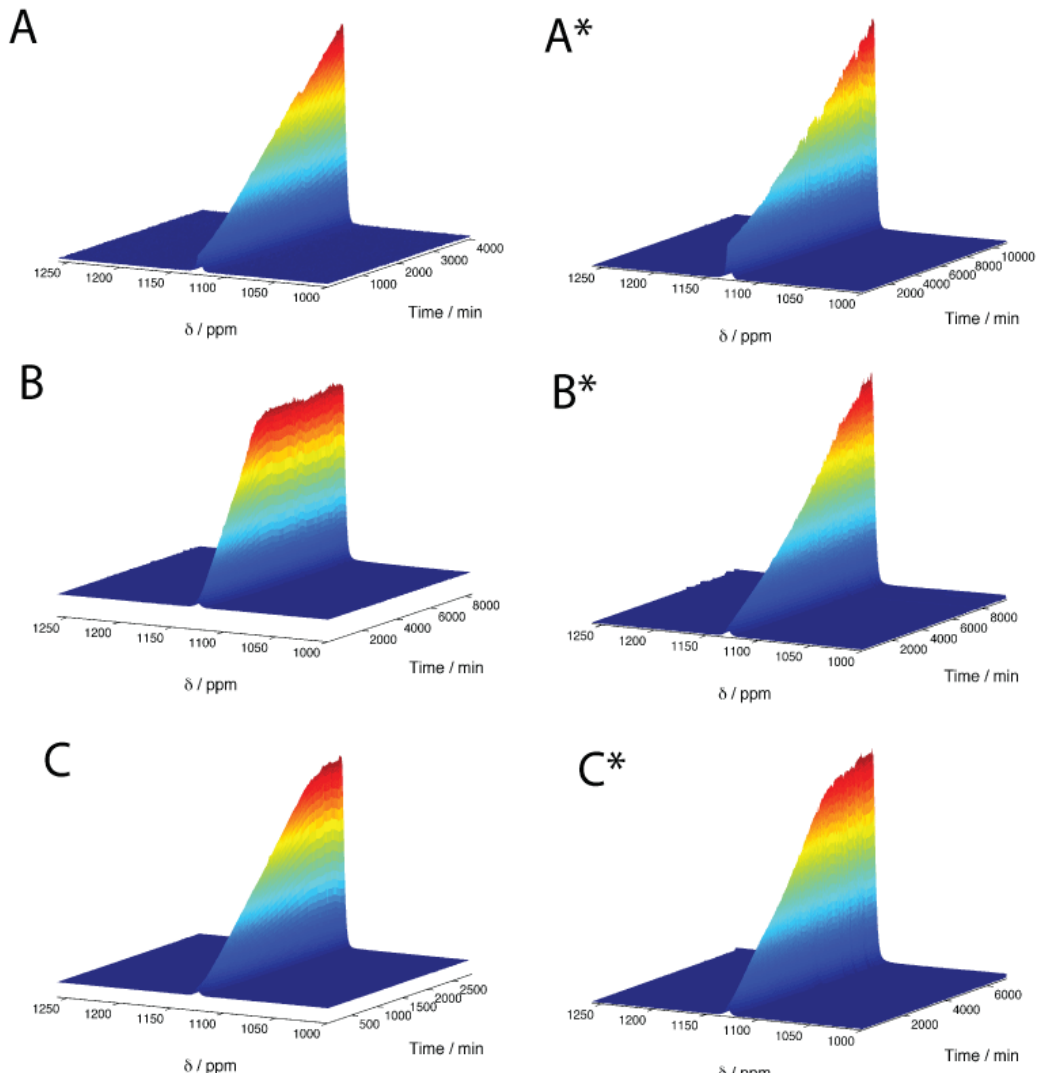


Figure V- 149: *In situ* ²³Na NMR spectra for continuous galvanostatic plating, and galvanostatically cycled samples, at currents of 0.5, 1 and 2 mA cm⁻² (A-C, and A*-C*, respectively) with the superscript (*) denoting galvanostatically cycled samples. Stack plots vs. time (in min.) are shown. The resonance assigned to Na metal continues to grow until the cell fails (e.g., 3000 mins for B) due to extensive short circuits

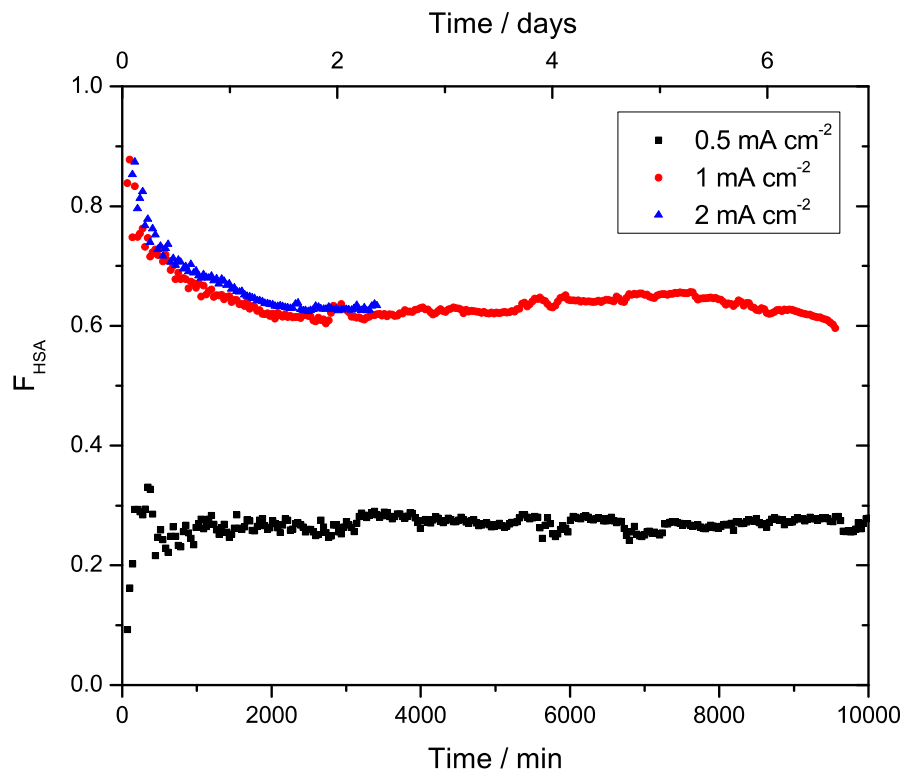


Figure V- 150: Fraction of high surface area (F_{HSA}) Na during galvanostatic cycling at various current densities. A ratio of 1 indicates complete microstructure deposition while 0 indicates smooth deposition

Using redox mediators to cycle Li-oxygen batteries via LiOH formation and decomposition

The commercial use of a lithium-air battery faces many challenges, such as its unrealized high capacity, poor cycling capability and rate performance, low round-trip efficiency and sensitivity to the presence of H₂O and CO₂. Our recent work has shown that we can use the redox mediator LiI to cycle a cell with high efficiency, large capacity and a very low overpotential. Figure V- 151 shows the electrochemical results for Li-O₂ batteries prepared with a Li metal anode, 0.25 M lithium bis (trifluoromethyl) sulfonylimide (LiTFSI)/dimethoxyethane (DME) electrolyte with and without 0.05 M LiI additive. Hierarchically macroporous reduced graphene oxide (rGO) electrodes were used, due to their low mass/large pore volumes and were compared to mesoporous SP carbon and mesoporous titanium carbide (TiC) electrodes. All these electrodes show good electrochemical stability within a voltage window of 2.4-3.5 V in a LiTFSI/DME electrolyte and can be used to reversibly cycle LiI ($I_3^- + 2e^- \leftrightarrow 3I^-$).

In the absence of LiI, cells using either mesoporous TiC or macroporous rGO showed much smaller overpotentials during charge, in comparison to that obtained with the SP electrodes. Addition of the redox mediator to the SP electrode, however, led to a noticeable drop in the overpotential over that seen with SP only. The charge voltage profile is not, however, flat, but gradually increases on charging. When LiI is used with rGO electrodes, a flat process is observed at 2.95 V. The discharge overpotential for rGO-based Li-oxygen cells also decreases by 0.15 V (arrows in Figure V- 151), from 2.6 (SP/TiC) to 2.75 V (rGO, regardless of the use of LiI). Overall, the voltage gap becomes only 0.2 V (indicated by arrows), representing an energy efficiency of 93.2%.

LiOH is the only observed crystalline discharge product for LiI/rGO electrodes (X-ray and NMR results), the LiOH being removed after a full charge. Without added LiI, Li_2O_2 is the predominant discharge product. A series of experiments performed with deuterated DME and D_2O reveal that trace water impurities are the source of protons in these cells. Cells cycled in the presence of 45,000 ppm or water or with wet air show no deterioration in performance. Optical and SEM images show that the electrode surface is completely covered by micron sized LiOH agglomerates, following discharge. When limiting the specific capacity to 1000, 5000 and 8000 mAh/g_c , the cells show no capacity fade with little increase in voltage polarization after 2000, 300 and 100 cycles, respectively. When cycled at 1 A/g_c the voltage gap is ~0.2 V; at higher rates the gaps widen to 0.7 V at 8 A/g_c . Although a certain level of scattering in the total capacity is observed, probably due to variations in the electrode structure, the cell capacity is typically 25,000-40,000 mAh/g_c (i.e. 2.5-4.0 mAh) for an rGO electrode of 0.1 mg and 200 μm thick. This corresponds to a specific energy of approximately 5800 Wh/kg. Mechanistic studies are ongoing.

References

1. Bhattacharyya, R., Key, B., Chen, H., Best, A. S., Hollenkamp, A. F., Grey, C.P. *Nat Mater* (2010), 9, 504–510.
2. Scharifker, B., and Hills, G. (1983). *Electrochimica Acta*, 28(7), 879–889.
3. Chazalviel, J. N. (1990). *Physical Review A*, 42(12), 7355–7367.

Conclusions and Future Directions

A new approach has been developed to investigate Li-dynamics “on the fly”, while the battery is being cycled. The approach is more efficient than *ex situ* studies of Li dynamics where multiple batteries need to be prepared at different states of charge. Furthermore, Li mobilities for non-equilibrium structures or Li-ordering schemes (formed during battery cycling) can be determined. The approach has been applied to study Li mobility and the nature of the phase transformations in spinel systems.

In a second project a careful multinuclear NMR study has been performed to investigate the organics in the SEI that form on the anode material. Since it is non-trivial to enrich the additives FEC and VC in the NMR active nucleus ^{13}C , a different approach was taken: these additives were reduced by using lithium naphthalenide, to produce large samples suitable for a detailed NMR analysis. The resulting NMR spectra suggested that both semicarbonates and polymers derived from FEC/VC were formed. The NMR spectra will

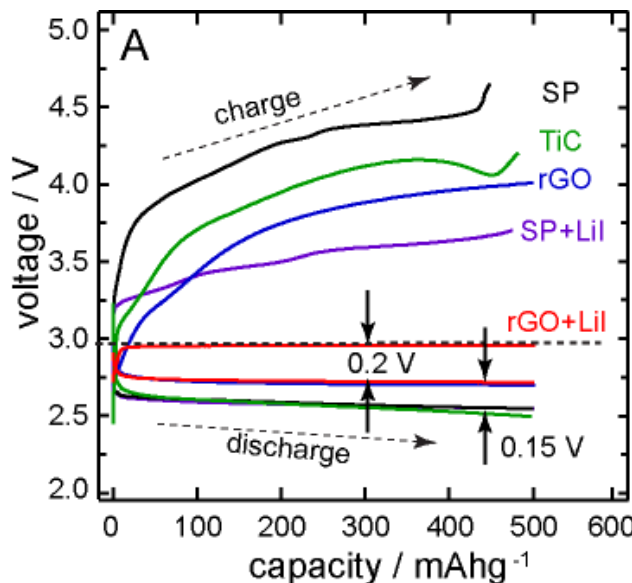


Figure V- 151: Discharge-charge curves for $\text{Li}-\text{O}_2$ cells using mesoporous SP and TiC, and macroporous rGO electrodes, with capacities limited to 500 mAh/g (based on the mass of carbon or TiC) and a 0.25 M LiTFSI/DME electrolyte. For SP and rGO electrodes, 0.05 M LiI was added to the LiTFSI/DME electrolyte in a second set of electrodes (purple and red curves). All cells in were cycled at 0.02 mA/cm^2 . The horizontal dashed line represents the position (2.96 V) of the thermodynamic voltage of a $\text{Li}-\text{O}_2$ cell

be used as fingerprints to help determine whether similar products are formed when these additives are used in a cell containing Si as an anode.

The third project involved an extension of our Li-metal anode work to Na batteries. We showed that Na dendrites are much more readily formed than Li dendrites, even at very low current densities.

Finally, we have shown that by using a combination of the additive LiI, electrolytes containing DME and trace water, the Li-oxygen battery can reversibly cycle via the formation of LiOH (and not Li₂O₂) at very low overpotentials (as low as 200 mV). The long term cycling behaviour of this battery is extremely good, if the battery is cycled slowly, batteries operating for >2 months in the laboratory. Use of a macroporous r-GO electrode helps to provide unimpeded diffusion of the I⁻/I₃⁻ ions and oxygen molecules, resulting in large LiOH particles and extremely high capacities. The battery is tolerant to high quantities of moisture. The results suggest that LiOH formation does not result in battery death and suggest new routes for optimising the functioning of a Li-oxygen cell.

FY 2015 Publications/Presentations

1. "NMR and Pulse Field Gradient Studies of SEI and Electrode Structure", ES055_Grey_2015_O, US DOE Vehicle Technologies AMR, 2015.
2. See, K. A., M. Leskes, J.M. Griffin, S. Britto, P.D. Matthews, A. Emly, A. Van der Ven, D.S. Wright, A.J. Morris, C.P. Grey, R. Seshadri, "Ab initio structure search and in situ Li-7 NMR studies of discharge products in the Li-S battery system," *J. Am. Chem. Soc.* 136 (2014): 16368-16377.
3. Chang, H. J., N.M. Trease, A.J. Ilott, D.L. Zeng, L.S. Du, A. Jerschow, C.P. Grey, "Investigating Li microstructure formation on Li anodes for lithium batteries by *in situ* ⁶Li/⁷Li NMR and SEM," *J. Phys. Chem. C* 119 (2015): 16443-16451.
4. Leskes, M. and C. P. Grey, "Finite pulse effects in CPMG pulse trains on paramagnetic materials," *Phys. Chem. Chem. Phys.* 17 (2015): 22311-22320.
5. Zhou, L., M. Leskes, T. Liu, C. P. Grey, "Probing dynamic processes in lithium-ion batteries by *in situ* NMR spectroscopy: application to Li_{1.08}Mn_{1.92}O₄ electrodes," *Angewandte* (2015), DOI: 10.1002/ange.201507632.
6. Grey, C. P., Presentation at the 3rd TYC Energy Workshop: Materials for Electrochemical Energy Storage Workshop, London, UK, September 2014.
7. Grey, C. P., Lecture at Nanqiang, Xiamen, China, October 2014.
8. Grey, C. P., Presentation at Queen Mary College, London, UK, November 2014.
9. Grey, C. P., Presentation at Japanese Battery Meeting, Kyoto, Japan, November 2014.
10. Grey, C. P., Presentation at the UK Energy Storage Conference 2014, Coventry, UK, November 2014.
11. Grey, C. P., Lecture at the Liverpool University, Liverpool, UK, February 2015.
12. Grey, C. P., Presentation at the International Workshop on Advanced Materials, Ras al Khaimah, UAE, March 2015.
13. Grey, C. P., Presentation at Wincools – ETH/EMFL Winter School, Champery, Switzerland, March 2015.
14. Grey, C. P., Presentation at Dupont CR&D, Wilmington, DE, March 2015.
15. Grey, C. P., Presentation at Princeton University, Princeton, NJ, March 2015.
16. Grey, C. P., Presentation at Beyond Lithium Ion VIII, Oak Ridge, TN, June 2015.
17. Grey, C. P., Presentation at International Society of Magnetic Resonance (ISMAR) conference, Shanghai, China, August 2015.
18. Grey, C. P., Presentation at the German Chemical Society Meeting (AS Award Address), Dresden, Germany, August 2015.
19. Grey, C.P., Presentation at the Joint Anglo-German Discussion Meeting, Darmstadt, Germany, September 2015.
20. Grey, C. P., Presentation at the 2nd Energy Materials Symposium, Bath, UK, September 2015.

V.F.5 Optimization of Ion Transport in High-Energy Composite Electrodes (UCSD)

Objectives

- This project aims to probe and control the atomic-level kinetic processes that govern the performance limitations (rate capability and voltage stability) in a class of high energy composite electrodes. A systematic study with powerful suite of analytical tools (including atomic resolution scanning transmission electron microscopy (a-STEM) and Electron energy loss spectroscopy (EELS), X-ray photoelectron spectroscopy (XPS) and first principles (FP) computation) will be used to pin down the mechanism and determine the optimum bulk compositions and surface characteristics for high rate and long life materials. Moreover, to help the synthesis efforts to produce the materials at large scale with consistently good performance. It is also aimed to extend the suite of surface-sensitive tools to diagnose the silicon anodes types.

Project Details

Ying Shirley Meng
(University of California, San Diego - PI)
Department of Nanoengineering
9500 Gilman Dr.
La Jolla, CA 92093
Phone: 858-822-4247; Fax: 858-534-9553
E-mail: shmeng@ucsd.edu

Start Date: April 2013

Projected End Date: March 2017

Technical Barriers

- Low rate and poor voltage stability of high-energy Li rich composite cathodes
- Unstable cycling performance of Si composite electrodes due to chemical and mechanical degradation
- Si Electrode Characterization: Excessive beam damage of solid electrolyte interphase from STEM-EELS characterization

Technical Targets

- PHEV: 96 Wh/kg, 5000
- EV: 200 Wh/kg; 1000 cycles (80% DoD)

Accomplishments

- Established a suite of surface and interface characterization tools, such as STEM/EELS, XPS and FP computation
- Improved the first cycle irreversibility to 90.6% for Li-rich Mn-rich oxide cathode and increased the discharge capacity.
- Established operando Neutron Diffraction technique to observe path specific migration of Li-ions through Li-rich transition metal oxide cathode.
- Improved the first cycle irreversibility to 85% for silicon composite electrode.
- Extended Time of Flight Secondary ion Spectroscopy, STEM/EELS and XPS to Si anode to investigate the morphology and chemical composition of the SEI after electrochemical cycling.
- SEI morphology plays a critical role in long term electrochemical cycling, where a dense uniform SEI promotes good cycling retention.

Introduction

A suite of advanced characterization techniques are a quintessential requirement for investigating the various electrode material electrochemical performance throughout long term electrochemical cycling. A single characterization technique alone is inadequate to fully understand performance-limiting processes of a material. Therefore, combining atomic resolution scanning transmission electron microscopy (a-STEM) and

Electron energy loss spectroscopy (EELS), X-ray photoelectron spectroscopy (XPS) and first principles (FP) computation will be used to help directly characterize the local structural and electronic changes of the material during electrochemical cycling. Of particular interest is that at the nanoscale, the Li-ion transport is significantly more complex in transition metal composite structures. Moreover, at the nanoscale the interphases separating different local structure affect the role of Li-ion transport. However, this phenomenon is not well understood. In some cases, some composite arrangements and spacings may promote significantly higher Li mobility, while others may suppress Li transport. To help promote Li-ion transport, clever engineering of surface coatings and bulk material compositions could improve the ion transport. If successful, this research will provide a major breakthrough in commercial applications of the class of high energy density cathode material for lithium ion batteries. Additionally, it will provide in-depth understanding of the role of surface modifications and bulk substitution in the high voltage composite materials. The diagnostic tools developed here can also be leveraged to study a wide variety of cathode and anode materials for rechargeable batteries.

Approach

The abovementioned objectives will be achieved by uniquely combining a-STEM and EELS, XPS and first principles (FP) computation to elucidate the dynamic changes of the bulk and surface structural changes in the complex oxide materials during electrochemical cycling. A systematic study with powerful analytical tools is necessary to hone a mechanism, determine the optimum bulk compositions and surface characteristics for high rate and long life cathode materials. Additionally, alternative synthesis methods will be explored to produce materials in large scale with consistently good performance. Finally, the developed advanced characterization tool will be extended to better understand the degradation mechanism of silicon anode to further improve the longevity of the material.

Combining several advance characterization tools and synthesis techniques will be used to accomplish the objectives of this effort:

1. Identify ways to extend the STEM/EELS and XPS techniques for anode materials, such as silicon anode.
2. Identify at least two high voltage cathode materials that deliver 200mAh/g reversible capacity when charged to high voltages .
3. Obtain the optimum surface coating and substitution compositions in lithium rich layered oxides when charged up to 4.8V (or 5.0 V).
4. Identify the appropriate SEI characteristics and microstructure for improving first cycle irreversible capacity of silicon anode.
5. Identify the mechanisms of ALD and MLD coated silicon anode for their improved chemical stability upon long cycling.

Results

The following progress has been achieved:

Investigate the Effects of Substitution on Oxygen Vacancy Formation Energy in Li-excess Material

First principles computation was applied to investigate the effects of cations substitution on the oxygen vacancy formation in high energy density $0.5\text{Li}_{4/3}\text{Mn}_{2/3}\text{O}_2 \cdot 0.5\text{LiNi}_{1/2}\text{Mn}_{1/2}\text{O}_2$ cathode material. Figure V-152(a) shows the cation ordering in the transition metal layer: Li ions (in red color), Mn ions (in green color), and Ni ions (in blue color), there are two different Li sites; one is surrounded by six Mn-ions, the other is surrounded by five Mn ions and one Ni-ion. Since Ni-ions contribute to the reversible capacity, we substitute one of Mn-ions with different cations. From our previous study, as Li is extracted from the structure, the oxygen vacancy formation energy decreased drastically. Figure V- 152a shows the oxygen vacancy formation energy as a function of different substitution elements. It can be seen that elements #9 and # 10 enhanced the oxygen stability in the lattice.

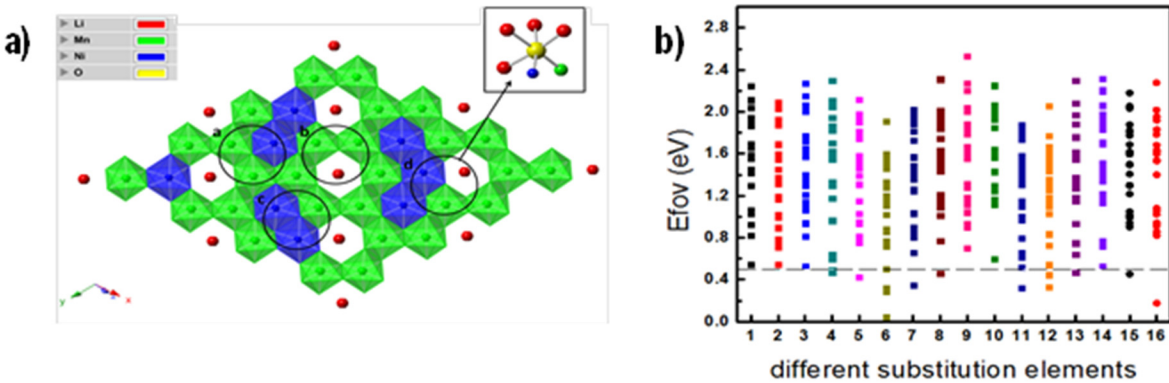


Figure V- 152: (a) cation ordering in transition metal layer: $0.5\text{Li}_{4/3}\text{Mn}_{2/3}\text{O}_2 \cdot 0.5\text{LiNi}_{1/2}\text{Mn}_{1/2}\text{O}_2$. (b) oxygen vacancy formation energy of $\text{Li}_{8/12}\text{Ni}_{3/12}\text{Mn}_{6/12}\text{M}_{1/12}\text{O}_2$ at different configurations. #1 is the model without substitution

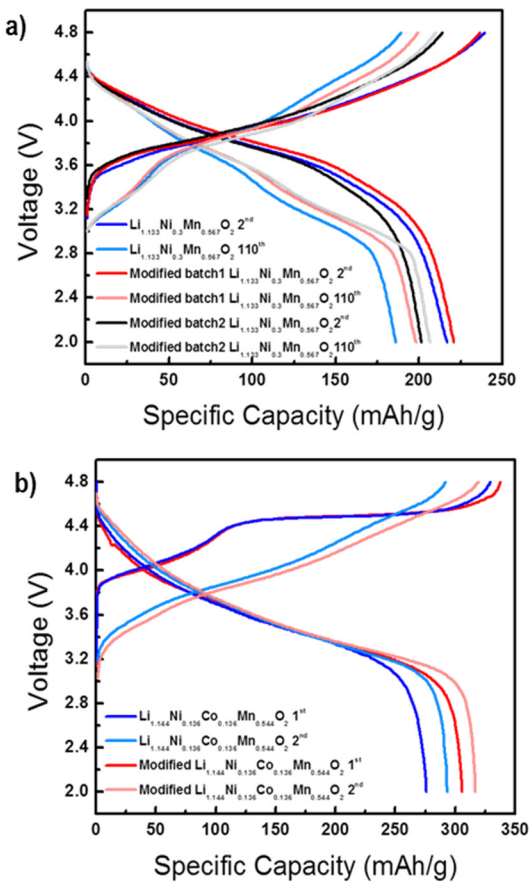


Figure V- 153: (a) Voltage profiles of the pristine and surface modified $\text{Li}_{1.133}\text{Ni}_{0.3}\text{Mn}_{0.567}\text{O}_2$ at different cycle numbers (0.1 C, 2-4.8V), (b) 1st and 2nd charge-discharge voltage profiles of the pristine and surface modified $\text{Li}_{1.144}\text{Ni}_{0.136}\text{Co}_{0.136}\text{Mn}_{0.544}\text{O}_2$ at 0.05 C

activation at high voltage were examined. Based on the $\bar{R}\bar{3}m$ layered structure, there are two different lithium sites within the Li-rich layered oxide cathode. Most of the lithium ions are located in the lithium layer, while the excess lithium ions are located in transition metal (TM) layer. Figure V- 154 demonstrates the lithium dynamics from HLR and LLR cathodes. First, the extraction of lithium in the slope region is largely dominated

Surface Modifications of Li-rich Mn-rich Oxide Cathode

Two different surface modification methods were applied to improve the first cycle efficiency, the capacity and voltage retention of Li-rich Mn-rich oxide materials upon high voltage cycling: Firstly, it was determined that 1 wt.% LLTO (Lithium Lanthanum Titanium Oxide) coating can improve the capacity and voltage retention of $\text{Li}_{1.133}\text{Ni}_{0.3}\text{Mn}_{0.567}\text{O}_2$. Figure V-153a compares the voltage profile of pristine and coated samples with LLTO at different coating conditions (batch1 and batch2), where they were cycled at low current density (0.1C). After 110 cycles, the coated samples show a significant improvement in capacity retention compared to the pristine sample. Secondly, the surface modification strategy manipulating gas-solid interface between Li-rich Mn-rich oxide and a type of common gas has been explored. The process yielded an increased specific capacity of 306 mAh g⁻¹ compared to 276 mAh g⁻¹ for the pristine electrode (Figure V- 153b). It also increased the initial coulombic efficiency from 83.8% to 90.6%. These increased electrochemical performances are highly related to the surface characteristics of particles after the surface modification process.

Operando Observation of Path-Specific Lithium-ion Migration via Neutron Diffraction

Neutron diffraction was utilized to investigate and quantify the lithium migration dynamics of various transition metal cathodes by *operando* battery cycling. In particular, high Li-rich $\text{Li}_{1.193}\text{Ni}_{0.154}\text{Co}_{0.106}\text{Mn}_{0.547}\text{O}_2$ (HLR) and low Li-rich $\text{Li}_{1.079}\text{Ni}_{0.251}\text{Co}_{0.262}\text{Mn}_{0.408}\text{O}_2$ (LLR) which exhibit different degrees of oxygen

by its migration within the lithium layer. In region 2, the lithium migration within the lithium layer decreases, and the migration from the TM layer occurs. Upon discharge, lithium ions from the TM layer are largely irreversible. After the first cycle, the lithium content in HLR and LLR TM layer irreversibly decreased from its open circuit voltage to 29% and 33% respectively. These results shed light into the lithium migration behavior and demonstrate the unique capabilities that one can observe light elements in bulk under *operando* neutron diffraction.

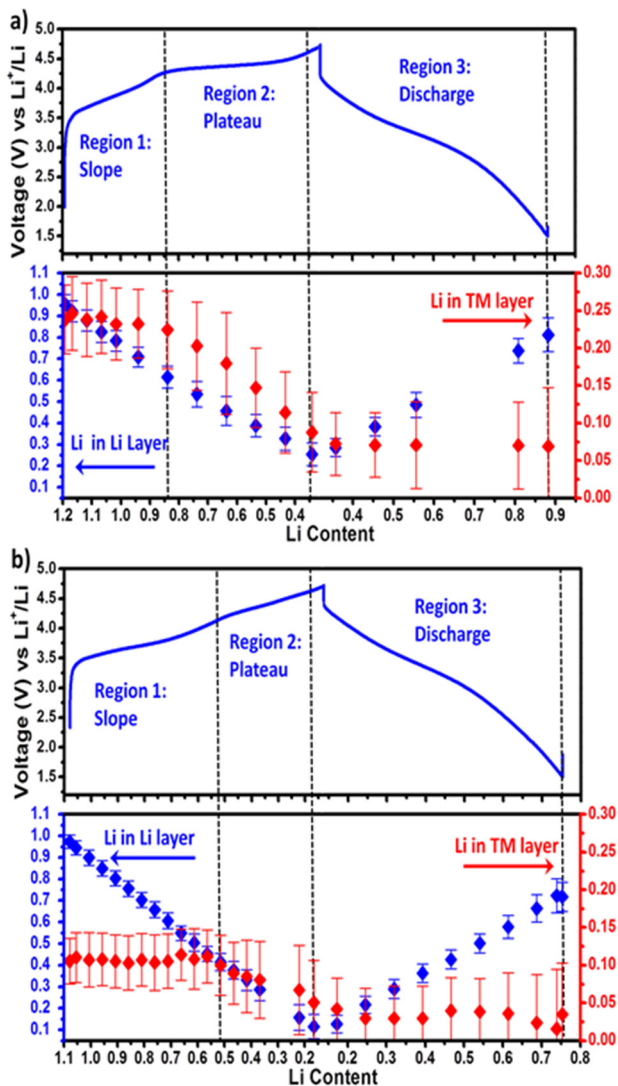


Figure V-154: Electrochemical charge/discharge profile with corresponding lithium occupancy at different states of delithiation/lithiation for a) HLR and b) LLR

Effect of FEC Additive on the Electrochemistry and Surface Chemistry on DC-sputtered a-Si Thin Film Electrodes

It is widely accepted that silicon suffers from mechanical and chemical degradation. In order to mitigate the mechanical degradation and focus on the forming a stable SEI, a-Si 50 nm thin film was cycled with traditional electrolyte (1:1 (wt%) ethylene carbonate (EC):diethylene carbonate (DEC)) and FEC-containing electrolyte (45:45:10 (wt%) EC:DEC:FEC) for 100 cycles. To understand how inclusion of FEC in the electrolyte affects SEI structure and evolution we attempt to reconcile these differing accounts of the reduction mechanism of FEC, by extending previously developed anoxic and anhydrous analytical characterization techniques (XPS and TOF-SIMS) on a-Si thin film electrodes. Figure V-155 presents the electrochemical data for the electrodes cycled with the traditional electrolyte and FEC containing electrolyte. After 100 cycles, the FEC containing electrolyte helps maintain capacity retention above 3000 mAhg^{-1} after the 100th delithiation. Conversely, the film in the traditional electrolyte suffers from severe capacity fading; after 100 cycles the delithiated capacity is only 1252 mAhg^{-1} . The high capacity and coulombic efficiency retained in the electrode cycled with FEC is largely due to the evolution of a stable SEI.

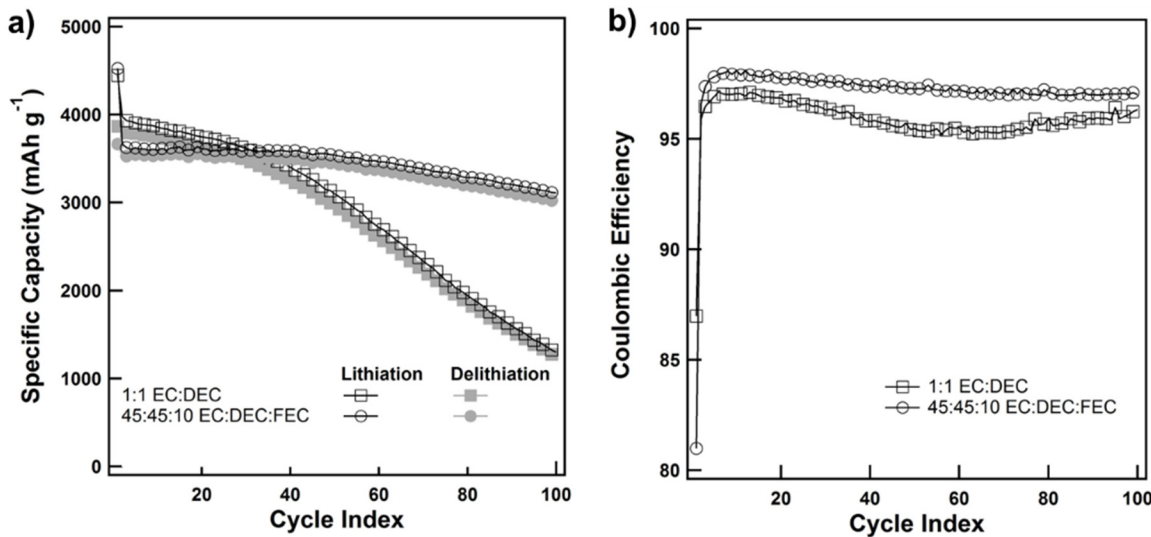


Figure V- 155: (a) Specific capacity versus cycling for galvanostatic cycling of a-Si thin films at C/2 rate and (b) Coulombic efficiency comparison of cells cycled with traditional electrolyte, 1:1 EC:DEC (squares), and FEC-containing electrolyte, 45:45:10 EC:DEC:FEC (circles)

Effect of FEC Additive on the Electrochemistry and Surface Chemistry on a-Si Thin Film Electrodes

The XPS and TOF-SIMS were used to investigate the differences in SEI formation as a function of electrolyte additive. DC-sputtered silicon electrodes in the same two electrolyte mixtures underwent the following galvanostatic conditions: (1) a single lithiation event; (2) one complete lithiation and delithiation cycle and; (3) 100 cycles. The relative chemical compositions were determined by XPS analysis, and are shown in Figure V- 156. We observed subtle yet critical changes in the chemical composition and structure between the SEI resulting from the two electrolytes. First, from the XPS, the SEI resulting from the EC/DEC/FEC electrolyte shows increase in inorganic species, specifically LiF which little change throughout cycling. Moreover, after 100 cycles the electrode cycled with the EC/DEC/FEC electrolyte, contains more ester and carboxylates (ROCO) and fewer carbonate species than its counterpart. These subtle differences allows for a more stable SEI in the EC/DEC/FEC electrolyte.

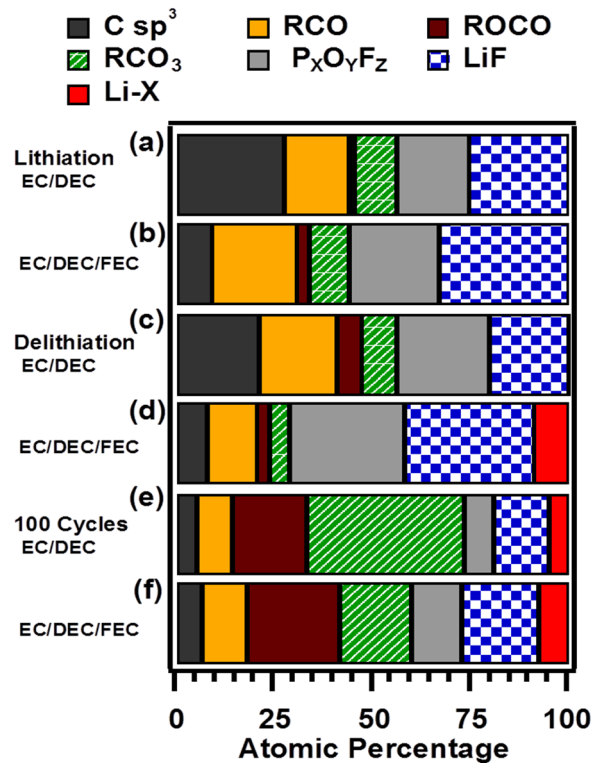


Figure V- 156: A relative composition of the 10nm outer SEI after: first lithiation; first delithiation; and 100 cycles

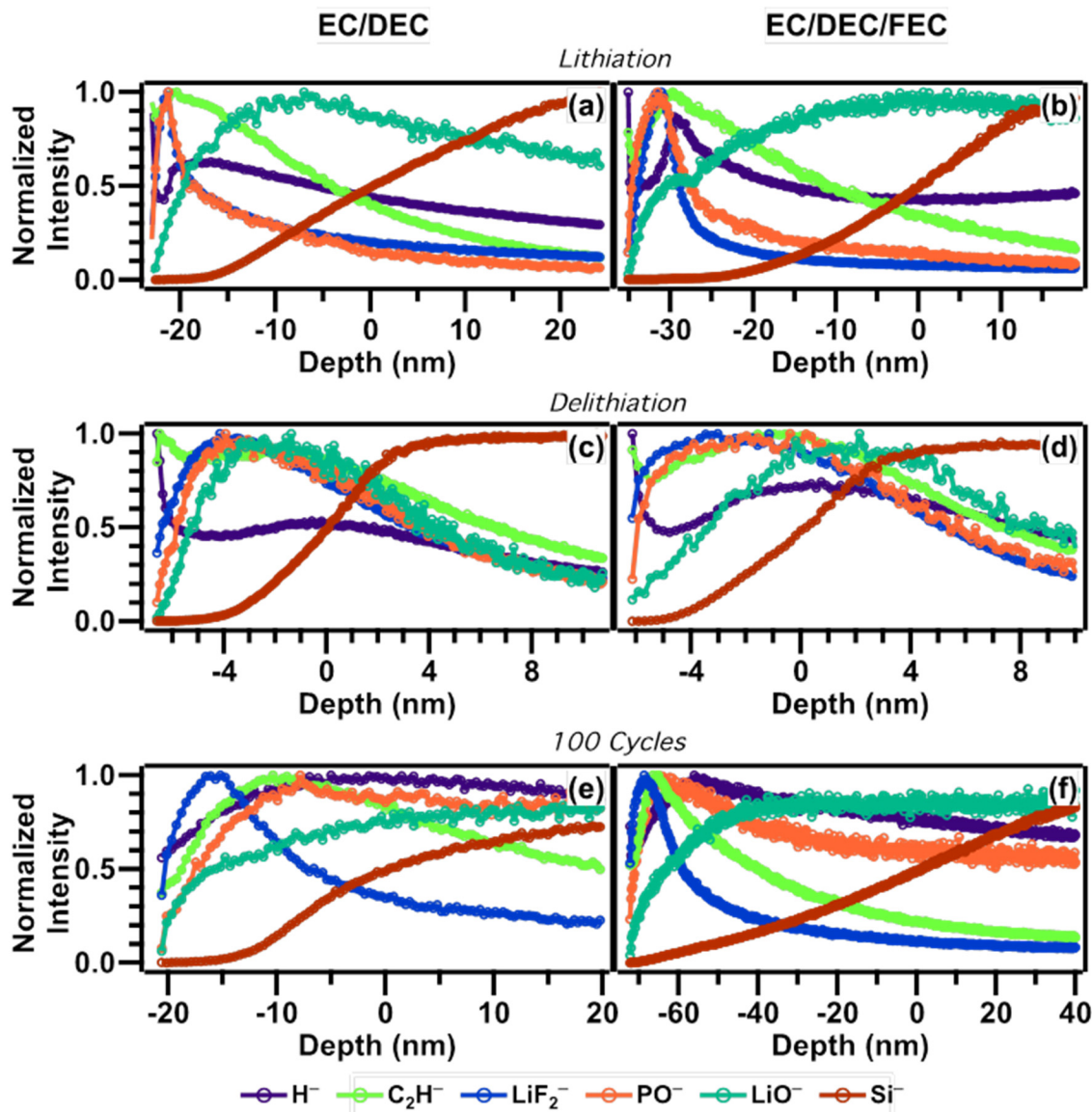


Figure V- 157: A relative composition of the 10nm outer SEI after 100 cycles. The layer is adjacent to and in contact with the electrolyte 1:1 EC:DEC and 45:45:10 EC:DEC:FEC when cycled

Figure V- 157 presents the DC-sputtered silicon electrodes in the same two electrolyte mixtures that underwent the following TOF-SIMS analysis: (1) a single lithiation event; (2) one complete lithiation and delithiation cycle and; (3) 100 cycles. The TOF-SIMS depth profiling shows subtle changes in the chemical composition and structure between the SEI resulting from the two electrolytes (Figure V- 156). After the initial lithiation, the electrode cycled in FEC containing electrolyte had a thicker SEI compared to the SEI produced by the traditional electrolyte. The LiF signal (LiF_2^-) in the FEC containing electrolyte was greater than in the SEI from traditional electrolyte, which correlated well with the XPS results. After 100 cycles, the LiF layer increased thicker for the electrode cycled in the FEC containing electrolyte compared to that for the electrode cycled in the traditional electrolyte. These results indicate that rather than producing a new subset of fluorocarbon/organic species proposed in the literature, FEC undergoes a ring opening reduction mechanism. The subtle chemical changes throughout electrochemical cycling in both electrolytes are expressed in the TOF-SIMS measurement of lithium fluoride/inorganic species (Figure V- 157).

Improvement on First Cycle Coulombic Efficiency for Optimized Si Powder-(50nm) Based Electrode and the Effect of FEC Additive on the SEI Evolution

We have optimized various mixing parameters in order to achieve a high performance electrode based on 50 nm Si powder. The electrode has an active mass loading of 0.5 mg cm^{-2} and cycled with the traditional electrolyte (without FEC). The electrode exhibits an initial coulombic efficiency of 88.8% with a charge capacity of 1.46 mAh cm^{-2} . The SEI formation on 50 nm crystalline silicon nanoparticles and carboxymethyl cellulose (250,000 MW) as a binder will be studied using STEM/EELS.

However, lithiated silicon (Li_xSi) and the SEI layer are extremely beam sensitive. Therefore, the electron dose and spatial resolution were optimized to prevent beam damage. Upon lithiation, crystalline Si (Figure V- 158a) transformed into the amorphous Li_xSi and two layers formed on the outermost surface of the electrode including, SEI and Li_xSiO_y . Based on Figure V- 158b an

uneven SEI layer formed at the edge of the particles in the electrode cycled without FEC. Figure V- 158d and e compare the O-K and Li-K edges of the SEI with the reference samples. The electrode cycled without FEC has an SEI layer that thickens upon cycling and mainly contains Li_2CO_3 (Figure V- 158d). However, the addition of FEC in the electrolyte suppresses the formation of Li_xSiO_y . More importantly, FEC leads to the formation of uniform and stable SEI that covers the Li_xSi particles (Figure V- 158c) with high LiF content (Figure V- 158d, e).

Visualization and Chemical Composition of the Solid Electrolyte Interphase on Silicon

Herein, a-STEM/EELS and XPS were used to directly decipher the effect fluoroethylene electrolyte additive on the solid electrolyte interphase (SEI). Given that lithiated silicon and the SEI are extremely sensitive, the electron dose and spatial resolution were optimized.

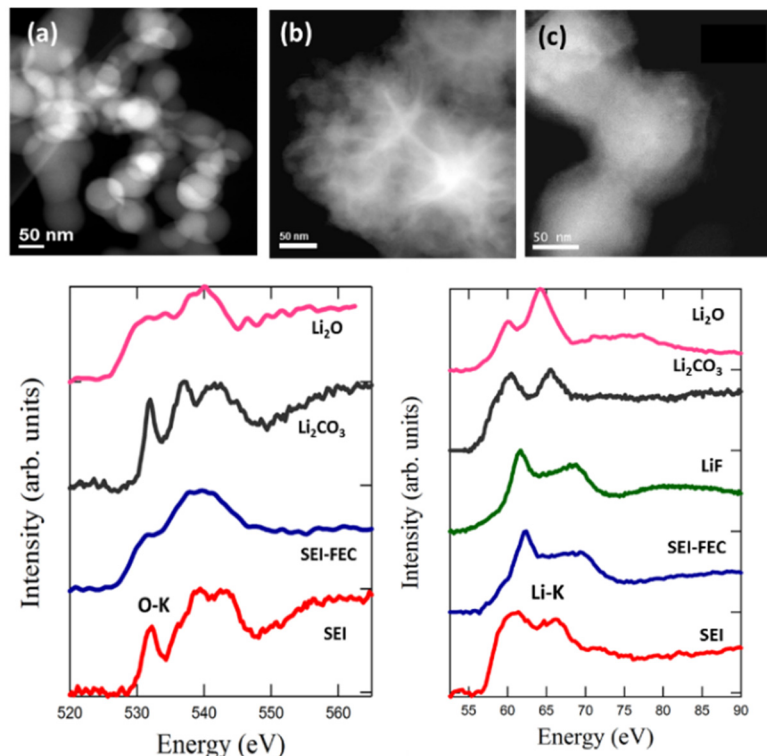


Figure V- 158: ADF-STEM image of (a) pristine Si, (b) lithiated Si after one cycle, (c) lithiated Si with FEC after one cycle, EELS spectra (d) O-K edge, and (e) Li-K edge

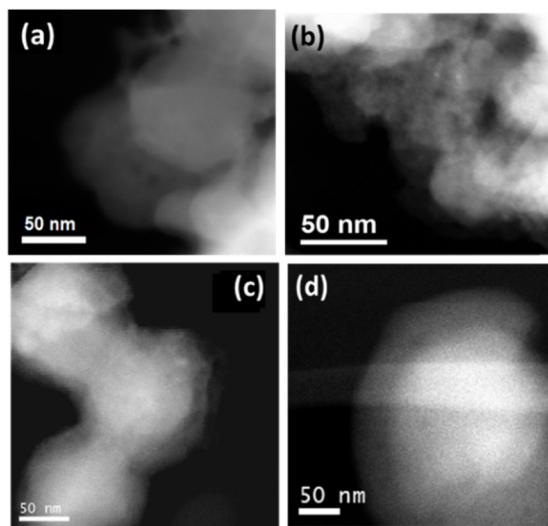


Figure V- 159: ADF-STEM images of the lithiated silicon nanoparticles cycled in EC/DEC at a) 1 cycle and b) 5 cycles

less LiF. On the other hand, the electrode cycled in EC/DEC/FEC contained fewer carbonate species and more LiF. These results correlate well with the a-STEM/EELS results.

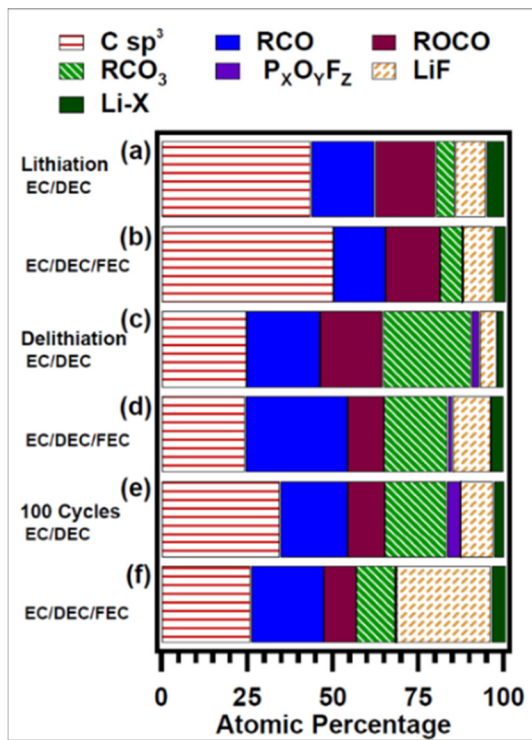


Figure V- 160: Relative composition of the SEI after (a, b) first lithiation, (c, d) first delithiation, and (e, f) 100 cycles in the delithiated state

Figure V- 159 shows the ADF STEM images of lithiated silicon nanoparticles cycled with EC/DEC and EC/DEC/FEC electrolyte at cycle 1 and 5. The electrode cycled in EDEC/FEC are covered by a dense and uniform SEI layer, however, the electrode cycled with EC/DEC forms a porous uneven SEI. More importantly, a-STEM/EELS is a local technique that focuses on single particles, therefore, XPS analysis was conducted in order to analyze large sample area. Figure V- 160 demonstrates the chemical evolution throughout electrochemical cycling for electrodes cycled with EC/DEC and EC/DEC/FEC. In the first lithiation, the electrode cycled in EC/DEC has a higher atomic percentage of RCO, ROCO, and LiX than its counterpart. Here, LiX corresponds to alkyl lithium, inorganic lithium oxide, and lithium phosphoro-oxy-fluoride compounds.

After 100 cycles, the electrode cycled in EC/DEC contained higher amount of carbonate species (CO_3) and

FY 2015 Publications/Presentations

1. Liu, H. D., D. Qian, M.G. Verde, M. Zhang, L. Baggetto, K. An, Y. Chen, K.J. Carroll, D. Lau, M. Chi, G.M. Veith, Y.S. Meng, “Understanding the Role of NH_4F and Al_2O_3 Surface Co-Modification on Lithium-excess Layered Oxide $\text{Li}_{1.2}\text{Ni}_{0.2}\text{Mn}_{0.6}\text{O}_2$,” *ACS Appl. Mater. Interfaces* 7, no. 34 (2015): 19189.
2. Shroder, K.J., J. Alvarado, T.A Yersak, J. Li, N. Dudney, L. Webb, Y.S Meng, K.J Stevenson, “The Effect of Fluoroethylene Carbonate as an Additive on the Solid Electrolyte Interphase on Silicon Lithium-ion Electrodes,” *Chem. Mater.* 27, no. 16 (2015): 5531.
3. Yersak, T. A., J. Shin, Z. Wang, D. Estrada, J. Whiteley, S-H Lee, M. J. Sailor, and Y. S. Meng, “Preparation of Mesoporous Si@PAN Electrodes for Li-Ion Batteries via the In-Situ Polymerization of PAN,” *ECS Electrochemistry Letters* 4, no. 3 (2015): A33.
4. Meng, Shirley, “Advanced Diagnosis and Characterization by In Operando Neutron Diffraction,” Invited presentation, 10th U.S.-China Electric Vehicle and Battery Technology Workshop, Beijing, China, March 2015.
5. Meng, Shirley, “Probing and Controlling Interface Stability and Oxygen Activities in High Voltage Cathode Materials in Li-ion Batteries,” Invited oral presentation, The Second International Forum on Cathode & Anode Materials for Advanced Batteries, Xiaoshan, China, April 2015.

6. Liu, H. D., D. Qian, M. Zhang, Y.S. Meng, “Understanding the Role of "AlF₃" Surface Modification on Lithium-excess Layered Oxide Li_{1.2}Ni_{0.2}Mn_{0.6}O₂”, Poster presented at the Jacobs School's Council of Advisors Board, La Jolla, CA, June 2015.
7. Zhang, Minghao, Bao Qiu, Danna Qian, Haodong Liu, Ying Shirley Meng, “STEM Characterization for Oxygen Activities in Li-rich Layered Oxides for High Energy Li-ion Batteries,” Poster presented at the Joint NSRC Workshop, Oak Ridge, TN, June 2015.
8. Sina, M., J. Alvarado, H. Shobukawa, Y.S. Meng, “Comprehensive insights into the SEI layer formation of Silicon anode using STEM/EELS,” Poster presented at the Microscopy and Microanalysis, Portland, OR, August 2015.
9. Liu, H.D., D. Qian, M. Zhang, Y.S. Meng, “Understanding the Role of "AlF₃" Surface Modification on Lithium-excess Layered Oxide Li_{1.2}Ni_{0.2}Mn_{0.6}O₂,” Poster presented at the Jacobs School's Council of Advisors Board, La Jolla, CA, May 2015.

V.F.6 Analysis of Film Formation Chemistry on Silicon Anodes by Advanced In Situ and Operando Vibrational Spectroscopy (UC Berkeley, LBNL)

Objectives

- Understand the composition, structure and formation/degradation mechanisms of the solid electrolyte interface (SEI) on the surfaces of Si anodes during charge/discharge cycles by applying advanced in-situ vibrational spectroscopies.
- Determine how the properties of the SEI contribute to failure of Si anodes in Li-ion batteries in vehicular applications. Per se this understanding to develop electrolyte additives and/or surface modification methods to improve Si anode capacity loss and cycling behavior.

Technical Barriers

- High energy density Si anodes have large irreversible capacity and are not able to cycle. These failures are due in part to loss of electrolyte by reduction and a SEI that is not stable on the surface with repeated cycling.

Technical Targets

- EV: > 200 wH/kg with > 1000 cycles to 80% DOD

Accomplishments

We found that in Si(100)-hydrogen terminated, a Si-ethoxy ($\text{Si}-\text{OC}_2\text{H}_5$) surface intermediate forms due to DEC decomposition. Other main products are lithium ethyl-dicarbonate (LiEDC) and poly-EC that are common SEI components in both oxide and hydrogen terminated crystalline Si. Our results suggest that the SEI surface composition varies depending on the termination of Si surface, i.e., the acidity of the Si surface. We provide the evidence of specific chemical composition of the SEI on the anodes surface under reaction conditions. This supports an electrochemical electrolyte reduction mechanism in which the reduction of DEC molecule to an ethoxy moiety plays a key role.

Introduction

Li ion batteries are one of the most common forms of energy storage devices. In a battery, electrical energy is generated by conversion of chemical energy via redox reactions at the anode and cathode. The battery's chemistry dictates the amount of charge that can be stored. The type of anode and cathode employed in Li-ion batteries exhibit a typical open current potential (OCP) of ~ 4 volts and rigorous research is conducted to increase it to 5 volts and above. The common anode today in portable electronic appliances is graphite based. Graphite has a theoretical capacity of 372 mAh/g (1 Li per 6 carbon atoms). However, for electric vehicles where higher capacity is needed, the silicon based anodes are attractive candidates to replace graphite based anodes. Silicon stores 3.75 Li atoms per one Si atom yielding a theoretical capacity of 4008 mAh/g.

However, the Si lattice expands up to four times its volume, which results in irreversible capacity loss and short cycling lifetime due to continued cracking and electrolyte consumption on the exposed Si surface. The key factor in long-term use (cyclability and stability) of such devices is the formation of an electrically

Project Details

Gabor A. Somorjai (University of California, Berkeley - PI)
Department of Chemistry
Berkeley CA 94720
Phone: 510-642-4053; Fax: 510-643- 9668
E-mail: somorjai@berkeley.edu

Philip Ross
(Lawrence Berkeley National Laboratory – co-PI)
Materials Sciences Division
1 Cyclotron Road
Berkeley CA 94720
Phone: 510-486-5821
E-mail: pnross@lbl.gov

Start Date: October 2012

Projected End Date: September 2015

insulating layer that allows lithium ion transport at a reasonable rate while hindering electrolyte consumption on the Si anode surface, and is termed the solid electrolyte interface (SEI).

Previous studies from Prof. Somorjai's laboratory have indicated that the nature of the electrolyte consuming reactions in lithium batteries is electrode material dependent. Specifically, a study using *ex situ* infrared vibrational spectroscopy observed two different SEI compositions on Sn and Ni electrodes even though the same electrolyte solution was used. Therefore we may expect the electrolyte consuming reactions on Si may be unique to this surface, and that the nature of the reactions may be a critical factor in determining the functioning of the surface layer formed, i.e. whether it functions as an SEI. The successful replacement of graphite by Si may require detailed understanding of these surface reactions and the ability to manipulate them by surface or electrolyte modification. SFG was used successfully in previous electrochemical systems on metallic electrodes (copper, gold) as well as on cathode oxide materials (LiCoO_2). We present the SFG spectra of surface-electrochemical reactions on a silicon anode and the differences between an oxide termination (SiO_2) and hydrogen one (Si-H). We took the SFG spectra under working conditions at three potential ranges.

Approach

Model Si anode materials including single crystals, e-beam deposited polycrystalline films, and nanostructures are studied using baseline electrolyte and promising electrolyte variations. In-situ sum frequency generation (SFG), vibrational spectroscopy is used to directly monitor the composition and structure of electrolyte reduction compounds formed on the Si anodes. Pre-natal and post-mortem chemical composition is identified using X-ray photoelectron spectroscopy. The Si films and nanostructures are imaged using scanning and transmission electron microscopies.

Results

We have achieved the following progress:

In Situ Spectro-Electrochemical Measurements

The spectroelectrochemical (ECC-OPTO-STD, EL-CELL) hence test cell serves to monitor the optical properties of an electrode material in the course of galvanostatic measurements (electrochemical charging and discharging). For this purpose, the working electrode (WE) Si anode is placed right below an optical window. In order to reduce IR absorption in the mid-IR ($2200 \text{ cm}^{-1} - 4000 \text{ cm}^{-1}$) we used IR grade sapphire and quartz windows as well as CaF_2 ones. We have deposited a 300 nm thick thin film on the windows themselves. This enabled us to have a reliable current collector ring that while minimizing IR losses due to solvent (electrolyte) absorption. The Si anode is sandwiched from below with a separator either glass fiber or Celgard 2400. Underneath the separator we added a 9 mm in diameter, Li disc that preforms as both counter electrode and reference electrode. In short, the IR and visible optical paths descend from above through the optical window onto the upside of the Si anode and the SFG signal is reflected upwards. Therefore, all the optical spectroscopy had been carried in the reflection mode. In order to minimize the IR absorption of the electrolyte solution we further diluted the electrolyte with deuterated tetrahydrofuran (*d*-THF) to about 2% in v/v. THF is known to be stable in the potential range that we chose. Prior to any experiment the test cell was dried over night at 80°C in vacuum. We assembled (and disassembled) the test cell in an inert (ultra-pure argon) atmosphere with 0.1-ppm concentration of water and oxygen (LabStar, MBruan). We have conducted cyclic-voltammetry measurements on a Si(100) hydrogen terminated surface. As expected three reduction peaks at $\sim 1.5 \text{ V}$, $\sim 0.5 \text{ V}$ and $\sim 0.10 \text{ V}$ that are consistent with values reported in the literature were observed. In Figure V- 161, the three reduction peaks at a Si(100)-H anode of the electrolyte (1.0 M LiPF_6 in EC : DEC, 1:2 v/v) are presented in this cyclic-voltogram. The reduction of DEC is around 1.5 V. The reduction of EC is about 0.5 V and Li intercalation (lithiation) occurs around 0.10 V. Scan rate was 1mV/sec. Figure V- 162 shows the Illustration of the in-situ spectro-electrochemical apparatus.

SFG of *ex situ* chemically modified Si(100)-H anode

By etching the oxide layer with hydrofluoric acid (HF) and later submerging the Si(100)-H wafer in hot ethanol solution ($\sim 65^\circ\text{C}$) we have produced a surface termination of Si(100)- OC_2H_5 with a surface coverage of up to one third of a monolayer. The SFG profile presented in Figure V- 163 shows major peaks that we observed and assigned at the following frequencies: 2875 cm^{-1} (s- CH_3), 2895 cm^{-1} (as- OCH_2), 2912 cm^{-1} (Fermi), 2952 cm^{-1} (as- CH_3) and at 2975 and 3040 cm^{-1} (both as- OCH_2).

Obviously, the presence (or absence) of these peaks tells us if indeed Si-ethoxy sites are present.

SFG of *in-situ* Si(100)-H anode electrochemistry

In Figure V- 164, Si(100)-H electrode, we show the divided the SFG spectrum after applying a 30 cycle cyclic-voltammetry potential near 1 V by the SFG in open circuit potential (OCP).

Dividing the SFG spectra emphasizes the appearance of ethoxy group vibrational peaks (black line). The SFG from the Si/SEI is interfered with the SFG generated from the Si substrate. We assume that if an intermediate specie ethoxy radical $\cdot\text{OCH}_2\text{CH}_3$ (or anion, $-\text{OCH}_2\text{CH}_3$) is formed near the Si anode surface it will react with Si-H to produce a Si- OCH_2CH_3 bond.

This reaction cannot take place if a passivating oxide layer is present (See Figure V- 165).

We assigned the SFG peaks corresponding to Si-ethoxy bonds according to Bateman et al.²⁵ work and SFG signals relating to the various SEI components as follows: 2875 cm^{-1} (s- CH_3), 2895 cm^{-1} (s- OCH_2), and at 2975 and 3040 cm^{-1} (both as- OCH_2). After a 30 cycle CV at $\sim 0.5\text{ V}$ (blue line), we observed peaks appearing at 2845 cm^{-1} (s- CH_2), 2895 cm^{-1} (s- OCH_2), 2920 cm^{-1} (as- CH_2) and 2985 cm^{-1} (as- OCH_2).

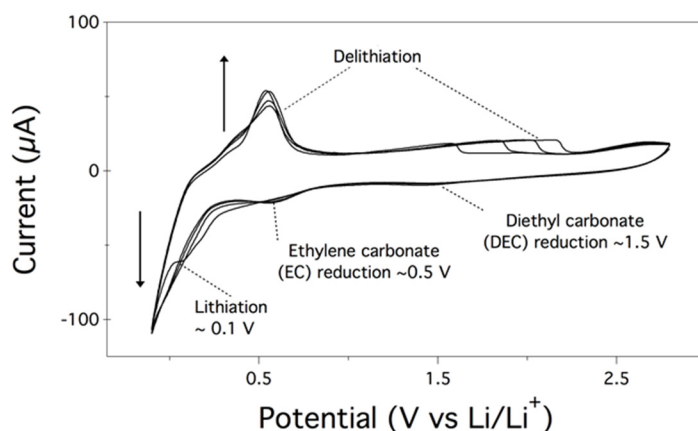


Figure V- 161: CV of Si(100)-hydrogen terminated

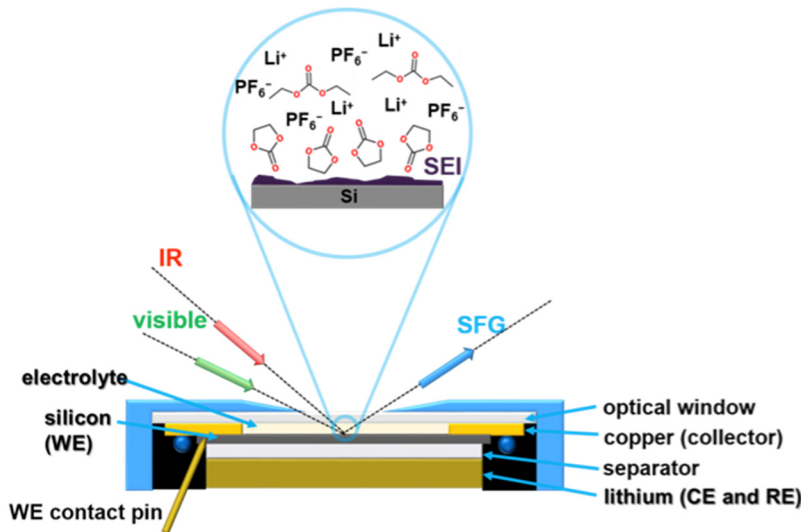


Figure V- 162: Illustration of the *in situ* spectro-electrochemical apparatus

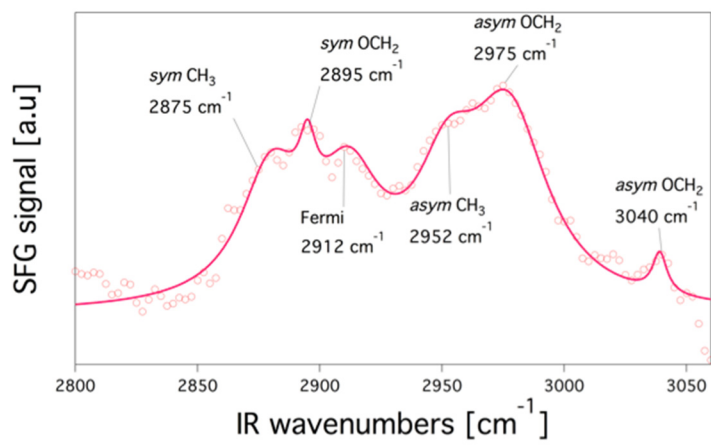


Figure V- 163: SFG profile of Si- OC_2H_5 (ethoxy) groups on Si(100)

In the case of Si(100) oxide we did not observe any change at ~ 1 V, therefore, we extended the CV potential range. In Figure V-165, we compared the SFG spectra of crystalline Si(100) oxide surface before and after lithiation. We performed a potential sweep in the range of 0.5 V to 2.0V (blue profile) and between -0.05 V to 3.0 V. Each CV had 30 cycles and the rate was 1mV/sec. The SFG profile of the first potential range (blue) has some SEI features but none that are related to a Si-O to Si-OC₂H₅ substitution reaction. After lithiation (red) prominent peaks appear and we assign them accordingly: 2817 cm⁻¹ (s-CH₂), 2848 cm⁻¹ (s-CH₃), 2895 and 2908 cm⁻¹ (both as-CH₂), 2960 cm⁻¹ (as-CH₃), 2985 and 3022 cm⁻¹ (both as-OCH₂).

In Figure V-166, we present the SFG intensity (i.e., the SFG of CV divided by the OCP spectrum) of EC on Si(100)-hydrogen terminated after cyclic-voltammetry at: 1.1 V \leftrightarrow 0.8 V (black) and 0.65 V \leftrightarrow 0.35 V (red). The SFG intensity profile at ~ 1 V has no detectable features as expected since EC

reduction onset potential is at ~ 0.5 V. Once, we lowered the applied potential to about 0.5 V (red curve) new peaks that we assign to poly-EC appeared and lithium alkyl dicarbonate (LiEDC). Nevertheless, at ~ 1 V the absence of a peak at 2895 cm⁻¹ cor-responding to the as-OCH₂ group stretch associated with the Si-ethoxy formation reveals that only the reduction of DEC leads to Si-ethoxy formation. For poly-EC we assign the peaks at 2948 cm⁻¹ and 3000 cm⁻¹ and the peaks related to lithium alkyl dicarbonate at 2890 cm⁻¹, 2965 cm⁻¹ and 2980 cm⁻¹.

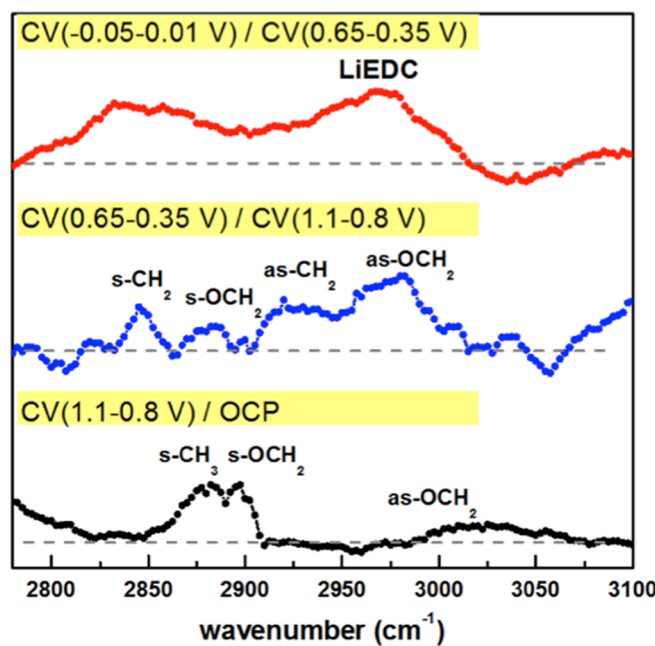


Figure V-164: We show the evolution of SFG signal under reaction conditions of crystalline silicon Si(100)-hydrogen terminated anode to that of Si(100)-OC₂H₅

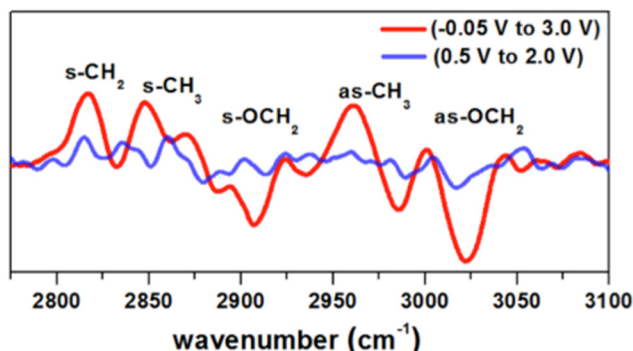


Figure V-165: The SFG profiles of crystalline silicon oxide Si(100)-Ox anode after cycling

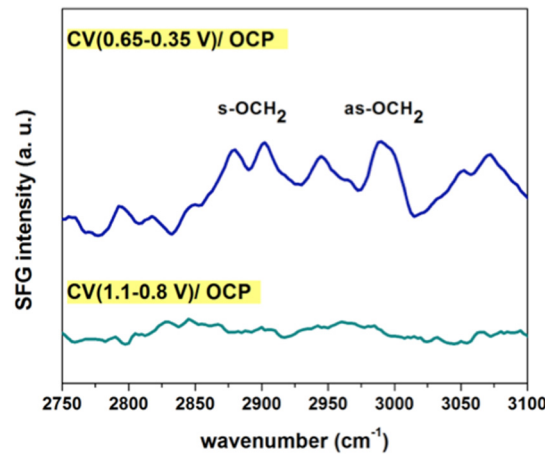


Figure V-166: The SFG profiles of crystalline silicon oxide Si(100)-Ox anode after cycling

Conclusions and Future Directions

In conclusion, we have observed that the Si hydrogen terminated layer has been changed to Si-ethoxy (Si-OCH₂CH₃) at ~ 1.0 V in the presence of 1.0 M LiPF₆ in EC DEC. The role of each electrolyte component (EC and DEC) was investigated separately. This substitution reaction at ~ 1.0 V did not take place when we changed the electrolyte to 1.0 M LiPF₆ in EC or when the Si(100)-O_x was used as the anode material. When we further reduced the potential to ~ 0.5 V only poly-EC and LiEDC formation was observed. Further in

operando spectroelectrochemical (SFG-VS) experiments of EC at reduction potentials of ~ 1.0 V and ~ 0.5 V suggests that it has been possibly reduced to poly-EC but no Si-ethoxy termination was detected. Future SFG-VS experiments in the C=O carbonyl stretch range are planned. Also, for Si anode research time-resolved radical formation (femtosecond SFG system) and ethylene carbonate ring opening mechanisms will be investigated in FY2016.

Moreover, the sample preparation protocol as well as the SFG technique are used in cathode material $\text{Li}_x\text{Mn}_{1.5}\text{Ni}_{0.5}\text{O}_4$ (LMNO) research in FY2016. Main research topics are: the effect of cathode material surface orientation, e.g., LMNO (112) vs. LMNO (111) and the chemical reactions at the cathode electrolyte interface.

FY 2015 Publications/Presentations

1. “Analysis of Film Formation Chemistry on Silicon Anodes by Advanced in-situ and operando Vibrational Spectroscopy”, ES215_Somorjai_2015_O, US DOE Vehicle Technologies AMR, 2015.
2. Horowitz, Yonatan, Hui-Ling Han, Philip N. Ross and Gabor A. Somorjai, “Potentiodynamic Analysis of Electrolyte Reactions with Silicon Electrodes Using Sum Frequency Generation Vibrational Spectroscopy Study”, *J. Am. Chem Soc.*, submitted.

V.F.7 Microscopy Investigation on the Fading Mechanism of Electrode Materials (PNNL)

Objectives

- The objective of this work is to use *ex-situ*, *in situ* and *operando* high-resolution transmission electron microscopy (TEM) and spectroscopy to probe the fading mechanism of electrode materials. The focus of the work will be on using *in situ* TEM under real battery operating conditions to probe the structural evolution of electrodes and interfaces between the electrode and electrolyte and correlate this structural and chemical evolution with battery performance. The following three questions will be addressed: How do the structure and chemistry of electrode materials evolve at a dimension ranging from atomic-scale to meso-scale during the charge and discharge cycles? What is the correlation of the structural and chemical change to the fading and failure of lithium (Li)-ion batteries? How does the interface evolve between the electrode and the electrolyte and their dependence on the chemistry of electrolytes?

Project Details

Chong-Min Wang (Pacific Northwest National Laboratory – PI)
Environmental Molecular Sciences Laboratory
902 Battelle Boulevard, Mail Stop K8-93
Richland, WA 99352
Phone: 509-371-6268; Fax: 509-371-7866
E-mail: Chongmin.wang@pnnl.gov

Start Date: July 2013

Projected End Date: September 2015

Technical Barriers

- Capacity and voltage fading of Li-ion batteries
- High theoretical capacity of electrode materials cannot be fully extracted reversibly

Technical Targets

- Develop new *ex situ*, *in situ*, and *operando* TEM diagnostic techniques for directly probing the structural evolution of electrode and interfaces
- Identify the quantitative correlation of the structural and chemical change with the fading and failure of Li-ion batteries
- Use *in situ* and *operando* TEM studies to guide smart microstructure design concepts for high capacity and long-cycle-life Li-ion batteries.

Accomplishments

- Demonstrated the first nano battery under *operando* TEM condition. A liquid cell based on closed window technique has been developed. This work paved the road for detailed study of SEI layer.
- Established a detailed mechanism on how the surface native oxide layer and artificial coating layer function in Si anode related to capacity fading and Coulombic efficiency.
- Discovered that capacity/voltage fading of $\text{Li}_{1.2}\text{Ni}_{0.2}\text{Mn}_{0.6}\text{O}_2$ cathode is closely related to Ni segregation, dissolution, corrosion, fragmentation, and phase transformation of the materials

Introduction

Most previous microscopic investigations on the structural/chemical evolution of electrode materials and the solid-electrolyte interphase (SEI) layer formation have been either *ex situ* studies or used low-vapor-pressure/solid electrolytes for *in situ* TEM studies. Therefore, these results do not reveal fully detailed dynamic information under practical conditions. It is necessary to develop new *operando* characterization tools to characterize the structural/chemical evolution of electrode and SEI formation and electrode/electrolyte interaction using a practical electrolyte. This will be critical for making new breakthroughs in this field. The success of this work will increase the energy density of Li-ion batteries and accelerate market acceptance of

electrical vehicles (EV), especially for plug-in hybrid electrical vehicles (PHEV) required by the EV Everywhere Grand Challenge proposed by DOE/EERE.

Approach

Extend and enhance the unique *ex situ* and *in situ* TEM methods for probing the structure of Li-ion batteries, especially for developing a biasing liquid electrochemical cell that uses a real electrolyte in a nano-battery configuration. Use various microscopic techniques, including *ex situ*, *in situ*, and especially the *operando* TEM system, to study the fading mechanism of electrode materials in batteries. This project will be closely integrated with other research and development efforts on high-capacity cathode and anode projects in the BMR Program to 1) discover the origins of voltage and capacity fading in high-capacity layered cathodes and 2) provide guidance for overcoming barriers to long cycle stability of silicon (Si)-based anode materials.

Results

Investigated the Artificial SEI Coating Layer on the Lithiation Kinetics of Si Anode for Lithium Ion Batteries

Using *in situ* transmission electron microscopy (TEM) through a nanoscale half-cell battery, in combination with chemo-mechanical simulation, the effect of thin (~5 nm) alucone and Al_2O_3 coatings on the lithiation kinetics of Si nanowires (SiNWs) was investigated. It was observed that the alucone coating leads to a “V-shaped” lithiation front of the SiNWs, while the Al_2O_3 coating yields an “H-shaped” lithiation front. These observations indicate that the difference between the Li surface diffusivity and bulk diffusivity of the coatings dictates lithiation induced morphological evolution in the nanowires. The experiments also indicate that the reaction rate in the coating layer can be the limiting step for lithiation and therefore critically influences the rate performance of the battery (Figure V- 167).

Structural and Chemical Evolution of Li_2MnO_3 and Correlation with Capacity and Voltage Fading

Using S/TEM equipped with HAADF/ABF detectors, EDS and EELS, the direct correlation between structural and electrochemical degradation of Li_2MnO_3 has been systematically investigated based on atomic level structural imaging, elemental mapping of the pristine and cycled samples (1-cycle, 10-cycles, 45-cycles) with the pristine sample, and density functional theory (DFT) calculations, it is found that structural degradation occurs from the very first cycle and is spatially initiated from the surface of the particle and propagates towards the inner bulk as cyclic number increase, featuring the formation of the surface phase transformation layer and gradual thickening of this layer. The structure degradation is found to follow a sequential phase transformation: monoclinic C2/m \rightarrow tetragonal I4₁ \rightarrow cubic spinel, which is consistently supported by the decreasing lattice formation energy based on DFT calculations. For the first time, high spatial resolution quantitative chemical analysis reveals that 20% oxygen in the surface phase transformation layer is removed and such newly developed surface layer is a Li-depleted layer with reduced Mn cations (Figure V- 168).

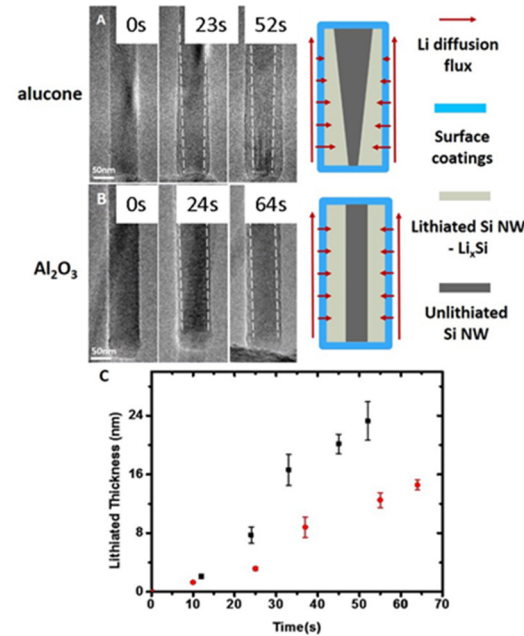


Figure V- 167: A) and B) Time-resolved TEM images show the development of lithiation profiles of the alucone and Al_2O_3 coated SiNWs and schematics of the Li diffusion paths through the SiNWs that dictate the lithiation behavior; C) Average lithiation thickness vs. time for the alucone (black square) and Al_2O_3 (red dot) coated SiNWs

EELS analysis indicates that the surface phase transformation layer (including I₄₁ and spinel phases) has little Li content and the tetravalent Mn cations are partially reduced to lower valence states. By combining the TEM microanalysis with electrochemical data, along with DFT calculations, the relationship between the structure degradation and cell performance degradation of Li₂MnO₃ cathode has been clarified. Since Li₂MnO₃ cathode is the parent compound for LMR cathode, this work will enhance our understanding on the degradation mechanism of LMR cathode materials during cycling.

Determined the Mixibility of Transition Metal with Lithium Column for the Layer Structured Cathode

Using chemical imaging with aberration corrected scanning transmission electron microscope (STEM) and DFT calculations, we directly visualized at atomic resolution on the interatomic layer mixing of transition metal (Ni, Co, Mn) and lithium ions in layer structured oxide cathodes for lithium ion batteries. As typically illustrated in Figure V- 169, we discovered that in the layered cathodes, Mn and Co tend to reside almost exclusively at the lattice site of transition metal (TM) layer in the structure or little interlayer mixing with Li. In contrast, Ni shows high degree of interlayer mixing with Li. The fraction of Ni ions reside in the Li layer followed a near linear dependence on total Ni concentration before reaching saturation. The general trend observed by EDS is consistent with the result based on XRD and neutron diffraction analysis, but only the EDS yields atomic level spatial resolution. The experimental observation is consistent with the DFT calculations using NMC442 cathode as an example. According to the DFT calculation, Li/Ni antisite defect pairs show much lower total energy increase than that of Li/Co and Li/Mn ones, which indicates Li/Ni interlayer mixing is the easiest one to happen while Li/Co and Li/Mn interlayer mixing are unlikely to happen.

Conclusions and Future Directions

We have made significant progress on exploring the fading mechanisms of electrode materials for lithium ion battery over the last year. The materials we studied typically include Si as high capacity anode and layer structured lithium transition metal oxide as cathode. For Si anode, we clarified the effect of nanometer scale coating layer on the lithiation kinetics and the effect of coating layer on the capacity retention. The result we captured on coating layer effect can guide the optimized design of coating layer on Si for enhanced performance. For the layer structured cathode materials, we discover that layer to spinel phase transition is initiated from the surface and propagate towards the inner part of the particle. We quantified surface oxygen loss and its correlation with the phase transition. We noticed that Ni migrates from inside towards particle surface during the cycling of the battery. Among Ni, Co, and Mn, we determined by experiment that Ni is prone to mix with lithium layer as compared with Co and Mn, which is consistently supported by the theoretical calculations. These structural and chemical evolution directly correlate with capacity fading and voltage decay. Looking into the future, we will continue our atomic to electrode scale diagnosis for both cathode and anode, intending to focus on probing lattice stability, interfacial interaction between electrode and

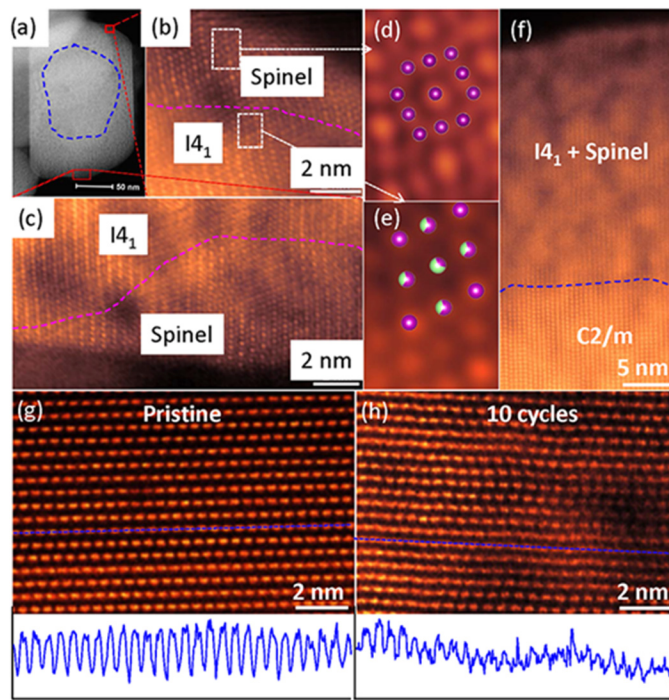


Figure V- 168: (a-c) [010] zone STEM-HAADF images to show a 10-cycles Li₂MnO₃ particle and its outer surface lattice structure. (d) and (e) highlight the lattice difference between Mn₃O₄-spinel and I₄₁ structure. Purple and green indicate Mn and Li, respectively. (f) [100] zone STEM-HAADF image of the surface layer after 10 cycles. STEM-HAADF images to show inner bulk lattice structure of pristine sample (g) and 10-cycles sample (h). The intensity profile along the blue lines in (g) and (h) are shown in each figure

electrolyte and their correlation with capacity fading. This research will guide optimized synthesis and modification of electrode materials for enhanced battery performance.

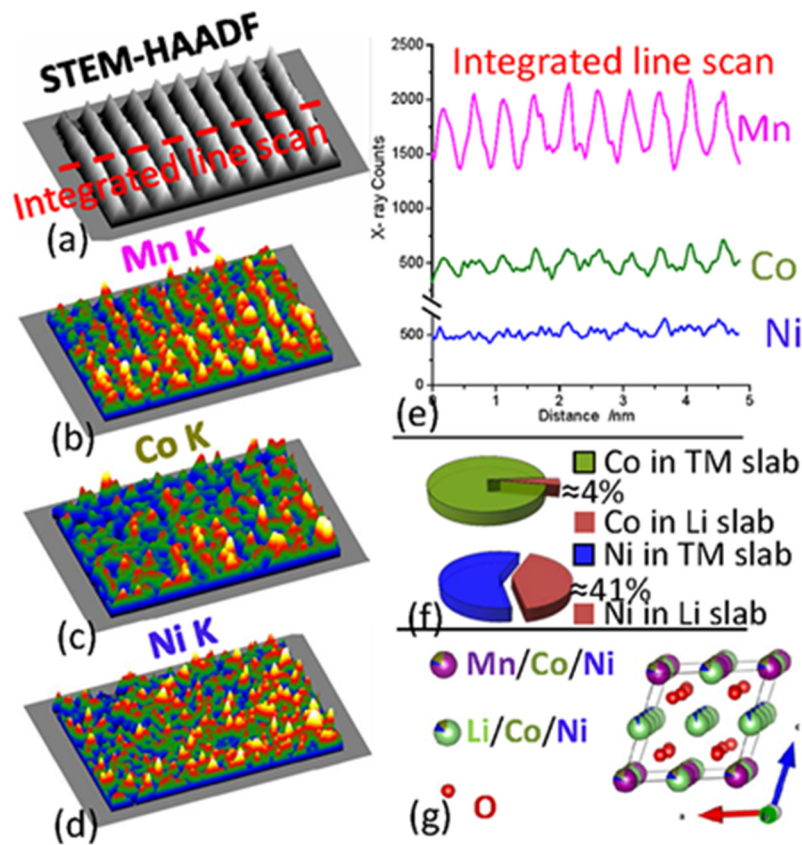


Figure V-169: $\text{Li}_{1.2}\text{Ni}_{0.13}\text{Co}_{0.13}\text{Mn}_{0.54}\text{O}_2$ (NC-LMR) sample. (a) [010] zone axis STEM-HAADF image showing the EDS mapping region. (b) Surface plot of Mn K map. (c) Surface plot of Co K map. (d) Surface plot of Ni K map. (e) Integrated line scan profile showing X-ray counts distribution across the layered structure. (f) Based on counts ratio that from TM-layer and Li-layer, 4% Co and 41% Ni were estimated to seat in Li-layer due to an interlayer mixing. (g) Optimized crystal model for NC-LMR based on EDS mapping results

FY 2015 Publications/Presentations

1. Luo, Langli, Peng Zhao, Hui Yang, Borui Liu, Ji-Guang Zhang, Yi Cui, Guihua Yu, Sulin Zhang, and Chong-Min Wang "Surface Coating Constraint Induced Self-Discharging of Silicon Nanoparticles as Anodes for Lithium Ion Batteries," *Nano Letters*, DOI: 10.1021/acs.nanolett.5b03047.
2. He, Yang, Chunmei Ban, Arda Genc, Lee Pullan, Jun Liu, Ji-Guang Zhang, Scott Mao, and Chongmin Wang, "In-Situ Transmission Electron Microscopy Probing of Native Oxide and Artificial Coating Layer on Silicon Nanoparticles for Lithium Ion Batteries", *ACS Nano* 8 (2014): 11816-11823.
3. Yan, Pengfei, Anmin Nie, Jianming Zheng, Yungang Zhou, Dongping Lu, Xiaofeng Zhang, Rui Xu, Ilias Belharouak, Xiaotao Zu, Jie Xiao, Khalil Amine, Jun Liu, Fei Gao, Reza Shahbazian-Yassar, Ji-Guang Zhang, and Chong-Min Wang, "Evolution of lattice structure and chemical composition of the surface reconstruction layer in $\text{Li}_{1.2}\text{Ni}_{0.2}\text{Mn}_{0.6}\text{O}_2$ cathode material for Lithium ion batteries," *Nano Letters* 15 (2015): 514-522.
4. Yan, Pengfei, Liang Xiao, Jianming Zheng, Yungang Zhou, Yang He, Xiaotao Zu, Scott X. Mao, Jie Xiao, Fei Gao, Ji-Guang Zhang, and Chong-Min Wang, "Probing the Degradation Mechanism of Li_2MnO_3 Cathode for Li-Ion Batteries," *Chem. Mater.* 27 (2015): 975-982.
5. Luo, Langli, Hui Yang, Pengfei Yan, Jonathan J. Travis, Younghlee Lee, Nian Liu, Daniela Molina Piper, Se-Hee Lee, Peng Zhao, Steven M. George, Ji-Guang Zhang, Yi Cui, Sulin Zhang, Chunmei Ban, and Chong-Min Wang, "Surface-Coating Regulated Lithiation Kinetics and Degradation in Silicon Nanowires for Lithium Ion Battery," *ACS Nano* 9 (2015): 5559-5566.

6. Lu, Ping, Pengfei Yan, Eric Romero, Erik David Spoerke, Ji-Guang Zhang, and Chong-Min Wang, "Observation of Electron-Beam-Induced Phase Evolution Mimicking the Effect of the Charge–Discharge Cycle in Li-Rich Layered Cathode Materials Used for Li Ion Batteries," *Chem. Mater.* 27 (2015): 1375–1380.
7. Yan, Pengfei, Jianming Zheng, Dongping Lv, Yi Wei, Jiaxin Zheng, Zhiguo Wang, Saravanan Kuppan, Jianguo Yu, Langli Luo, Danny Edwards, Matthew Olszta, Khalil Amine, Jun Liu, Jie Xiao, Feng Pan, Guoying Chen, Ji-Guang Zhang, and Chong-Min Wang, "Atomic-Resolution Visualization of Distinctive Chemical Mixing Behavior of Ni, Co, and Mn with Li in Layered Lithium Transition-Metal Oxide Cathode Materials," *Chem. Mater.* 27 (2015): 5393–5401.
8. Yan, Pengfei, Jiguang Zhang, Chongmin Wang, "Microscopic Characterization of Structural and Chemical Evolution of $\text{Li}_{1.2}\text{Ni}_{0.2}\text{Mn}_{0.6}\text{O}_2$ Cathode Material upon Cycling," Presented at the 2014 MRS Fall Meeting, Boston, MA, November 2014.

V.F.8 Characterization Studies of High Capacity Composite Electrode Structures (ANL)

Objectives

- The primary objective of this project is to broaden the scope of studies of electrode materials relevant to the BMR program, using DOE and international user facilities through collaborative efforts.
- More specifically, the goal is to use a range of X-ray techniques, including *in situ* methods, such as X-ray diffraction (XRD), X-ray absorption (XAS), and X-ray reflectivity (XR) at the Advanced Photon Source (APS); high-resolution transmission electron microscopy (HRTEM) at Argonne's Electron Microscopy Center (EMC) and elsewhere; and neutron scattering at the ISIS facility, Rutherford Appleton Laboratory (RAL), UK and/or ORNL's Spallation Neutron Source (SNS).

Project Details

Michael Thackeray (Argonne National Laboratory - PI)

9700 South Cass Avenue
Argonne, IL 60439

Phone: 630-252-9184; Fax: 620-252-4176
E-mail: thackeray@anl.gov

Jason R. Croy (Argonne National Laboratory - co-PI)

9700 South Cass Avenue
Argonne, IL 60439
Phone: 630-252-5917; Fax: 620-252-4176
E-mail: croy@anl.gov

Start Date: October 2014

Projected End Date: September 2015

Technical Barriers

- Low energy density.
- Poor low temperature operation.
- Abuse tolerance limitation.

Technical Targets (USABC – End of life)

- 142 Wh/kg, 317, W/kg (PHEV 40 mile).
- Cycle life: 5000 cycles.
- Calendar life: 15 years.

Accomplishments

- Developed a successful model of stacking fault defects in Li_2MnO_3 and composite cathode materials in collaboration with the Rutherford Appleton Laboratory (U.K.).
- Established joint study with Pacific Northwest National Laboratory's Environmental Molecular Sciences Laboratory for high resolution microscopy of complex, integrated cathode structures.
- Established ongoing studies of integrated layered and spinel structures with the Northwestern Atomic and Nanoscale Experimental Center (NUANCE).
- Initiated joint experimental and theoretical studies on the role of active and non-redox active cations in layered structures.

Introduction

Multi-component electrodes, $y[\text{xLi}_2\text{MnO}_3 \bullet (1-\text{x})\text{LiMO}_2] \bullet (1-y)\text{LiM}_2\text{O}_4$ (M=Mn, Ni, Co), are currently the most promising class of cathodes for next-generation Li-ion batteries. However, the degradation mechanisms of these cathodes are not well understood. This lack of understanding is due to the complexity of the pristine materials, control over their synthesis, and the complex atomic-level processes that occur on cycling. In order to create more robust structures, a detailed understanding of the structure-electrochemical properties of these materials must be obtained.

Approach

The objectives outlined above will be accomplished by:

1. Utilizing DOE's user facilities and beyond to gain fundamental insights into complex $y[x\text{Li}_2\text{MnO}_3 \bullet (1-x)\text{LiMO}_2] \bullet (1-y)\text{LiM}_2\text{O}_4$ electrodes.
2. Combining data sets from multiple, advanced characterization techniques to enable a more complete understanding of complex structures across multiple length scales.
3. Combining experimental results with computation to advance the design of robust cathode structures.
4. Establishing national and international collaborations with experts in the field to foster innovation.

Results

Modeling of Stacking Faults in $x\text{Li}_2\text{MnO}_3 \bullet (1-x)\text{LiMO}_2$ Cathode Materials

The first difficulty in understanding $y[x\text{Li}_2\text{MnO}_3 \bullet (1-x)\text{LiMO}_2] \bullet (1-y)\text{LiM}_2\text{O}_4$ ($M=\text{Mn, Ni, Co}$) structures results from stacking fault disorder that occurs along the c-axis of the monoclinic ($C2/m$) structure in either pure or integrated Li_2MnO_3 -based materials. Collaborations with W.I.F. David and T. Wood at the Rutherford Laboratory/Oxford University, UK, were established to model these faults as a first step. Figure V- 170(a) shows a view along the c-axis for pure $C2/m$ stacking where $C2/c$ and $P3_{12}$ are also possible. Simulations showed that the $C2/m$ stacking is most representative and was used in subsequent modeling. Figure V- 170(b) shows a zoomed image of the “superstructure” peaks that appear in Li_2MnO_3 as a result of LiMn_6 ordering throughout the mixed Li/Mn planes. The diffuse background, above the model curve, is a result of faulted stacking along the c-axis. It is clear from Figure V- 170(b) that standard methods do not describe the faulted stacking. Figure V- 170 (c) shows the results of a DIFFaX model where the background and the superstructure peaks have been fitted. The diffuse background and peak intensities above the background are described well by the DIFFaX model. An important implication of these results is the possibility of modeling “domain” geometries within composite structures and relating that information to electrochemical performance.

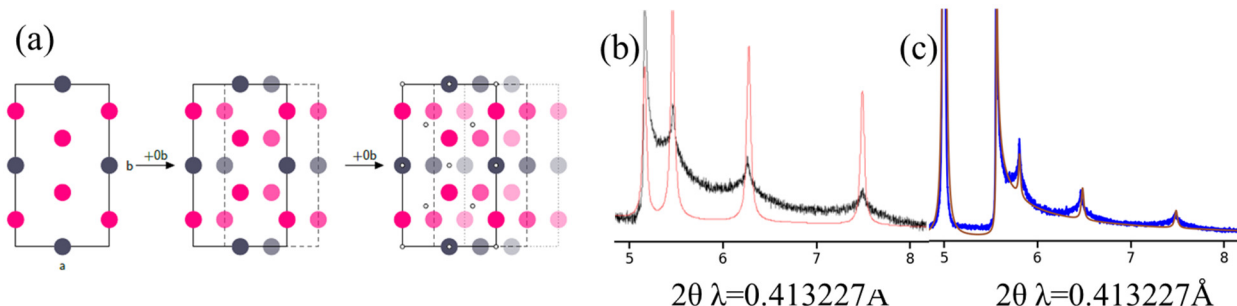


Figure V- 170: a) Pure $C2/m$ stacking in Li_2MnO_3 . (b) Standard Reitveld refinement (red) of Li_2MnO_3 diffraction data (black) showing the misfit due to stacking faults. (c) Fit of the data in (b) using a stacking fault model derived from DIFFaX analysis

For example, the current model indicates that ~25% of the layers within the sample have pure $C2/m$ stacking. Figure V- 171(a) and (b) show similar analysis for a composite $0.5\text{Li}_2\text{MnO}_3 \bullet 0.5\text{LiMn}_{0.5}\text{Ni}_{0.5}\text{O}_2$ ($\text{Li}_{1.2}\text{Mn}_{0.6}\text{Ni}_{0.2}\text{O}_2$) cathode powder where including regions of pure $C2/m$ stacking captures these peaks and a better fit to the data is obtained. X-ray and neutron data has been collected on a series of end-member and integrated $y[x\text{Li}_2\text{MnO}_3 \bullet (1-x)\text{LiMO}_2] \bullet (1-y)\text{LiM}_2\text{O}_4$ ($M=\text{Mn, Ni, Co}$) materials. Similar analysis on this series of integrated structures is ongoing.

Electron Microscopy of Integrated Structures

A major objective of this project is to establish collaborations across the community and engage various experts in the challenge of characterizing these complex systems. While nominally denoted as $y[x\text{Li}_2\text{MnO}_3 \bullet (1-x)\text{LiMO}_2] \bullet (1-y)\text{LiM}_2\text{O}_4$, it is likely that the small “spinel” components of these materials are rather complex, localized, and possibly incoherent to averaging techniques. Nevertheless, electrochemical results have unequivocally shown their important effects on cathode performance. In FY15 collaborations and joint studies were established between the BMR cathode group at Argonne and the Northwestern Atomic and Nanoscale Experimental Center (NUANCE) as well as Pacific Northwest National Laboratory’s (PNNL) Environmental Molecular Sciences Laboratory (EMSL) for high resolution microscopy. These world-class facilities will be used to follow the evolution of local structures in integrated cathode materials as a function of synthesis conditions and cycling protocol, post-mortem. Figure V-172 shows the first- (solid) and second-cycle (dashed) charge/discharge voltage curves for a series of $\text{Li}_{2-x}\text{MnO}_y$ cathode powders. Integration of a Mn spinel component is achieved by starting with the Li_2MnO_3 stoichiometry (i.e., $x=0$) and systematically reducing the lithium content in the mixed precursors before firing. The voltage profiles clearly indicate spinel-like plateaus increasing in complexity and magnitude (e.g., capacity) with increasing x . Of note, and clearly visible in the first-charge (solid) for $x \geq 0.5$, are plateaus at ~ 4.5 V and ~ 4.9 V which have been attributed to defects in the LiMn_2O_4 structure (e.g., tetrahedral Mn).

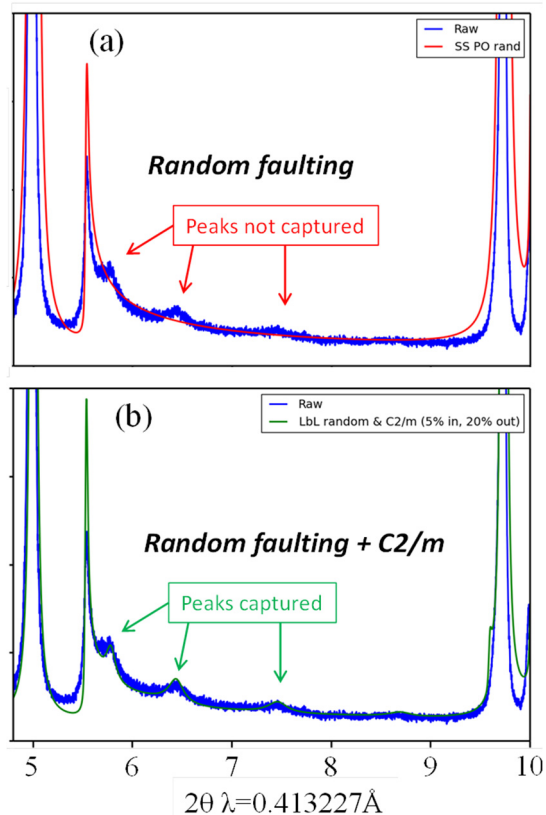


Figure V-171: a) Raw X-ray powder diffraction data for $\text{Li}_{1.2}\text{Mn}_{0.6}\text{Ni}_{0.2}\text{O}_2$ with no coherent stacking. (b) Fit to the data in (a) using randomly faulted + coherent $\text{C}2/\text{m}$ regions calculated from DIFFaX

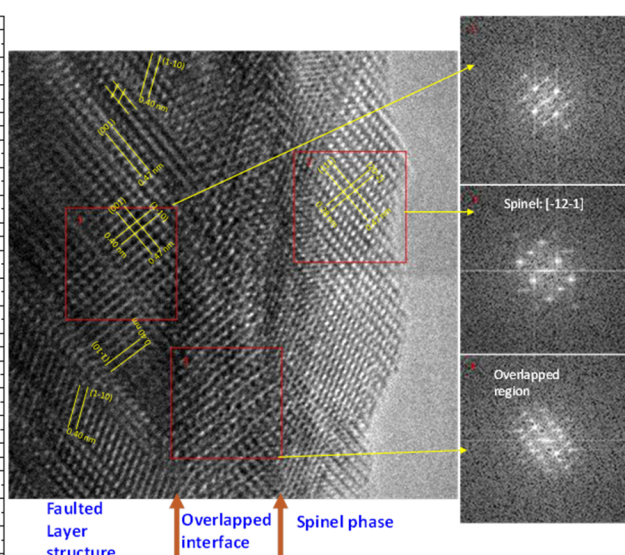
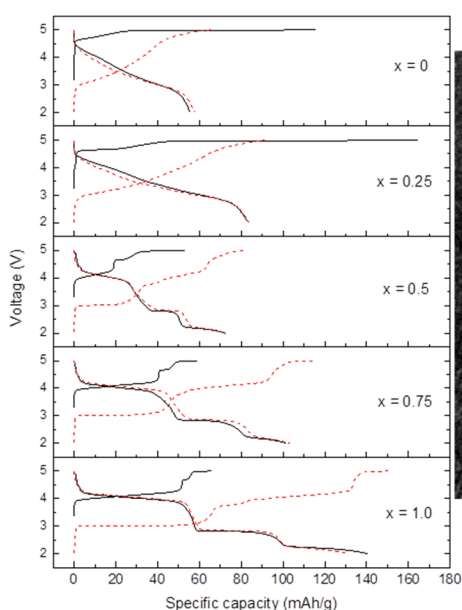


Figure V-172: (left) First- (solid) and second-cycle (dashed) charge/discharge voltage profiles for a series of layered-spinel $\text{Li}_{2-x}\text{MnO}_y$ cathode powders. (right) Electron microscopy/diffraction data, acquired at NUANCE, for the $x=1$ sample

The right hand side of Figure V- 173 shows electron microscopy/diffraction data acquired at NUANCE, in collaboration with V. Dravid, J. Wu, and Q. Li (for the x=1 sample). An interesting progression can be seen from the bulk to the surface of the particles. The bulk of the particles consist mainly of a highly faulted structure which gives way to a complex interface leading into a highly crystalline spinel phase on the surface. This result is interesting in that it has obvious implications for affecting the stability of cathode surfaces. Control over these structures and defects will play an important role in stabilization of electrodes.

Cation Migration in Layered Structures

The migration of cations M and M' in $\text{Li}_{1+x}(\text{MM}')_{1-x}\text{O}_2$ cathodes ($\text{M=Mn, Ni, Co...; M'=Mg, Ga, Al...}$) is a subject of significant importance. Although the stabilities of many elements have been studied both experimentally and theoretically, it is not clear that the underlying mechanisms and connection with calculations of migration are well understood. A recent report shows that non-redox active Ga, in $\text{LiCo}_{1-x}\text{Ga}_x\text{O}_2$ ($x=0.05, 0.075$), migrates from the octahedral sites of the TM layers immediately on charge with significant migration at just 10% state-of-charge and that the first-cycle voltage profiles are altered with respect to pure LiCoO_2 . Figure V- 173 (a) shows DFT calculations (H. Iddir, ANL) on Ga-doped LiCoO_2 . In agreement with experiment, Ga prefers to be situated in the octahedral sites of the Co layers. Furthermore, Ga-O distances are slightly larger than Co-O distances, in agreement with EXAFS analysis, Figure V- 173 (b). As a second model system, redox-active Cr substitution in $\text{LiCo}_{1-x}\text{Cr}_x\text{O}_2$ ($x=0, 0.05, 0.075$) was also studied. Figure V- 173 (c) shows the initial portion of the first-charge profile for $x=0, 0.05$, and 0.075 . As in the non-redox case of Ga, low-level Cr substitutions clearly alter the voltage profiles when substituted in the LiCoO_2 matrix, even at very low lithium removal; although the voltage profiles are altered in completely different ways. Detailed EXAFS, NMR, and DFT studies are currently ongoing for these and other systems.

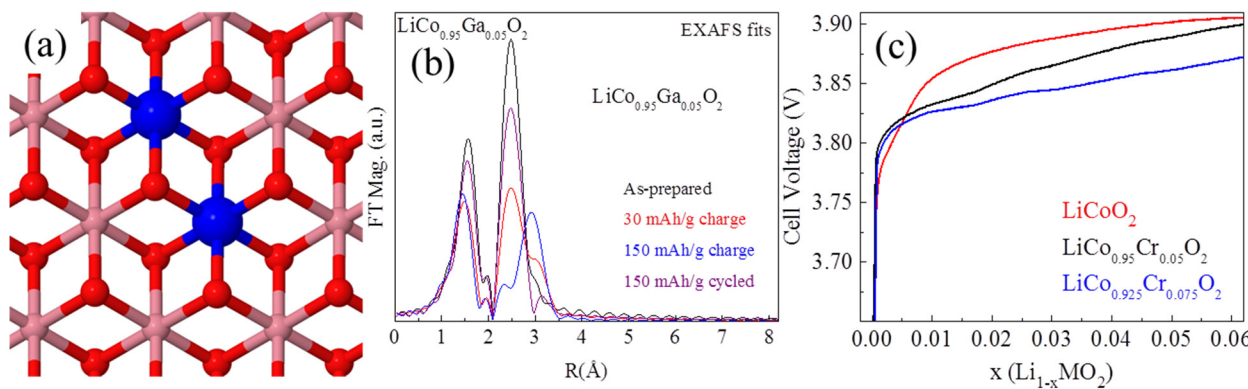


Figure V- 173: (a) DFT simulation of Ga-substituted LiCoO_2 . (b) EXAFS fits of $\text{LiCo}_{1-x}\text{Ga}_x\text{O}_2$. (c) First-cycle voltage curves for $\text{Li}_{1-x}\text{Cr}_x\text{O}_2$

Conclusions and Future Directions

Integrated $y[\text{xLi}_2\text{MnO}_3 \bullet (1-\text{x})\text{LiMO}_2] \bullet (1-y)\text{LiM}_2\text{O}_4$ (M=Mn, Ni, Co) cathode structures have shown promise for achieving high energy densities with bulk structural stability. However, to fully ascertain the potential of this class of electrodes requires a detailed understanding of how stoichiometry and synthesis conditions influence not only bulk structure but, perhaps more importantly, what role they play in the complex local structures that form in the final products. These structures can have a large impact on the mechanisms of cation migration, oxygen loss, surfaces, and electrode stability. Important collaborations have been established and detailed studies of local environments and cation migration as a function of composition and synthesis conditions are revealing important clues about the nature of integrated cathode structures. Future work will focus mainly on the characterization of layered-layered-spinel compositions in order to understand how synthesis parameters can be manipulated to control both structural and elemental compositions of promising materials.

FY 2015 Publications/Presentations

1. Thackeray, M.M., B. R. Long, J. R. Croy, J. S. Park, Y. Shin, G. Krumdick, J. G. Wen and D. Miller, "Progress and Challenges in Designing High Capacity Cathodes for Lithium-Ion Cells," Invited presentation at the Annual Battery Seminar & Exhibit, Fort Lauderdale, FL, March 2015.
2. Croy, Jason R., "User Facilities for Energy Storage Materials Research," ES235_Thackeray_2015_O, U.S. DOE Vehicle Technologies AMR, 2015.
3. Croy, Jason R., "Current Research on High-energy Li-Ion Batteries at Argonne National Laboratory," Invited presentation, Advanced Automotive Battery Conference, Detroit, MI, June 2015.
4. Croy, Jason R., K. Gallagher, M. Balasubramanian, J.S. Park, B.R. Long, and M.M. Thackeray, "High Energy Lithium-Ion Research and Development at Argonne National Laboratory," Invited presentation, IAOEES-EEST, Vancouver, BC, Canada, August 2015.
5. Croy, Jason R., Joong Sun Park, Kevin G. Gallagher, Brandon R. Long, Michael M. Thackeray, Mahalingam Balasubramanian, Fulya Dogan, Matthew Suchomel, Dean Miller, and Jianguo Wen, "High-Energy, Composite, Lithium-Ion Cathodes," Invited lecture, Argonne Outloud Public Lecture Series, Lemont, IL, 2015.